Numerical modeling of magnetic reconnection in laser-induced high energy density plasmas

Andrey Sladkov



Universite Pierre et Marie Curie
Institute of Applied Physics of the Russian Academy of Sciences

Ecole doctorale 127: Astronomie et Astrophysique d'Ile-de-France
LPP - UMR7648

NUMERICAL MODELING OF MAGNETIC RECONNECTION IN LASER-INDUCED HIGH ENERGY DENSITY PLASMAS

Présentée par
Andrey Sladkov

Thèse de doctorat de Physique des plasmas

Présentée et soutenue publiquement à Paris, le 27 Septembre 2019, devant le jury composé de

Composition du Jury :

Caterina RICONDA	Professeure des Université	Président du Jury
Valery BYCHENKOV	Professeur	Rapporteur
Emmanuel D'HUMIÈRES	Professeur des Université	Rapporteur
Artem KORZHIMANOV	Chercheur principal	Directeur de thèse
Mikhail STARODUBTSEV	Directeur du Laboratoire	Examinateur
Roch SMETS	Maître de conférence	Directeur de thèse

October 15, 2019

Contents

Page

1 Magnetic Reconnection in HEDP **1**
1.1 General consideration . . . 1
1.1.1 Definition and fundamental concepts . . . 1
1.1.2 Magnetic configurations of the current sheet . . . 5
1.1.3 Slow reconnection . . . 9
1.1.4 Fast reconnection . . . 10
1.1.5 The GEM challenge : a corner stone . . . 12
1.2 Fast magnetic reconnection . . . 14
1.2.1 How to define and use a reconnection rate . . . 15
1.2.2 Reconnection with a guide-field . . . 16
1.2.3 Asymmetric current sheet . . . 18
1.2.4 Driven reconnection . . . 21
1.3 Satellite observations . . . 23
1.3.1 Reconnection in solar coronna . . . 23
1.3.2 Reconnection in the Earth magnetosphere . . . 24
1.3.3 The revolution of multi-points measurements . . . 25
1.4 Laboratory experiments . . . 28
1.4.1 Z-pinch: the MAGPIE facility . . . 28
1.4.2 Magnetic Reconnection eXperiment (MRX) . . . 29
1.4.3 Large Plasmas Device at UCLA . . . 31
1.4.4 High power lasers . . . 33

2 Numerical simulations **37**
2.1 Fluid and kinetic formalisms . . . 37
2.1.1 What are the relevant scales ? . . . 38
2.1.2 Kinetic effects for both populations . . . 39
2.1.3 Finite Larmor radius effects . . . 40
2.1.4 Effects of mass ratio and speed of light . . . 42
2.2 Why is the hybrid approach relevant ? . . . 43
2.2.1 Kinetic treatment of ions : particles or Vlasov approach . . . 43
2.2.2 Quasineutrality . . . 45
2.2.3 Transverse component of the displacement current . . . 45

2.2.4 The electron Ohm's law . . . 46
2.3 Closure equation for the electron pressure . . . 47
2.3.1 Isothermal closure . . . 47
2.3.2 Time evolution of the pressure tensor . . . 48
2.3.3 The driver term . . . 48
2.3.4 The cyclotron term . . . 49
2.4 Closure equation for the electron heat flux . . . 50
2.4.1 How to consider the heat flux ? . . . 50
2.4.2 The Landau-fluid closure of Hammet & Perkins . . . 51
2.4.3 Non-local vs local heat flux . . . 52
2.4.4 Heat flux in a magnetized plasma : Righi-Leduc effect . . . 52
2.4.5 Nernst effect : Nernst velocity in the Ohm's law . . . 53
2.5 Numerical issues . . . 53
2.5.1 Normalization . . . 54
2.5.2 Smoothing the ion density and velocity . . . 54
2.5.3 The necessity to consider an ion background . . . 54
2.5.4 Resistivity and hyper-viscosity . . . 55
2.5.5 Numerical treatment of the cyclotron term . . . 55
2.5.6 Smoothing the electron pressure tensor . . . 56

3 Non-gyrotropic pressure effects 59
3.1 Reconnection in a Harris sheet . . . 59
3.1.1 The Harris kinetic equilibrium . . . 59
3.1.2 The tearing mode in an unperturbed Harris sheet . . . 62
3.1.3 The role of the electron magnetization . . . 63
3.1.4 Reconnection neighbor : a 3 scales region . . . 63
3.2 Structure of the full electron pressure tensor . . . 65
3.2.1 Diagonal components . . . 66
3.2.2 Off-diagonal components . . . 70
3.2.3 The role of $P_{xx} - P_{yy}$ . . . 73
3.2.4 The role of P_{xy} on separatrix . . . 74
3.3 Consequences for the reconnection process . . . 76
3.3.1 Bifurcated current sheet . . . 76
3.3.2 Reconnection rate . . . 78
3.3.3 Consequences of the isotropization operator . . . 81

4 Driven reconnection 85
4.1 Reconnection in laser-generated plasmas . . . 85
4.1.1 Biermann-Battery effect . . . 85
4.1.2 Experimental set-up . . . 87
4.1.3 Righi-Leduc and Nernst effects . . . 87
4.1.4 Results from hydro-radiative simulations . . . 89
4.1.5 Initial analytical profiles . . . 91

4.1.6 Initial setup for bubbles . . . 92
4.2 Role of the ions temperature . . . 96
4.2.1 Reconnection electric field . . . 97
4.2.2 Density structure . . . 100
4.2.3 Magnetic structure . . . 104
4.2.4 Inflow and outflow velocity structure . . . 107
4.2.5 On the role of the background . . . 109
4.3 Physics of the electron fluid . . . 111
4.3.1 Time evolution of E_z . . . 112
4.3.2 Density structure . . . 114
4.3.3 Magnetic structure . . . 116
4.3.4 Velocity structure . . . 117
4.3.5 Including the full electron pressure tensor . . . 119
4.3.6 Vacuum problem in colliding bubbles . . . 122
4.4 Driven magnetic reconnection . . . 128
4.4.1 The magnetic piston to drive reconnection . . . 129
4.4.2 Radial expansion velocity profile . . . 130
4.4.3 Spot-size and amplitude of the magnetic driver . . . 131
4.5 Ellipsis initialisation . . . 134
4.5.1 How to define a divergence free magnetic field . . . 135
4.5.2 Numerical validation and gain . . . 137
4.5.3 A test case for LMJ experiments . . . 138

Bibliography **152**

A Algorithm **153**
.1 Main part . . . 153
.2 Implicit scheme for the pressure tensor . . . 154
.3 Explicit Subcycling scheme for the pressure tensor . . . 156

Introduction

In space and astrophysical plasmas, many phenomena are associated with sudden and intensive releases of energy: magnetic substorm, solar flares, accelerated jet in accretion disks around compact objects,... The origin of strong energetization processes was a quite intensive topic for astrophysical plasmas. The idea is that the processes of turbulence, shocks and magnetic reconnection are very important:

- turbulence is up to now the best candidate to explain the heating of the solar wind, by Alfvénic magnetic turbulence, widely studied by in-situ spacecrafts
- crossing a shock is also an efficient way to gain energy, so the diffusion shock acceleration (resulting from magnetic fluctuations) is the best scenario for the acceleration of cosmic rays at super nova remnant
- magnetic reconnection is certainly the central process in accelerating particles from the solar wind which are associated with aurora borealis

In this thesis, we focus on the reconnection process, and more specifically occurring in collisionless plasmas.

As a first rough picture, magnetic reconnection consists in opening two neighboring magnetic field lines and "plug" one piece of each newly opened magnetic field lines with the other one. Opening of the magnetic field lines is not that easy to do, and we will see that in collisionless plasmas, such a mechanism should be prohibited from a theoretical point of view. Furthermore, a net of magnetic field lines drawing a closed curve is called a flux tube. According to the Lorentz force, the flux tube is filled with charged particles where they gyrate around the magnetic field lines and after that it is a kind of trapped lines in the flux tube. Opening a flux tube offers new perspectives for the particles which can swap from one flux tube to the other.

The topology of the magnetic field lines is modified by magnetic reconnection. So occurring such a process has to satisfy an energy principle, meaning some energy is needed to make these changes. This point will be extensively discussed in this thesis but we find out that this process is associated with a significant energetization of the particles and their kinetic energy coming from the magnetic energy stored in this associated topology.

Magnetic diffusion, resulting from collisions between particles, is a way for these particles to drift across the flux tubes, and to halt their trapping inside a given flux tube. But while collisions are mandatory, such a process is generally very slow. Furthermore, most

of space and astrophysical plasmas are collisionless. For instance, in the solar wind the mean free path is about the Sun-Earth distance. Magnetic diffusion is not that interesting in this frame as it is doubtful about its efficiency and fastness (which is very poor).

Magnetic Reconnection (MR) is an interesting process for essentially two reasons :

i it allows particles to travel in region a priori not reachable because magnetically isolated

ii it is an efficient way to accelerate particles and create a supra-thermal component of this plasma.

Up to now, most of the experimental data, when studying magnetic reconnection, are coming from in-situ observation on board satellites, cruising in the heliosphere. While the investigated spatial and temporal scales are pretty large compared to the size of the satellites and their antennas, such approach allows to perform very nice measures and gives insights into the micro-physics. But the drawback is that, because of their orbits we do not totally control the region of space they explore, neither the time at which they go there. Hence, there are no ways to "ask" a satellite to go and investigate a coronal mass ejection, if the orbit of the satellite is not appropriate. Satellite measures suffer from the lack of reproducibility of the events. Furthermore, there is generally one point of measure which is moving both in space and time, meaning it is not that easy to make the difference between temporal effects and spatial gradients.

Quite recently several laboratory experiments have been built as an alternative, in a new discipline generally called "laboratory astrophysics". In order to investigate magnetic reconnection, a promising setup has been explored, first in 2006, using high power lasers. Two lasers are impinging a solid target to create, because of Biermann-Battery effect, two magnetic fields shells with anti-parallel magnetic fields. If these two structures are close enough (as controlled by the distance between the two focal spots), because of the anti-parallel configuration, MR can occur. This configuration has highly appreciable qualities, because of the diagnostics can be made of the magnetic field (through the co-called proton radiography technique employing an auxiliary beam of energetic laser-accelerated protons) and of the plasma parameters (density and temperature).

Such conditions are called High Energy Density Plasmas (HEDP), because the associated pressure is above 10^{12} Pa. This is of course very different from astrophysical plasmas where, as an example, the pressure in the interstellar medium is around 10^{-14} Pa. Nevertheless, in laboratory experiments the conditions can be quite similar as in space plasmas: the plasma is collisionless and the magnetic pressure is of the order of the kinetic pressure. Such laboratory experiment is a promising way for understanding MR at play in space and astrophysical plasmas.

While the experimental set-up to study magnetic reconnection with high-power lasers is nice, we need to work on the way to simulate such topologies from a numerical point of view. More precisely, the three-dimensional geometry of the problem, as well as the physics at play, both need some work in order to be able to interpret the laboratory experiments of magnetic reconnection. The work presented in the thesis is intended to help, by means

of numerical simulations, the investigation of data collected in a very recent experiment at Laser Mega Joule, in May and June 2019. Because of substantial delay for this experiment (the collected data being at this date not yet explored), comparison between numerical simulations and experiments are lacking, but it is nevertheless an opportunity to discuss most aspects of collisionless magnetic reconnection in HEDP.

The first chapter describes the definitions we need during the work and also observes experimental and numerical works on magnetic reconnection problem. The second chapter challenges the numerical approach and its issues and complexity. The third chapter shows how to outflank the problem of closure equation for electron fluid in context of Harris sheet configuration. The last chapter overviews a numerical study of the laboratory magnetic reconnection in HEDP.

Chapter 1

Magnetic reconnection in High-Energy-Density-Plasmas

This chapter describes the fundamental aspects of magnetic reconnection. By fundamental we mean that it can be applied to different reconnection problems wherever they occur: on solar arches, at the interface between the solar wind and a planetary magnetosphere, or in a laser plasma experiment. The first section is dedicated to definitions and historical models of magnetic reconnection. The second section highlights the importance of the topological constraints on magnetic reconnection and states the problem of the reconnection rate, which allows to quantify the efficiency of the process. The third section is a discussion on what has been recently obtained with satellites observations. The last section describes modern laboratory experiments which can be applied to magnetic reconnection.

1.1 General consideration on magnetic reconnection

1.1.1 Definition and fundamental concepts

We postpone the definition of magnetic reconnection to the end of this section because we need to introduce concepts, like "moving" magnetic field lines, "frozen-in" condition and "diffusion region" of reconnection.

Let's start with a two-dimensional problem: two parallel electric current of equal magnitude I, perpendicular to the $X-Y$ plane. Such configuration is fully defined by the vector potential $\mathbf{A}(0,0,A_z)$ which out-of-plane component is

$$A_z(x,y,t) = \frac{I}{c}(\log(x^2+(y-l(t)/2)^2) + \log(x^2+(y+l(t)/2)^2)) \tag{1.1}$$

l being the distance between the two currents. The magnetic field is

$$\mathbf{B} = \nabla \times \mathbf{A} \tag{1.2}$$

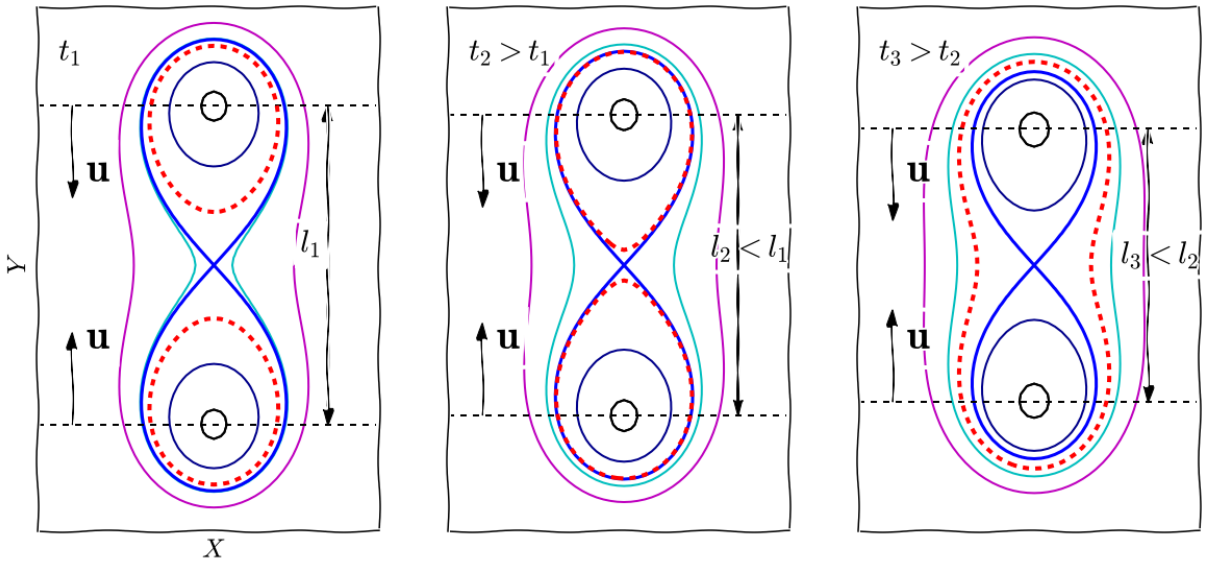

Figure 1.1: Isocontours of the vector potential A_z of two parallel currents approaching each other. Each color line represents a magnetic field line, the blue line is a special one called separatrix.

Substituting that expression in the equation of *magnetic field lines* $d\mathbf{l} \times \mathbf{B} = 0$, the last term gives $-d_x(\partial_x A_z) - d_y(\partial_y A_z) = 0$. Hence, $d\mathbf{l}$ is normal to the gradient of A_z, that is $d\mathbf{l}$ is along the iso-A_z. One of the useful simplification of the two-dimensional case is to get magnetic field lines one can use isocontours of the only one component of the vector potential, while in the three-dimensional case we also have A_x and A_y components.

Fig. 1.1 portrays the isocontours of the vector potential A_z in the $X - Y$ plane. Each color is associated with a given constant value of A_z. The blue line represents the separatrix, defined as the boundary between magnetic field lines of different connexion: inside the separatrix, the field lines are closed around each current, while outside of it, the magnetic field lines enfold both currents. The coordinates origin is at the saddle point of the vector potential. This singular point is called the "*X point*", and also can be defined as the point where separatrices are crossing. As the magnetic field vanishes in the vicinity of this point, it can also be named as a "neutral point". When generalizing this topology to the three-dimensional case, one talks about "X line" and "neutral line".

Considering the closed field lines moving toward each other with a velocity $2\mathbf{u}$, the red lines of left panel expand in an essentially radial direction. In the middle panel, they get close to each other, and once the lines touch, they become the topological definition of the separatrix. After their *reconnection*, they continue the expansion, forming a single magnetic field line, which encloses both current structures (right panel). When considering the plasma in the reconnection region, its particles are accelerated because of the electric field associated with the global motion of the magnetic field lines.

The electric field associated with this time evolution of the vector potential is

$$\mathbf{E} = -\partial_t \mathbf{A} \tag{1.3}$$

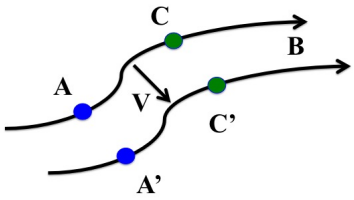

Figure 1.2: Schematic illustration of the frozen-in theorem; the two point A and C, initially on the same magnetic field lines advect at velocity u, and transform in A' and C' after convection.

The local value of the Z component of this electric field, at the X point, is a key feature of the magnetic reconnection process. If the amount of magnetic flux δA_z initially in one of the closed structure is transported in the large enclosing structure by magnetic reconnection in a time δt, $E_z = -\delta A_z/\delta t$ quantifies the efficiency of the magnetic reconnection process. Near the X point, the magnetic potential $\mathbf{A}$ can be expanded in a Taylor series $\mathbf{A}(x, y, t) = \mathbf{A}(0, 0, t) + 2I/(c(x^2 - y^2))$. Hence, the induced electric field is in the Z direction, as $\mathbf{A}$ has only a Z component, and the magnitude of the electric field is $E_z = 8I|\mathbf{u}|/(cl)$. The induced *out-of-plane electric field* is widely used as a quantitative characteristic of the reconnection process.

To be able to talk about the magnetic field lines motion in real space, we need to visualize them. To introduce the speed of magnetic field lines, we start by introducing the plasma *frozen-in condition*. In 1942 Alfvén [Alf42] introduced the conception of a colissionless plasma frozen in the ambient magnetic field. The frozen-in condition states that the colissionless plasma and the magnetic field move together at the $\mathbf{V}$ velocity. To understand when the frozen-in condition is applicable, we choose two points A and C on a moving magnetic field line Fig. 1.2, and wonder about conditions for these points to stay on the same line $\mathbf{AC}$ during the motion of the plasma with velocity $\mathbf{V}$. This writes

$$d_t(\mathbf{AC} \times \mathbf{B}) = 0 \tag{1.4}$$

One can decompose $d_t(\mathbf{AC}) = \mathbf{AC}.\nabla\mathbf{V}$, and $d_t(\mathbf{B}) = -\nabla \times \mathbf{E} + \mathbf{V}.\nabla\mathbf{B}$. Therefore,we need to introduce the form of the electric field $\mathbf{E}$. To do so, we write our the momentum equation for the MHD fluid which looks like this:

$$\mathbf{E} = -\mathbf{V} \times \mathbf{B} + \mathbf{E}' \tag{1.5}$$

where terms associated with inertia, pressure, etc. are in the last $\mathbf{E}'$ term. After some algebra, the condition (1.4) is

$$\boldsymbol{\nabla} \times \mathbf{E}'_{\|} = 0 \tag{1.6}$$

where the parallel subscript denotes the component along the local magnetic field direction. The MHD hypothesis consists in considering fluctuations of low frequency and small wave number. As a consequence, in the momentum equation of the MHD fluid all spatial and temporal gradient vanish giving Eq.(1.7), where E' contains the non-ideal terms, i.e. the ones associated with whatever kind of collisions. It arises that for ideal MHD magnetic reconnection can not happen.

As we discuss the motion of magnetic field lines, we need to introduce the definition of the speed of a magnetic field line. The speed of a magnetic field line is the speed of the frame in which there are no electric field associated with the magnetic field. Write a transformation of $\mathbf{E}$ from the rest frame K of a given medium volume to a frame K' (resulting from the Lorentz transformation) we get

$$\mathbf{E}' = -\mathbf{V}_{K'/K} \times \mathbf{B} + \mathbf{E} \tag{1.7}$$

The frame K' is called the *de Hoffmann-Teller frame* [DHT50] and its speed is

$$\mathbf{V}_{HT} = \frac{\mathbf{E} \times \mathbf{B}}{B^2} \tag{1.8}$$

It appears that in ideal MHD, $\mathbf{V} = \mathbf{V_{HT}}$, the MHD velocity equals the de Hoffman-Teller frame velocity, and $\mathbf{E}' = 0$. It has an important consequence known as the frozen-in condition : in ideal MHD, the plasma and the magnetic field are traveling at the same velocity, as if one were frozen in the other. As a consequence, in ideal MHD the plasma is flowing at the velocity $-(\mathbf{E} \times \mathbf{B})/B^2$. One of the problem in studying magnetic reconnection is to identify the terms in the momentum equations which can break the condition $\boldsymbol{\nabla} \times \mathbf{E}_{\parallel} = 0$.

While most of the astrophysical plasmas can be studied in the frame of ideal MHD, magnetic reconnection can occur in the so-called *diffusion region*, where ideal MHD hypothesis is no more valid. As electrons and ions have different masses electrons need weaker magnetic field than the ions to be demagnetized or decoupled from magnetic field. That defines two diffusion regions, the *electron diffusion region* (EDR), smaller and embedded in the *ion diffusion region* (IDR).

Fig. 1.3 shows a sketch of the reconnection site. Electrons and ions drift toward the X point, where the magnetic field weakens, while their motion is associated with an out-of-plane electric field. The fluid motion of Fig. 1.3 is quite different from the individual motion of each specie of particles. Once ions or electrons enter their respective diffusion region they become demagnetized, turn in the outflow direction and drift outward. Ions demagnetization occur on a scale $d_i = c/\omega_{pi}$ called *ion inertia length* or ion skin depth, which defines the size of the ion diffusion region. Out of the ion diffusion region, the ideal MHD works well, while inside, we need to find the physical process to explain the E' term on the RHS of Eq. 1.7. Due to the smaller mass of electrons they stay magnetized longer. The diffusion of electrons region is embedded inside the ion diffusion region and has a size $d_e = c/\omega_{pe}$, called the *electron inertia length* or electron skin depth.

Two-dimensional reconnection is resulting from an initial configuration and appropriate physical conditions. The initial configuration is a current sheet where a strong

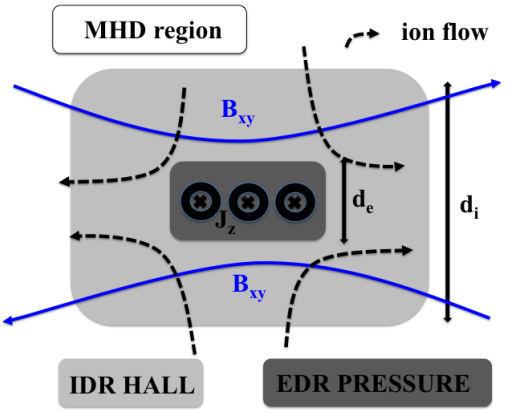

Figure 1.3: Sketch of the reconnection site: white region is the ideal MHD region, in light grey is the ion diffusion region and in dark grey is the electron diffusion region.

small-scale current is associated with the reversal of a magnetic field on a small scale length, of the order of the ion inertial length. If the plasma structure is such as the ideal hypothesis is no more valid, magnetic reconnection occurs. This assertion needs a comment: once the current sheet is thin enough, the hypothesis of small spatial/temporal gradients is generally no more valid. If reconnection is triggered, the associated inflow and outflow motion of particles is associated with an electric field. Furthermore, the demagnetization of both species (but in different region) gives rise to an associated current pattern, and to an electric field pattern. The clearest picture of the structure of the electric field, magnetic field, current, flow velocity are given in section 3.1.4.

1.1.2 Magnetic configurations of the current sheet

Magnetic reconnection occurs where magnetic field lines of opposite direction approach each other and merge. The Maxwell-Ampère equation allows to calculate the associated electric current density for a steady state condition:

$$\mu_0 \mathbf{J} = \nabla \times \mathbf{B} \tag{1.9}$$

A strong current sheet is embedded between the magnetic field lines of different orientation. The strong excess of magnetic energy on each side of the current sheet is the "tank" of energy, needed to fuel the process of magnetic reconnection. The existence of such a current sheet is always mandatory to observe magnetic reconnection.

At the very beginning of the space exploration in the early 60's, Dungey suggested the first qualitative model of an open magnetosphere [Dun61]. This model made it possible to give an explanation to the aurora borealis on the Earth. Fig. 1.4a shows the plasma flow resulting in a mixing of the interplanetary plasma into the outer atmosphere. In the

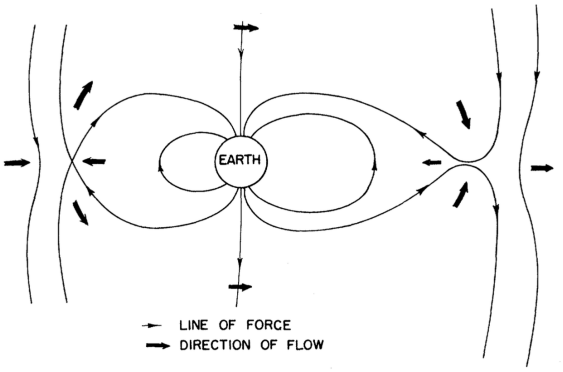

(a)

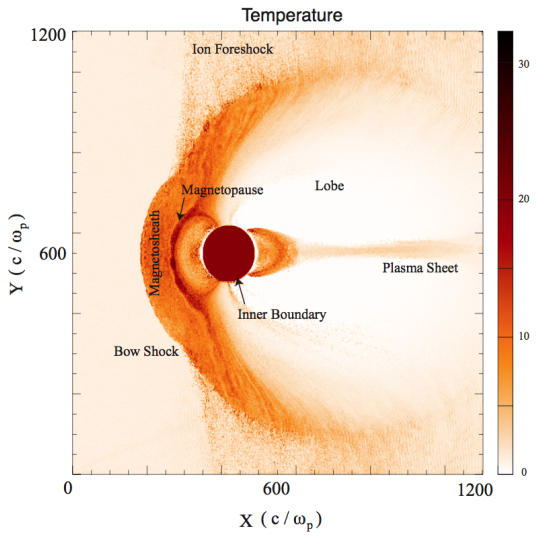

(b)

Figure 1.4: (a) Interplanetary plasma flow in a meridian plane, containing the neutral points, from Dungey 1961 [Dun61]. (b) Ion temperature as a function of X and Y in a global hybrid simulation. As denoted, regions representing various parts of the outer Earth magnetosphere are formed in the simulations. The size of the simulation is roughly $19R_E \times 19R_E$. From Winske 2003 [WYO+03]

.

model the dipolar field lines open in the day side of the magnetopause, convect over the auroral regions and reconnect again on the night side of the magnetosphere.

Recently, many numerical simulations of the Earth magnetosphere were done. As a nice example, we present one of the first massive kinetic simulations from 2003, where ions were treated as particles and electrons as a massless fluid. Fig. 1.4b portrays in color code the ion temperature. One can observe the formation of the bow shock, the ion foreshock (region of accelerated ions because of the shock), the *magnetosheath* (region of shocked solar wind plasma), the *magnetopause* (the magnetic boundary between the solar wind and the Earth magnetosphere), the lobe (cold empty region of magnetized plasmas) and the plasma sheet (dense plasma in the magnetic field reversal). In this run, the simulation domain is 1200 ion inertial lengths (in the solar wind) in X and Y directions and consists of 1 440 000 cells. Assuming the ion inertial length to be 100 km, the size of the simulation box is about $19R_E \times 19R_E$ (R_E being the Earth radii), which is smaller than the actual size of the magnetosphere. Initially the plasma is uniformly distributed in the simulation box and continuously injected from the X = 0 (left) boundary. Because of the two-dimensional nature of the simulations, the system does not necessarily reach a steady state solution. This implies that these simulations cannot be used to determine the standoff position of the various discontinuities in the magnetosphere. Many details of the solar wind interaction with the magnetosphere require a kinetic treatment, such as transport

at the dayside magnetosphere, are properly modeled in these simulations. [WYO+03] For the work presented in the thesis we also use a hybrid code and the necessary details are given in chapter 2.

To break the frozen-in condition, we need to find a source for the term $\mathbf{E}'$ appearing in Eq. (1.7). The first quantitative models of Sweet in 1958 [Swe58] and Parker in 1957 [Par63], and Petschek in 1964 [Pet64] have been historically the most important. For the Sweet-Parker model, the plasma resistivity is on the origin of breaking the frozen-in condition. In the following sections we give detailed information about these models, but in the frame of the thesis they are caducous as the plasma is collisionless, the plasma's resistivity being zero. In 1962, Harris formalized the topology of a kinetic equilibrium associated with a magnetic field reversal [Har62]. He proposed an exact solution of the Vlasov equation, which describes a plasma layer confined between two regions of an oppositely directed magnetic field. The magnetic field and density have the following distribution:

$$B_x(y) = \mathbf{B}_0 \tanh\left(\frac{y}{\lambda}\right) \tag{1.10}$$

$$n(y) = n_0 \cosh^{-2}\left(\frac{y}{\lambda}\right) \tag{1.11}$$

Here, λ is the half-thickness of the sheet depending on the Debye length, X is the field reversal direction, and Y is the gradients direction for both magnetic field magnitude and density. The detailed calculations are given in chapter 3, where we observe and discuss magnetic reconnection in the Harris sheet configuration.

In 2002, Nakamura [NBR+02] investigated the four-point measurements of the Cluster II spacecrafts in the Earth magnetotail, and interpolating a Harris-type current sheet model and they estimated the thickness of the current sheet. The thickness changes from about 1 R_E (Earth Radii) before the flow observation down to 400 km during the reconnection, i.e. close to the ion inertia length. Also they found that the magnetotail current sheet sometimes exhibits a double-peaked profile of the electric current density. Such structure is extensively discussed later in chapter 3.

According to the work of Runov (also using observations of the Cluster mission), currents can be subdivided into three classes [RSN+06]:

1. *central* sheets with a single (centered) peak (given in Fig. 1.5a), characterized by a width of the order of 2000 km

2. *bifurcated* sheets with two off-equatorial maxima of the current density and local minimum of the current density between them (see Fig. 1.5b)

3. *asymmetric* off-center current sheets with the current density maximum shifted from equatorial plane (Fig. 1.5c).

The recent multi-point mission THEMIS also provided data showing the presence of a non-Harris current sheet configurations [Sai15]. The conclusions one can draw from these studies is the current sheet in the Earth magnetotail may have a current structure more complicated than the one of a Harris current sheet. Fig 1.6 shows the average property

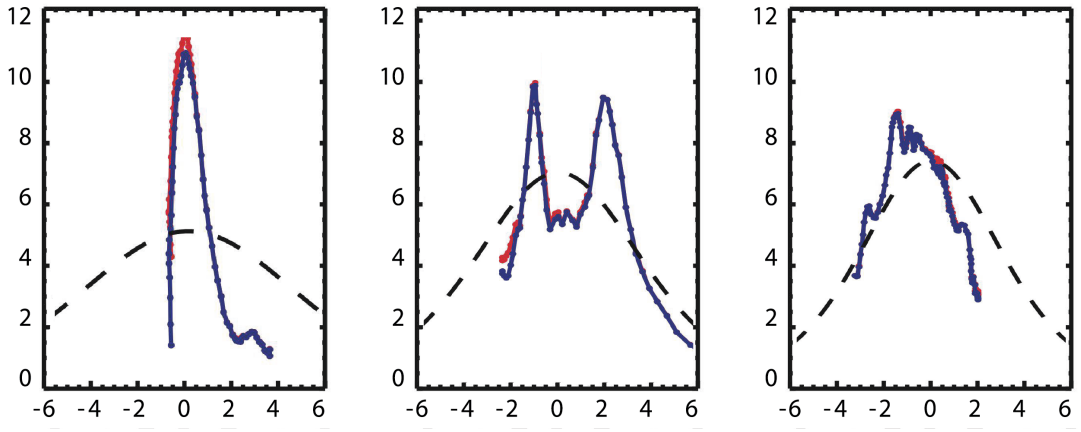

(a) (b) (c)

Figure 1.5: Profiles of the absolute values of the current densities $\mathbf{J}$ (blue) and $\mathbf{J}_\perp$ (red) in nA/m^2 versus the effective vertical coordinate (of the order of 1000 km) taking into account the time of the neutral sheet crossing by the Cluster barycenter and the gradient of magnetic field. Dashed lines show the corresponding Harris profiles. Left panel – central sheets with single peak centered, central panel – bifurcated sheets with two off-equatorial maxima of the current density and local minimum of the current density between them, and right panel – asymmetric off-center current sheets. Cluster observations from Runov 2006 [RSN+06].

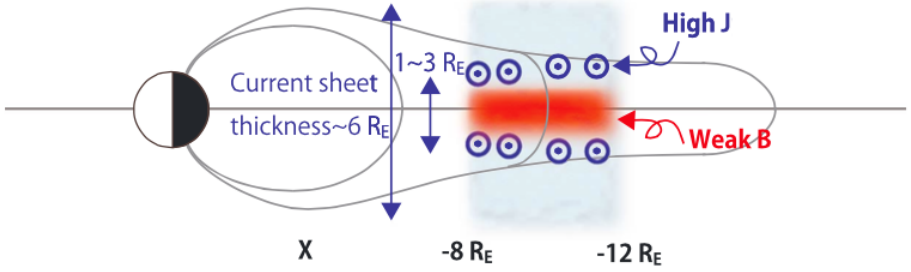

Figure 1.6: Illustration of the average current sheet profile on the night-side of the magnetoshere. From Saito 2015 [Sai15].

of the near-Earth current sheet for a tail structure, the bifurcated structure is a typical and stable structure.

While many studies outline that a current sheet can have an eventually different structure from the one of a Harris sheet, this topology is still quite interesting from the numerical point of view to investigate the magnetic reconnection process. As it is only

an initial conditions, the thinning, thickening, pinching, compression... of the magnetic field can be evidently observed depending on the boundary conditions. We use this configuration in chapter 3.

1.1.3 Slow reconnection

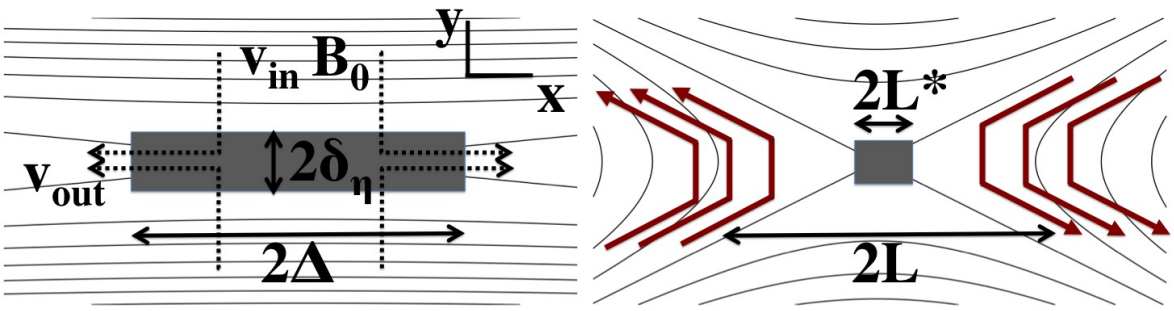

(a) (b)

Figure 1.7: (a) Sweet-Parker model. (b) Petschek model.

We present the first stationary MHD model, which uses plasma resistivity to break the frozen in condition. Fig. 1.7a schematically displays a perturbed current sheet, which is pinched at the center. The Sweet[Swe58]-Parker[Par63] model uses the MHD framework and the plasma as a single fluid where electrons and ions move together, even when electrical currents exist. It is characterized by six quantities, the inflow and outflow velocities v_{in} and v_{out}, the upstream field pushed against the sheet B_0, the length Δ, the width δ_η, and the classical resistivity η. The quantities obey three relations.

• conservation of mass (assuming incompressibility):

$$v_{in}\Delta = v_{out}\delta_\eta \tag{1.12}$$

Considering the incoming energy is essentially electromagnetic, and the outgoing energy is essentially kinetic, one gets

• conservation of energy: the ingoing magnetic energy flux equals the outgoing kinetic energy flux:

$$B_0^2/2\mu_0 = nmv_{out}^2/2 \tag{1.13}$$

where n is the plasma density. This gives

$$v_{out} = v_A \tag{1.14}$$

the plasma outflows the reconnection region with approximately the Alfvén velocity. The assumption of steady state reconnection means $\partial_t = 0$ for whatever quantity. Thus $\nabla \times \mathbf{E}$ = -$\partial_t \mathbf{B} = 0$, hence E_z = const. Then, one needs the form of the electric field:

• Ohm's law: the ideal electric field outside the sheet $E = v_{in} B_0$ is balanced by the resistive electric field inside the sheet $E = \eta J$:

$$v_{in} B_0 = \eta J = \eta B_0 / (\mu_0 \delta_\eta) \tag{1.15}$$

from Ampère's law $J = \frac{1}{\mu_0} \nabla \times B_0 \sim B_0 / (\mu_0 \delta_\eta)$. The velocity of the magnetic flux entering into the sheet verifies:

$$v_{in} = v_A / \sqrt{S} \quad \delta_\eta = \Delta / \sqrt{S} \tag{1.16}$$

where

$$S = \Delta v_A / \eta \tag{1.17}$$

is the *Lundquist number*, that is the ratio of the Alfvén velocity over the diffusion velocity. The inflow velocity of the stream is therefore the rate of diffusion of the fluid through the magnetic structure. Therefore the reconnection rate can be measured by this upstream velocity or by the value of the associated electric field.

As an example, one can look at the Sun corona: for a coronal electron temperature $T_e \sim 10^6$ K (100eV) the magnetic diffusivity is $\eta \sim 10^4 cm^2/s$, a typically flare diffusion region of diameter $L \sim 10^4$ km would require a time-scale $\tau_\eta = L^2/\eta \sim 10^{14}$ s. The observed flash phase of a flare takes less than $\sim 10^3$ s, meaning the Sweet-Parker model is too slow for solar flares and is referred to a *slow reconnection*. The efficiency of reconnection is strongly limited by the weak diffusive magnetic field breakdown inside the elongated current sheets. So, the reconnection rate remains small, as all plasma has to be pushed through a narrow outflow channel of the size of just the sheet width and since the outflow velocity is limited to the smaller Alfvén speed.

1.1.4 Fast reconnection

The first model for *fast reconnection* was proposed by Petschek. The Petscheck model [Pet64] accepts the same topology of the Sweet-Parker model, but with an additional argument: there is always a dissipative zone in which non-ideal term allows the topological reconfiguration of the field lines, but the plasma is not forced to pass through it. This makes allow to overcome the bottleneck of the Sweet-Parker model which is at the origin of the low reconnection rate. However, it is necessary to find the process that accelerates the plasma no longer passing through the diffusion zone: it is a slow shock. Thus we introduce two characteristic scales in the plasma expulsion direction: L is the characteristic dimension of the reconnection zone, and L^* is the diffusion scale. The slow-mode shock waves extend from a tiny central diffusion region of size $2L^*$ on Fig. 1.7b.

These shocks start at the ends of a short Sweet-Parker sheet, and spread out with an angle v_R/v_A, here v_R is the reconnection rate. Petschek pointed out that a much higher efficiency of energy conversion can be achieved if the change of the magnetic connection occurs just in a small region near the X point. At the same time, the plasma inflow can be collected from a broad region and expand into a broad outflow. In Petschek-type reconnection magnetic shock waves are formed in the plasma flow, since the local Alfvén speed drops considerably from inflow to outflow region. These shock waves provide much more of the energy dissipation than the magnetic diffusion inside the non-ideal plasma region near the X point. The Petschek-solution predicts a higher reconnection rate $v_R = v_A\pi/(8\log S)$ than the Sweet-Parker model.

The Petschek's model is a powerful energy converter, transforming magnetic energy into plasma flow energy, but it does not match to the diffusion region for small resistivity. Petschek-type process requires the presence of an efficient reconnection mechanism. In this sense, the model is not a self-consistent theory of magnetic reconnection, but only a phenomenological model. In 2000, it was demonstrated [UK00] that Petschek-like initial configuration representing shocks showed the reconnection rate as predicted by Petschek. But the shocks quickly run away at the Alfvén speed, and after a transient period the system reached a steady state as Sweet and Parker predicted.

While we presented collissional models in collisionless plasmas, the resistivity can not be on the origin of breaking the frozen-in theorem. Because of the small spatial gradients the ideal MHD is not applicable. To start to discuss fast magnetic reconnection in collisionless plasmas, we need to present the generalized Ohm's law. This one results from the electron momentum equation:

$$\mathbf{E} = -\mathbf{v}_e \times \mathbf{B} - \frac{1}{en}\boldsymbol{\nabla}.\mathbf{P}_e - \frac{m_e}{e}(\partial_t \mathbf{v}_e + \mathbf{v}_e.\boldsymbol{\nabla}\mathbf{v}_e) \tag{1.18}$$

here, $\mathbf{v}_e$ is the electron bulk velocity, n is the electron density, one should note that in the general case, electron pressure $\mathbf{P}_e$ is a tensor. This is a general notation which is used in the community of collisionless plasma, while for people coming from hydrodynamics this tensor is generally decomposed in a scalar pressure (time the identity tensor) plus a stress tensor. Writing the electron velocity as:

$$\mathbf{v}_e = \mathbf{v}_i - \frac{\mathbf{J}}{en} \tag{1.19}$$

where, $\mathbf{v}_i$ is the ion bulk velocity and $\mathbf{J}$ is the current density, one can get (neglecting the inertia terms proportional to electron mass):

$$\mathbf{E} = -\mathbf{v}_i \times \mathbf{B} + \frac{1}{en}(\mathbf{J} \times \mathbf{B} - \boldsymbol{\nabla}.\mathbf{P}_e) \tag{1.20}$$

The first term on the RHS is the ideal term already introduced in the ideal MHD. The second is the Hall term which plays a crucial role in fast magnetic reconnection. The Hall

term results from the decoupling between the ion and electron motion on scale lengths less than an ion inertial length. To show the scale where the Hall term is important we compare it with the ideal term. The ratio ideal over Hall term is

$$\frac{v_A^2 k}{\Omega_i v_i} \tag{1.21}$$

Next, for Alfvénic perturbations (v_i is of the order of the Alfvén speed), this ratio equals kv_A/Ω_i. The Hall term is important compared to the ideal if the spatial scale of the order (or less) than the inertial length (which is equal to v_A/Ω_i).

1.1.5 The GEM challenge : a corner stone

Before 2000 there were a lot of numerical studies of magnetic reconnection with different parameters and conclusions. The *Geospace Environmental Modeling* (GEM) Reconnection Challenge [BDS+01] addresses the question of fast reconnection in collisionless plasmas by means of several numerical simulations using the same initial and boundary conditions. The equilibrium chosen for the reconnection challenge problem was a Harris equilibrium with a floor in the density outside of the current sheet. Four types of codes were used: 1. single-fluid MHD code; 2.two-fluid Hall MHD code, including Hall and pressure divergence terms in Ohms law; 3. hybrid code where ions are treated as particles and electrons as a massless neutralizing fluid; 4. full particle-in-cell code, where each specie is teated as particles. A magnetic perturbation is initially superimposed on the initial Harris sheet, resulting in a single X point at the center of the sheet. Such a way to trigger reconnection became a trend in simulations of the magnetic reconnection with a single X point.

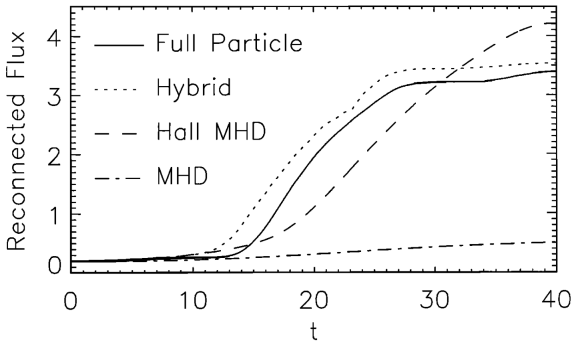

Figure 1.8: The reconnected magnetic flux versus time for four types of numerical approaches. From Birn 2001 [BDS+01].

Fig. 1.8 displays the reconnected magnetic flux versus time for different numerical models. The reconnection electric field is the slope of the flux versus time defined by

Eq. (1.3). An important conclusion of GEM Challenge is that all of the models which include the Hall effect produce essentially the same rates of reconnection, while the resistive MHD case gives a substantially smaller reconnection rate (slow reconnection).

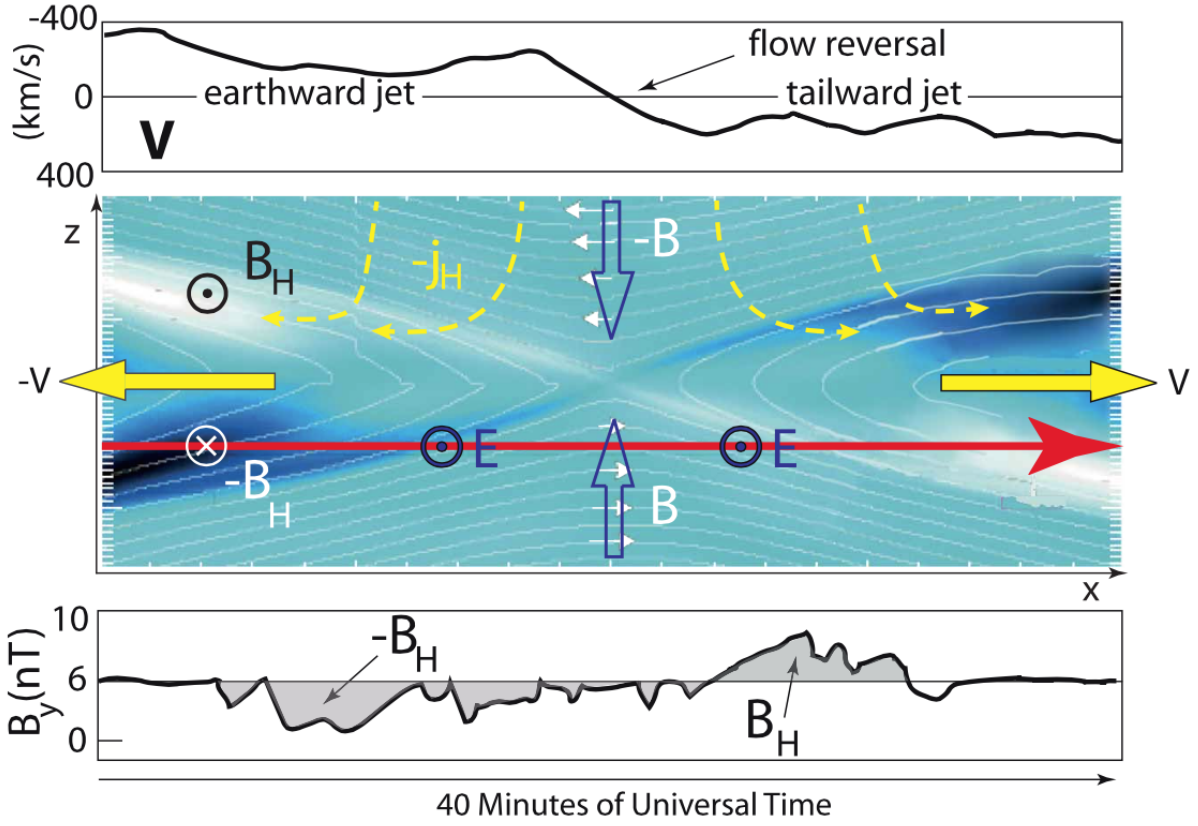

Figure 1.9: (a) out-of-plane magnetic field from PIC simulation with superposed spacecraft orbit (long red arrow in the central panel). Dark blue indicates positive and white indicates negative regions of the out-of-plane magnetic field. Open arrows show convective inflow, yellow arrows outward jetting of plasma. The top panel shows the plasma velocity measured along the spacecraft orbit in Earth magnetotail during a substorm reconnection event and the bottom panel shows the measured out-of-plane magnetic field. From Treumann 2013 [TB13].

Another important feature raised by the GEM challenge was the high importance of the Hall effect for collisionless reconnection. The Hall term in Eq. (1.20) is important in the ion diffusion region where the frozen-in flux constrain is broken as ions are demagnetized. The scale length around the X line, where ions are demagnetized, is of the order of the ion inertial length d_i. At scale lengths below d_i the motion of electrons and ions decouple. Fig. 1.9 depicts two-dimensional simulations of reconnection in the Earth's magnetotail compared with data taken from spacecraft observation by Vaivads [VKA+04] and Oieroset [ØPF+01]. The out-of-plane magnetic fields concentrate along and inside the separatrices,

and arise from the in-plane electric field (by Maxwell-Faraday equation). While the in-plane electric field is due to the Hall term, involving the in-plane magnetic field and the out-of-plane current.

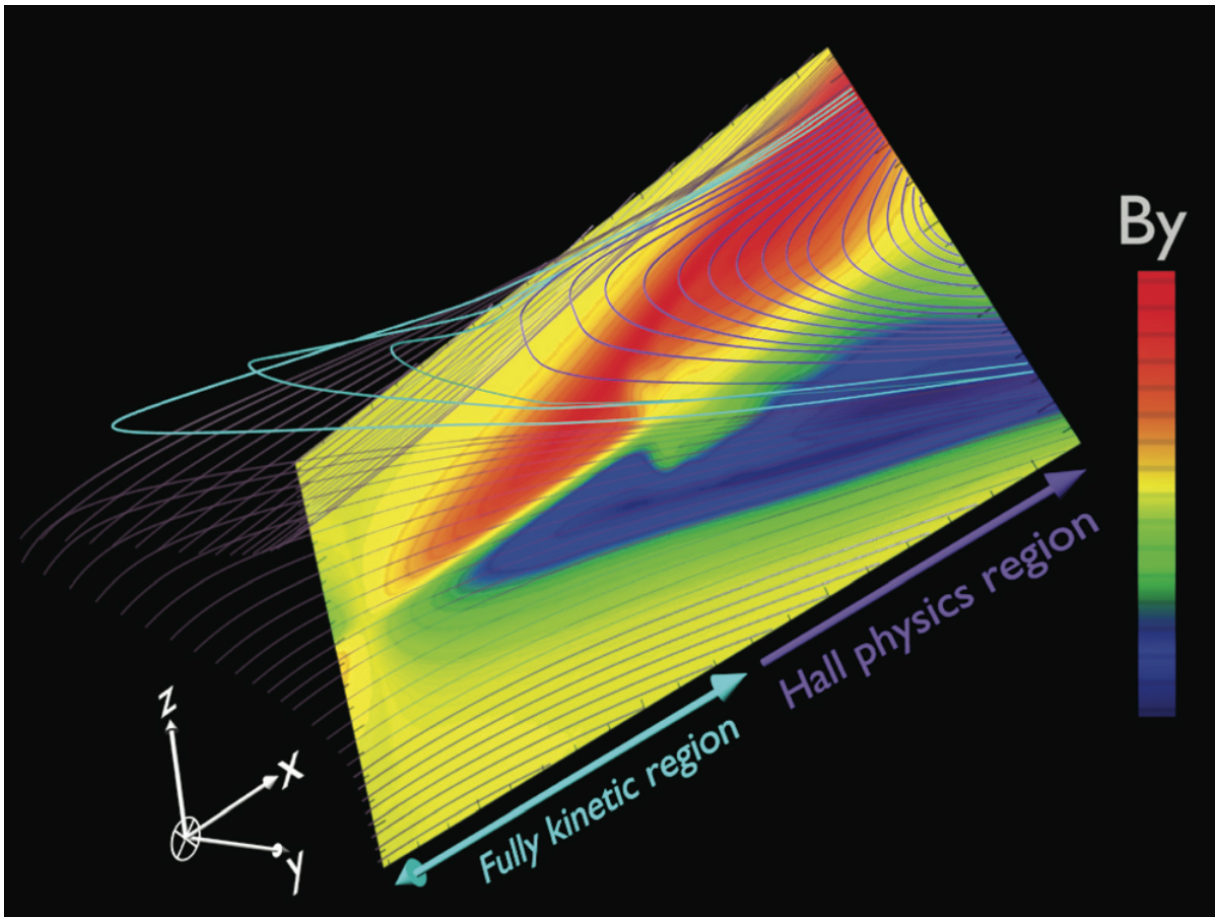

Figure 1.10: A 3D view of the magnetic field lines. From Zenitani 2013 [ZSNW13].

The result of the Hall effect is that the magnetic field lines are dragged out from the initial plane. Fig. 1.10 gives a 3D view of the magnetic field lines from Zenitani 2013 [ZSNW13]. The field lines between Hall physics region correspond to the fully kinetic region where electrons physics is important, as well as the pressure term in Eq. 1.20.

1.2 What do we know about fast magnetic reconnection ?

In this section we introduce the reconnection rate and give details on what we have already known about the fast reconnection essentially from numerical simulations.

1.2.1 How to define and use a reconnection rate

As we already saw in the first section of this chapter the efficiency at which the plasma is reconnected can be evaluated by the inflow velocity of the plasma when flowing toward the reconnection region. Well upstream in the ideal MHD region the magnetic field is frozen in the plasma, and the plasma inflow velocity is also the one of the magnetic field. The same holds well downstream of the reconnection region. For the two-dimensional case for steady reconnection the out-of-plane component of the electric field is homogeneous across the reconnection region. Furthermore, the outflow velocity is limited by the Alfvén velocity, since the creation of a super-Alfvénic flow should satisfy the Rankine-Hugoniot conditions, that is the jump conditions across a shock. Hence, while inward and outward velocities are related through the small angle between the two separatrices, the inward velocity is well smaller than the outward one.

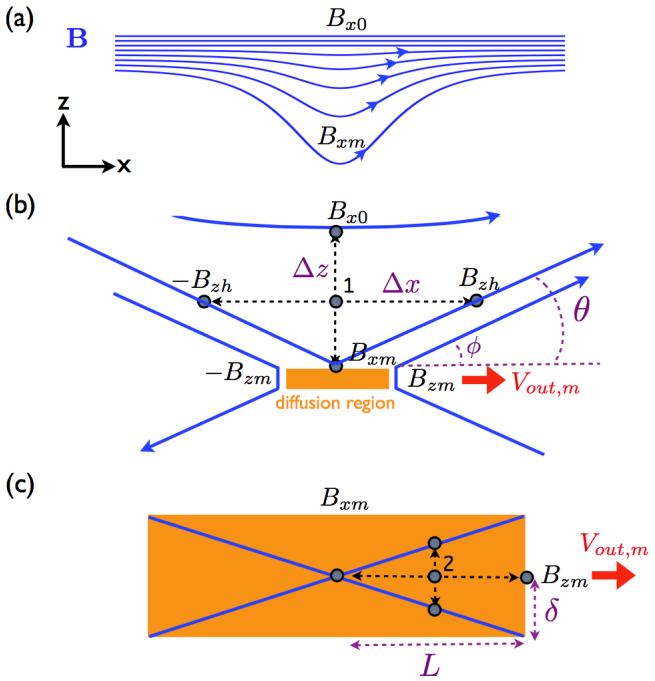

Figure 1.11: (a) Sketch of magnetic field lines upstream of the diffusion region ($z > 0$). (b) Geometry of reconnection at the local-scale. (c) Dimensions of the diffusion region at the micro-scale. From Liu 2017 [LHG+17].

In 2017 Liu offered a simple model of steady-state reconnection in a Harris-type sheet gaving a good agreement with simulations. Fig. 1.11 illustrates the inflow region from the Liu study [LHG+17]. If the opening angle made by the upstream magnetic field is small, the diffusion region is long and thin resulting in a slow reconnection rate, as in Sweet-Parker reconnection. As the opening angle increases, reconnection becomes faster. The

diffusion region thickness δ is controlled by micro-scales like inertial or gyro-radius scales in collisionless case, hence the diffusion region becomes embedded in a wider structure of local-scale Δz, where the magnetic field and plasma parameters achieve relatively uniform upstream conditions ("0" indicates asymptotic quantities). The magnetic field B_{xm}, where "m" indicates quantities at the micro-scale, immediately upstream of the diffusion region becomes smaller than the asymptotic magnetic field B_{x0}. This is crucial because it is B_{xm} driving the outflow from the diffusion region; as it becomes smaller reconnection proceeds more slowly. The *reconnection rate* is defined as:

$$R_0 \equiv E_R/(B_{x0}V_{A0}) \tag{1.22}$$

where E_R is the reconnection out-of-plane electric field. They found a reconnection rate which is a function of $\Delta z/\Delta x$, valid for any opening angle. The maximum value for the normalized reconnection rate is 0.2, when $\Delta z/\Delta x = 0.31$, and the rate is not strongly sensitive to the opening angle for intermediate values. They suggested why the reconnection rates in various kind of current sheet are so similar, whatever the dissipation mechanism.

The reconnection rate can therefore be measured by this upstream velocity, or by the value of the associated electric field. Observations and numerical simulations in a wide variety of settings suggest that the global rate of magnetic reconnection is approximately 0.1 in normalized units and independent of dissipation mechanism. From collisionless two-and-a-half-dimensional simulations of thin Harris-type current sheets, we know that the steady-state reconnection has a rate of 0.1[SDRD99] when normalized by the upstream magnetic field and Alfvén speed. This rate is independent of the system size[SDRD99, HSBK99] as well as the electron mass, when considered [SDDB98, HSBK99]. In particular, the GEM challenge [BDS+01] showed that the rate is approximately the same, whatever the type of simulation, as soon as the Hall effect is considered.

1.2.2 Reconnection with a guide-field

The reconnection process can be extended to plasmas where the upstream and downstream magnetic fields are not anti-parallel. The so-called *guide field* is imposed parallel to the out-of-plane current. The superposition of a large guide field compared to the asymptotic in-plane magnetic field magnetizes the electrons even inside of the electron diffusion region, suppressing their chaotic motion. In space plasmas (solar wind, planetary magnetospheres), the current configurations are in most cases associated with such guide-field. As we saw on Fig. 1.9 the ambient magnetic field is around 6 nT, and directed in the out-of-plane direction, along the current direction. In the magnetotail, such a normal field component is widely observed. When there is a large guide field the Hall term can become inactive, but reconnection in such a regime also has a similar rate. As a consequence, the Hall term and its associated dispersive waves are not necessary to get a

reconnection rates near 0.1. [CLS17], while without a strong guide field fast reconnection in collisionless systems depends on the dynamics of whistler and/or kinetic Alfvén waves at small scales [RDDS01]. Few observable features are coming from such a guide-field:

i a density asymmetry develops across the mid-plane

ii the X line and the out-of-plane field are tilted relative to the mid-plane

iii the current sheet gets thinner

The parallel electric field exists along the separatrix from the upper left to the lower right and results from the electron pressure term, and the associated with diamagnetic drift. After the electrons are accelerated by the parallel electric field, they flow away from the X line along the magnetic field lines. The induced electric field causes the ions to drift across the current layer, that charge neutralizes the electrons. Fig. 1.12 displays the plasma density from a PIC simulation with an ambient guide field, from the study of Le [LED+09]. The depletion of the density along one separatrice is clearly seen, as well as the enhancement along another.

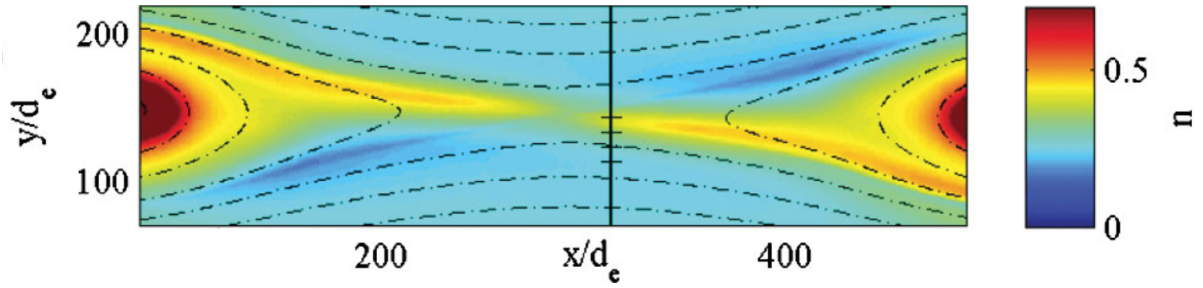

Figure 1.12: Plasma density from PIC simulation for guided reconnection. From Le 2009 [LED+09].

An important question is how large the guide-field has to be to magnetize the electrons in the dissipation region and therefore impact the dynamics of the electrons. The dynamics of the antiparallel system should significantly change if the guide-field is sufficient to magnetize the electrons injected into the field reversal region. In 2005, Swisdak [SDSM05] used PIC simulations and showed that a guide-field of the order of 0.1 (time the asymptotic magnetic field) was sufficient to magnetize the electrons in the vicinity of the X line, thus causing significant changes in the structure of the electron dissipation region.

Fig. 1.13 shows the out-of-plane magnetic field and electron current. The electron current is mainly in the out-of-plane direction along the induction electric field. The guide field causes an asymmetry in the field and ion flows. The separatrix with the enhanced density carries most of the current, resulting in a clear bend of the current sheet in contrast to symmetric case without guide field. A guide field not only distorts the out-of-plane magnetic field introducing an asymmetry, but also compresses the spatial range down to the electron gyro-scale. [TB13]

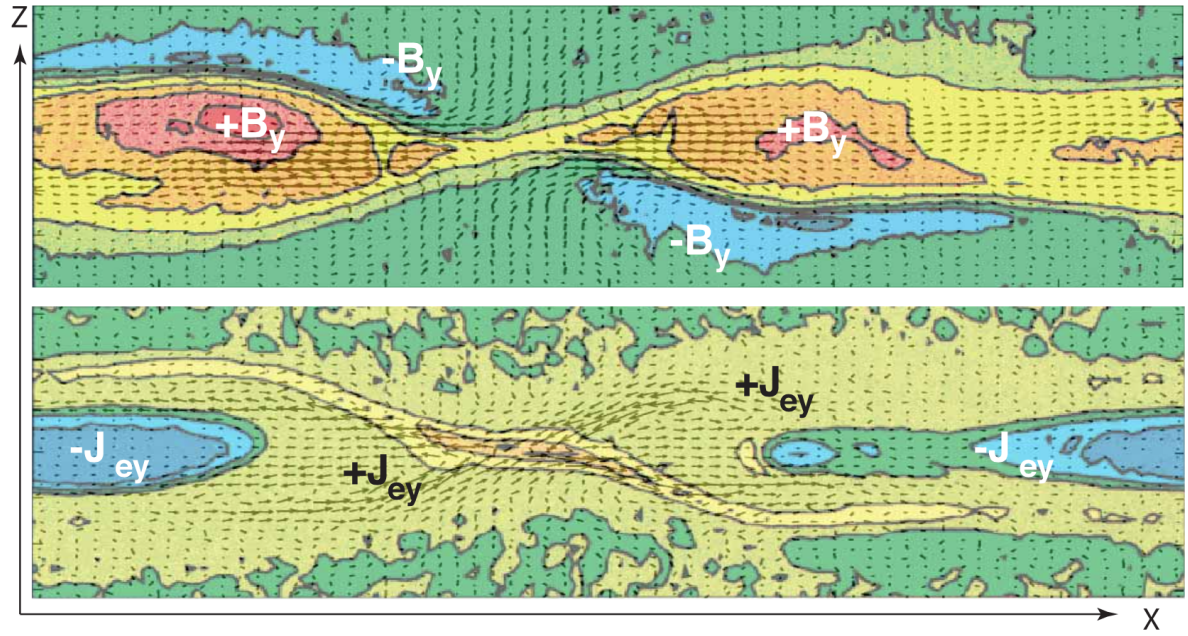

Figure 1.13: PIC simulation of the guide field reconnection. Top - out-of-plane magnetic component of the magnetic field. Bottom - out-of-plane electron current. Yellow-to-red colors indicate positive, blue-to green colors negative values. From Treumann 2013 [TB13]. Y is the out-of-plane direction.

Simulations done before the GEM challenge showed that for a guide field being 0.3 time the reversal magnetic field, the evolution proceeded identically to the run without guide magnetic field with the exception of small differences in the magnetic field structure around the X point at intermediate times [HSBK99]. Although for guide fields large enough to significantly modify the magnetic pressure in the system, simulations indicated a strong reduction of the reconnection rate.

1.2.3 Reconnection in an asymmetric current sheet

The reconnection process between the interplanetary magnetic field of solar wind and the magnetospheric one at the Earth's magnetopause is asymmetric. The Earth's magnetosphere is the region of influence of the Earth's magnetic field. The dayside magnetopause is the boundary of the magnetosphere on the dayside of the Earth (closest to the Sun). At the dayside magnetopause, configuration for reconnection involves asymmetries of magnetic field strengths, particle densities and temperatures on the two sides of the current sheet. The magnetosheath plasma (which magnetic field is around 20 nT and density around 20 cm^{-3}) contacts with the magnetospheric plasma (with a 50 nT magnetic

field and a 0.4 cm^{-3} density). Also we can point out from Fig. 1.4b that magnetosphere is hot with typical value 2 keV while magnetosheath is relatively cold 200 eV. For the *asymmetric reconnection* we point two main features:

(i) significant asymmetry of the magnetic fields lines and of the plasma flows across them

(ii) the quadrupolar out-of-plane magnetic field and bipolar in-plane electric field of symmetric reconnection are not found in the asymmetric case

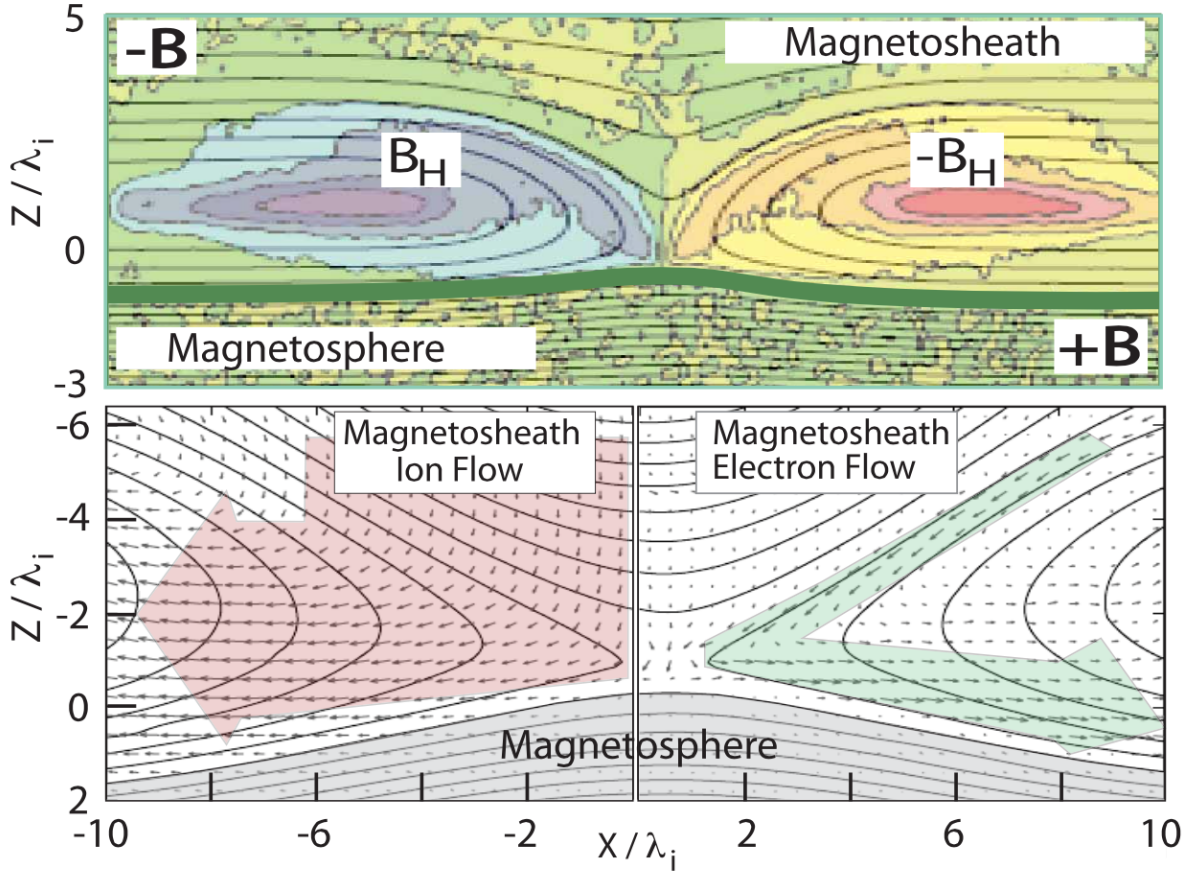

Figure 1.14: Non-guide field particle-in-cell simulations of asymmetric magnetopause reconnection with Hall field B_H. From Treumann 2013 [TB13]

Fig. 1.14 shows the results of simulation of asymmetric reconnection without any guide-field [TB13]. The out-of-plane magnetic field is concentrated on the magnetosheath side. The magnetosphere is well separated from the distorted magnetosheath by a stable magnetopause. In contrast to the symmetric case, only one half of the out-of-plane Hall magnetic field exists. The lower Hall dipole is suppressed as there is no electron inflow from below. The lower part of figure displays the electron and ion flows and how electron

flow becomes diverted into jets along the magnetopause. The magnetopause coincides approximately with the inner separatrix. This is a clear result from the larger magnetic tension on the magnetosphere side than on the magnetosheath side. Hence, this asymmetry can be significantly lowered with a symmetric magnetic field magnitude. Only two large Hall field vortices develop on the magnetosheath side. From the bottom panels, ion (left) and electron (right) bulk flow can be observed on the magnetosheath side. Jetting of electrons is restricted to a narrow domain only along the magnetopause. The north-south asymmetry would be inverted if reversing the guide magnetic field direction. Without any guide magnetic field the asymmetry would presumably disappear.

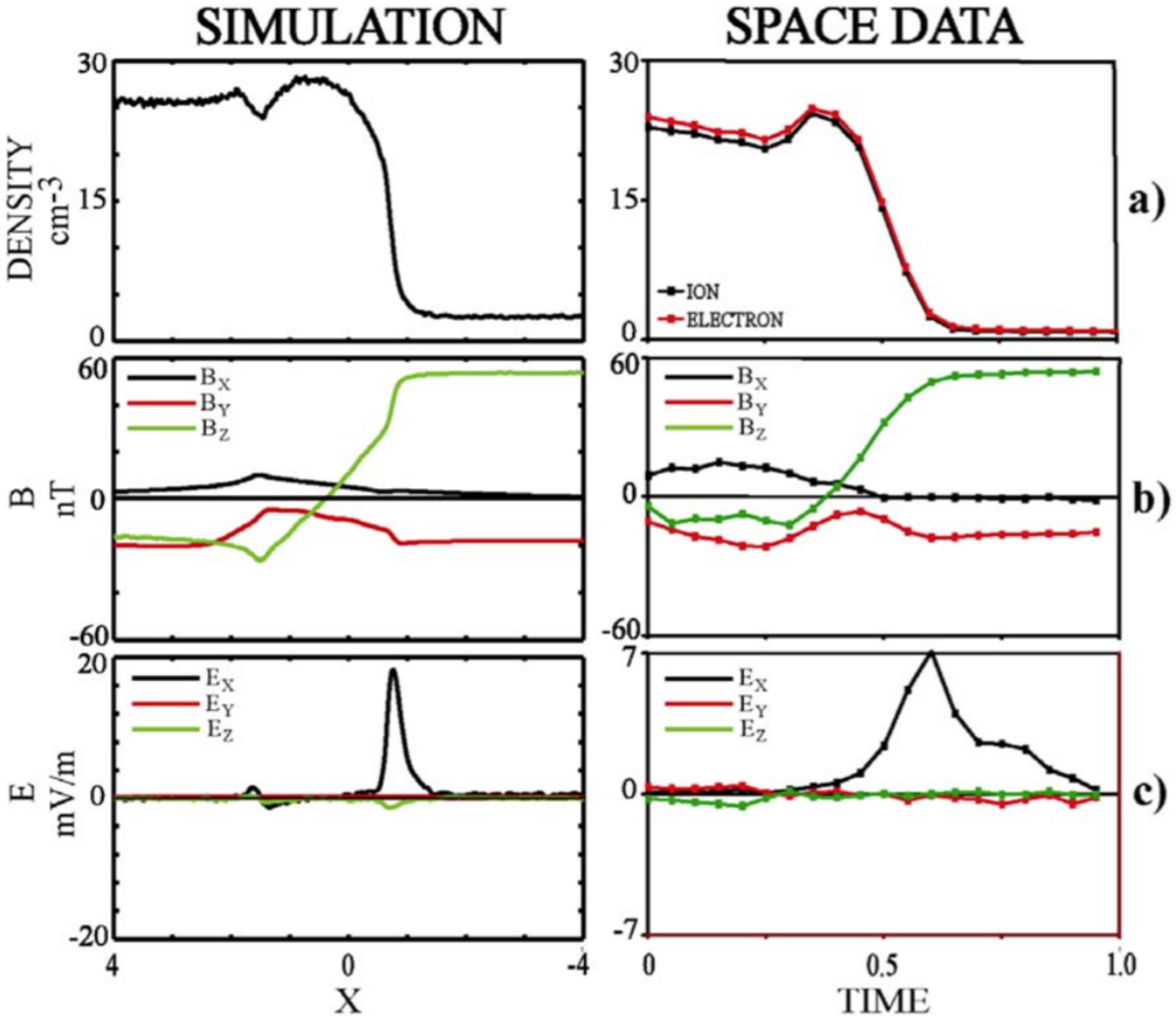

Figure 1.15: Comparison of plasma density and fields between a simulation and subsolar observations of asymmetric reconnection on the THEMIS satellite. From Mozer 2008 [MPB+08]. X is the gradient direction, Y is the out-of-plane direction, and Z is the field-reversal direction.

Fig. 1.15 (left) presents the plasma density, magnetic field, and electric field as functions of X (gradient direction) at Z = -6 (field-reversal). Fig. 1.15 (right) presents the average fields and density found in a superposed epoch analysis of the spin-period-averaged fields measured during six THEMIS magnetopause crossings [MPB$^+$08]. The density variation across the current layer is from n_0 on the magnetosheath side to $n_0/10$ on the magnetosphere side. The magnetic field variation is from $B_0/2$ on the magnetosheath side to $3B_0/2$ on the magnetosphere side. The experimental and simulation plasma densities are in agreement in that they both show a relative minimum of plasma density near the high-density magnetosheath. Other quantities are also in good agreement.

An important question is whether the reconnection rate is enhanced or lowered by such an asymmetry. A clear problem arise: the out-of-plane electric field should be normalized by an upstream magnetic field and an Alfvén velocity... but from which side ? Investigating scaling laws, Cassak et al. published a major study in 2007[CS07]; they concluded that the reconnection rate can be evaluated with a hybrid formula where magnetic field and densities from both sides have to be considered. Labeling 1 and 2 each sides, the outward velocity is

$$v_{out} = \frac{B_1 B_2}{\mu_0 m} \frac{B_1 + B_2}{n_1 B_1 + n_2 B_2} \tag{1.23}$$

Two-dimensional full-particle simulations show that the combination of shear flow and/or guide field with density asymmetry induces the sliding motion of the X-line along the magnetopause. The direction of the X-line motion is controlled either by the ion flow at the X-line when the shear flow effects is dominant or by the electron flow at the X-line when the guide field effects is dominant. [TFS10]

1.2.4 Driven reconnection

Until now, we discussed the case of spontaneous reconnection with a thin current sheet initially pinched and decaying in a two current structure separated by an X points of weak magnetic fields. The picture is different when reconnection is *driven* by an inflow of plasma into the current layer. The increase of the inflow velocity should also increase the reconnection rate. Continuous plasma inflow forces the current sheet to digest the excess plasma and magnetic fields. This can happen only by violent reconnection and plasma ejection from the X points [TB13]. The experiments on magnetic reconnection also suggest the importance of an external driving force in determining the reconnection rate, and supports an important aspect of a driven-reconnection model. But it does not mean we have appropriate micro physics to make reconnection faster.

One of the first kinetic investigation of forced reconnection was reported by Birn in 2005 [BGH$^+$05], who exposed the thick Harris current sheet, four times as thick as in the GEM study, to a temporary inflow of plasma from both sides. Such an inflow is produced

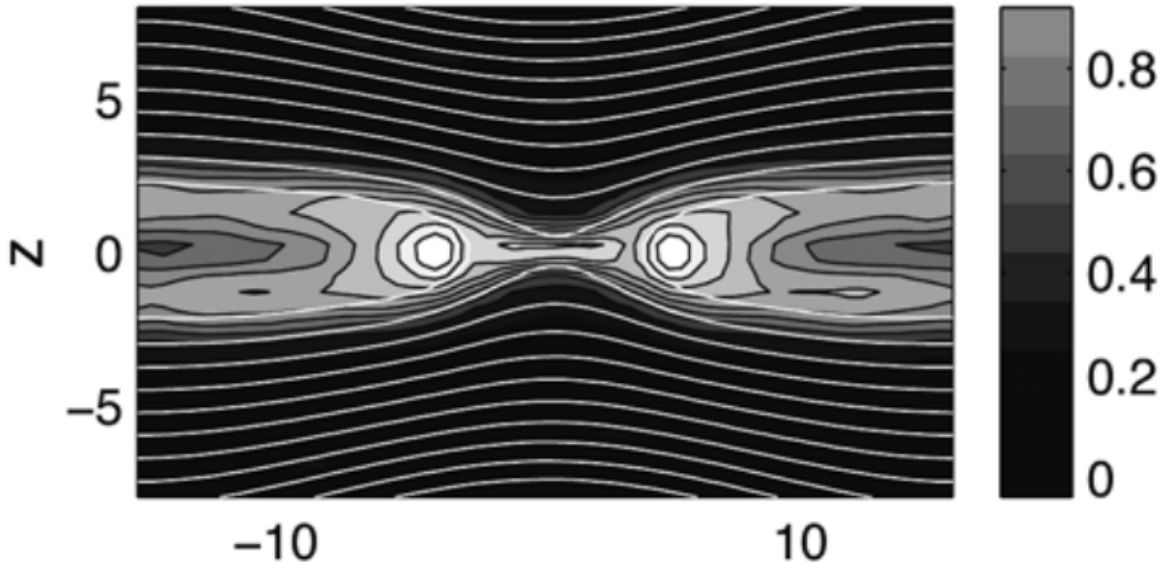

Figure 1.16: Contour plots of the out-of-plane current density with magnetic field lines superimposed for the standard Newton Challenge at the maximum of the reconnection electric field. From Pritchett 2005 [Pri05].

by imposing a temporally limited cross-magnetic electric field close to the boundaries. It results in a compression of the initial current sheet causing a current thinning, which leads to a local magnetic field enhancement of 20 – 40%. Such increase of the lobe field, for instance, can happen in the Earth's magnetotail during the substorm growth phase. This study was called "*Newton Challenge*", as it grew up from a collaborative work initiated during a workshop on Magnetic Reconnection Theory, held in 2004 at the Isaac Newton Institute (Cambridge, UK). It demonstrated that, whatever the kind of numerical simulation, driven reconnection leads to the same fast reconnection rates, apparently independent of the dissipation mechanism, although the onset times differ.

Another important work on 2D driven simulation was reported by Pritchett [Pri05], in which an external temporally limited cross-magnetic electric field was imposed at the boundaries above and below a symmetric electron-proton Harris current sheet. The main finding is the slightly enhanced growth rate of driven reconnection in a wider current sheet is due to the considerable extent of an electron anisotropy $T_\perp/T_\parallel < 1.1$ and an electron current layer (below the ion inertial scale). These effects lead to reconnection based on non-diagonal pressure tensor elements in thin current layers, significantly different from the case of an isotropic Harris layer. This suggests that an important element in constructing a reduced model of collisionless reconnection is to retain an evolution equation for the electron pressure tensor.

Fig. 1.16 shows the out-of-plane current density with magnetic field lines superimposed near the time of the peak reconnection rate. Field lines have reconnected and

the peak in the current density is displaced away from the center of the system as plasma is being expelled away from the X line region. These displaced peaks are due to the ions, while the electron contribution is still peaked at the center. The reduction in the total current near the X boundaries is due to a reversal in sign of the electron contribution, relative to the initial current direction.

As a general result, whatever the driver, magnetic reconnection does not happen substantially faster than in the non-driven cases. While most of these studies were conducted with a β plasma parameter of the order of unity, the efficiency of driven reconnection is questionable for different β values.

1.3 Magnetic reconnection by means of satellite observations

In this section we give a brief overview of what we recently gained from observations of recent spacecraft missions —in the Earth magnetosphere and in the solar wind— about fast reconnection.

1.3.1 Reconnection in solar coronna

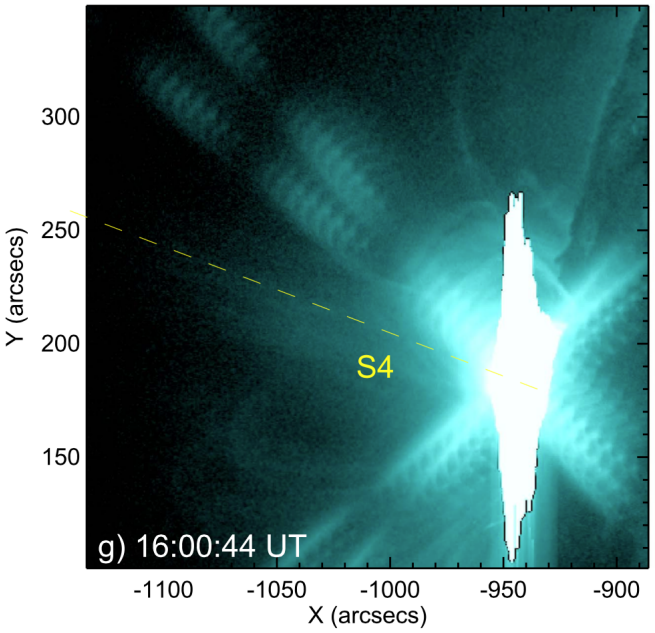

Figure 1.17: Snapshots of SDO/AIA 131. From Gou 2017 [GVD+17].

Data obtained by remote and in situ observations show that, reconnection occurring at the surface of the sun is a localized process, essentially three-dimensional and dynamic. It corresponds to a configurational instability rather than to a stationary process. This is clearly illustrated in the recent work of Gou 2017 [GVD+17], which reported the two stage magnetic reconnection of the magnetic loops on the Sun. Fig. 1.17 shows a snapshots of SDO/AIA (Atmospheric Imaging Assembly) observations, using wavelength 131 $\mathring{A}$. The virtual slit S4 is placed on the image in the direction perpendicular to the Sun surface along the outward-moving plasmas (OPs), that has been a result of the second stage of the reconnection.

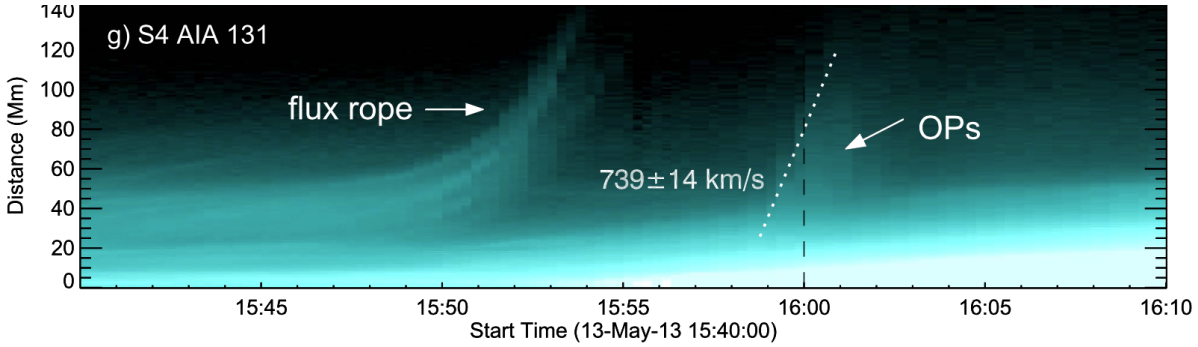

Figure 1.18: Dynamic evolution seen through the slit S4 on Fig. 1.17. OP - outward-moving plasmas. From Gou 2017 [GVD+17].

Fig. 1.18 shows the time evolution along the slit S4. We observe the erupting flux rope (the first stage of the reconnection) as well as the diffusive OPs with the out-moving velocity ~ 740 km.s^{-1}, which is roughly equal to the Alfvén velocity. The hot diffusive plasmas quickly moves upward comparing with the inflow direction. The authors concluded that the plasma was related to the reconnection outflow. The estimated reconnection rate at that time is 0.18, using the lower inflow speed of ~ 130 km.s^{-1}, which was measured near the reconnection site in the inflow direction. It is clear that the reconnection of magnetic loops on the Sun is sudden and not steady.

Such features does not fit with a stationary reconnection process. To describe theoretically the dynamics of magnetic reconnection, one usually consider the reconnection is a stationary process. It means the rate of magnetic field convection into the dissipation region is balanced by the rate of magnetic field diffusion inside of the dissipation region. In case of imbalance of convection and dissipation the system is not in a steady-state. In the following sections we present observation of the near-Earth magnetosphere, where satellites have a possibility to measure locally the physical quantities.

1.3.2 Reconnection in the Earth magnetosphere

The first observational evidence that the reconnection may take place in the near Earth-tail (Earthward of 30 R_E) comes from a statistical study of changes in the magnetic field configuration during substorms [NN73]. Spacecraft measurements help to identify

the reconnection zone (active current sheet) as well as they provide the first evidence of the localized nature [BPL90] of magnetic reconnection. Significant statistics of substorm and reconnection observations in the magnetotail, solar wind, inner magnetosphere were collected in the 1990's. Acquired information helped to establish the causal links from solar wind to magnetotail, and further to the inner magnetosphere and auroral zone. A quadrupole magnetic field disturbance was found [ØPF+01] due to the Hall current system in the ion diffusion region, where the decoupling of ion and electron motion occurs. The detailed characteristics of magnetotail reconnection site resolved the different distributions of inflowing and outflowing electrons and ions and the field-aligned currents closing the Hall current system [NZS+13].

1.3.3 The revolution of multi-points measurements

Modern multi-point missions allow direct observations of the spatial configuration of the reconnection on ion and sub-ion scales (thousands and hundreds of kilometers). The spatial gradients of magnetic field components (and hence the current density) can be obtained from the four-point magnetic field measurements based on linear gradient estimation [CH98]. The tetrahedron form of the spacecraft position helps to resolve the three directions. With on-board diagnostic, one can only measure a piece of space. To measure the 4 π steradians all over the spacecraft, the satellites have to be spined, meaning they are rotating around a given axis. Such spin is also required for more technical reasons and an associated better quality of the measures. One of the restrictions is to turn fast enough to be able to measure all the space during a sheet crossing. Modern missions are spinning faster than the older one allowing a better time resolution, as for example, a full distribution function needs at least one spin to be calculated. The detailed profile of the current density in the current sheet can be obtained when the spacecraft is vertically crossing the current sheet rapidly enough to assume the current sheet is simply translated without any change of its structure. Integration of the translation velocity projected onto the local current sheet normal during the crossing gives an estimate for the vertical scale of the current sheet.

For a single spacecraft observation, the structure of the reconnection region needs to be deduced by assuming the X-line motion as well as the orientation of the current sheet. Multi-point observations have the advantage to allow the calculation of the spatial gradient in addition to estimate the motion of the magnetic structures, such as X line or current sheet. The first four-spacecraft Cluster2 mission, launched in 2000, has revealed a vertical profile of the tail current sheet by direct measurements during current sheet crossings [RNB+03]. The THEMIS (*Time History of Events and Macroscale Interactions during Substorms*) mission, launched in 2007, used a group of five NASA satellites to study the energy released from the Earth's magnetosphere or sub-storms near Earth's poles. But we focus on results obtained with the recent one MMS giving the most accurate data.

The Magnetospheric Multiscale Mission (MMS), launched in 2015, is a NASA solar-terrestrial science mission consisting of four identically instrumented spacecraft. MMS

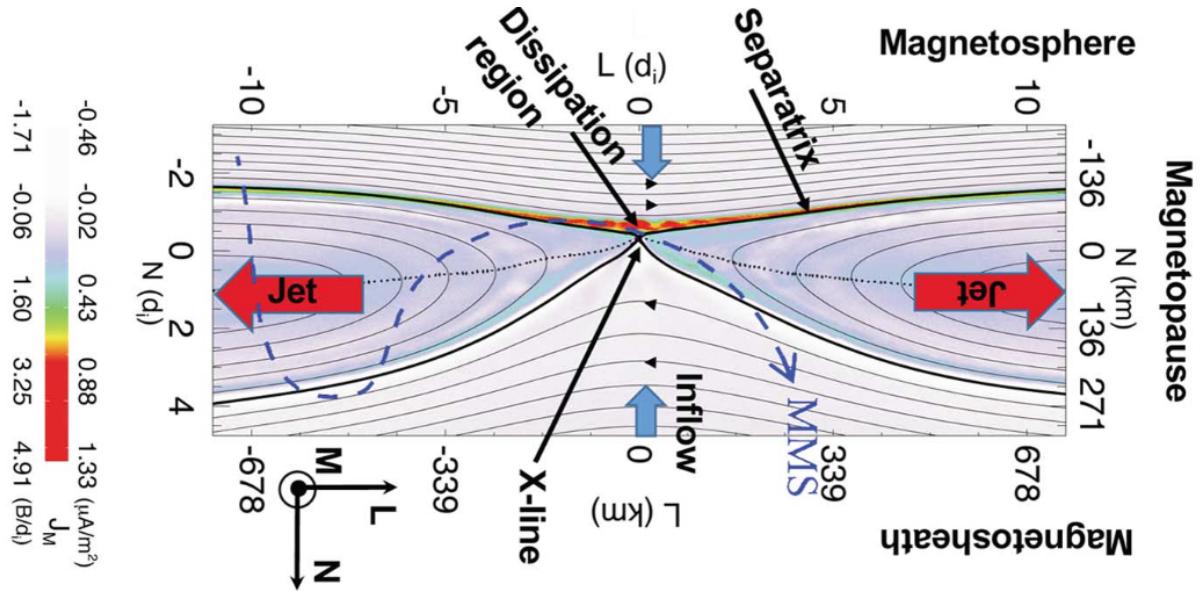

Figure 1.19: This scheme results from a numerical simulation using the parameters from the magnetopause crossing. Spatial coordinates in the diagram are shown both in km and in ion diffusion lengths. Color scale indicates out-of-plane current density. From Burch 2016 [BTP+16].

targets on investigating two reconnection regions known to exist around the Earth: the dayside magnetopause and the nightside magnetotail, which represent different plasma parameter regimes. The spacecraft were launched in a stacked fashion to cruise in a tetrahedron configuration, and uses an elliptic orbit around the Earth. Flying in a known formation, the four spacecraft are able to separate local and time-dependent variability and make measurements with high temporal resolution. One of the goals of the mission was to resolve the electron diffusion region. MMS studied magnetospheric properties on scales of a few tens of Kilometers to 100's of kilometers at time scales of milliseconds to several seconds. The observations revealed detailed structure of current sheet down to ion Larmor scale.

During its first phase (2015–2016), the four MMS spacecraft investigated reconnection in the dayside magnetopause [BTP+16], where the inflow conditions are highly asymmetric, with different plasma and magnetic pressures in the two inflow regions. Fig. 1.19 shows the typical structure of a magnetopause in which asymmetric reconnection is occurring, taken from a numerical simulation of the observed magnetosheath and magnetospheric conditions. This scheme shows the northward magnetic field on the magnetosphere side of the boundary and the southward magnetic field on the magnetosheath side. The converging plasma flows carry the two nearly oppositely-directed magnetic-field domains toward to each other. An X line directed normal to the plane of the diagram denotes the small region in the reconnection plane where the field lines interconnect, and this X line is likely to extend by hundreds to thousands of kilometers in the east-west direction, that is why

a large number of exhaust regions are typically crossed by spacecraft near the magnetopause. Another reason why reconnection events are routinely observed is the presence of the exhaust jets (red arrows) flowing northward and southward from the X line and the nearby dissipation region. While the results of reconnection are observed with measurements at the fluid and ion scales, it is the electron-scale physics inside of the dissipation region, that determines how reconnection occurs.

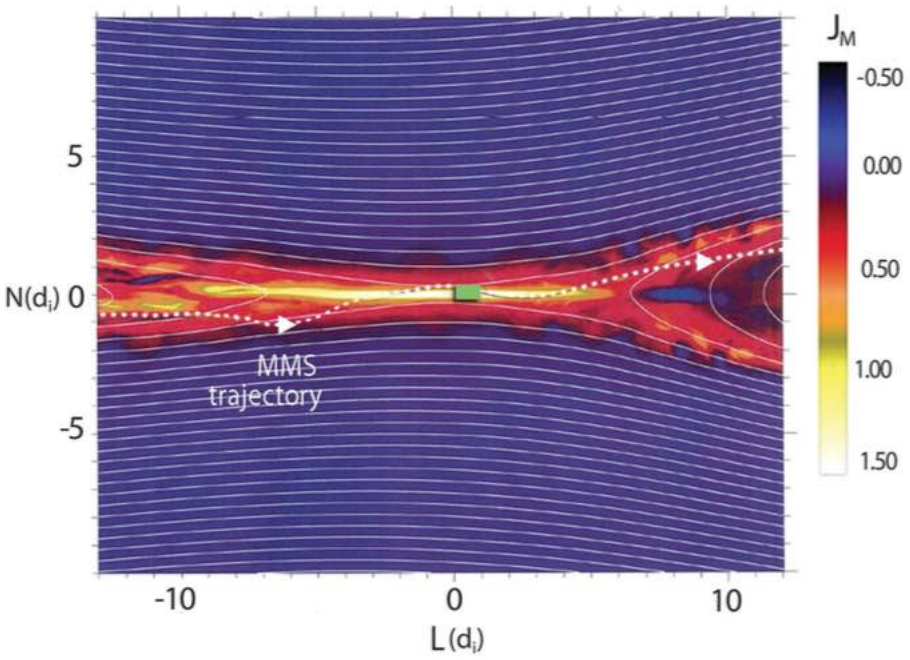

Figure 1.20: Magnetic configuration of a computer simulation, with color-coded reconnection current and the inferred MMS trajectory overlain. From Torbert 2018 [TBP+18].

In its second phase (2017), MMS explored the kinetic processes of reconnection in the Earth's magnetotail. The magnetotail reconnection electron diffusion region differs from that on the dayside as it involves symmetric conditions on both sides of the reconnecting current sheet. The available magnetic energy per particle is more than an order of magnitude higher than on the dayside. The reconnection rate has been studied theoretically and with simulations. Fig. 1.20 shows magnetic configuration of a computer simulation, with color-coded reconnection current, and superposed path of the satellite through magnetotail [TBP+18]. The spacecraft went through the edge of the inflow region and close to the neutral sheet. The MMS observations showed that electron dynamics in the diffusion region was nearly laminar despite the effects of turbulence and associated fluctuations. Electron flow velocity peaked at $\sim 1.5\times10^4$ km/s, on the same order as the Alfvén velocity, estimated as 2×10^4 to 2.5×10^4 km/s. Starting from the X line the electron perpendicular outflow speed increased and greatly exceeded the ion speed. While the ion outflow speed increased with increasing distance from the X-line, the electron perpendicular outflow speed reached a peak $\sim 7\times10^3$ km/s before slowing and approaching the ion flow speed.

The sstimated normal half-width of the current sheet thickness is 30 km ($\sim 1d_e$). The aspect ratio of the electron diffusion region is 0.1-0.2, which is consistent with predictions for fast reconnection.

1.4 Laboratory experiments on magnetic reconnection

The pioneering experiments on magnetic reconnection were carried out in short pulse pinch plasmas or fast high-density pulsed plasma discharges of a few micro-seconds duration [BY70, SFK73, Fra74, OOK74]. These experiments covered regimes of collision-dominated MHD with low Lundquist number S given by Eq. (1.17) (of the order of unity), and exhibited higher reconnection rates than the classical Sweet-Parker value one could expect. Using magnetic probes, they measured magnetic field profile across the neutral layer. It was shown that the current sheet has a final thickness determined by the balance between kinetic pressure of the plasma and pressure of the reconnecting magnetic field. While non-exhaustive, we give few details on such experimental facilities.

1.4.1 Z-pinch: the MAGPIE facility

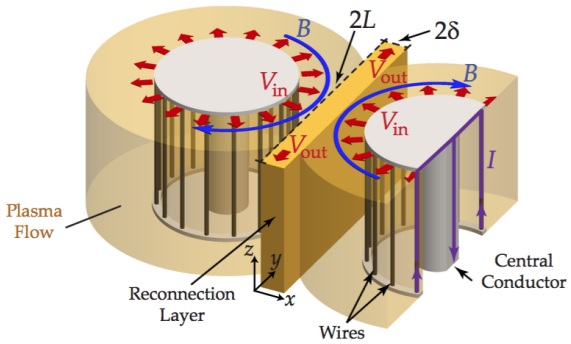

Figure 1.21: MAGPIE experimental setup with the geometry of the reconnection layer. From Hare 2017 [HSL+17].

The Mega Ampere Generator for Plasma Implosion Experiments (MAGPIE) is a pulsed-power generator at Imperial College London, capable to deliver an electrical current pulse of $\sim 1.4 \times 10^6$ Amperes in ~ 250 nanoseconds, which is equivalent to a Tera Watt of electrical power. Fig. 1.21 shows a schematic of the experimental setup. Two exploding wire arrays are placed side by side and produce radially diverging outflows moving with the frozen in azimuthal magnetic fields generated by the currents in the wires. The

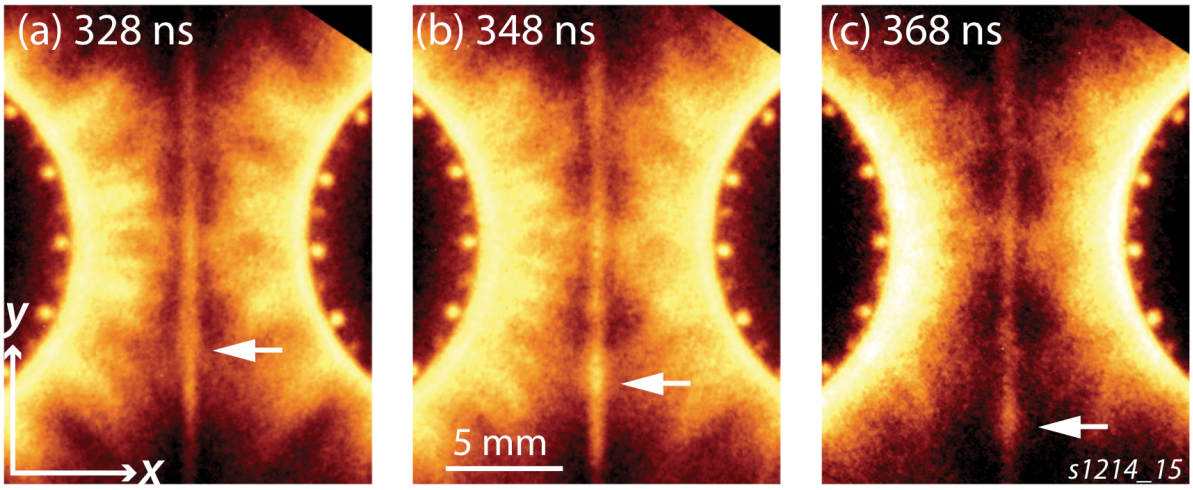

Figure 1.22: Plasmoid formation and dynamics in three optical self-emission images from the same experiment: 5 ns exposure, 20 ns between frames. The location of one plasmoid in each frame is indicated with a white arrow. From Hare 2017 [HSL+17].

plasma is continuously ablated from the resistively heated wires, and the $\mathbf{J} \times \mathbf{B}$ force acts on the plasma driving supersonic plasma flows, which are sustained during the current discharge. The possible diagnostics include magnetic probes for direct measurements, self emission diagnostics optical and X-UV fast framing camera, laser interferometry, Thomson scattering to measure magnetic fields and Faraday Rotation imaging. Therefore, both the plasma and the magnetic field of the sheet, before or after reconnection, can be investigated.

Fig. 1.22 displays the electron density from the recent work [HSL+17], which exhibits the formation of plasmoids, one of them being marked by white arrow. The peak density is near the wire cores, where ablation occurs, while it radially decreases. The density perturbations in the reconnection layer remains uncorrelated with the density perturbations in the inflow. The depletion layer just outside of the reconnection layer occurs all the times. Plasmoids are observed inside the reconnection layer, moving, merging and breaking apart, always denser than the surrounding reconnection layer. They conjecture such plasmoids results from the semi-collisional "plasmoid instability"[LU15] as the experiment is conducted with a modest Lundquist number $S = 120$. The plasmoid instability breaks the current sheet into several smaller sheets.

1.4.2 Magnetic Reconnection eXperiment (MRX)

The *Magnetic Reconnection eXperiment* (MRX) device was built at Princeton Plasma Physics Laboratory (PPPL) in 1995 to study the fundamental physics of Magnetic Reconnection, under the supervision of Pr. Yamada[YJH+97]. The analysis focused on the

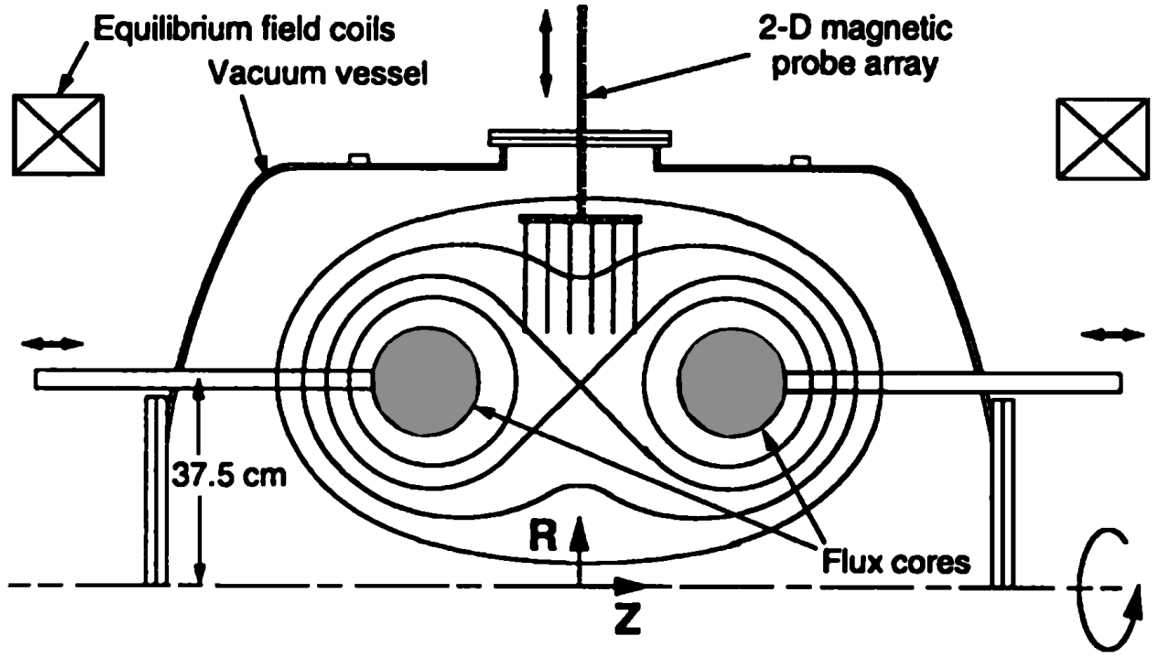

Figure 1.23: Cross-sectional view of MRX device also shows the public flux domain and two private flux domains surrounding each flux core. From Yamada 1997 [YJH+97].

coupling between local microscopic features of the reconnection layer and global properties such as the external driving force and the evolution of plasma equilibrium. Fig. 1.23 shows the geometry of the MRX device. The MRX device contains two flux cores, each with a major radius of 37.5 cm and minor radius of 9.4 cm. The flux cores contain both poloidal field (PF) and toroidal field (TF) windings. First, an X point-like magnetic configuration is established by parallel currents in the PF coils, the currents in the TF coils are pulsed, creating an inductive electric field around the flux-cores to break down the gas. Simultaneously, a common annular plasma is formed, which surrounds the two plasmas created around each flux core. After the annular plasmas are created, the PF coil current is decreased, and the poloidal flux in the public domain is "pulled" back toward the X point into the private domains, which triggers reconnection.

The MRX experiment allows to investigate how global conditions affect the microphysics of the reconnection process. In MRX, a large downstream pressure was found to slow both the outflow in the reconnection layer and the reconnection rate, demonstrating the importance of boundary conditions [JYHK98]. It was also found out that, with the same plasma parameters the reconnection rate decreased when increasing the distance between flux cores or equivalently when increasing the system size [KJG+07]. The reduced reconnection rates in larger systems were attributed to longer current sheets.

In MRX, the measures of the density profiles of the neutral sheet changes radically from the high-density (collisional) to low-density (nearly collisionless) cases, as illustrated

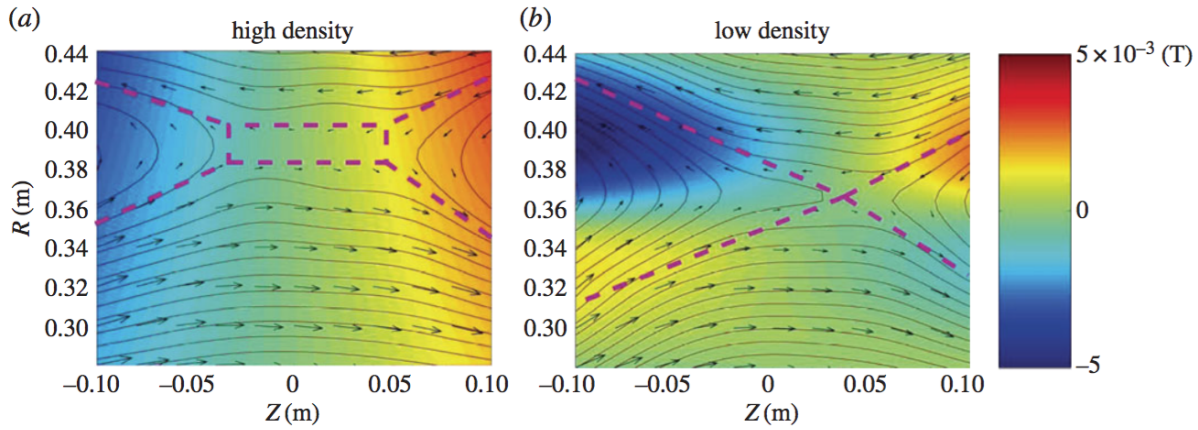

Figure 1.24: The in-plane magnetic field is shown as arrows and the out-of-plane magnetic field component is shown in color code, ranging from -50 G to 50 G. Dashed pink lines show that the magnetic configuration changes from an elongated current sheet (Sweet-Parker type in (a)) to a double-wedge shape (Petschek-like) as collisionality is reduced. From Zweibel 2016 [ZY16].

in Fig. 1.24 which shows the magnetic fields for these two regimes of reconnection. In the high plasma density case (left), where the mean free path is much shorter than the sheet thickness, a rectangular-shaped neutral sheet profile is seen together with the observed classical reconnection rate like the Sweet–Parker model. There is no out-of-plane magnetic field in this case, associated with the Hall effect. In the case of low plasma density (right), where the electron mean free path is larger than the sheet thickness, the Hall MHD effects become dominant as indicated by the out-of-plane magnetic field depicted by the color code. A double-wedge-shaped sheet profile of Petschek type, which is shown in the flux contours of the reconnecting field, is significantly different from that of the Sweet–Parker model, and a fast reconnection rate is measured. The observed fast reconnection is also consistent with the expanding shape of the outflow region just as in the Petschek model. However, a slow shock, an important signature of the Petschek model, has not yet been identified to date even in this collisionless regime.

1.4.3 Large Plasmas Device at UCLA

As in three dimensions, reconnection can occur even in the absence of a true magnetic null [SHB88], experiments that reproduce the three dimensional effects are very appreciable. *The Large Plasma Device* (LAPD) is a facility at the University of California, where the plasma is produced with a continuous discharge. The LAPD plasma column is 60 cm in diameter and 18 m long, the axial magnetic field is produced by solenoidal magnets and may be varied, power supplies generate current for the magnets therefore

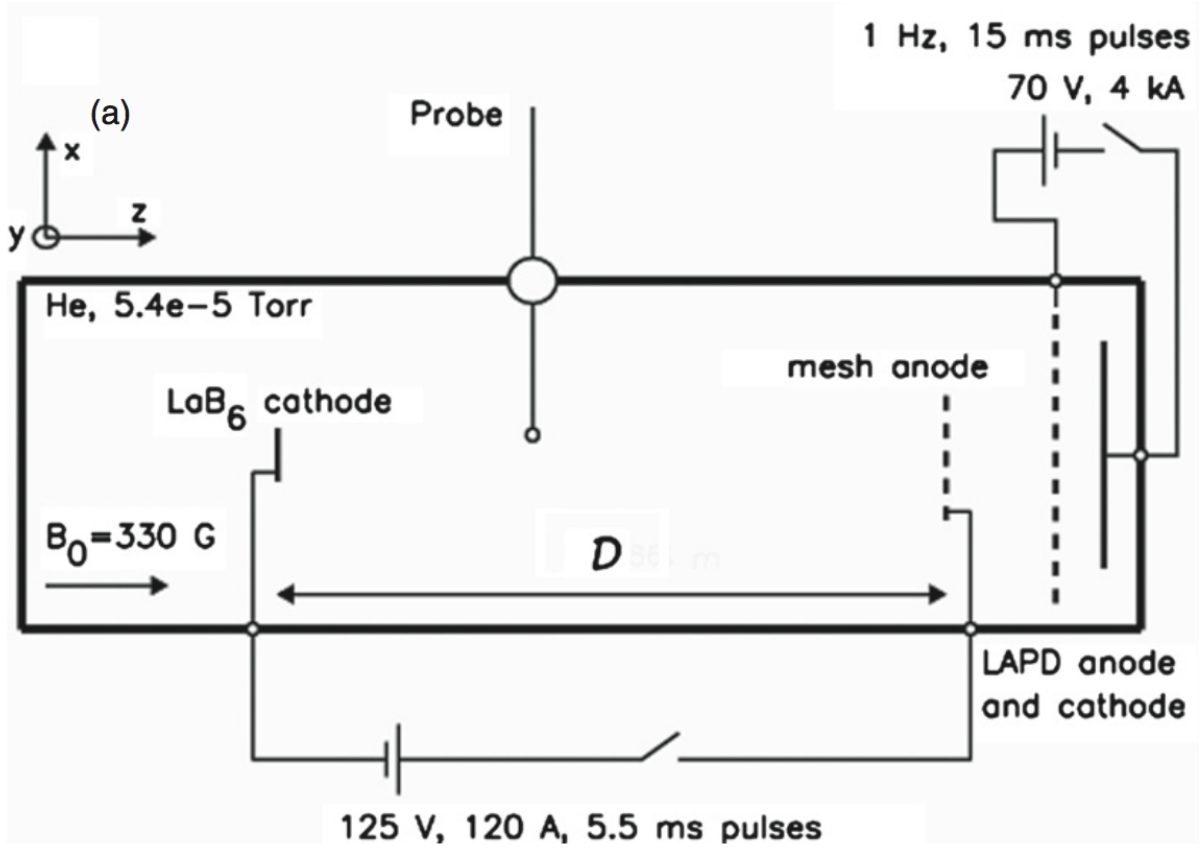

Figure 1.25: Schematic of the experimental setup LAPD. From Gekelman 2012 [GLVC12].

the axial magnetic field profile is variable [GLVC12]. The facility can provide a full three dimensional picture of the magnetic field lines involving few magnetic flux ropes. The experiments are reproducible and use computer-controlled stepper motors to slowly move probes throughout the volume of the device and collect data. A schematic of the device is shown in Fig. 1.25. The background plasma is formed when electrons emitted from a large cathode on the right are collected on an anode 55 cm away. The plasma is 17 m long and 60 cm in diameter. Solenoidal coils (not shown) produce an axial magnetic field B_{0z}. Two or three LaB_6 cathodes are placed on the other side of the machine to make the flux ropes.

Fig. 1.26 (a) shows two sets of representative field lines; one for each cathode. The field lines are seeded at a radial distance of 0.5 cm from the center of each flux rope at $Z =$ 64 cm. They can identify the two types of twisting of the field lines. One is the "writhe" which is the kinking up of the entire flux rope. The other is the "twist" which is the curling of a field line about the axis of the flux rope. By tedious inspection of axial locations one can find reconnection events in the transverse plane by studying the morphology of field lines as a function of time, Fig. 1.26 (b). The field lines approach each other, reconnect and move apart. In three dimensions the large component of B_z is shadowing this picture. Since the flux tubes are moving, any two of them could cause a reconnection site at any

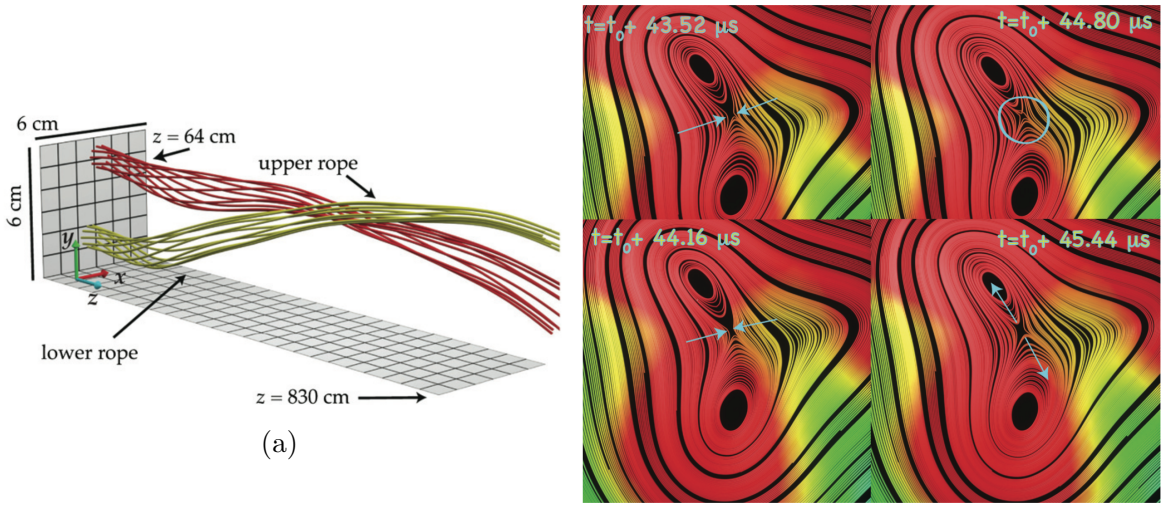

(a) (b)

Figure 1.26: (a) Two sets of field lines representing each flux rope at the same time. (b) Magnetic field lines and vectors in the transverse plane as a function of time. As time goes by the field lines move toward each other, reconnect in the top right-hand figure and move apart. From Gekelman 2012 [GLVC12].

position in the volume and at any given time reconnection could be happening at several locations. For 3D experiments the reconnection rate is the induced electric field generated by flux annihilation, as classical models are not appropriate.

1.4.4 High power lasers

Many measurements of magnetic reconnection in plasma created by two or more laser beams have been made in the last two decades. [NWK+06, LSF+07, WNK+10]. To create HED plasma bubbles, terawatt-class lasers simultaneously focus on plastic or metal targets. The solid target is ionized into bubbles-like plumes that expand supersonically off the surface of the target. The bubbles expand into one another, and the anti-parallel magnetic fields are compressed one against the other and reconnect. Each bubble self-generates a strong magnetic field of order of hundreds of Tesla, thanks to the Biermann-Battery effect [BS51]. The experimental results are deeply discussed in Chapter 4. In this section we briefly overview the possible configurations, and look at the typical picture obtained with a widely used diagnostic, which is called proton radiography [SKH+00].

Fig. 1.27 schematically shows a global picture of plasma bubbles and the associated self-generated magnetic fields in the target plane for symmetric reconnection [NWK+06]. Two heater beams, with wavelength $\lambda = 1.054\mu$m, irradiated either aluminum or gold targets. A 1 ns duration square pulse was used with an average energy of 200 J per heater

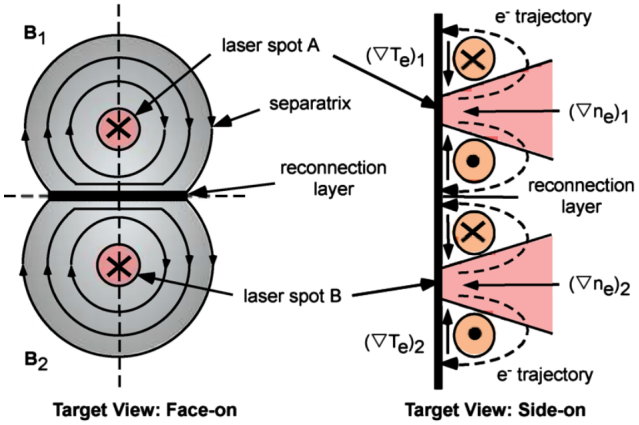

Figure 1.27: The target geometry and field configuration. From Nilson 2006 [NWK+06].

beam. The targets were 3 by 5 mm foils of 20–100 μm thickness. Each beam was focused to a focal spot diameter of 30–50 μm full width at half maximum, giving an incident laser intensity of 10^{15} W.cm^{-2}.

From PIC simulations of symmetric reconnection in such conditions [FBG11], there are two distinguishable phases:

1. small reconnection rate is associated with a compression or pile-up phase. The reconnection field is supported by the $\mathbf{E} \times \mathbf{B}$ plasma flow of the ribbons

2. maximum reconnection rate for which the electric field is supported (a) by the Hall effect in the current sheet ($\sim \mathbf{J} \times \mathbf{B}$), since the current sheet is now of the ion scale, and (b) by the electron pressure tensor at the X line.

They also pointed out in this work the importance of the off-diagonal pressure tensor component $\sim \partial_x P_{xz}$ (X being the outflow direction and Z being the out-of-plane direction). This term represents about 80 % of the electric field in the vicinity of the X point.

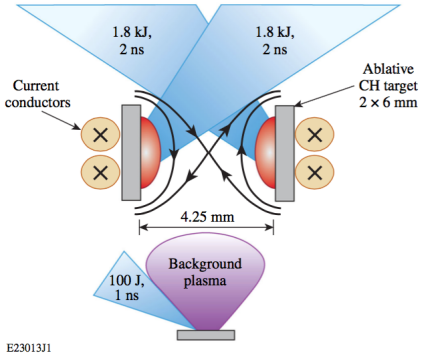

Figure 1.28: Reconnection experiments with externally controlled background plasma. From Fiksel 2014 [FFB+14].

The experimental results of colliding plumes obtained with an externally controlled background plasma (Fig.1.28) as well as the associated numerical simulations showed the formation and collision of magnetic ribbons, pile-up of the magnetic flux, and reconnection of the magnetic field [FFB+14]. Even accounting for flux pile-up [FBG11], the simulated reconnection rates are extremely fast, close to 100 % of the local Alfvénic rate $B_0 V_{A0}$, calculated based on the compressed magnetic fields and the plasma density in the current sheet.

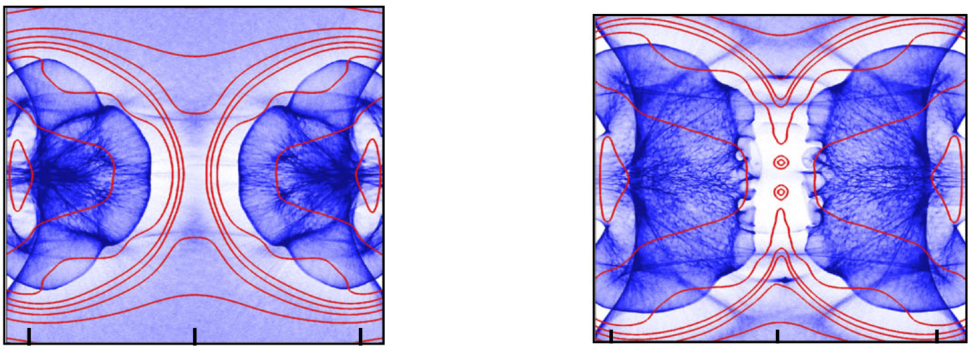

(a) (b)

Figure 1.29: Results of simulated proton radiography during (a) formation of magnetic ribbons and the sweeping up of magnetic field, and (b) the magnetic field annihilation. From Fiksel 2014 [FFB+14].

Fig. 1.29 shows the picture obtained with proton radiography during the formation of magnetic ribbons and the magnetic field annihilation [FFB+14]. To do so, beam of energetic protons pass through the target and ablated plasma, and are deflected by the magnetic and electric fields encountered during their fly. The informations collected on the obtained films contain the "memory" of the electric and magnetic field integrated in space and time along the protons orbit (such diagnostic are detailed in chapter 4). The cellular structures in the mid-plane are interpreted as magnetic islands or plasmoid structures growing inside the current sheet. The annihilation (and indeed the entire evolution of the ribbons) occurs on a significantly faster time scale than the resistive diffusion time (of the order of 10 ns) through the smallest plasma structures (at a scale of 100 μm), hence neither reconnection nor disruption are simply due to resistive dissipation. The remarkable feature we can also observe in our simulations, is a bulge of plasma in the outflow direction, connected to the background plasma expelling.

Few works were done on an asymmetric magnetic reconnection in laser-produced plasmas. For such topologies, two driving lasers are focused on a target with a time delay. From the experiment of 2015 [RLF+15], It was concluded that the rate of magnetic flux annihilation is dictated by the relative flow velocities of the opposing plasmas and is insensitive to initial asymmetries. While not already published, asymmetric reconnection could also be obtained by using two different solid targets (to create plasmas of different density and/or temperatures), or different energies for each lasers.

In Chapter 4 we focus on symmetric reconnection. To be able to integrate the generalized Ohm's law we have to keep background in our numerical simulations.

Chapter 2

Numerical simulations of magnetic reconnection

In this chapter, we discuss the different numerical approaches that one can adopt to investigate the dynamics of magnetic reconnection process. We also introduce the equations for the plasma and the electromagnetic fields and the way we numerically integrate them. The last part is dedicated to the numerical issues arising from such approach.

2.1 Fluid and kinetic formalisms

In plasma physics particles are charged, for this reason we need to solve the Maxwell equations to properly describe the time evolution of the electromagnetic fields. As source term, the current density $\mathbf{J}$ and particle density n are needed. There are two ways to solve such problems:

- describe the plasma by the distribution functions
- use a finite number of the moments of the distribution function

The simulation codes are commonly divided into two categories: (a) kinetics, and (b) fluids. As collisions make the distribution function close to Maxwellian, the moments of order 0 (density), 1 (fluid velocity) and 2 (scalar pressure) are enough to describe the plasma. Even in weakly collisional or collisionless cases the distribution functions can be close to a Maxwellian, and the fluid approach can be followed. Otherwise we use kinetic approach in the situations in which we need to describe specific structures of the distribution function.

2.1.1 What are the relevant scales ?

A plasma is generally a media where multiple scales, in space and time, are at play. The macroscopic evolution of the whole system is often relatively slow and develops on large scales, but is tightly coupled with smaller and faster scales. When modeling a plasma, we have to resolve the following spatial scales: Debye length, Larmor radius, and inertia scales for both electrons and ions. The associated time scales are the inverse plasma frequency and the inverse cyclotron frequency. While the proton to electron mass ratio is of the order of 10^3, it is complicated and expensive from the computational point of view to treat realistic mass ratio because of the fast electron gyrations comparing with the protons one. In Space and laboratory experiments we also have a ratio between the speed of light and the Alfvén speed of the order of 10^3. We present the different ways to circumvent these problems.

While simpler, the fluid approach is generally the first one to investigate a problem, even if the justification of its use is sometime questionable. From the theoretical point of view the first analytical model, as detailed in chapter 1, were also proposed using the fluid approach. But of course, such approach fails describing the microphysics at play in the regions of small scale gradients.

From the numerical point of view the kinetic approach is associated with two kinds of codes: Particle-In-Cell (PIC) codes and Vlasov codes. The PIC technique simulates "macro-particles" that represent many plasma particles, and solve their motion equation. The Vlasov approach discretizes (in the real space and velocity space) the complete distribution function and solve the Vlasov equation in the associated six-dimensional space. Both methods are quite heavy, and require much more computational resources than fluid codes. We discuss both methods in Section. 2.2.1.

The mass ratio of ions and electrons is a common difficulty in numerical simulations. The spatial and temporal dimensions of the simulation domains are limited by fast electron gyrations over a small spatial scale. To overcome this difficulty, one solution is to use artificially heavy electrons[1]. Another way is to treat the electrons as a massless fluid and the heavier ions as macro-particles following the PIC formalism[WQ86]. Such approach is generally called "hybrid", as both formalisms are mixed-up. The hybrid models allow to study kinetic ion physics, while ignoring the electron kinetic effects. Several of these codes exist, generally with the same assumptions: (i) quasi neutrality, meaning that at each grid points, the ion density is equal to the electron density (ii) the electron fluid is massless (iii) the transverse component of the displacement current is neglected (the generalized Ohm's law is used to calculate the electric field) (iv) a closure equation for the electron pressure, which is often isotherm [WYO$^+$03]. Codes, where electrons are treated as particles, and ions as fluid, exist, and are important to describe the non-linearities in the electron dynamics [LL92].

To save computational time, but at the same time to keep the appropriate physics, one can use the following hybridization: to use fluid nature of plasmas in MHD part to model large-scale plasma dynamics and use PIC part to resolve small-scale kinetic

[1] the degenerate case is to simulate electron-positron plasmas

dynamics near the reconnection region. The challenges are to make numerically feasible approximations for the MHD and PIC interlocked region. The main problem is that, at the interface between these two types of description, one needs to set boundary conditions for one model, using the informations coming from the other model. As there is more information in a distribution function than in a set of fluid moments, this step can be hard to manage. One of the first algorithm was applied to Alfvén wave propagation problem in an one-dimensional system. The wave smoothly propagated from MHD into PIC domain and ejected again into MHD with almost the same form and amplitude [SK07].

As a partial conclusion, due to large scale separation both in time (between electron plasma oscillation time and reconnection time) and in space (between Debye length and system size, which is typically on the MHD scale), various approximations have to be used to be able to cary the simulations in a realistic time. The prominent approach is a hybrid, that keeps the ions kinetic effects, but remove fast electron gyration. In the following sections we justify the relevance of using such method.

2.1.2 Kinetic effects for both populations

By kinetic effects, we mean wave-particle interaction (Finite Larmor radius effect is the topic of the next section). We can roughly consider that these effects can be decmpposed in two families: (i) the Landau and inverse Landau damping (this last one is also called Cerenkov effect) and (ii) the cyclotron resonnances. The first case can be observed for demagnetized particles, while the second one needs the particles to be magnetized. If one wants to correctly treat these cases, the kinetic treatment is mandatory, whatever PIC or Vlasov. The question we need to address for reconnection is whether ions and/or electrons can resonate with the fluctuations.

For the tearing mode, i.e. the self-development of a plasmoid instability in a magnetic field reversal, it has been demonstrated [**?**] that the Cherenkov effect on the electron is on the origin of the associated dissipation. The ion tearing has been challenged [PCP91], but no clear proof of its existence has been provided yet. For the X point reconnection it is not the case, and the role of the kinetic effects for the electrons is not demonstrated, as treating the electrons as particles or as a fluid give rather the same results.

Another important question is to evaluate in which ways, the development of small-scale electromagnetic fluctuations can be associated with any diffusion process on the particles. While being trendy during the 1980's, the so-called "turbulent dissipation" has never been clearly demonstrated. Nonetheless, we should mention that this is still the topic of hard investigation in the field of cosmic rays, as the fluctuations in the interstellar medium could play an important role for their confinement, and define their lifetime.

As a last comment, we should also mention that a small community is developing around the close interplay of magnetic turbulence and magnetic reconnection [LV99, LEV12]. As it could have strong and importance consequences, it is yet unclear why

we should treat the ions in a kinetic way. The next subsection clarifies the importance of ion kinetic effects.

2.1.3 Finite Larmor radius effects

In 1989, Bucher and Zeleniy [BZ89] worked on the particle motion in magnetic field reversals with an arbitrary curvature radii. They introduced the curvature parameter:

$$\kappa^2 = \frac{R_{\min}}{\rho_{\max}} \tag{2.1}$$

where $R_{\min}$ is the minimum curvature radius of the magnetic field lines, $\rho_{\max}$ is the largest possible Larmor radius [BZ89]. In the case $\kappa \gg 1$ one can use the adiabatic approach, as the Larmor radius is much smaller than the curvature radius. That means wherever particles are adiabatic, the plasma could be described in a fluid way. But once finite orbit size effects become important, we have to treat non-adiabatic trajectories.

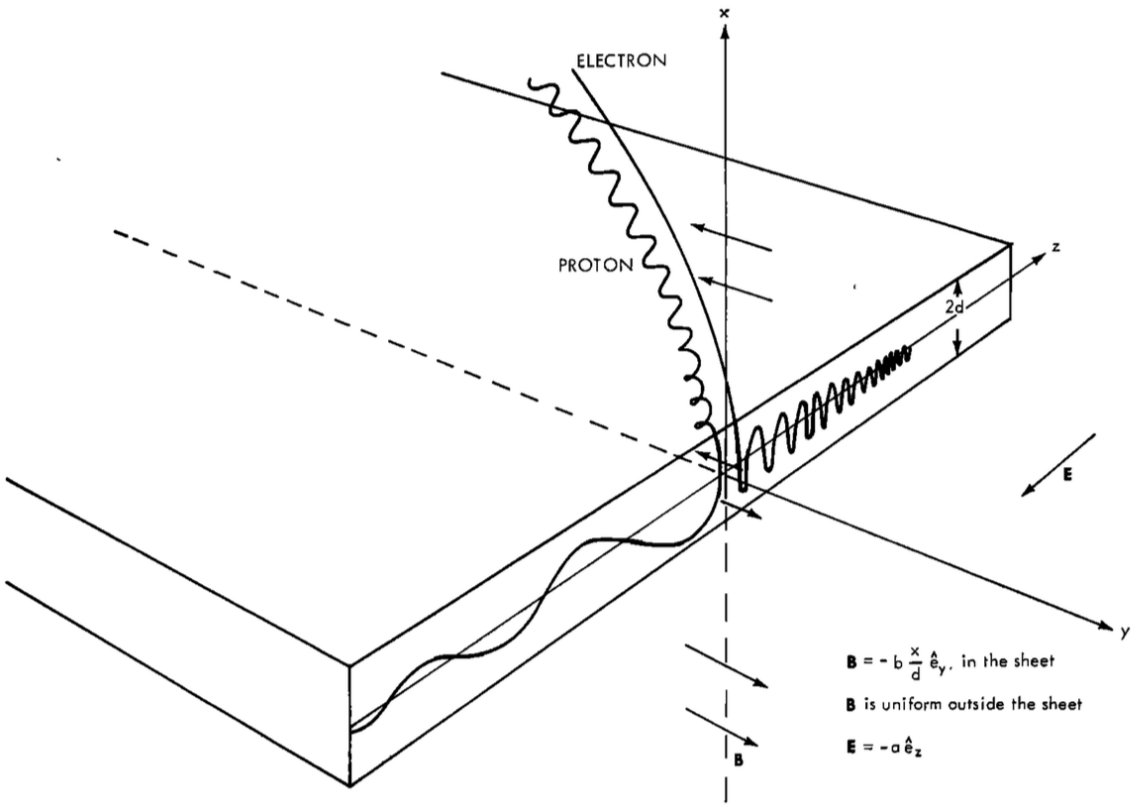

Figure 2.1: A schematic diagram of the electron orbits near the reconnection site. From Speiser 1965 [Spe65].

From the frozen-in condition in ideal MHD, particles gyrate around the same magnetic field line for infinite time. But ideal MHD is not valid if particles experience different magnetic field strengths during one gyro-orbit. If a particle goes through a magnetic field pointing in the opposite direction during its orbit, it will gyrate in the opposite direction, thus disconnecting from its original magnetic field line. Such dynamics is called "*meandering motion*". As consequence, even in the absence of collisions, ideal MHD breaks down due to *finite Larmor radius* (FLR) effects. In 1965 Speiser found an approximate analytical solution of the reverse magnetic field system with uniform electric field, perpendicular to the magnetic field and parallel to the neutral sheet. Fig. 2.1 shows a sketch of the ions exhibiting the *Speiser orbits* ([Spe65]): the particles have half of a cyclotron turn on the one side of the field reversal and another half on the other side. Because of the change of sign of the magnetic field these motions are in opposite directions.

The FLR effects introduce important corrections to the dispersion relations for MHD waves and drift instabilities. Expansion of plasma into magnetic field leads to filamentation of the plasma boundary and to creation of structures with a thickness smaller than an ion gyroradius. Large Larmor radius effects in curved magnetic field geometry lead to stochastic behaviour of particle trajectories and to deterministic chaos. In collisionless plasmas, meandering motion, while performing Speiser orbits, results in non-diagonal electron pressure tensor components [YWDC04]. The spatial scale of the orbit amplitude of meandering electrons in the region of the weak magnetic field is approximately equal to the half thickness of the region where the non gyrotropic contribution to the out-of-plane electric field dominates all the other components. This suggests that the electron meandering motion can give rise to non-gyrotropic terms in the electron pressure tensor [KHW98].

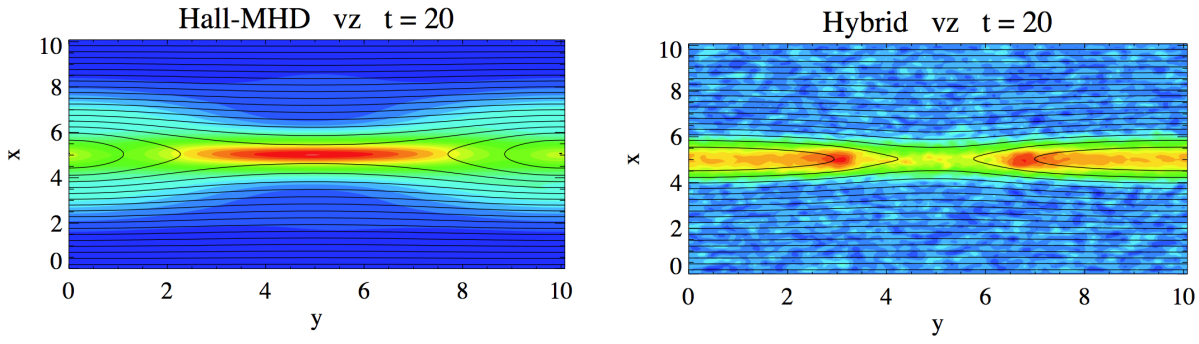

(a) (b)

Figure 2.2: Color code for the ion out-of-plane velocity component at comparable times in Hall-MHD (left panel) and hybrid (right panel) simulations, showing differences at the X point, due to finite ion-gyroradius effects. From Winske 2003 [WYO+03].

Fig. 2.2 shows the color contours of the ion out-of-plane velocity component at comparable times in Hall-MHD and hybrid simulations, showing differences at the X point due to ion FLR effects. The velocity structure from the hybrid simulation shows a re-

duction of the momentum at the X point, in contrast to the Hall-MHD run, where the velocity is peaked at the X point and remains so peaked to the end of the run. The ion FLR effects are important to correctly model the ion out-of-plane momentum transport from the X point. In Hall-MHD codes ion dynamics is described by the ion momentum equation with a scalar ion pressure. Thus, ion finite Larmor radius effects contained in the off-diagonal terms of the ion pressure tensor are not modeled in the Hall-MHD code. This results in a significant difference in the spatial configuration of the out-of-plane ion velocity [WYO$^+$03].

2.1.4 Effects of mass ratio and speed of light

One of the fundamental restrictions in numerical models for explicit schemes is the Courant–Friedrichs–Lewy (CFL) condition $v\Delta t < \Delta x/\sqrt{n}$, where v is the phase speed of any wave contained in the dynamical equations and $n = 1, 2, 3$ is the number of spatial dimensions for the computational grid. This condition states that in one time step, a wave travels a distance that must be smaller than the grid size. If considering light waves, the velocity to consider is the speed of light, being generally higher compared to the Alfvén velocity. One can artificially remove these constraint by either neglecting the displacement current in the Maxwell-Ampère equation, or by artificially decreasing the ratio c/V_A. The similar condition exists for particles, that cannot fly more than the grid size in one time step.

The other smallest time scales we potentially need to resolve are electron plasma and gyro frequency. The mass ratio problem is coming from the fact that using realistic ion to electron mass ratio, we have to resolve the smallest time step, that is electron one. Electron turns 1836 times while ion finishes one gyro period, as result to include realistic electron dynamics is at great cost from the numerical point of view. The similar problem holds with the spatial scales, as electron Larmor radius and inertial lengths depend on mass ratio. As a result, in many numerical simulations, artificially small mass ratio or c/V_A ratio are considered to have tractable results.

As was pointed out before, the Hall effect plays a crucial role in the plasma particle dynamics of collisionless magnetic reconnection. The electron and ion motion decouple on scale lengths of the order of the ion inertia length around the dissipation region, allowing the reconnection rate to become independent of the electron mass and thus to depend only on the ion dynamics. The resulting rates greatly exceed those based on reconnection controlled by electrons. It also resolves the long-standing controversy over whether the electrons or ions control magnetic reconnection in the Earth's magnetotail.[BSD95]

Finite electron mass hybrid codes have been applied to magnetic reconnection to show the role of short-scale physics in the reconnection process [SDDB98, KHW98]. The inclusion of electron inertia changes the whistler dispersion relation at short wavelengths, the real frequency no longer varies as the square of the wavenumber. Also a smaller

electron mass results in a smaller electron skin depth which has to be resolved by the grid. At the same time the numerical time step has to be reduced to resolve the electron gyro frequency. Both effects together imply that, in a spatially two-dimensional simulation, the computational cost increases with the square of the mass ratio for all kinetic simulations independent whether they use PIC or Vlasov methods.

A nice example is an electron-positron plasmas, or pair plasmas, that is potentially important for astrophysical applications like pulsar winds and extragalactic jets. It is also important for fundamental physics because the Hall term in such a plasma is not present. Electron-positron plasmas do not support a Hall current, because there is no scale separation between the ion and the electron motion. But such systems demonstrate a similar reconnection rate supported by electron pressure around the X point, although there were no Hall current in the system and no quadrupolar out-of-plane magnetic fields [BB07].

2.2 Why is the hybrid approach relevant ?

Hybrid codes can handle finite Larmor radius effect becoming important close to the neutral line, and can also take into account the wave particle interaction. Both processes are important to properly describe the magnetic reconnection. If we treat ions as particles and electrons as a fluid, the relevant scales are the ion gyro-radius and ion inertia length, and inverse ion gyrofrequency time. Treating any phenomena on these scales requires assumptions about the descriptions of the ions and electrons as well as the electromagnetic fields. In this section we describe the assumptions and equations of the hybrid model. We use the hybrid code HECKLE [Sme13].

The main aim of the work is to simulate the laser-plasma reconnection experiment. Full three-dimensional PIC simulations of the experiments are costly from the computational point of view, as increasing the system size results in increasing the number of particles. For instance, in two-dimensional hybrid simulations one needs to put at least 100 particle per cell to provide statistically reliable simulation. For a 100 per 100 cell simulation one gets 10^6 particles. Adding the third dimension of the same size we already have 10^8 particles, and the total CPU time increases by two orders of magnitude. While an average two-dimensional simulation takes 10 hours with 1000 cores, adding the third dimension would give at least 40 days, that is clearly not doable for a parametric study. Since the reconnection plasma inflow and outflow relative to the current sheet lay in the same plane, we focus on the so-called 2.5D simulations, where the 3rd components of any vector quantities are evolved through time, but their derivatives in the normal to the reconnection plane Z direction are zero.

2.2.1 Kinetic treatment of ions : particles or Vlasov approach

The basis for the analytical treatment of a collisionless plasma is the Vlasov equation:

$$\partial_t f + \mathbf{v}.\partial_{\mathbf{x}} f + \frac{q}{m}(\mathbf{E} + \mathbf{v} \times \mathbf{B}).\partial_{\mathbf{v}} f = 0 \tag{2.2}$$

$f(\mathbf{x}, \mathbf{v}, t)$ is the distribution function of a given specie, the electric $\mathbf{E}$ and magnetic $\mathbf{B}$ fields are determined by Maxwell's equations. The Vlasov equation represents a partial differential equation in a six-dimensional phase space plus time. To fully resolve this entire phase space, one needs a huge amount of computer memory. The more common approach to kinetic modeling of plasma is to represent the distribution function by a number of macro-particles and to compute the particle orbits in the self-consistent electric and magnetic fields. This is equivalent to solving the Vlasov equation by the method of characteristics.

In contrast to PIC simulations, Vlasov codes discretize the complete distribution functions of electrons and ions on a grid in phase space. This has the advantage of allowing a more detailed investigation of the tails of the distribution functions, since numerical noise is completely absent from the Vlasov approach [SG06]. To focus on particle dynamics there are two ways. The first one is to take a microscopic point of view by looking at the detailed structure of the distribution function. The second one is to look at the moments of the distribution function and their importance for the Ohm's law. The Vlasov approach allows to do both with a high accuracy. Few simulations of magnetic reconnection by Vlasov codes were done [SB03], but these studies are still relatively rare.

In a full particle model one follows the motion of both electrons and ions in the self-consistent electric and magnetic fields obtained by solving the Maxwell's equations. Relativistic effects can be included by the use of the Lorentz equations of motion for the particles. Such a model represents the closest approach to mimic the real plasma behavior of all simulation models. The Maxwell's equations are solved on the grid, and the forces acting on the particles are obtained by interpolating the fields back to the particles. Such technique eliminates fluctuations at scales smaller than the grid size.

The hybrid model we use, solves the ion kinetic dynamics using the PIC method. Instead of solving Vlasov equation, the macro-particle with mass m and charge q obeys the equation:

$$d_t \mathbf{x} = \mathbf{v} \tag{2.3}$$

$$m d_t \mathbf{v} = q(\mathbf{E} + \mathbf{v} \times \mathbf{B}) \tag{2.4}$$

where $\mathbf{x}$ and $\mathbf{v}$ denote the particle position and velocity, $\mathbf{E}$ and $\mathbf{B}$, which have values given on a spatial grid, are the electric and magnetic fields interpolated to the particle location. The equation is solved using the Boris algorithm [BS72], that is important as it saves computation time compared to other schemes, and is quite accurate. Generally PIC codes spend 80% of the computational time for the particle pushing. Electromagnetic fields are calculated on two staggered grid to preserve a time centering of the scheme. The predictor-corrector scheme [WQ86] is used to preserve a second order scheme. For the details of the algorithm, see Appendix A A.

2.2.2 Quasineutrality

At large scale, a plasma is quasi-neutral, meaning that the total charge of negative species equals the total charge of positives species. But at smaller scale nominal space charge can arise. As an example, such charge imbalance are observed in high frequency electrostatic modes, like in the Langmuir waves. Such fluctuations are always associated with high frequency modes, close to the electron plasma frequency, and at small scale, close to the electron Debye length. If, for any reason, we are not interested in describing such fluctuation, we can neglect these fluctuations by assuming *quasineutrality*. Such hypothesis writes

$$en_e = \sum_i q_i n_i \tag{2.5}$$

where e and n_e are the charge and number density of the electrons and q_i and n_i are the charge and number density of ions of specie i. The main advantage of this approach is we get rid of the limitations on the grid size and time step associated with the electron scales.

It is important to note that the ion electrostatic process can still be handled. As an example, in a hybrid code where we make the quasineutral assumption, we are still able to simulation the propagation of the ion acoustic wave, or of the Bernstein modes. It means the electric field is not necessarily divergence free.

2.2.3 Transverse component of the displacement current

One of the approximations to solve the full set of Maxwell's equations is based on the assumption $v_A/c \ll 1$, where v_A is the Alfvén speed and c is the speed of light. As result the displacement current is small compared to the conduction current. But nonetheless, this term can not be neglected, otherwise, several linear modes could not be resolved, like, as cited above, the ion acoustic modes or the Bernstein mode. To clarify this point we project the Maxwell-Ampère equation on the longitudinal (along the wave number vector $\mathbf{k}$) and transverse (perpendicular to $\mathbf{k}$) direction:

$$0 = \mu_0 \mathbf{J}_L + \frac{1}{c^2}\frac{\partial \mathbf{E}_L}{\partial t} \tag{2.6}$$

$$\boldsymbol{\nabla} \times \mathbf{B} = \mu_0 \mathbf{J}_T + \frac{1}{c^2}\frac{\partial \mathbf{E}_T}{\partial t} \tag{2.7}$$

The first equation is satisfied: taking the divergence of this equation, one gets the continuity equation associated with the charge conservation. But as we make the quasineutral hypothesis, the associated longitudinal current can not be explicitely calculated, which does not mean than this term is null. This remark is associated with the fact that the electric field can be electrostatic.

We only have to consider the second equation of (2.7). If neglecting the last term associated with the displacement current, we have a close relation between the transverse current and the curl of the magnetic field. This is the relation we numerically solve in a hybrid code. One should note we only consider the transverse component of the total current.

2.2.4 The electron Ohm's law

As we neglect the transverse component of the displacement current, we need to write an equation to get the electric field. The electric field clearly appears in the momentum equation of whatever specie of the plasma. But as we already solve the full dynamics of the ions, all the fluid equations for the ions are implicitly taken into account. We need to write a momentum equations for the electrons. When explaining the electric field depending on the fluid quantities of the electrons and on the magnetic field, we obtain what usually call the *electron Ohm's law*. This name is coming from the fact that in an unmagnetized, cold and collisional plasma, this equation simply write $\mathbf{J} = \sigma\mathbf{E}$ where σ is the plasma conductivity. In chapter 1 we have already introduced the electron momentum equation Eq. 1.18. The way to derive the equation is to integrate the first moment of the Vlasov equation. The Vlasov equation being the one that describes a collisionless plasma, one would need to consider a Fokker-Planck equation in the collisional case. In this section we discuss numerical Ohm's law, that we use:

$$\mathbf{E} = -\mathbf{v}_i \times \mathbf{B} - \frac{1}{en}(\mathbf{J} \times \mathbf{B} - \boldsymbol{\nabla}.\mathbf{P}_e) + \eta\mathbf{J} - \eta'\Delta\mathbf{J} \tag{2.8}$$

where, $\mathbf{v}_i$ is the ion bulk velocity, n is the electron density (equal to the total ion density by quasineutrality), $\mathbf{J}$ is the current density, $\mathbf{P}_e$ is the electron pressure tensor, η is the plasma resistivity and η' is the hyper-viscosity. The resistivity is a term associated with electron-ion collision, and the hyper-viscosity is an ansatz, also giving a dissipative terms, close to the viscous term one gets in the Navier-Stokes equation for neutral fluids. While not mandatory, these dissipative terms generally help to stabilize the numerical simulations, without altering the physics, as η and η' are small enough.

We neglect the inertial term for the electrons. As already shown[KHW98], the electron inertial term is negligible compared to the non-gyrotropic pressure effect in the electron Ohm's law. One of the important limits of the fluid electron approximation is it eliminates the electron Landau damping tending to suppress growth of whistler-like modes at short wave-lengths. This is why we use additional smoothing or hyper-resistivity to reduce the amplitude of the short wavelength fluctuations.

It has to be emphasized that in the electron Ohm's law the current involved in the Hall term is in fact, because of Eq. (2.7), only the transverse one, while the longitudinal one being neglected.

2.3 Closure equation for the electron pressure

To calculate the Ohm's equation Eq. 2.8, one needs an electron pressure to find the pressure divergence term. In the same way we need to consider the heat flux to calculate the electron pressure tensor. This is the classical problem of closing the hierarchy of fluid equations (resulting from the BBGKY hierarchy). In this section we overview two classical approaches to close the pressure system: the isothermal closure and the full electron pressure tensor.

2.3.1 Isothermal closure

As already said, the electrons are described as a fluid, meaning we only consider the first moments of their distribution function. In many codes, as well as in HECKLE, we consider the first three moments:

- the electron density equals the ion density by quasineutrality. At each grid points one sum the contribution of each ions to obtain the ion density, depending on their weight and charge

- the electron velocity is defined by Eq. (2.15). We neglect the electron mass, as the electrons reach the needed velocity to satisfy Eq. (2.15) whatever the situation. As it could be associated with an important acceleration, it means the electrons are mass-less.

- the electron pressure needs an hypothesis to be calculated

In the simplest hybrid model, one assumes a scalar electron pressure and an isothermal closure relation:

$$P_e = n_e k_B T_e \tag{2.9}$$

where k_B is the Boltzmann constant, n_e is the electron density and T_e is the electron temperature.

In many numerical studies[AHB+13], the pressure is scalar and evolves through time in an isothermal way. Although simple, this hypothesis is generally hard to justify, and the consequence for the reconnection process is unclear. Furthermore, the electron temperature has to be uniform, otherwise, the temperature gradient initially given would stay frozen-in; associated transport processes generally act in a way to reduce such gradients. In the next section, we review in which way we can consider a different hypothesis.

2.3.2 Time evolution of the pressure tensor

In a hybrid code, electrons are described as a fluid. Its zero order moment (density) is the same as the ion density, by quasineutrality. Its first order moment (fluid velocity) is a consequence of the ion fluid velocity and the total current Eq. 2.15. The pressure tensor is the second order moment of the distribution function, associated with the width of the distribution function around the mean velocity:

$$P(\mathbf{x},t) = m \int (\mathbf{u} - \mathbf{v}(\mathbf{x},t)) \otimes (\mathbf{u} - \mathbf{v}(\mathbf{x},t)) f(\mathbf{x},\mathbf{u},t) d\mathbf{u} \tag{2.10}$$

$$n = \int f(\mathbf{x},\mathbf{u},t) d\mathbf{u} \tag{2.11}$$

$$\mathbf{v}(\mathbf{x},t) = \frac{1}{n} \int f(\mathbf{x},\mathbf{u},t) \mathbf{u} d\mathbf{u} \tag{2.12}$$

$f(\mathbf{x},\mathbf{u},t)$ and m denote the distribution function and the mass of the specie, $\mathbf{u}$ is the phase space velocity, and $\mathbf{v}(\mathbf{x},t)$ the bulk flow speed.

In collisionless plasmas, the time evolution of the full pressure tensor is the third equation in the equation hierarchy governing the time evolution of a magnetized fluid. The evolution equation is obtained by multiplying the Vlasov equation by $\mathbf{u} \otimes \mathbf{u}$ and integrating over phase space:

$$\begin{aligned} \partial_t P_{ij} &= -v_{ek}\partial_k P_{ij} - P_{ij}\partial_k v_{ek} - P_{ik}\partial_k v_{ej} - P_{jk}\partial_k v_{ei} \\ &\quad -\frac{e}{m_e}[P_{ik}B_n\varepsilon_{knj} + P_{jk}B_n\varepsilon_{kni}] \\ &\quad -\partial_k Q_{ijk} \end{aligned} \tag{2.13}$$

We call $D(\mathbf{P},\mathbf{v}_e)$ the *Driver term* which equals the first line of the right hand side, $C(\mathbf{P},\mathbf{B})$ the *cyclotron term* which equals the second line, and I the *isotropization term* which equals the last last line, following a nomenclature already used by M. Hesse[HW94] . This last term is discussed only as a way to consider the divergence of the heat flux. Each terms of the right hand side of this equation has to be discussed to understand the underlying physical effects, as well as the numerical associated constraints.

2.3.3 The driver term

The driver term can be written in vectorial form (i.e. without indices):

$$D(\mathbf{P}) = -\mathbf{v}_e.\boldsymbol{\nabla}\mathbf{P} - \mathbf{P}\boldsymbol{\nabla}.\mathbf{v}_e - \mathbf{P}.\boldsymbol{\nabla}\mathbf{v}_e - (\mathbf{P}.\boldsymbol{\nabla}\mathbf{v}_e)^T \tag{2.14}$$

where we remind that the electron bulk velocity $\mathbf{v}_e$ is expressed through the ion bulk velocity and the current density:

$$\mathbf{v}_e = \mathbf{v}_i - \frac{\mathbf{J}}{en} \tag{2.15}$$

We decide to split the four terms involved in D in three parts:

(i) $D_A = -\mathbf{v}_e.\boldsymbol{\nabla}\mathbf{P}$ is the advection of the electron pressure at the electron velocity

(ii) $D_C = -\mathbf{P}\boldsymbol{\nabla}.\mathbf{v}_e$ is a term associated with the compressibility of the electron fluid because the velocity divergence is zero in the case of an incompressible fluid

(iii) $D_S = -\mathbf{P}.\boldsymbol{\nabla}\mathbf{v}_e - (\mathbf{P}.\boldsymbol{\nabla}\mathbf{v}_e)^T$ is the symmetric part of the driver term

While these terms are different in nature, they are integrated in a different ways:

(i) for the advective term, we use the first order upwind scheme which is well designed in advecting a term at a velocity which can be either positive or negative.

(ii) the compressible term is numerically integrated with an explicit second order scheme, centered both in space and time.

(iii) the symmetric term is also integrated with a second order space and time centered scheme.

It is worth noticing that no electron time scale are present in these terms as the electron mass is not involved. Hence, no particular numerical constraints arise because of the time integration of these terms. A second important remark is that both D_A and D_C acts on a P_{ij} component by only involving this same P_{ij} component. This is not the case for the D_S term, for which time evolution of diagonal terms depends on off-diagonal ones and vice-versa.

2.3.4 The cyclotron term

The cyclotron term also writes:

$$C(\mathbf{P}, \mathbf{B}) = -\frac{e}{m}[\mathbf{P} \times \mathbf{B} + (\mathbf{P} \times \mathbf{B})^T] \tag{2.16}$$

This symmetrical term depends on the electron mass. Consequently, a constraint arise on the time step needed to integrate it. In previous study[HWK95], this term was integrated in an implicit way, as such numerical scheme is unconditionally stable. In our study, we develop a different explicit numerical scheme using a sub-cycling method. We also have an implementation of the implicit method for the purpose of comparison. The

reason is to confirm the results by two different methods, and see what can we gain from a physical and/or numerical point of view.

The Cyclotron term depends on the electron gyro frequency, that is three orders of magnitude smaller than the ion gyro frequency. The explicit integration of this term for the sub-cycling method requires to reduce the time step in the same order of magnitude. This point is discussed further in the next section on numerical issues.

2.4 Closure equation for the electron heat flux

2.4.1 How to consider the heat flux ?

In this section, we discuss the last term of the right hand side of Eq. (2.13), the divergence of the electron heat flux. The heat flux is the third order moment of the distribution function:

$$Q = m \int (\mathbf{u}-\mathbf{v}) \otimes (\mathbf{u}-\mathbf{v}) \otimes (\mathbf{u}-\mathbf{v}) f(\mathbf{x},\mathbf{v},t) d\mathbf{u} \tag{2.17}$$

The time evolution equation for Q is obtained by multiplying the Vlasov equation by $\mathbf{u} \otimes \mathbf{u} \otimes \mathbf{u}$ and integrating over phase space which gives:

$$\begin{aligned}
\partial_t Q_{ijk} = & -\sum_l \partial_{x_l}(\Gamma_{ijkl} + Q_{ijk} v_l) \\
& + \frac{1}{mn}(P_{ik}\sum_l \partial_{x_l} P_{ij} + P_{jk}\sum_l \partial_{x_l} P_{li} + P_{ij}\sum_l \partial_{x_l} P_{lk}) \\
& - \sum_l Q_{lij}\partial_{x_l} v_k - \sum_l Q_{ljk}\partial_{x_l} v_i - \sum_l Q_{lik}\partial_{x_l} v_j \\
& + \frac{e}{m}\sum_{r>l}[[Q_{ijs}B_r - Q_{ijr}B_s]\epsilon_{rsk} \\
& + [Q_{iks}B_r - Q_{ikr}B_s]\epsilon_{rsj} \\
& + [Q_{jks}B_r - Q_{jkr}B_s]\epsilon_{rsi}]
\end{aligned} \tag{2.18}$$

where Γ_{ijkl} is the fourth order moment of the electron fluid. As for pressure tensor, there is a part representing the effects of particle cyclotron motion on the heat flux tensor (last three lines). Eq. 2.18 is absolutely intractable for numerical treatment.

Many simplification were done to avoid to solve such heavy tensor equation. The simple and best known form for heat flux is the one proposed by Spitzer and Harm [SH53] for collisional plasmas, which is proportional to the temperature gradient. Braginskii[Bra65]

proposed an alternative form in the magnetized case but still for collisional plasmas. In the collisionless case, Hammett and Perkins[HP90] proposed an Ansätz form for the reduced heat flux using a free parameter. This so-called Landau-fluid closure is well designed in spectral code as it is local in wave-number space, but non-local in real space.

2.4.2 The Landau-fluid closure of Hammet & Perkins

In the collisionless case, the expression of the heat flux is a complex problem, as the equation for its time evolution is a heavy third order tensor equation involving the divergence of the fourth order moment of the electron fluid. Hammett and Perkins[HP90] proposed an Ansätz form for the reduced heat flux using a free parameter, it equals the third order moment of linearized fluctuations around a maxwellian zeroth order distribution. This so-called Landau-fluid closure is well designed in spectral code as it is local in wave-number space, but non-local in real space.

They proposed a closure method which (1) ensures particle, momentum, and energy conservation, (2) takes on a simple form in wave-number space, and (3) has a linear-response function close to one of a colissionless Maxwellian plasma. This closure method successfully models kinetic resonances (such as Landau damping). The closure is straightforward in wave-number space:

$$\mathbf{q}_e(\mathbf{k}) = -n_0\chi_1\frac{\sqrt{2}}{k}i\mathbf{k}V_T T(\mathbf{k}) \tag{2.19}$$

where χ_1 is dimensionless coefficient, $V_T = \sqrt{T/m}$ is the thermal velocity, and $T = (p - T_0 n)/n_0$ is the perturbed temperature. This closure Ansätz can be written symbolically in the standard Fick's law form $\mathbf{q} = -n\kappa\partial_z T$ except that κ is an integral operator in physical space because it is proportional to V_T/k in wave-number space. By performing the inverse Fourier transform of $\mathbf{q}_e$, one can get its form in real-space.

If considering a single dominant wave-number k_0, Wang[WHBG15] proposed a simplified form which can be used in non-spectral codes :

$$\partial_k Q_{ijk} = k_0 V_T(P_{ij} - p\delta_{ij}) \tag{2.20}$$

where p is the third of the trace of the full electron pressure tensor. As a consequence, this term essentially acts as an isotropization term for the full electron pressure tensor which strength is governed by the product $k_0 V_T$.

In this thesis we use the form:

$$I(\mathbf{P}) = -\frac{1}{\tau}[\mathbf{P} - \frac{\mathbf{1}}{3}\mathrm{Tr}(\mathbf{P})] \tag{2.21}$$

where, τ is the characteristic time scale at which the full electron pressure tensor is smoothed out. Such approximation is a consequence of the Hammett and Perkins model if considering a single dominant wave-number. This closure is extensively used in chapter 3.

More specifically, it has to be noted this form does not depend on the magnetic field, while it was proportional to electron gyro frequency in previous studies [HW94]. Moreover,

it mocks only isotropization nature of the heat flux, this last term is called isotropization. Furthermore, it is obvious this isotropization term operates with the same efficiency for the diagonal and off-diagonal terms. Different isotropization rates and their consequences are discussed in chapter 3. Also we emphasize that I_{ij} only depends on this ij component (no cross terms) except implicit relation in Tr($\mathbf{P}$) for diagonal components.

2.4.3 Non-local vs local heat flux

The problem of non-local in real space heat flux is an open question for many plasma physics problems, as most of the time space plasma is collisionless, meaning heat carrying particles can travel great distances without collisions. Another important example for us is the laser produced plasma, demonstrating the fraction of hot collisionless electrons that are frozen in magnetic field and responsible for transport of magnetic field down steep temperature gradients [LMV83]. The linear theory is not valid for the cases where long mean free path of the heat carrying electrons is larger than the temperature gradient lengths. Generally there could be many causes of non locality of the heat flux, both in space and in time, depending on the problem. In this thesis, we do not implement any non local effect for heat flux, and take it into account only as isotropization term in equation for the pressure tensor 2.13.

2.4.4 Heat flux in a magnetized plasma : Righi-Leduc effect

In this section we give a brief overview of *Righi-Leduc effect* as it is an important effect for magnetic field transport. An open question is the way to calculate the electron heat flux $\mathbf{q}_e$ in a magnetized plasmas. Looking at the classical Braginskii model[Bra65], the electron heat flux $\mathbf{q}_e$ in the plane orthogonal to the magnetic field $\mathbf{B}$ can be written :

$$\mathbf{q}_e = -k_1 \nabla T_e - k_2 \mathbf{b} \times \nabla T_e \tag{2.22}$$

where $k_{1,2}$ are the heat conduction coefficients, and $\mathbf{b}$ is a unit vector along magnetic field $\mathbf{b} = \mathbf{B}/B$. Writing the heat flux with classical Fick's law formalism:

$$\mathbf{q}_e = -\mathbf{K}.\nabla T_e \tag{2.23}$$

we get heat conduction coefficient K as a tensor:

$$\mathbf{K} = \begin{bmatrix} k_1 & -b_z k_2 \\ b_z k_2 & k_1 \end{bmatrix}$$

Non-symmetry of the conductivity tensor is a consequence of the presence of the magnetic fields, known as the Righi-Leduc effect. This effect results in the rotation of the heat flux vector in the $\mathbf{b} \times \nabla T_e$ direction without changing its absolute value.

2.4.5 Nernst effect : Nernst velocity in the Ohm's law

The classical Braginskii [Bra65] plasma transport theory shows that the magnetic field advects down the temperature gradient at the Nernst velocity :

$$\mathbf{v}_N = -\beta_\wedge \nabla_\perp T_e / eB \tag{2.24}$$

where $\beta_\wedge$ is a component of the thermo electric tensor as defined by Epperlein and Haines [EH86]. The advection of the magnetic field with the characteristic velocity $\mathbf{v}_N$ may be included in the Ohm's law (2.8). The resulted electron velocity is given by the contribution of magnetic convection by plasma flow velocity Eq. 2.15 and by the Nernst velocity v_N.

The Nernst velocity can be approximated by:

$$\mathbf{v}_N = \frac{\mathbf{q}_e}{p_e} \tag{2.25}$$

where $\mathbf{q}_e$ is the reduced electron heat flux and p_e is the scalar electron pressure. We should notice that $\mathbf{q}_e$ is the reduction of $\mathbf{Q}$, given by Eq. 2.17, the third order moment of the electron distribution function and p_e is the second order moment. As a result, their ratio is homogeneous to a velocity.

Such effect is important for laser produced plasma that we discuss in chapter 4, for the amplification of magnetic fields in overdense plasma due to transport by heat flow. The physics behind this advection is that the magnetic field tends to be frozen more to the hotter electrons, being less collisional and responsible for the heat flux, than to the colder and more collisional electrons through which the magnetic field can more easily diffuse [Hai86]. The mean free path of the hot electrons, being responsible for the heat-carrying, is greater than the electronic temperature gradient length, making the nature of the heat flux in magnetized plasmas is non local [LAB+14].

In this thesis we do not take into account any of the mentioned above effects. Since equation for the heat flux is non local, one needs to use a wave number space to solve it, and do a Fourier transform to come back to real space. But parallel Fourier transform has a crucial numerical constraint as, in domain decomposition method, one can parallelize only along one direction (which the case for the widely used FFTW library[fft]).

2.5 Numerical issues

In a hybrid code we need to gather moments of the ion distribution function in each cell and at each time step, such as ion density Eq. 2.11 and flow velocity Eq. 2.12. The density value at each cell depends on how many particles are in the cell. Hence, for dynamical process, the density (zero order moment) can significantly fluctuate, which results in fluctuations for the higher order moments. In this section we observe potential numerical issues we have faced treating the numerical approximations.

2.5.1 Normalization

In the code as well as for the results discussed in this thesis, all physical quantities are normalized to a quantity labeled with zero: Magnetic field and density are normalized to asymptotic values $\mathbf{B}_0$ and n_0 respectively, lengths are normalized to the ion inertial length d_0 (calculated using the density n_0), times are normalized to the inverse of the ion gyrofrequency Ω_0^{-1} (calculated using the magnetic field $\mathbf{B}_0$) and velocities are normalized to the Alfvén velocity $\mathbf{V}_{A0}$ (calculated using $\mathbf{B}_0$ and n_0). The Ohm's law Eq. 2.8 is normalized to asymptotic electric field $\mathbf{E}_0 = \mathbf{V}_{A0}\mathbf{B}_0$.

2.5.2 Smoothing the ion density and velocity

On the numerical point of view the particle moments such as ion density n and velocity $\mathbf{v}_i$ are statistical quantities contaminated by fluctuations. At each time step, they are computed in each cell using a first order assignment function S (also called shape factor) for each macro-particles. Density and fluid velocity result from the summation:

$$n(\mathbf{x}) = \Sigma_{s,h} q_s S(\mathbf{x} - \mathbf{x}_{s,h}) \quad (2.26)$$

$$\mathbf{v}_i(\mathbf{x}) = \Sigma_{s,h} \mathbf{v}_{s,h} S(\mathbf{x} - \mathbf{x}_{s,h}) / \Sigma_{s,h} S(\mathbf{x} - \mathbf{x}_{s,h}) \quad (2.27)$$

where s index is standing for the specie of particle and h index for the index of the particle, $S(\mathbf{x})$ is the first order shape factor. In the zero order weighting, one simply counts the number of particles within distance of $\pm\Delta x/2$ (on cell width) about a grid point and assign that number to that point [BL91]. If particles move into the cell density jumps up, if the particles move out density jumps down. Because of density fluctuations we have electric field fluctuations, both are noisy in space and in time. To remove the noise we use the first order weighting, taking into account the relative distances to the vertices of the rounding grid points.

Such weighting is not enough to remove fluctuations. As a consequence, the ion moments are smoothed out each time step using a three-points stencil, that is symmetric in the cell. Such smoothing helps to prevent the growth of small-scale electric fields in low-density areas and has limited consequences for the associated diffusion processes.

2.5.3 The necessity to consider an ion background

With an hybrid code we cannot simulate an empty space because in the Ohm's law we have terms proportional to the inverse density, that would diverge. We cannot simulate too low density neither as it potentially would increase these terms dramatically. To prevent such situations we introduce a background particles population, that is uniformly distributed all over the simulations box making the density level high enough to stabilize the integration scheme.

To integrate the full electron pressure tensor given by Eq. 2.13, we need to calculate the electron flow velocity from Eq. 2.15, requiring the density value. It is important to investigate how this background population affects the physics at play. In the chapter 4 we introduce an alternative method to avoid the use of a high background density values and while keeping the run stable. To do so, we introduce a function of density, that is zero when density is lower than a threshold, and one otherwise. In between it is a fifth order growing polynomial. If the density is small at given points, it means we have an epsilon in front of the distribution function $\epsilon f(\mathbf{x}, \mathbf{u}, t)$ defined by Eq. 2.11, but we also have the same epsilon for higher order moments. In section. 4.3.6 we suggest to multiply the diverging terms by the function of density to lower its value.

2.5.4 Resistivity and hyper-viscosity

To introduce the smallest dissipation scales for the reconnection process it is necessary to take into account two terms in the Ohm's law:

$$\mathbf{E} = \eta \mathbf{J} - \eta^{'} \Delta \mathbf{J} \tag{2.28}$$

where η is resistivity due to collisions (zero in this study), and $\eta^{'}$ is the hyper-viscosity or hyper-resistivity. Previously it was shown that varying slightly the hyper-viscosity coefficient does not change the reconnection rate [AHB+13]. Another reason to have such dissipation is coming from the limits of the fluid electron approximation, that eliminates electron Landau damping and tends to suppress whistler growth at short wavelengths. This is why we use an additional smoothing or small resistivity to reduce the amplitude of the short wavelength fluctuations, that helps to prevent numerical instabilities.

In the frame of the thesis the resistive term is negligible for collisionless reconnection but we use a small hyper-viscous term ($\eta^{'} = 10^{-3}$) to keep a small dissipation process at sub-ion scales. As most of hybrid codes, when resistivity and hyper-viscosity are turned-off, the runs turn to be unstable in the lobe regions where the density can drop to a low value.

2.5.5 Numerical treatment of the cyclotron term

The three key concepts connected to finite differences approximations for the differential equations are Consistency, Convergence and Stability. They are gathered by the Lax Equivalence Theorem [LR56]: for a properly posed initial value problem, a consistent approximation is convergent if and only if it is stable. Consistency only requires the finite difference scheme approximates the differential equations, which is of corse the case for us. Stability is the key property, as consequence we have to ensure the numerical approximation does not diverge through time.

In the temporal scheme, if the new field and particle values are calculated from field and particle values at previous times only, such a scheme is called "explicit". In contrast, in an "implicit" scheme the solution of the new quantities involves knowledge of these quantities at the new time, thus forming a potentially considerable system of coupled nonlinear equations. The advantage of an implicit scheme is that it should be stable for large time steps. We implemented two ways to integrate the cyclotron term in Eq.2.13: implicit and explicit.

In the implicit scheme, the Cyclotron term Eq. 2.16 is split in two part with in an α coefficient, to weight the contributions of the pressure at the next time step and the one at the previous time step [HW93]. This method is sometime referred as Θ method. This can be written:

$$[\mathbf{1} - \alpha\Delta t C](\mathbf{P}_{n+1/2}) = \mathbf{P}_{n-1/2} + \Delta t[(1-\alpha)C(\mathbf{P}_{n-1/2}) - I(\mathbf{P}_{n-1/2}) + D(\mathbf{P}_n)] \equiv \mathbf{F} \quad (2.29)$$

The solution of the linear system gives pressure tensor components for the next time step. More details are given in Appendix A.

As a new approach to integrate the cyclotron part of Eq.2.13, we have implemented a subcycling method to explicitly integrate the cyclotron term. The time step Δt we use for the other equations is small enough to resolve the gyromotion of the ions. Hence, defining $N = M/m$ the ion to electron mass ratio, a time step $\Delta t/N$ is small enough to properly treat the electron gyromotion. Because of the time centering the full electron pressure tensor is defined at half time step, and advancing from $P_{n-1/2}$ to $P_{n+1/2}$ is done using N subcycles with the algorithm

$$\mathbf{P}_{n-\frac{1}{2}+\frac{m}{N}+\frac{1}{N}} = \mathbf{P}_{n-\frac{1}{2}+\frac{m}{N}} + \frac{\Delta t}{N}\sum_{m=0}^{N}[C(\mathbf{P}_{n-\frac{1}{2}+\frac{m}{N}}) + D(\mathbf{P}_n)] + I(\mathbf{P}_{n-\frac{1}{2}}) \quad (2.30)$$

The two methods give a comparable picture for pressure tensor components, while subcycling gives an advantage in computational time. Fig 2.3 displays the off-diagonal pressure tensor components for simulations of Harris sheet using explicit and implicit schemes for Cyclotron term integration at the same time. Small discrepancies can arise, but the average pattern is pretty well conserved, meaning both methods are converging toward the same result.

2.5.6 Smoothing the electron pressure tensor

For the isothermal case given by Eq. 2.9, we use the density that is already smoothed each time step. Hence, there is no need to smooth the pressure. While using the full electron pressure tensor, because of the large number of terms and gradients, we need to smooth it out. But smoothing has also consequences for the numerical results, because while removing the small-scale fluctuations, it also alters the large scale gradients of

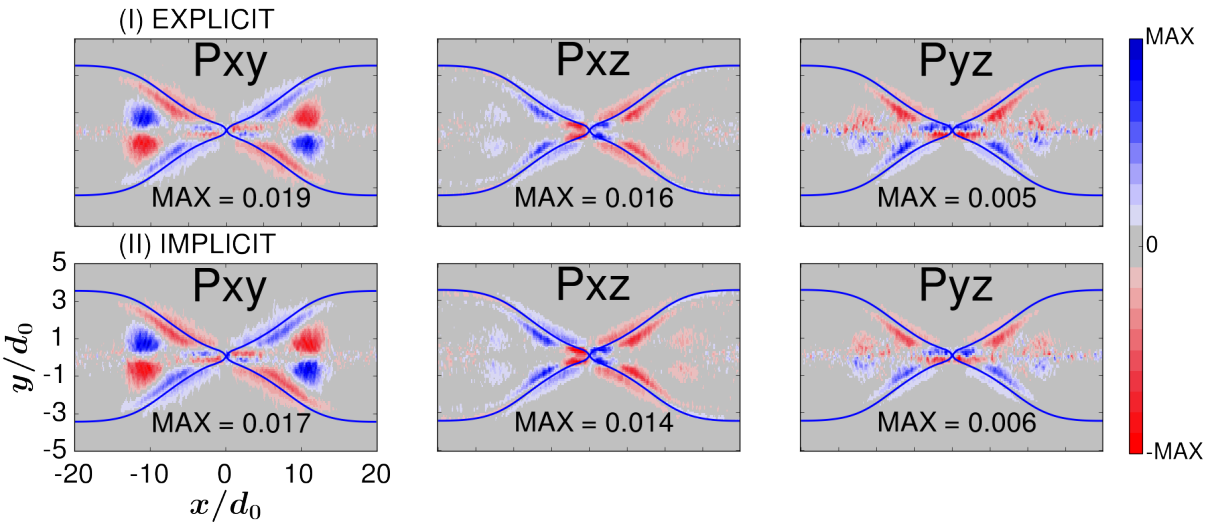

Figure 2.3: Off diagonal pressure tensor components for simulations of Harris sheet using explicit and implicit schemes for Cyclotron term integration at the same time using the same isotropization. Blue line represents separatrix.

physical origin. It is an open question, what should be the efficiency of smoothing to preserve the large scale gradients?

For simulations of reconnection without any external forcing term (Chapter 3), all the terms of the full electron pressure tensor are smoothed out every 8 time steps, in a thin region, close to boundaries, where density is small, and pressure can significantly fluctuate. This value of 8 time step is the largest one to drive the system in a stable state. Such smoothing does not affect the gradients and helps to stabilize the runs.

For simulation of reconnection including an external forcing term (Chapter 4) a smoothing on $\mathbf{P}$ is at play all over the computational domain every 10 time steps, as pressure significantly fluctuates.

Chapter 3

Non-gyrotropic electron pressure effects for magnetic reconnection

In this chapter we revisit the problem of two-dimensional magnetic reconnection in a Harris sheet [Har62] and investigate the role of the closure equation for the electron pressure tensor. A part is dedicated to investigate the consequences from the numerical and physical point of view of dealing with an isothermal closure, and compare it with a general closure. We discuss the consequences for the reconnection rate, as well as for the structure of the reconnection region.

3.1 Reconnection in a Harris sheet

3.1.1 The Harris kinetic equilibrium

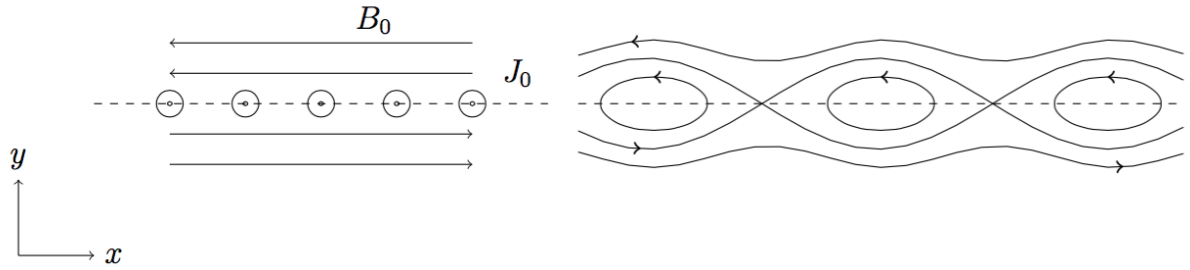

Figure 3.1: Left panel is initial Harris sheet. Right panel is the change of magnetic configuration because of the tearing instability.

In his work entitled "On a plasma sheath separating regions of oppositely directed magnetic field" Harris found an exact solution of the Vlasov equation describing a layer

of plasma confined between the regions of oppositely directed magnetic field. We present the equations, the assumptions and the resulting kinetic equilibrium. We call X the field reversal direction, Y the gradient direction for both magnetic field magnitude and density, and Z the direction of the current associated with the field reversal, Fig. 3.1 left panel.

Based on Harris's work we want to find a kinetic equilibrium in the system with two oppositely directed magnetic fields. To do so, we need to solve the system of Vlasov and Maxwell equations for proton electron plasmas. One of the assumptions is that the protons and electrons have Maxwell distribution. The magnetic field depends only on the Y component $\mathbf{B} = B(y)\mathbf{e}_x$. The vector potential has a single component $\mathbf{A} = A(y)\mathbf{e_z}$. Starting from a parametric form of the distribution function depending on the constant of motion, one can write the Maxwell-Gauss and the Maxwell-Ampère equations depending on the vector potential A and the scalar potential ϕ.

$$\frac{d^2A(y)}{dy^2} = \mu_0 en \left\{ V_p \exp\left(-\frac{e\phi}{k_B T_p} + \frac{eAV_p}{k_B T_p}\right) - V_e \exp\left(\frac{e\phi}{k_B T_e} + \frac{eAV_e}{k_B T_e}\right)\right\} \tag{3.1}$$

where V_p and V_e are the proton and electron velocity in the out-of-plane direction, respectively, and T_p and T_e are the proton and electron temperature, respectively.

$$\frac{d^2\phi(y)}{dy^2} = \frac{en}{\epsilon_0} \left\{ \exp(-\frac{e\phi}{k_B T_p} + \frac{eAV_p}{k_B T_p}) - \exp\left(\frac{e\phi}{k_B T_e} + \frac{eAV_e}{k_B T_e}\right)\right\} \tag{3.2}$$

The problem can be simplified by considering the case $\phi = 0$. This solution, while not universal, means there are no electric fields inside the current sheet. Furthermore, from the momentum equation of both species it shows that an equilibrium implies the condition

$$\frac{V_e}{T_e} = \frac{V_p}{T_p} \tag{3.3}$$

in the de Hoffmann-Teller frame the electric field remains zero, and the electrons move with the same velocity as protons $V_p{=}{-}V_e{=}V$. That gives a restriction on temperature $T_e = T_p = T$. The simplified equation for the vector potential:

$$\frac{d^2A(y)}{dy^2} = 2\mu_0 enV \exp\left(-\frac{eAV}{k_B T}\right) \tag{3.4}$$

One of the solutions of the Eq. 3.4 is

$$A(y) = \Gamma \ln(\cosh(\eta y)) \tag{3.5}$$

where

$$\Gamma = -\frac{2k_BT}{eV} \tag{3.6}$$

$$\eta = \sqrt{\frac{\mu_0 n e^2 V^2}{4k_BT}} = \frac{V}{2c\lambda_D} \tag{3.7}$$

Hence, the magnetic potential depends on the Debye length λ_D. From the form of A we can deduce the form of the magnetic and density profile

$$B_x(y) = \sqrt{\mu_0 n k_B T}\tanh\left(\frac{Vy}{2c\lambda_D}\right) \tag{3.8}$$

$$n(y) = n_0\cosh^{-2}\left(\frac{Vy}{2c\lambda_D}\right) \tag{3.9}$$

Such kinetic equilibrium is entirely defined by the temperature ratio $T_p/T_e = \theta$. The total magnetic pressure $P_m = B^2/2\mu_0$ is zero along the neutral line $Y = 0$ and maximum in the lobes. The total ion and electron pressure is $P_k = (n_p k_B T_p + n_e k_B T_e)$. As $n_p = n_e = n$ everywhere due to quasineutrality, we can write $P_k = nk_BT_e(\theta+1) = nk_BT_p(1+\theta^{-1})$. This pressure equals to magnetic pressure due to equilibrium giving $T_e = P_m/(n(\theta+1))$ and $T_p = P_m\theta/(n(\theta+1))$. For this study $\theta = 1$.

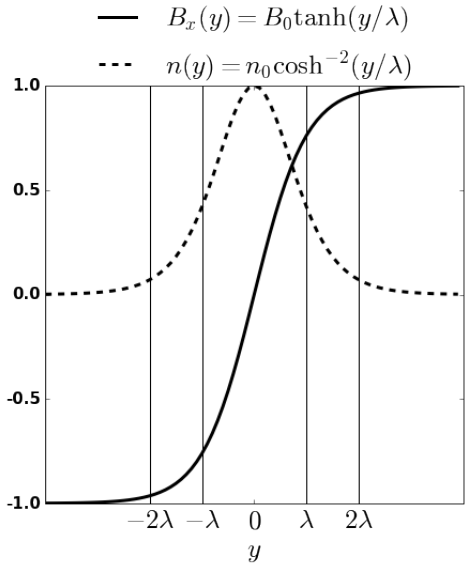

Figure 3.2: Magnetic field profile (solid line) and density profile (dotted line) for the Harris kinetic equilibrium, with $B_0 = 1$ and $n_0 = 1$.

Fig. 3.2 depicts the initial condition that we use in our numerical model. The half-thickness of the sheet equals to ion inertia length $\lambda = d_0$, the asymptotic magnetic field $\mathbf{B}_0 = 1$ and the maximum density $n_0 = 1$.

3.1.2 The tearing mode in an unperturbed Harris sheet

Because of the Maxwell-Faraday equation the magnetic field $\mathbf{B_0}$ is associated with the out-of-plane current $\mathbf{J_0}$ as shown in the left panel of Fig. 3.1. The current sheet can be splited in an assembly of parallel current wires. That results in a force of attraction between each of the wires constituting the system, the modulus being inversely proportional to the square of their distance. An initial disturbance of bringing together two currents is amplified, which turns to be an unstable situation if the amount of available energy is sufficient enough to support the instability.

This initial equilibrium can be perturbed by a superposed perturbation at the center of the simulation domain to trigger reconnection. But without any perturbation the Harris sheet is unstable. In 1963 Furth identified a class of resistive instabilities known as tearing modes [FKR63], resulting in the current sheet break-up into filaments, leading to the formation of many X-points and plasmoids. If the homogeneous current distribution along the sheet is slightly modulated, the modulation tends to grow, as the force of attraction between the individual current filaments grows with their approach, while connection with the neighbor filaments is weakened due to motion away. When this happens, the configuration of the magnetic field is rearranged, a part of the magnetic field lines, initially directed along the sheet, reconnects around the current bunch. The right panel of Fig.3.1 shows the change of magnetic configuration.

A potential source of energy for the instability development and violation of the frozen-in condition can be the Cherenkov effect. To develop the Cherenkov needs the particles to be demagnetized otherwise gyromotion does not allow the resonance of the particles. It was shown [PCP91] that the Harris-type current layer was completely stable against the ion tearing mode in the presence of a finite value of a transversal magnetic component.

The Sweet–Parker model is a steady state model, and does not address any reconnection onset or its cause. As first demonstrated by means two-dimensional MHD simulations [Bis86], reconnecting SP-like sites become unstable once the Lundquist number exceeds a critical value of order $S \sim 10^4$, leading to increase the local reconnection rate. The nonlinear structures formed by the instability are called *plasmoids*, and the instability is referred to the plasmoid instability. Because the instability is driven by the gradient of current, the instability growth rate increases with Lundquist number.

Experiments and astrophysical observations, contrary to theoretical predictions, demonstrate that reconnecting current sheets can be stable for a long time. In parallel with the investigation of the tearing instability, the problem of stabilization is raised. For the collisionless case hybrid simulations have already demonstrated the instability developing without an initial perturbation [HW93]. In the work we focus on the single point reconnection, which is initially triggered, making easier the comparison for different closure.

3.1.3 The role of the electron magnetization

In two-dimensional anti-parallel reconnection, the magnetic field is zero at neutral line, meaning that the electrons are demagnetized. Upstream from the neutral sheet, the electrons are magnetized. As we mentioned in chapter 2, electrons are adiabatic only when the curvature parameter given by Eq. (2.1) is much larger than one [BZ89]. During the reconnection process regions of vanishing magnetic field persist around neutral points, where electrons are demagnetized, that leads to chaotic motion.

It was shown that the sign of the energy of the tearing mode perturbations can be changed from negative to positive one due to the drift motion of magnetized electrons inside the reconnecting current layer [LP82]. It means that the collisonless tearing mode can not develop once a large enough component of the magnetic field arise inside the current to magnetize the electrons. The reason is that, when electrons are magnetized, they are no more able to resonate through the Cherenkov effect.

3.1.4 Reconnection neighbor : a 3 scales region

Fig. 3.3 depicts a sketch of the magnetic field, the current, and the electric field in the $X-Y$ plane. The reconnection rgion can be split into three regions:

(i) ideal MHD region : in this region, the electric field is essentially resulting from the ideal term in the Ohm's law. The inflow velocity is $\mathbf{V}_{iy}$ across the $\mathbf{B}_x$ magnetic field, while the outflow velocity is $\mathbf{V}_{ix}$ across $\mathbf{B}_y$

(ii) ion diffusion region: in this regions, ions are demagnetized while electrons are not, resulting in a net current. The electric field is dominated by the Hall term $\mathbf{J}\times\mathbf{B}$. In this region, the in-plane electric field (and its non-zero curl value) is associated with the development of an out-of-plane magnetic field $\mathbf{B}_z$ which is associated with an in-plane current $\mathbf{J}_{xy}$

(iii) electron diffusion region: in this tiny region even the electrons are demagnetized. Their distribution function is non-gyrotropic, meaning that the associated full electron pressure tensor has off-diagonal terms. We see that the out-of-plane electric field at the vicinity of the X point is defined by P_{xz} and P_{yz}

Far enough from the reconnection region, where the frozen-in constraint is valid, ions and electrons move together with the field lines. That defines the first region, where ideal MHD is valid and the out-of-plane electric field is defined by the ideal term. Approaching the mid-plane ions become demagnetized, while electron are still frozen in the field lines, that defines the transition region, where the Hall term is important. The in-plane current $\mathbf{J}_{xy}$ and the in-plane magnetic field $\mathbf{B}_{xy}$ provide the out-of-plane electric field $\mathbf{E}_z$. This out-of-plane electric field drives the ions in and out of the ion diffusion region (IDR) when

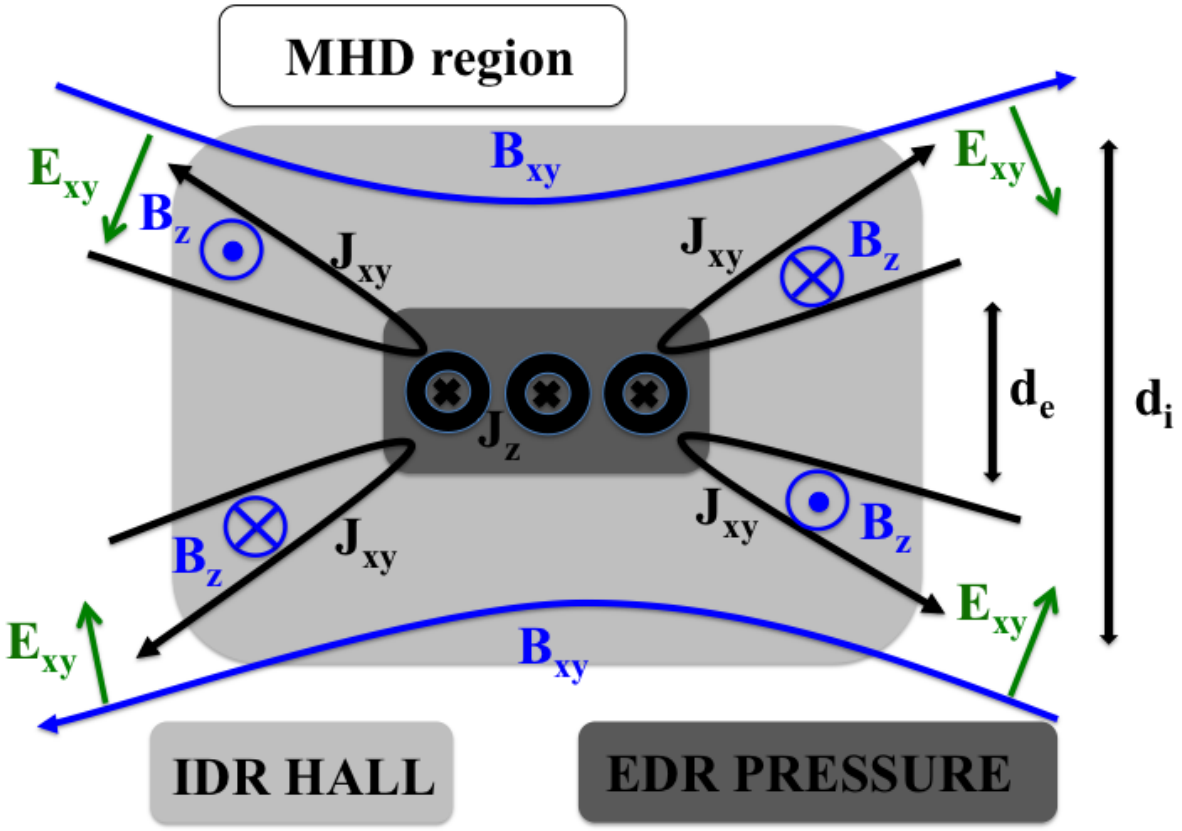

Figure 3.3: Sketch of the magnetic field, current, and electric field in the $X - Y$ plane.

reconnection occurs. The third scale is defined by the electron demagnetization scale , that happens on scales much smaller than the ion one, and of the order of the electron inertial length.

Fig. 3.4 shows the typical picture of the terms of the Ohm's law equation for PIC and 10-moments MHD simulations of antiparallel reconnection in the Harris sheet [WHBG15]. One can see how in both cases the out-of-plane electric field in electron dissipation region is supported by the divergence of the electron pressure tensor (yellow-green curves), while inertia terms (blue and cyan curves) are negligible. In the ion dissipation region, the electric field is supported by the counterbalance between the electron ideal term and the pressure gradient, the resulting field (red) being different from the electron ideal term $[\mathbf{V_e} \times \mathbf{B}]$ (green). The outer region is defined only by the ideal term.

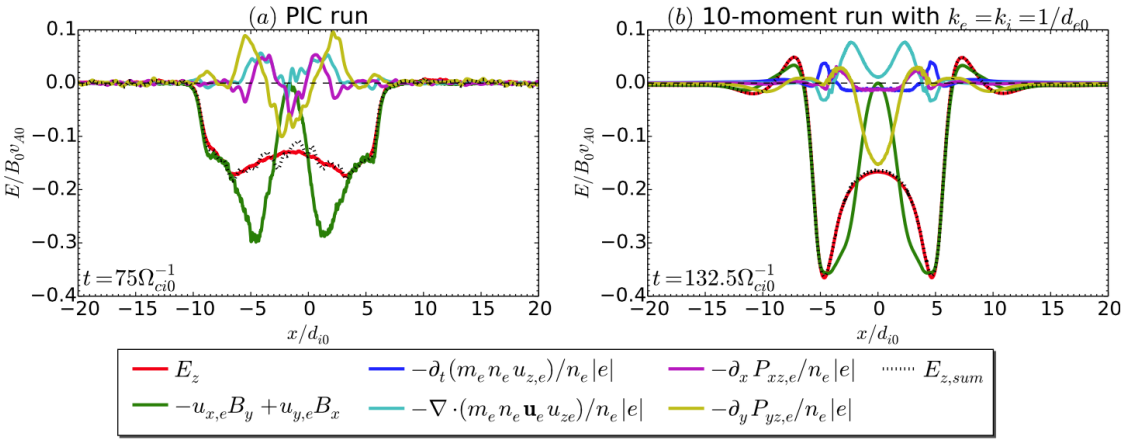

Figure 3.4: lineout of the Ohm's law terms along the outflow cross section (from the work of Wang at al. [WHBG15])

3.2 Structure of the full electron pressure tensor

We study the role of the full electron pressure tensor for the dynamics of magnetic reconnection in a Harris sheet as this topology has been extensively studied; this will ease the comparisons with former studies.

While particle codes hardly manage vacuum, we include a uniform background density n_b (equal to 0.5 in this study) with the same temperature as the foreground ions. A small initial magnetic perturbation[ZHK+11] is superposed to the Harris equilibrium to trigger reconnection at the very middle of the box.

The simulation domain is rectangular, with a length $L_X = 102.4$ and a width $L_Y = 20.8$ using a 1024×208 grid, the mesh size equals 0.1 in both directions. We chose a simulation box 5 times greater in the X direction than in the Y direction as we use periodic boundary condition in X direction. Such an elongated box should prevent the outflow moving in the X direction to reach the boundaries and move back after reflection in the direction of the X point. In fact the outflow velocity being smaller than the Alfvén speed, with a maximum time of simulation equal 100 Ω_0^{-1}, we do not observe the boundary crossing. In Section 3.3.3 we show that such boundaries could be a problem for $t > 150$. We use approximately 40 millions of particles, corresponding to at least 180 particles in the lowest-density regions. Such a quantity allows to create a big enough tank of particles in the lobes, where the maximum magnetic pressure pushes the particles toward the X point direction. Also it prevents the electric field divergence close to the Y boundaries, as particles leave the lobes and concentrate in the mid-plane. The time-step is 2×10^{-4} which is small enough to satisfy the CFL conditions for the fastest whistler modes. We use perfect conducting boundaries in the Y direction. As there is no plasma flow in the

Run tag	Closure equation
A	isothermal closure, $P = nk_BT$ with $T = \text{const}$
B	full $\mathbf{P}$ (with subcycling for $[C]$ term)
C	full $\mathbf{P}$ with $[I]$ only on P_{xx} and P_{xy}
D	full $\mathbf{P}$ with $P_{xx} = P_{yy}$

Table 3.1: Meaning of the four tags used for runs A, B, C and D.

Y direction close to the borders of the simulation box, this assumption should not bring any artificial or unphysical structures.

In this study, we discuss four types of run, depending on the closure equations. These runs are labeled with a tag (ranging from A to D), which meaning is given in Table 3.1. Run A is the reference run with an isothermal closure while the other runs, namely B, C and D, are done with the time integration of the full electron pressure tensor in which we used a subcycling method to explicitly integrate the cyclotron term $[C]$. The isotropization term $[I]$ is characterized by a characteristic time scale τ as given in Eq. 2.21. By default we use $\tau = 1$ for each cases, unless the τ value is explicitly given. For run D, P_{xx} and P_{yy} are calculated using their original equation without approximations, but for the next time step they are set to half of their sum. The anisotropy between the P_{xx} and P_{yy} terms is quenched, while these terms are calculated with their appropriate time evolution equation.

3.2.1 Diagonal components

This section is dedicated to the close analysis of the time evolution of each term of the full electron pressure tensor, to understand and describe the different structures one observes, their origin (physical or numerical), and provide insights in the way the isotropization operator $[I]$ should be treated. The structure of the diagonal components of the pressure tensor is discussed in this section, while the off-diagonal components are discussed in the next one. In each cases, we distinguish two different regions : the separatrices and a region we call the electron layer, close to the mid-plane $Y = 0$, at electron scale.

The upper panel of Fig. 3.5a displays the P_{zz} component of the pressure tensor and shows a clear structure of enhanced pressure in a thin and elongated layer close to the mid-plane $Y = 0$. The length of this layer is hard to define as it reaches the bulge of pressure usually observed downstream of the reconnection X point and associated with the ejection of plasma. Although this length also depends on the time one observes it, the length is between 10 d_0 and 15 d_0, namely at ion scale. On the other hand, this structure has a thickness smaller than the ion inertial length, of few electron inertial

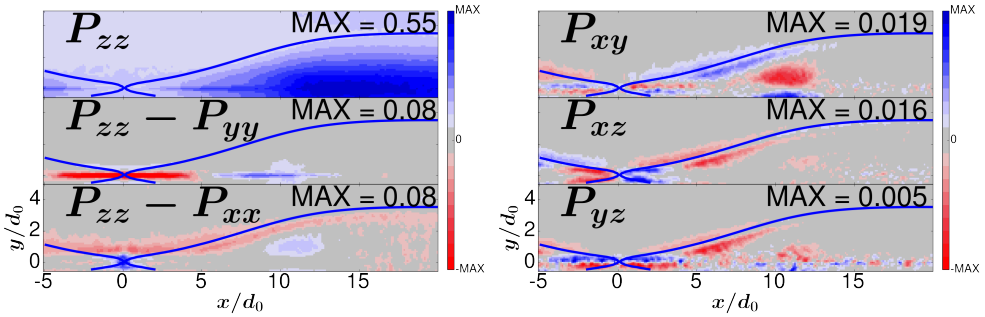

Figure 3.5: Left column (a) displays the diagonal components of the electron pressure tensor and right column (b) displays the off-diagonal components at $t = 80\ \Omega_0^{-1}$. For each panels, the same colorbar and the respective maximum values are indicated in the frame. The separatrices are indicated in blue lines.

length. While this thickness also depends on the location (this one vanishing close to the X point) and on the time, we call it electron layer as this thickness is always at electron scale. It is worthwhile to note that such electron layer is also observed in fully kinetic simulations[WHBG15]. Furthermore, we computed different simulations with mass ratio ranging from 0.1 to 0.01 where we observed a similar geometry of this electron layer. Because of the CFL condition, realistic mass ratio is hardly reachable as the constraint on the time step is too large (remembering that in an explicit hybrid code, the whistler mode makes the time step evolving as the square of the grid size). Recent full-PIC simulations show a decrease of height for the agyrotropic layers while mass ratio increases[SD08].

The two lower panels of Fig. 3.5a displays the difference of the P_{zz} components with the two other diagonal components of this tensor. There is one order of magnitude between the maximum values of P_{zz} and its difference with the two other terms, meaning that for each of these diagonal components, the structure of the electron layer and of the bulge of pressure are comparable. But two clear structures appear that outlines the anisotropy of the electrons. In the electron layer the P_{yy} component is larger close to the X point (until 5 d_0 from the X point) and gets smaller at the end of this electron layer. On the separatrices, the P_{xx} component gets larger than P_{zz} (and P_{yy}). The origin of these structures will be discussed, but one can already suspect the key role of the electron velocity (mainly due to the total current as ions are demagnetized in these regions) associated with the current in the electron layer and to the quadrupolar magnetic field at the separatrices.

Fig. 3.6 displays the $[D_{\mathrm{C}}]$ (red), $[D_{\mathrm{A}}]$ (green), $[D_{\mathrm{S}}]$ (blue), $[C]$ (black) and $[I]$ (magenta) terms controlling the time evolution for P_{xx} (left panel), P_{yy} (central panel) and P_{zz} (right panel). These values are averaged over 3 time steps contiguously recorded in an output file (which is 0.1 for these runs) to get rid of the fluctuating nature of these operators. In Fig. 3.6, solid lines indicate where the operator increases the associated components of the pressure tensor while dotted lines are used when it decreases. In the electron layer, the picture is pretty clear, and exhibit a strong enhancement of the P_{yy} component

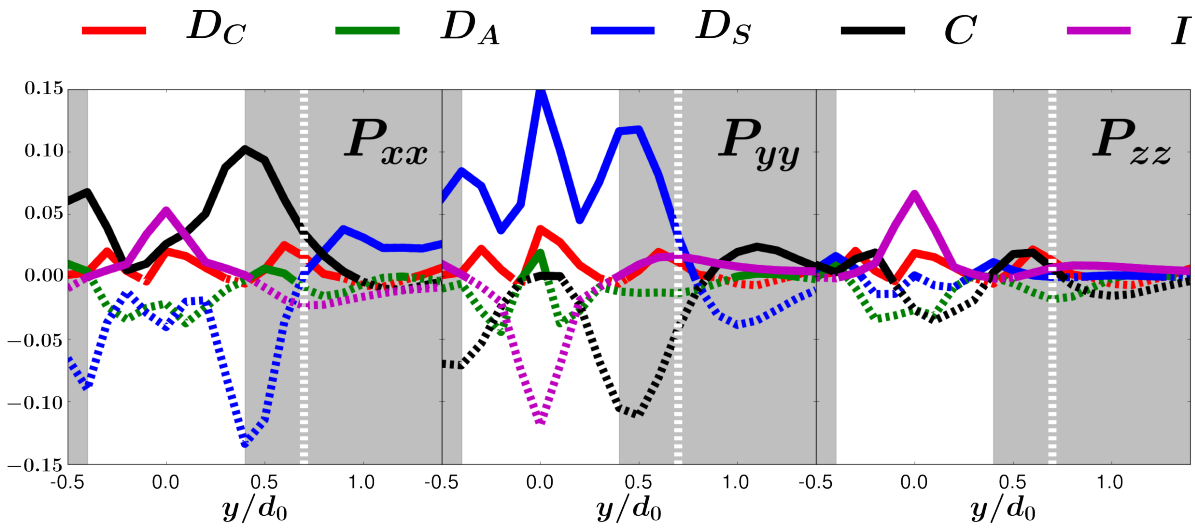

Figure 3.6: Cross section along the Y direction (at $X = 2\ d_0$) for the $[D_{\rm C}]$ (red), $[D_{\rm A}]$ (green), $[D_{\rm S}]$ (blue), $[C]$ (black) and $[I]$ (magenta) terms defined in Eq. 2.13. The three panels, from left to right, are for P_{xx}, P_{yy} and P_{zz} at $t = 80\ \Omega_0^{-1}$. White region is the extent of the electron layer and vertical dotted white line indicates the position of the separatrix. For each component solid lines are used when the associated term increases the pressure component, while dotted lines are used when this term decreases the pressure component.

because of the $[D_{\rm S}]$ term. There is also a small contribution of the $[D_{\rm C}]$ term, certainly because this is where the density gradient is important. As a consequence, an anisotropy $P_{yy} > P_{xx}, P_{zz}$ is developing, and the $[I]$ term acts to reduce this anisotropy. It can be clearly observed as the $[I]$ term decreases the P_{yy} value while it increases the P_{xx} and P_{zz} terms. It appears that the structure of the electron layer is intrinsically growing only for the P_{yy} term, and is affecting the other diagonal components because of the regularizing effect of the heat flux modeled by the $[I]$ term.

The terms contributing to $[D_{\rm S}]$ and $[C]$ are portrayed in Fig. 3.7 using the same definition for solid and dotted lines as in Fig. 3.6. One understands that the origin of the P_{yy} structure in the electron layer results from the component of $[D_{\rm S}]$ involving P_{yy} itself. This suggests the possible unstable nature of this growth which could have dramatic numerical consequences if not controlled by the isotropization term. To investigate this, we run a simulation where the isotropization term of P_{yy} is removed. The result is quite clear and unexpected : this kind of simulation is in fact non-diverging because the growth of P_{yy} is limited by the $[D_{\rm A}]$ term. While there are no clear structures for P_{xx} and P_{zz} in the electron layer, one can note that a component of the $[C]$ term (black line in Fig. 3.7) increases these components at the edges of the electron layer, but another component of the $[C]$ term (blue line) counterbalances for both. For P_{xx}, a component of $[D_{\rm S}]$ (red line) also counterbalances the $[C]$ term. It is important to note that all these terms in the $[C]$ operator involve off-diagonal components of the pressure tensor. As displayed in Fig 3.5a,

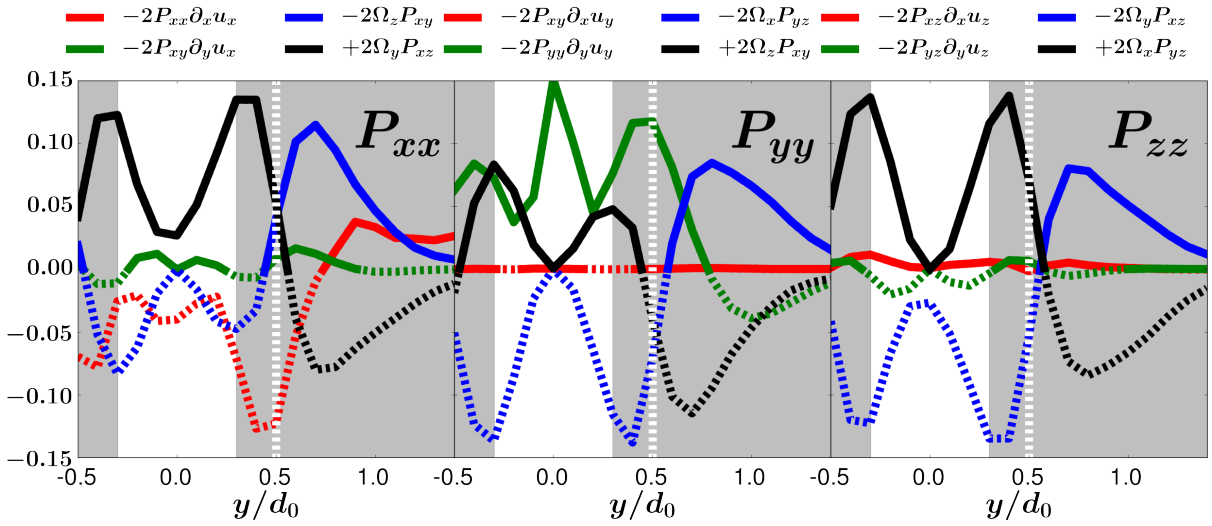

Figure 3.7: Cross section along the Y direction (at $X = 2\ d_0$) for each two terms in the $[D_S]$ and $[C]$ of Eq. (2.13) at $t = 80\ \Omega_0^{-1}$. Electron layer and separatrices are indicated as in Fig 3.6, and the meaning of solid and dotted lines is as in Fig 3.6.

each of these terms vanish at the middle of the electron layer, which explain why the terms at play in $[C]$ also vanish in the middle of the sheet.

Fig. 3.7 also suggests that the edges of the electron layer (i.e. the associated enhanced value of the P_{yy} component) are also resulting from the off-diagonal components of the pressure tensor in the $[C]$ term. This can be verified if running this case with a strong isotropization rate, namely $\tau = 0.01$ for run B conditions. The result is clear : the electron layer totally vanishes. If such strong isotropization only acts on off-diagonal components of the pressure tensor while a moderate one ($\tau = 1$) is kept on the diagonal components, the electron layer still develops, but later in time. As a consequence, the contribution of the off-diagonal terms in $[C]$ is significant and defines the width of the layer. This case with hybrid isotropization rate is not discussed anymore, but we should mention that we observed different topologies including Y points, and plasmoids formation.

Lets now focus on the separatrices region. Remembering Fig. 3.5a, we have a clear structure of enhanced pressure for the P_{xx} component. It appears from Fig. 3.6 that this structure results from the $[C]$ term which is not counter-balanced by the $[D_S]$ term, with the help of $[D_C]$ and $[D_A]$. It is a common point which will be even more clear for the off-diagonal components of the pressure : the $[C]$ term always acts as counter-balancing the $[D_S]$ term, these two terms being larger than the others. This in agreement with the conjecture that the cyclotron operator acts as an isotropization term[WH94]. With the help of Fig. 3.7, one observes that for P_{xx}, the two terms of $[C]$ contribute to its growth, as well as the $[D_S]$ term involving the P_{xy} component. This explains the enhanced value of P_{xx} at the separatrices. The $[D_S]$ term seems large enough to control this growth, but a close look at Fig. 3.5a shows that the P_{xx} structure at the separatrices has local gradients, hence P_{xx} is larger just around the separatrices than at the middle of this one.

As a results, one should not focus on the separatrix, but rather on its vicinity. The picture is quite different for P_{yy} as $[D_S]$ term increases this component and $[C]$ term efficiently limits this growth.

As a partial conclusion of this section, while we have clear structures in the electron layer, it is not mandatory from the numerical point of view to control their growth, as the physical terms are efficient enough to do so. On the other hand, at the separatrices, the enhanced values of P_{xx} can be problematic. To complete this analysis, the off-diagonal components of the pressure tensor are inspected in the same way in the next subsection, for both the electron layer and the separatrices. We should also mention that for run B, a strong isotropization ($\tau = 0.01$) totally quenches the development of the electron layer. This is because a larger $[I]$ term cancels out the $[D_S]$ term which increases P_{yy} in the electron layer.

3.2.2 Off-diagonal components

Fig.3.5b displays the three off-diagonal components of the pressure tensor at $t = 80\ \Omega_0^{-1}$ for run B. The first important point is that the off-diagonal components of the pressure tensor are about one order of magnitude smaller than the diagonal ones, as already pointed out by the other studies of this kind[YWGB01, WHBG15]. The second point to notice is that the patterns we observe are located in the electron layer and at the separatrices. The off-diagonal components of the pressure tensor being a direct consequence from the agyrotropy of the associated distribution function, this outlines the fact that agyrotropy of the electron distribution functions can be observed in regions where these electrons are magnetized. The enhanced agyrotropy regions along the separatrices have been already illuminated in 2D simulations with realistic mass ratio, as well as with lower ones[SD08]. For P_{xy} the pattern is a quadrupolar structure in the electron layer embedded in a second one of opposite polarity at the separatrices. For P_{xz} and P_{yz} this is a bipolar structure in the electron layer embedded in a second one at the separatrices. For these two patterns, one notes the different direction of symmetry for each structure as well as for each component.

Fig. 3.8 is a cross section at $Y = 0.3\ d_0$ along the X direction of the five terms (see Eq. 2.13) involved in the time evolution of each off-diagonal component of the pressure tensor. The choice of this cross section is intended to focus on the electron layer. It is clear that $[D_S]$ and $[C]$ are the only terms contributing to the structure of the off-diagonal components of the pressure, and that one of this terms is always balanced by the other one. For P_{xy}, the inner part of the electron layer structure results from the $[C]$ term, while the outer part results from the $[D_S]$ term. For P_{xz}, the pattern in the electron layer results from the $[D_S]$ term while for P_{yz}, it results from the $[C]$ term. It is important to note for each of these off-diagonal components, that the isotropization term $[I]$ seems to be ineffective.

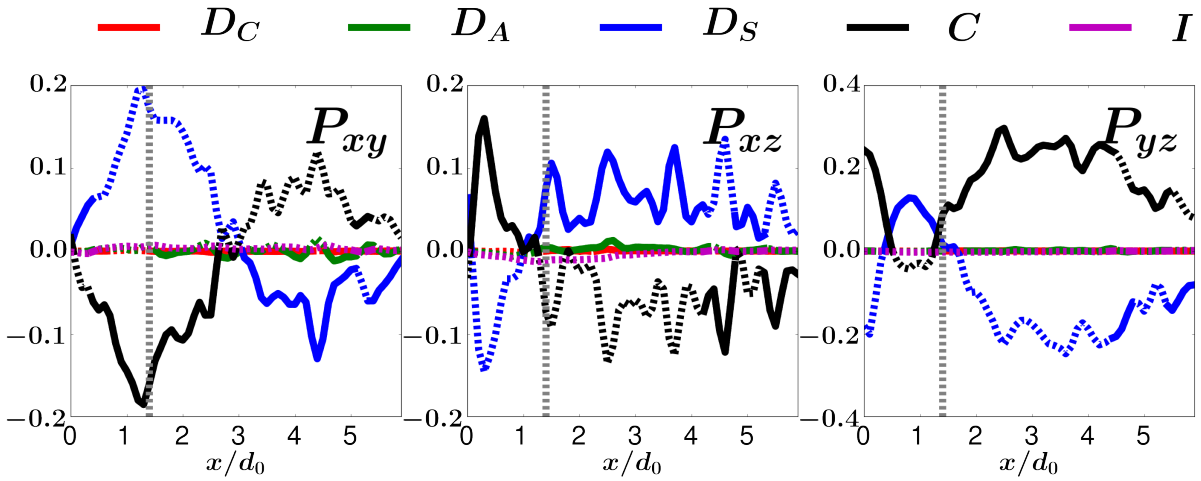

Figure 3.8: $[D_{\rm C}]$ (red), $[D_{\rm A}]$ (green), $[D_{\rm S}]$ (blue), $[C]$ (black) and $[I]$ (magenta) from Eq. 2.13 for P_{xy} (left panel), P_{xz} (central panel) and P_{yz} (right panel), cross section along X through $Y = 0.3\ d_0$ for run B at $t = 80$. Vertical grey dashed line is a separatrix position.

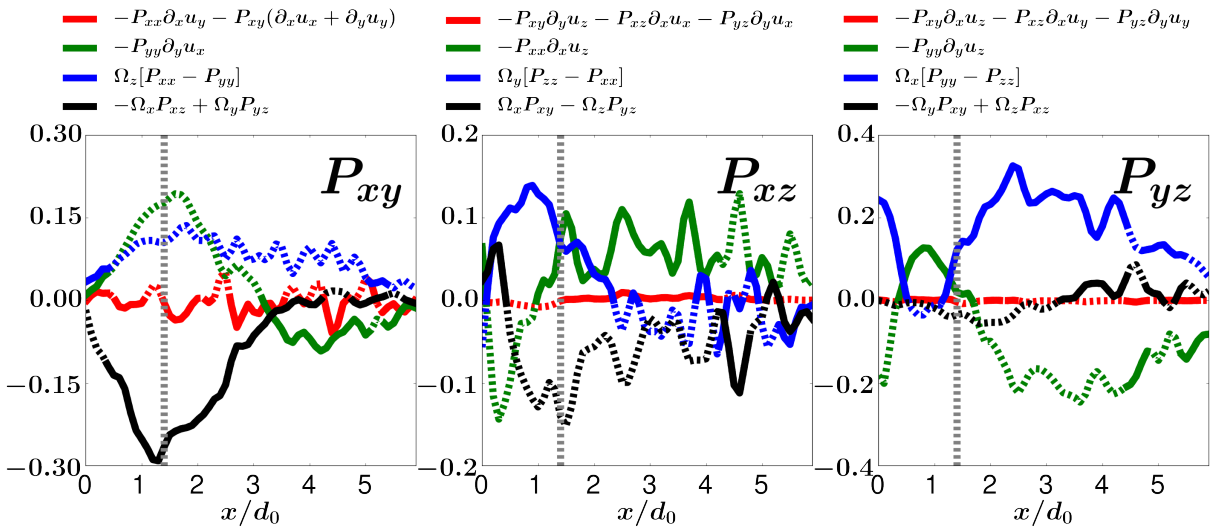

Figure 3.9: Terms of $[D_{\rm S}]$ and $[C]$ of Eq. (2.13) for P_{xy} (left panel), P_{xz} (central panel) and P_{yz} (right panel), cross section along X through $Y = 0.3\ d_0$ for run B at $t = 80$. For all panels: red - weak part of $[D_{\rm S}]$, green - the dominant term of $[D_{\rm S}]$, blue line is a part of $[C]$ proportional to $P_{ii} - P_{jj}$, black - two rest terms of $[C]$. Grey area represents inside the layer region. Vertical grey dashed line is a separatrix position.

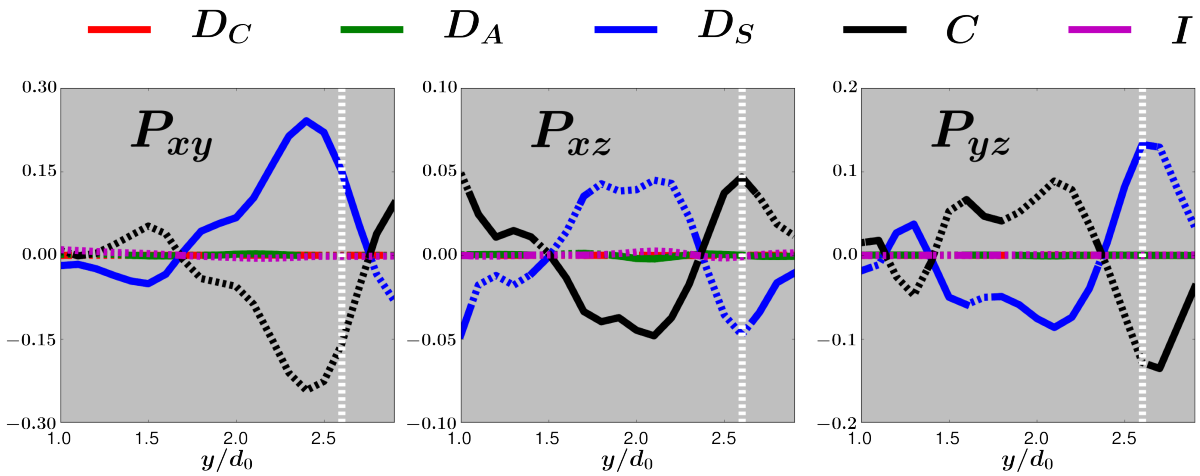

Figure 3.10: $[D_{\rm C}]$ (red), $[D_{\rm A}]$ (green), $[D_{\rm S}]$ (blue), $[C]$ (black) and $[I]$ (magenta) from Eq. 2.13 for P_{xy} (left panel), P_{xz} (central panel) and P_{yz} (right panel), cross section along Y direction through $X = 10\ d_0$ for run B at $t = 80\ \Omega_0^{-1}$. Grey area represents outside the layer region. Vertical white dashed line is a separatrix position.

To investigate the terms at play for these structures, Fig. 3.9 displays each of these terms using the same format as in Fig. 3.7. The dominating term for P_{xy} is coming from the $[C]$ term associated with non-gyrotropy (i.e. non-diagonal components of pressure tensor). On the other hand, this P_{xy} component is stabilized by the anisotropic $P_{xx} - P_{yy}$ term of $[C]$. P_{xz} grows essentially because of $[D_{\rm S}]$ term involving P_{yy} and P_{yz} is mainly growing because of anisotropy $P_{zz} - P_{yy}$ in the $[C]$ term. Playing with different values of the τ parameter to investigate the numerical stability of the associated run, we never saw any problem arising from the electron layer associated with the growth of an off-diagonal component of the pressure tensor.

We now focus on the separatrix. Fig. 3.10 displays a cross section at $X = 10\ d_0$ along the Y direction using the same format as Fig. 3.8, to survey the separatrix. Such cross section shows active terms in a problematic region, where we observed the growth of instability. P_{xy} results from the $[D_{\rm S}]$ term under separatrix (to the left of the white line) while the growth of P_{xz} results from the $[C]$. P_{yz} also results from the $[D_{\rm S}]$. Hence, the growth of P_{xz} could be problematic, but we saw in the previous sub-section that only P_{xy} plays a role in the growth of P_{xx} in an eventually unlimited way. Below we show how the growth of P_{xz} affects the P_{xy} component.

Fig. 3.11 shows that P_{xy} grows because of the $[D_{\rm S}]$ term involving P_{yy}, but also because of P_{xz} and P_{yz} terms in $[C]$. On the other hand, P_{xy} is stabilized by the anisotropic $P_{xx} - P_{yy}$ term of $[C]$. Without any isotropization, while the run is diverging at some points, we observe the growth of P_{xy} in this region because of the $[C]$ term involving P_{xz}, that leads to limitless growing of P_{xy}. For P_{xz}, it essentially grows because of the anisotropic $P_{zz} - P_{xx}$ term in $[C]$, with a counterbalance of the P_{xy} and P_{yz} terms. For P_{yz}, it grows because of P_{yy} term in $[D_{\rm S}]$, with a counterbalance of the anisotropic $P_{yy} - P_{zz}$

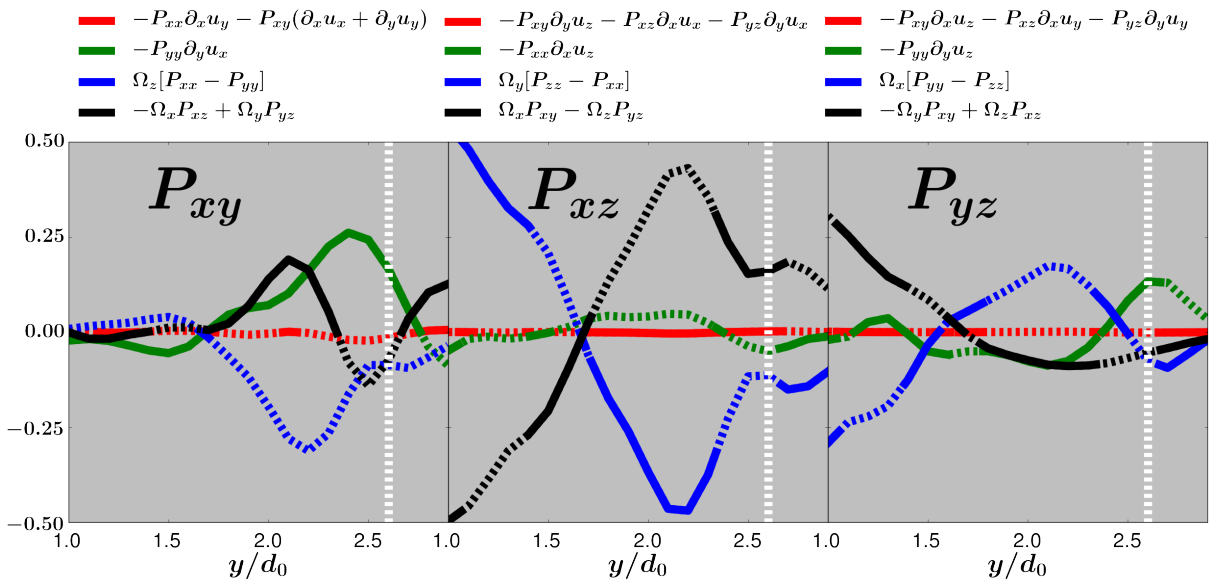

Figure 3.11: Terms of $[D_S]$ and $[C]$ of Eq. (2.13) for P_{xy} (left panel), P_{xz} (central panel) and P_{yz} (right panel), cross section along Y through $X = 10\ d_0$ for run B at $t = 80$. For all panels: red - weak part of $[D_S]$, green - the dominant term of $[D_S]$, blue line is a part of $[C]$ proportional to $P_{ii} - P_{jj}$, black - two rest terms of $[C]$. Grey area represents outside the layer region. Vertical white dashed line is a separatrix position.

term in $[C]$.

As for the diagonal components, the problem of components growing in an unlimited way only occur at the separatrices. P_{xx} grows essentially because of P_{xy}, but also because of P_{xz}. P_{xy} grows because of $[D_S]$, but also because of $[C]$ term involving P_{xz}. The general idea is that at the separatrices, the growth of P_{xz} feeds the growth of the P_{xy} term. Hence, this terms help P_{xx} to grow, as well as an anisotropy $P_{xx} - P_{zz}$. Finally, this anisotropy feed P_{xz}, resulting in an unstable growth of each of these components. From various runs it also appears that even if both P_{xy} and P_{xz} play a role in the growth of P_{xx} at the separatrix, the role of P_{xy} is the most important one. To discuss and validate these assertions, in the next section we discuss the results for run C and D, already introduced in Tab. 3.1.

3.2.3 The role of $P_{xx} - P_{yy}$

As concluded in the previous section, the growth of P_{xx} (and the associated anisotropy $P_{xx} - P_{yy}$) as well as the growth of P_{xy} seems to be a key point in the numerical stability of the scheme. But from the physical point of view it also means that the isotropization term associated with the heat flux should act in a way to limit the growth of both P_{xx} and

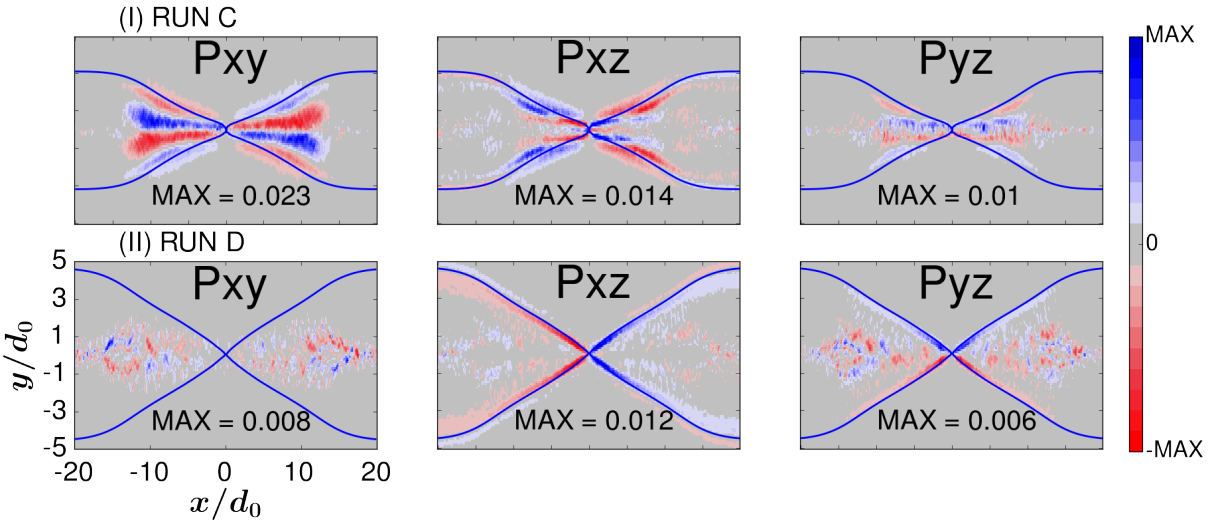

Figure 3.12: Off diagonal components of the pressure tensor for runs C *(first row)* and D *(second row)* at $t = 80\ \Omega_0^{-1}$.

P_{xy}. To test this hypothesis, we have run C and D. The reason for run C is pretty obvious : we want to evaluate how the problem is evolving if the isotropization operator only acts on the P_{xx} and P_{xy} components. The reason of run D is less obvious : P_{xy} happens to play a key role in the time evolution of both P_{xx} and P_{yy}. But the summation of the equations governing their time evolution cancels out the term involving P_{xy}, meaning that run D is the one where the destabilizing effect of P_{xy} is artificially removed.

For run C, P_{xy} is the only off-diagonal term that is isotropized. Fig. 3.12 displays the off diagonal components for run C and D. The patterns for P_{xz} and P_{yz} are similar to the one of run B displayed in Fig. 3.5b, meaning that their isotropization by the $[I]$ term do not determine their structure. Unsurprisingly, the pattern of P_{xy} is also unchanged. The case of run D is more complex : on one hand, the P_{xy} component is clearly quenched, whatever in the electron layer or at the separatrix. This outlines the fundamental role of the anisotropic $P_{xx} - P_{yy}$ term in its evolution. On the other hand, the structure in the electron layer also totally vanishes for P_{xz} and P_{yz}, while it appears to be stronger at the separatrix.

3.2.4 The role of P_{xy} on separatrix

Without any isotropization the numerical scheme for the pressure tensor evolution equation is unstable, and leads to the divergence of its Cyclotron part. In whatever situations the isotropization on the P_{xy} component is mandatory. Otherwise, the simulations turns to be unstable with problems arising at the separatrices. We have done one simulation with a strong isotropization $\tau = 0.01$ only on the P_{xy} component. Such

isotropization term stabilizes the simulation, but the diagonal components of the pressure tensor are not isotropized downstream for $|X| > 10$, that has no consequences on stability, P_{xx} having a greater value than P_{yy} and P_{zz}. To investigate the importance of the τ value, we performed a simulation using a moderate isotropization rate $\tau = 1$ only for the P_{xy} term. Such simulation diverges with the similar ongoing to simulations without any isotropization, from what we conclude that an instability develops on electron time scales.

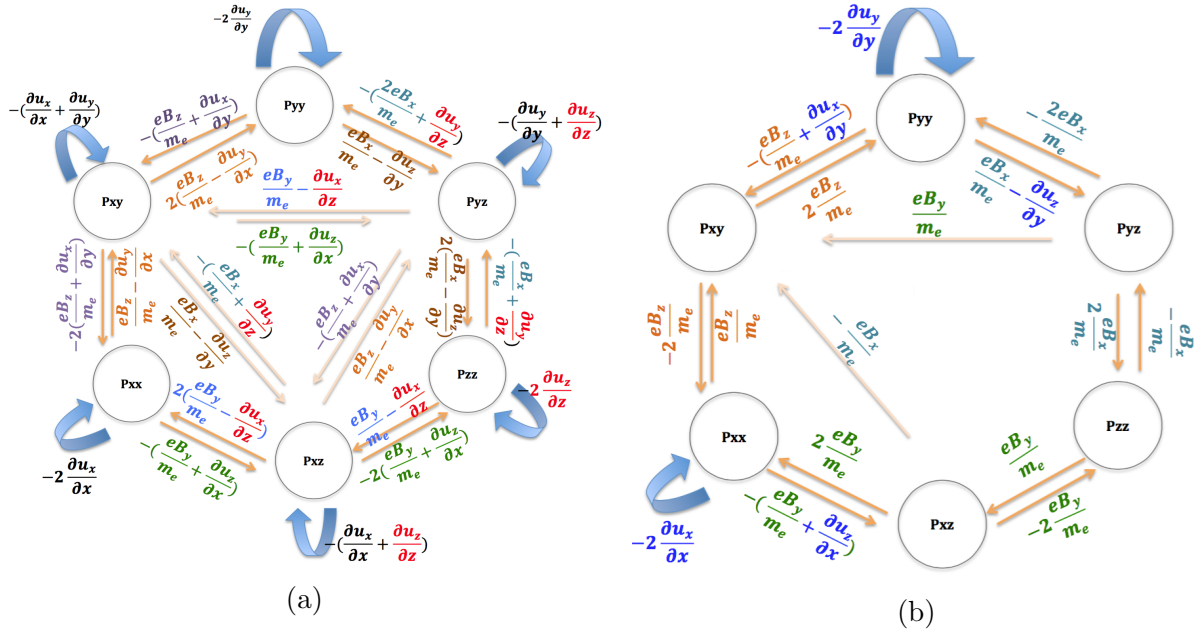

Figure 3.13: Graph representation of the evolution system for 6 pressure tensor components. (a) All terms, and (b) dominant terms on separatrix.

To outline the relations between each component of the system given by Eq.2.13, Fig. 3.13a depicts the evolutions of these terms (the signs are explicitly given), the six vertices being the time derivatives of each of the six components of the pressure tensor. For each of these components, the arrows exhibit all the terms controlling its time evolution. Terms $[D_A]$, $[D_C]$ and $[I]$ are indicated by the thick blue arrows. The other thin arrows indicate the interplay between cross terms of this tensor by $[D_S]$ and $[C]$. Fig. 3.13b shows the dominant terms around the separatrices presented previously. We can conclude that left triangle containing P_{xx}, P_{xy}, and P_{xz} has a dominant part in stability of the system, while it is also a driver of the system. To remove the discrepancies for the diagonal components downstream of the reconnection site, except the isotropization on the P_{xy} (required for stability), one needs to isotropize also P_{xx} component as in run C. We have also performed a simulation using a strong isotropization $\tau = 0.01$ only on the P_{xz} component. The sheet stays almost unperturbed until the end $t = 100\Omega^{-1}$ and the reconnection proceeds with a vanishing rate. From what we conclude that P_{xz} is the

mediator between P_{xx} and P_{xy} components, while this pair interacts in a non-stable way on separatrices.

3.3 Consequences for the reconnection process

In this section we investigate the consequences of the structure of the full electron pressure tensor for the reconnection process.

3.3.1 Bifurcated current sheet

In the Harris-type current sheets, the field reversal is associated with a strong electron current in the out-of-plane Z direction. As we saw from the Cluster observation [RSN$^+$06], the Earth magnetotail can be approximated by a Harris sheet. More specifically, three types of current sheets are observable up to now (Fig. 1.5). Two types of the central sheets, namely with a single peak or bifurcated, and one type of asymmetric current sheets with the current density maximum shifted out from the equatorial plane. In this section we compare the current sheets from simulations with the one observed in space.

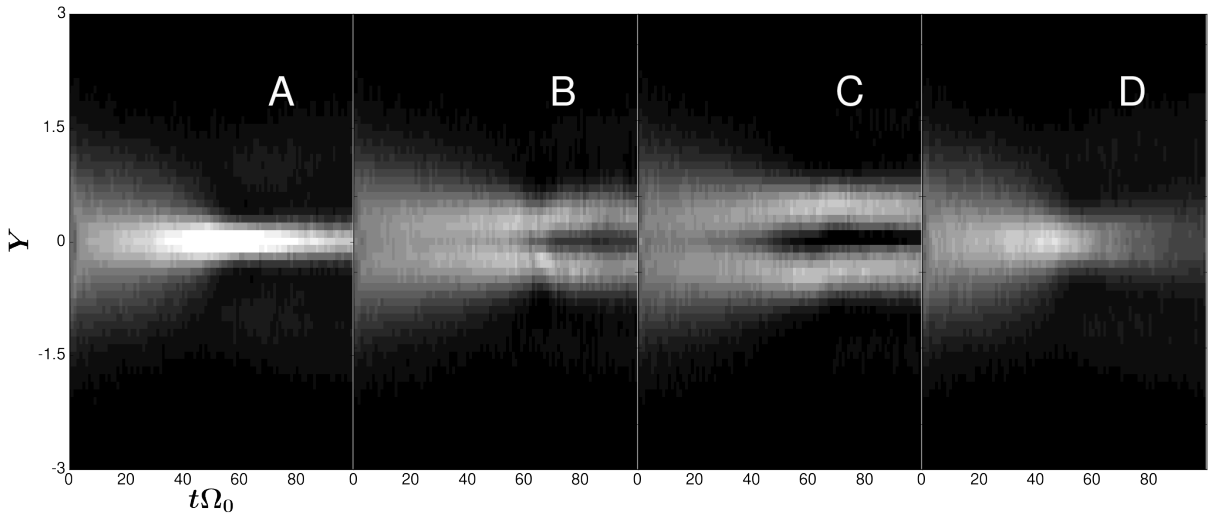

Figure 3.14: Evolution of the lineout through the X point for out-of-plane current J_z. Black is 0, and white is -1.5

To observe how the initial Harris sheet with an initial half width around the ion inertial lengths shrinks down to electron scales, we propose, as already displayed in section 1.3.1, a way to represent the current formation process in a more appropriate way: a color code picture with the time on the abscissa-axis and the Y coordinate on the ordinate-axis. It is a two-dimensional generalization of a lineout (at a given X position) including its time

evolution. Fig. 3.14 displays the time evolution of such vertical lineout through the X point. We see that for the isothermal case, run A, the current sheet shrinks to sub ion scales, while for run B and C using full pressure tensor and isotropization, the current sheet is split. One can note the resulting two current sheet have a thickness of the order of the ion inertial length, quite constant in time. For run D, which imposes $P_{xx} = P_{yy}$, the current sheet is shrinking until $t = 50\ \Omega_0^{-1}$ (J_z being peaked and enhanced), and thickening. Hence, the pressure tensor not only changes the scales of current sheet during the reconnection, but also changes its topology leading to bifurcation.

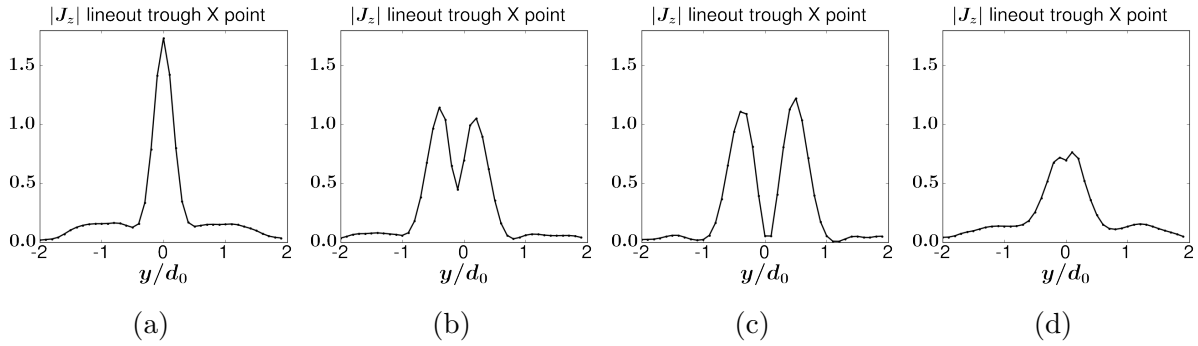

Figure 3.15: Lineout through the X point for out-of-plane current J_z averaged over 5 time steps for $67.8 < t < 68.2\ \Omega_0^{-1}$. (a) run A, (b) run B, (c) run C, and (d) run D.

To distinguish between the different kinds of current sheets, Fig. 3.15 shows a lineout through the X point for the out-of-plane current J_z. We see the one for run A is similar to the single peak current sheet in the classification proposed by Runov et al. [RNB+03], cases B and C represent the bifurcated structure of the current sheet developing due to the pressure term divergence. The P_{yy} component of the electron pressure tensor creates a *drag force* in the inflow Y direction. The case of run D is asymmetric and has a smaller magnitude as the third kind of the sheets (Fig. 1.5c).

To finish the discussion, we look at the two-dimensional spatial configuration of the sheet. Fig 3.16 displays the J_z component of the total current. As previously observed in two-dimensional reconnection studies, for run A and D, the out-of-plane current sheet is diminished close to the reconnection X point, and advected downstream of it. The picture is quite different for run B and C: this current is totally vanishing at $Y = 0$, but expelled above and below the mid-plane, resulting in a double-humped structure. Such bifurcated current sheet has already been discussed, both theoretically[ZMP03], numerically[DMZ04] and with in-situ data observations[GMF+05]. Nongyrotropic electron pressure effects have been pointed out in the frame of three-dimensional PIC simulations of magnetic reconnection, that demonstrated a bifurcated structure[LDK+13] of the current sheet. Bifurcated parallel ridges of electron agyrotropy has also been observed in two-dimensional PIC simulations with a realistic mass ratio[SD08]. Nonetheless, the distance between the two peaked values of the current is of the order of ion inertial length, which is in agreement with the Cluster observations already reported the bifurcated current sheet in the Earth

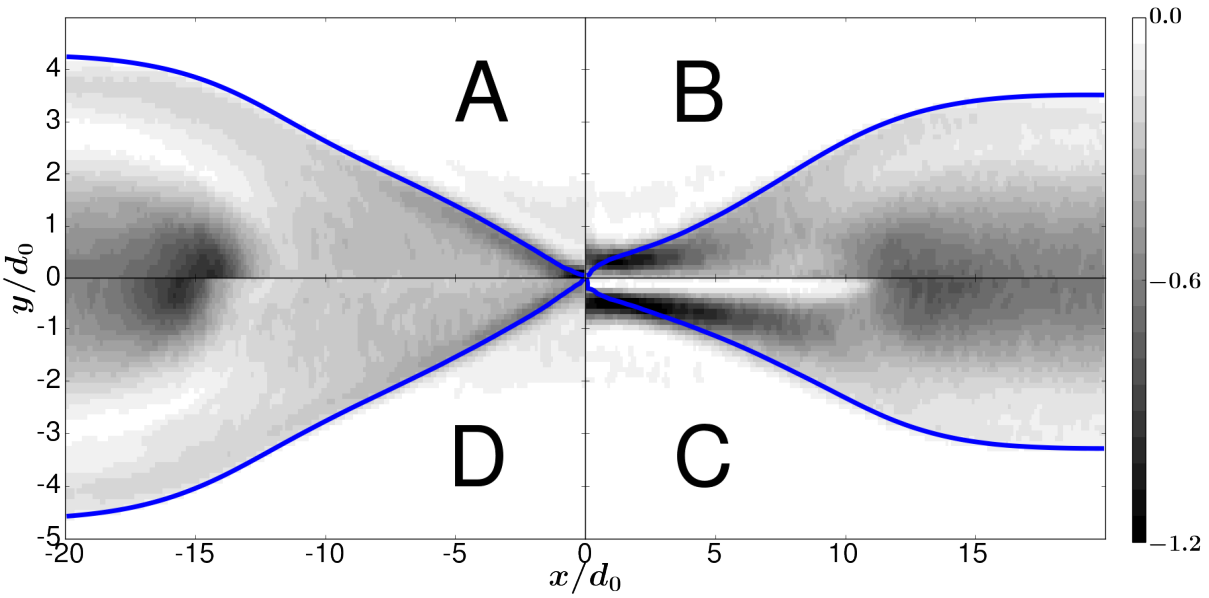

Figure 3.16: $\mathbf{J}_z$ at $t = 80\ \Omega_0^{-1}$, for runs *A (top left)*, *B (top right)*, *C (lower right)* and *D (lower left)*, blue lines represent separatrix of the in-plane projection of the magnetic field lines.

magnetotail[GMF+05]. It is also important to note the X-extent of the bifurcated current sheet, of the order of 5 ion inertial length for run B. It is even larger (about 10 ion inertial length) for run C, which supports the fact that the enhanced value of P_{yy} in the electron layer (not isotropized in run C) is on the origin of this structure. We can conjecture the origin of the bifurcated current sheet: in this quiet stationary current sheet the increase of P_{yy} in the electron layer has to be associated with a decrease of the magnetic pressure by force balance. A clear way to do so is to split the current decreasing the associated magnitude of the magnetic field.

3.3.2 Reconnection rate

Fig. 3.17 displays the time evolution of the reconnection rate. It is computed as the local value of the out-of-plane electric field E_z at the X point, normalized to the upstream magnetic field and Alfvén speed. As classically observed in numerical studies of magnetic reconnection [BDS+01], the reconnection rate grows from zero during a transient phase, and reaches a quite constant value outlining the stationarity of the reconnection process. This reconnection rate reaches a maximum value close to 0.1 for run A and D, 0.08 for run B and 0.06 for run C. While not spectacular, these differences are to be noticed, and show that the full pressure tensor makes the efficiency of the reconnection process decrease.

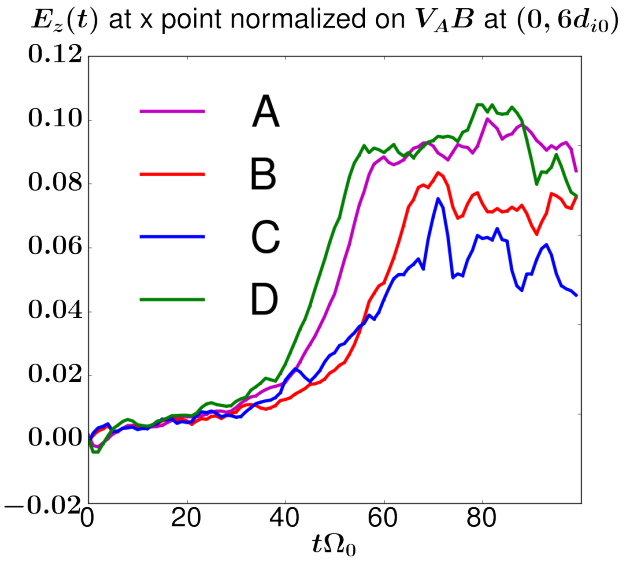

Figure 3.17: E_z electric field at the X point normalized to upstream magnetic field and Alvfen speed. The lines in purple, red, blue and green stand for run A, B, C and D, respectively.

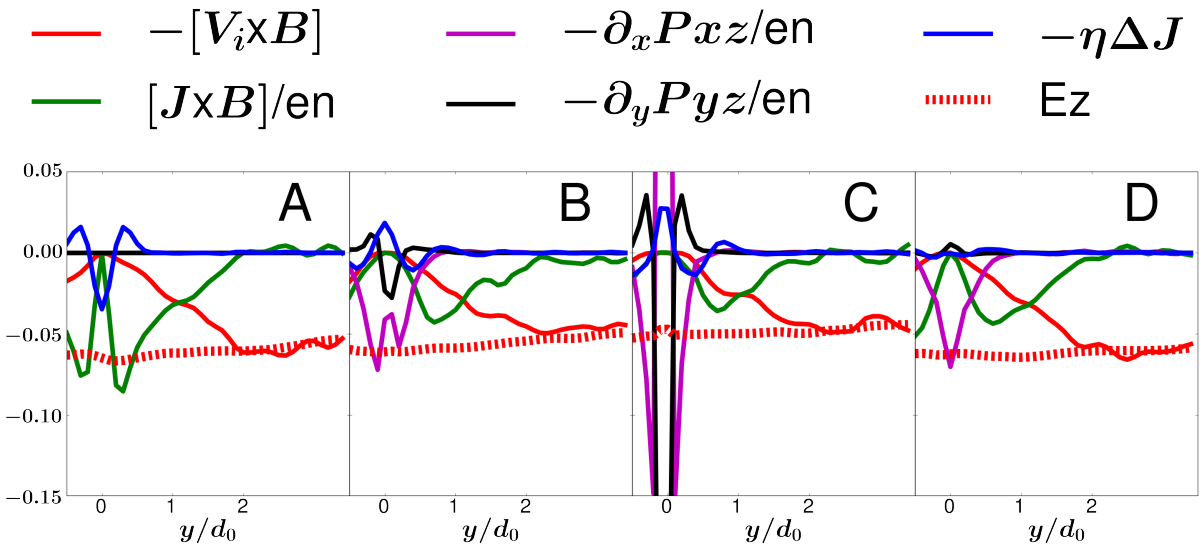

Figure 3.18: Cross section along Y at $X = 0$ for the terms of Ohm's law in the Z direction, averaged over 10 time steps for $79.5 < t < 80.5\ \Omega_0^{-1}$ for run A, B, C and D.

On Fig. 3.18, we display the E_z component of the electric field (thick red dotted line) depending on the Y value for a cross section performed at $X = 0$. One observes the classical pattern for run A : in the MHD region, where ions are magnetized ($Y > 2d_0$), the electric field is mainly due to the ideal term associated with the inward advection of plasma in the reconnection region. Closer to the field reversal, the dominant term

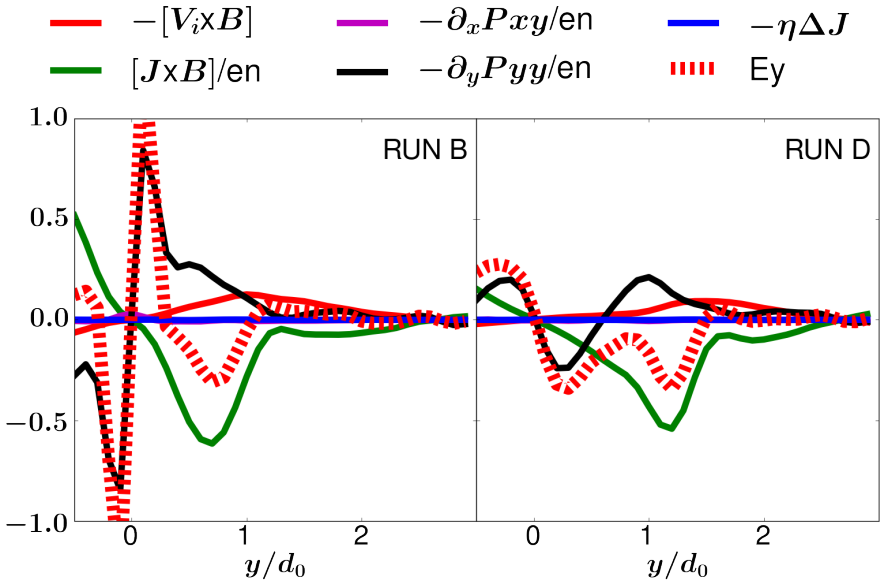

Figure 3.19: Cross section along the Y direction at $X = 4\ d_0$ at $t = 80\ \Omega_0^{-1}$ for the terms of the Ohm's law in the Y direction for run B (left panel) and D (right panel).

is the Hall term, associated with the main B_x component of the magnetic field and the J_y current. At the very middle of the current sheet, as B_x vanishes, the hyperviscous dissipative term is the only one at play, this one being restricted to few grid points. The case of run D is quite similar, except that the Hall term has a smaller amplitude. Furthermore, the pressure term associated with P_{xz} is the leading one at the very middle of the current sheet, the hyperviscous one being negligible. This results from the modified structure of the J_z current and the associated smaller value of its laplacian.

The cases of run B and C are quite different in Fig. 3.18 : while dominating in the MHD region, the ideal term is less important as the ion velocity is smaller than in classical case of run A. The reduction of the ion velocity could result from the drag force already discussed by Yin et al.[YWGB01]. To investigate this, Fig. 3.19 displays for run B and D the E_y component of the electric field in the Y direction at $X = 4\ d_0$ and $t = 80\ \Omega_0^{-1}$. In run D, one can observe the classical bipolar component of E_y, which is negative above the mid-plane, and positive below. This structure is mainly supported by the pressure gradient close to the mid-plane, and by the Hall term farther. We remind the importance of this term as its curl is on the origin of the out-of-plane quadrupolar magnetic field development. In the very middle of the current sheet, the situation is quite different : because of the enhanced value of the P_{yy} term, the associated component of the electric field is highly peaked with a sign opposite to the one of the Hall term. We can suspect this strong electric field to be important in slowing down the ion fluid when convecting through the reconnection region.

Closer to the mid-plane the Hall term is less important than for run A, for run B and C displayed in Fig. 3.18. This is also a clear consequence of the bifurcated structure

of the current sheet, and this also contributes to reduce the reconnection rate in the ion diffusion region. Closer to the middle of the current sheet for run B the electric field is dominated by the electron pressure term associated with P_{xz}. The electron pressure term associated with P_{yz} is also at play, while less important. This pattern is also observable for run C, but as P_{xz} and P_{yz} components are not isotropized, the contribution of these terms for the E_y component of the electric field is larger. One should also notice the hyperviscous term is also present but with a sign opposite to the one observed for run A. As already pointed out, it results from the bifurcated nature of the current sheet.

To resume:

- reconnection rate reaches a maximum value 0.1 for run A and D, 0.08 for run B and 0.06 for run C.
- in the MHD region, where ions are magnetized ($Y > 2d_0$), the electric field is mainly due to the ideal term associated with the inward advection of plasma in the reconnection region.
- closer to the field reversal, the dominant term is the Hall term, associated with the main B_x component of the magnetic field and the J_y current.
- for isothermal simulation at the very middle of the current sheet, as B_x vanishes, the hyperviscous dissipative term is the only one at play.
- using the full pressure tensor equation, the pressure terms associated with both P_{xz} and P_{yz} are the leading components close to the mid-plane of the current sheet.

3.3.3 Consequences of the isotropization operator

As it is not straightforward why the isotropization time scales should be the same for diagonal and off diagonal components, we performed a simulation using different τ values. We have done simulations with a mixed isotropization rate, that is for diagonal components $\tau = 1$ and for off diagonal $\tau = \mu = 100$, where μ is the mass ratio μ. We observe the reconnection process takes more time to achieve a steady phase, as well as to develop the electron scale layer on the diagonal pressure components. Fig. 3.20a shows the reconnection rate where steady phase starts for $t > 100$. Fig. 3.20b displays the terms of the Ohm's law given by Eq. 2.8. One can see the similar picture as for run C using a moderate isotropization only on P_{xx} and P_{xy}. At the vicinity of the X point, the out-of-plane electric field is mainly supported by the P_{xz} component, while at the very middle of the current sheet, the P_{yz} term dominates.

The simulations using the mixed isotropization rate show the formation of an O point which means there is a plasmoid that is ejected. Fig. 3.21a shows the out-of-plane current on later times during steady state where we can clearly see the plasmoid at the ion scale.

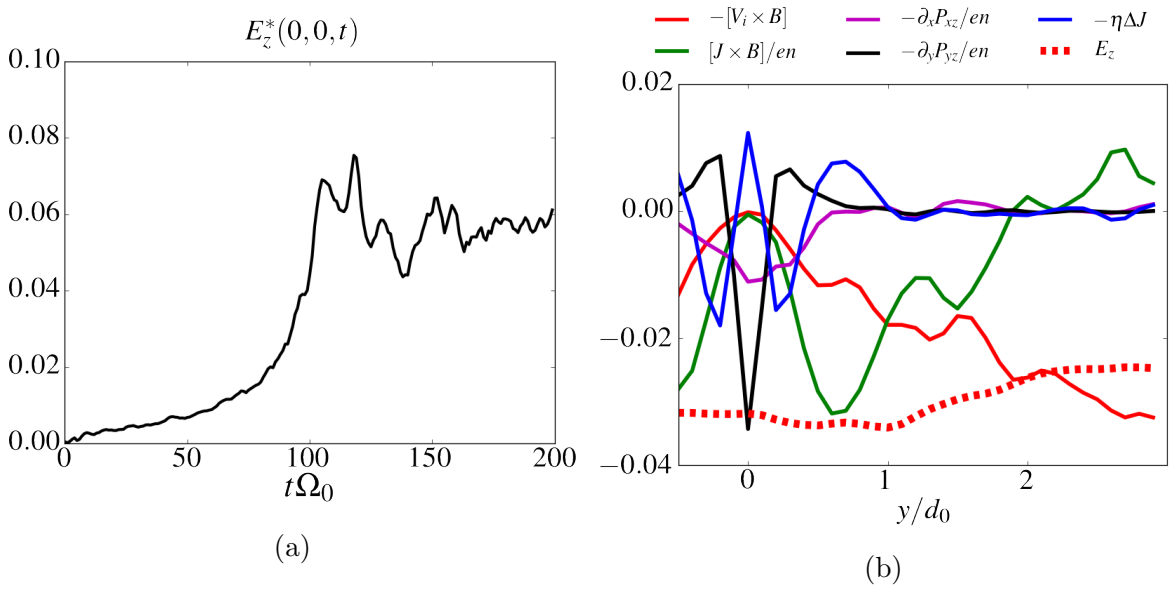

Figure 3.20: Mixed isotropization case, for diagonal components $\tau = 1$ and for off diagonal $\tau = \mu = 100$: (a) normalized reconnection electric field at the X point, and (b) Ohm's law terms at $t = 140\ \Omega_0^{-1}$.

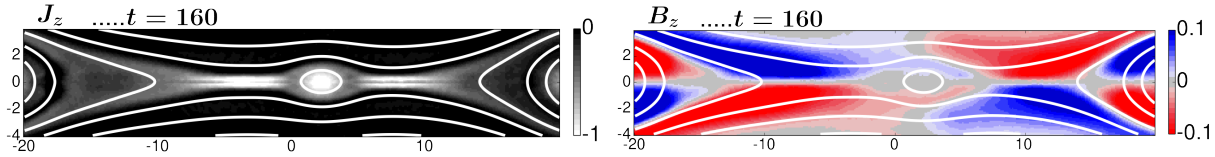

Figure 3.21: Mixed isotropization case, with $\tau = 1$ for the diagonal components and $\tau = 100$ for the off-diagonal components. (a) out-of-plane current, (b) out-of-plane magnetic field at $t = 160\Omega_0^{-1}$. White lines represent the magnetic field lines.

As a result, the quadrupolar structure of the out-of-plane magnetic field on the Fig. 3.21b is perturbed by the strong current. The X point is positioned on the right from the plasmoid $X = 8$, that is why we see penetration of the Hall field inside the plasmoid. The outflow in the $-X$ direction feeds the plasmoid.

Fig. 3.22 displays the evolution of the mid-plane lineout $Y = 0$ for (a) modulus of magnetic field and (b) electron density. At $t = 0$ the magnetic field has a seed perturbation in the Y direction, growing and moving in the outflow direction with 0.2 V_A. Around $t = 150\ \Omega_0^{-1}$ we see the slowdown of the expansion because of the periodic boundary conditions for particles in the X direction, that have already crossed boundaries and press back the downstream plasma. The density profile reveals many electron scale plasmoids for $t < 150$ accelerating up to the Alfvén speed and stopped by the downstream plasma bulge. For $t > 160$ we observe ion scale plasmoid, that moves in $-X$ direction with half of Alfvén

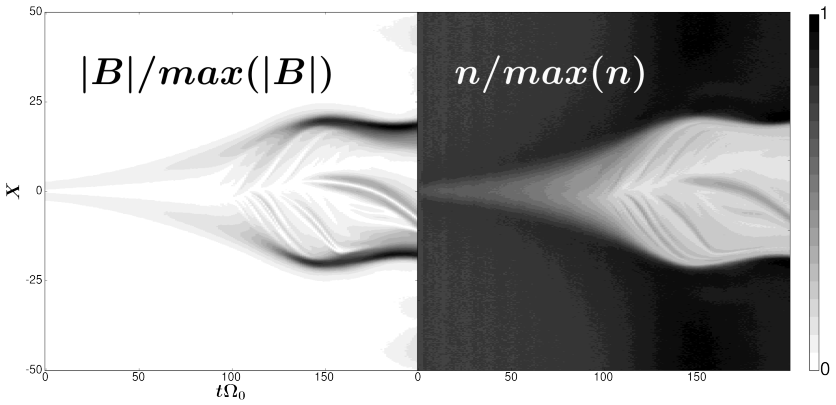

Figure 3.22: Mixed isotropization case with the $\tau = 1$ for diagonal components and $\tau = 100$ for the off-diagonal components. Lineout through the mid-plane $Y = 0$ for (a) modulus of magnetic field (left panel) and (b) electron density (right panel).

speed.

We should emphasise again the importance of the isotropization, as the consequence of the heat flux divergence in the evolution of the pressure tensor by Eq.(2.13). To summarize:

- a minimum isotropization (for stability) is required only for the P_{xy} component
- a moderate isotropization on all the pressure components yields to an electron scale layer in the mid-plane
- the isotropization on P_{xx} is required to remove downstream variations for diagonal components
- a strong isotropization quenches the layer development
- a moderate isotropization on diagonal components and a strong one on the off-diagonal components exhibits the formation of ion scale plasmoids
- to avoid any isotropization, one can set $P_{xx} = P_{yy}$ or $P_{xx} = P_{zz}$, while this is questionable from the physical point of view.

We have studied in this section the effect of the time integration of the full electron pressure tensor. Aside from an existing implicit method to integrate the fast electron cyclotron part of this tensor, we propose an explicit method based on subcycling. We put forward such method converges to the same results as the one obtained with the implicit method, but saving about 30% of CPU time. We also outline the requirement of an isotropization operator of this tensor (both diagonal and non-diagonal components) to restrain the growth of these components, located at the separatrices. Such isotropization is physically associated with the divergence of the electron heat flux. While this term is

numerically sensitive to handle, several approximation have been proposed to model it correctly.

We observe two characteristic structures in the development of magnetic reconnection : (1) an electron scale layer close to the mid-plane where P_{yy} is increased, and (2) an increase of P_{xx} component at the separatrices. These structures are also associated with more complex patterns for the off-diagonal components of the electron pressure tensor. As result we have the following consequences on the evolution

- the electron layer creates a drag force acting on the ions, located in the mid-plane
- we observe the increase of the P_{yy} component in the electron layer, and an associated anisotropy for the two others diagonal components
- a bifurcated current sheet develops, resulting from the local decrease of the magnetic pressure (by pressure balance) in the electron layer
- the reconnection rate is smaller for the bifurcated current sheet
- P_{xz} and P_{yz} are the main contributors to the out-plane electric field in the EDR.

Chapter 4

Driven reconnection using colliding bubbles

This chapter presents how to perform realistic simulations of driven reconnection in laser-generated plasmas. The first section presents the physical mechanisms at play in laser plasma experiments and how the magnetic field is created. The second section describes how important are the effects of ion temperature for the dynamics of magnetic reconnection process. The third section is focused on the importance of electron fluid physics for reconnection. The fourth section introduces a method on how to include laser effects for the plasma as a forcing current in the Ampere's law. The last section describes an alternative configuration to model such reconnection, which helps to save computational resources.

4.1 Reconnection in laser-generated plasmas

In this section we introduce the physical processes at play in a laser-generated plasma and emphasize the included effects as well as the postponed for future work.

4.1.1 Biermann-Battery effect

The last two decades provided a set of measurements of magnetic reconnection in plasmas created by two or more laser beams focused on a solid target[NWK$^+$06, LSF$^+$07, WNK$^+$10]. To create High Energy Density (HED) plasma bubbles, the one with an energy density larger than 10^6 bar, terawatt-class lasers simultaneously are focused on plastic or metal target leading to ionization and formation of the bubbles-like plumes expanding supersonically off the surface of the target. Fig. 4.1a schematically shows a global picture of the plasma bubbles and the associated self-generated magnetic field in the target plane $X - Y$. The expanding bubbles collide, and the anti-parallel magnetic

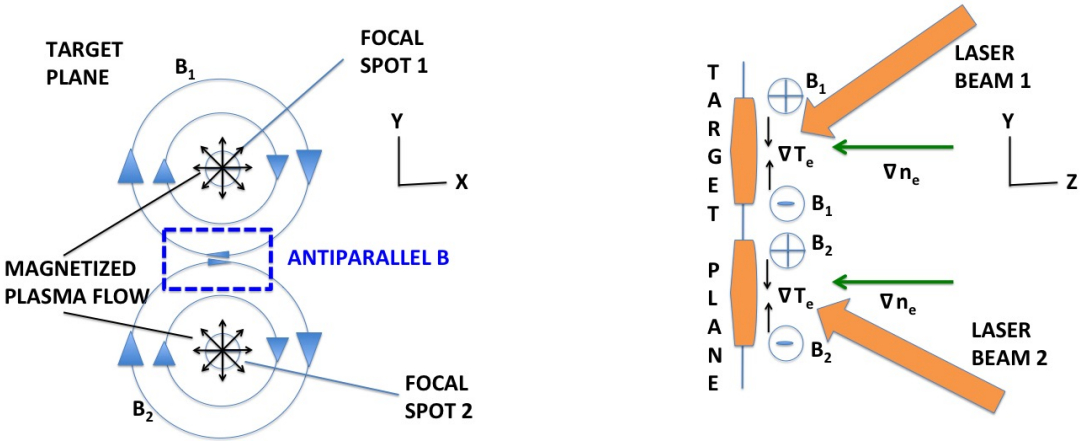

(a) (b)

Figure 4.1: Schematic of the magnetic reconnection topology between expanding plasma bubbles (a) target plan, top view, (b) normal to target direction, side view.

fields are pressed together to eventually reconnect. Each bubble self-generates a magnetic field of the order of hundreds Tesla because of the Biermann-Battery effect [BS51].

To establish the equation for the time evolution of the magnetic field, we substitute the Ohm's law Eq. (2.8) into Maxwell-Faraday equation. The dominant term being the pressure term, one gets:

$$\partial_t \mathbf{B} = \boldsymbol{\nabla} \times \left(\frac{\boldsymbol{\nabla} P_e}{e n_e} \right) \tag{4.1}$$

Writing the electron pressure as $P_e = n_e k_B T_e$, and keeping the largest term, one gets:

$$\partial_t \mathbf{B} = \frac{k_B \boldsymbol{\nabla} n_e \times \boldsymbol{\nabla} T_e}{e n_e} \tag{4.2}$$

A magnetic field is self-generated when density gradient and temperature gradient are not parallel. The difference from dynamo effect is that magnetic field can arise from zero rather than from a seed. Fig. 4.1b shows schematically the configuration of a laser plasma experiment. We see electron density n_e decreases in the axial direction (Z) as plasma expands, and electron temperature T_e decreases in the radial direction (r), as the hottest particles are in center of the hot spot. As a consequence, the Biermann-Battery effect produces a magnetic fields in the azimuthal direction, i.e. around the laser beam direction.

As detailed in chapter 2, three-dimensional kinetic simulations of such configuration is yet too resource-consuming to be carried out. As a result, as in chapter 3, we present two-dimensional simulations of bubbles collisions in this chapter. While the Z gradient of

the density (which is essential in the Biermann-Battery effect) can not be kept, we need to impose the magnetic field as an initial conditions. The main drawback of doing so is that the magnetic field can not be continuously provided by Biermann-Battery effect during the irradiation, as result an artificial erosion of the magnetic field is at play.

4.1.2 Experimental set-up

The geometry where driven magnetic reconnection can occur needs magnetic fields of opposite direction in close proximity. Fig.4.2a shows a scheme of the experimental setup. To retrieve informations on the B-field topology, the best diagnostic in such a case is the proton radiography [SKH$^+$00]. An auxiliary short intense laser pulse irradiates the target, positioned behind the main target regarding the detector. It produces a proton beam typically up to 20 MeV by means of the target normal sheath acceleration (TNSA) mechanism [WLC$^+$01]. The probing protons, passing through the target, are deflected by the magnetic and electric fields encountered during their fly. The information collected on the Radio-Chromic Films (RCF) contains the "memory" of the electric and magnetic field integrated along the protons orbit in space and time. By comparison with numerical simulations, it is possible to get information about geometry and magnitude of the magnetic field.

Fig.4.2b presents the typical picture obtained with proton radiography. The darker areas illuminate regions of higher proton intensity, where protons deposed maximum energy in RCF [BBB$^+$14]. The base of a film is a polyester substrate containing an active layer. Because of irradiation, the active layer becomes darker due to polymerization which depends on absorption. Dark line is a result of accumulation of deflected protons by the investigated magnetic fields. We clearly see the contours of the plasma plumes and formation of the boundary layer in between them.

For the purpose of comparison, time in simulations is normalized to the inverse of gyro-frequency, while real time is in nanoseconds. The typical magnitude of the magnetic field generated by metal target irradiated by kilo-Joule laser pulse, is about 200T. The associated proton gyro-frequency is 3 GHz. The typical pulse duration is equal to the typical time of observation and about 5 ns. To simulate the whole experiment with hybrid code, we need to achieve a maximum time of 3GHz$\times$ 5 ns = 15 ion gyro periods. For time step equal 10^{-3}, the total number of steps is 1.5×10^4, which is achievable by modern computers.

4.1.3 Righi-Leduc and Nernst effects

The Nernst effect is the advection of the magnetic fields at the Nernst velocity $\mathbf{v}_N$ Eq. 2.25. Kho and Haines[KH85] have introduced the form of the fluid equations in the collisional case, and showed that a velocity term arise in the electron momentum equation, resulting

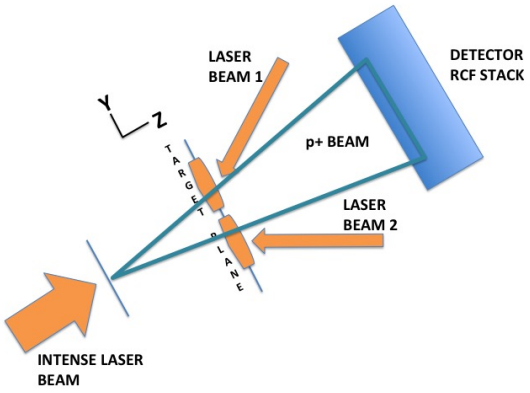

(a)

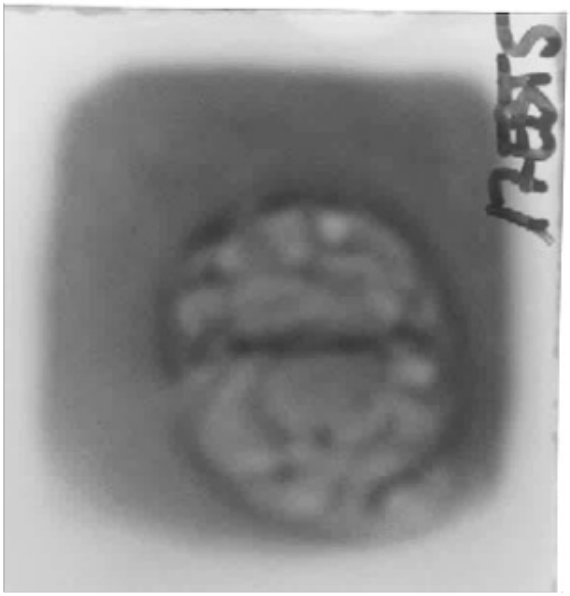

(b)

Figure 4.2: (a) proton radiography setup (b) Film obtained at LULI2000 in 2017 from a reconnection experiment (courtesy of S. Bolaños).

from the structure of the heat flux. The physics behind this advection is that the magnetic field tends to be frozen more to the hotter electrons, which are less collisional and responsible for the heat flux, than to the colder and more collisional electrons through which the magnetic field can more easily diffuse [Hai86]. As consequence the heat flux in magnetized plasmas is non local, as mean free path of the hot electrons being responsible for the heat-carrying, is greater than the electron temperature gradient length [LAB+14].

Another questions is the way to calculate electron heat flux $\mathbf{q_e}$ in magnetized plasmas Eq. 2.22. The non-symmetry of the conductivity tensor is a consequence of the presence of the magnetic fields, known as the Righi-Leduc effect. It results in the rotation of the heat flux vector in the $\mathbf{b} \times \nabla T_e$ direction, without changing its absolute value.

The study of magnetic fields in plasmas is directly connected to the electron heat transport, which in laser produced plasmas is commonly nonlocal. In magnetized plasmas, the linearized Spitzer-Harm theory [SH53] breaks down because of the long mean free path of high velocity electrons compared to the temperature gradient scale length [LAB+14]. Hence, the non classical heat flux modifies the Nernst velocity, which results in magnetic field advection and compression by the heat flow down a temperature gradient, i.e., towards denser and colder regions [NYH+84]. Finally, it influences the magnetic fields evolution [KH85, LMB85] while the magnetic field acts back on electron transport by reducing the mobility of heat-carrying electrons. Through the Righi-Leduc effect, magnetic field influences the electrons dynamics in the direction orthogonal to both the magnetic fields and to the electron temperature gradient, causing a bending of the heat

flux [RKT08].

Unfortunately, both Nernst and Righi-Leduc effects can not be considered in two-dimensional simulations as the electron heat flux is mainly in the axial direction. For the work presented in this thesis, we have decided to account for the magnetic field as an initial condition, as it has already been done in [FBG11, FBG12]. To date, there is (to our knowledge) only one Vlasov simulation of magnetic reconnection including the Nernst velocity[JRKT16], which concluded to a significant contribution of the Nernst velocity to the reconnection electric field. While these effects need to be considered in three-dimensional simulations, we omit them. In the next section we focus on the results of hydro-radiative simulations to quantitatively describe the structure of each magnetic bubble prior their reconnection.

4.1.4 Results from hydro-radiative simulations

The magnetic field is generated near the electron ablation front because of Biermann-Battery effect, resulting from the nonparallel gradients of electron density and temperature. For a correct description of the diffusion of magnetic field through the dense part of the plasma in direction of the target, one needs to take into account the electron heat flux. The resulting magnetic field is trapped between the solid target and the electron ablation front. In this section we overview results obtained with hydro-radiative simulations using code FCI2, and justify this choice.

FCI2 is a 2D axi-symmetrical (R-Z cylindrical geometry), arbitrary Lagrangian-Eulerian, two-temperature hydro-radiative code [DSM$^+$01] using different heat transport models. The code takes into account the Nernst and Righi-Leduc effects; the Nernst velocity is calculated using Eq. 2.25, where the electron heat flux is written in a nonlocal formalism [NFS06].

We used the FCI2 simulation to set initial condition for the hybrid simulations. This numerical work is intended to help the interpretation of LMJ experiment performed in May 2019. The experimental results are discussed in section 4.5.3. We consider a gold foil of 5 μm thickness irradiated by a 5 nanosecond laser pulse carrying 10kJ on a focal spot of diameter 800 μm, with an incident angle of 40^o. Fig. 4.3 displays the magnetic field and plasma density extracted from FCI2 simulations at $t = 2$ ns. The solid target is at the bottom and the laser pulse moves in the Z direction from the top. In the work we call L_R the radius of plasma bubble, and use it for density initialization. We call L_W the half width of magnetic shells around the bubble, and use it to define the boundaries of the shells. The magnetic ribbon is limited by the black dashed lines ($L_R - L_W$ and $L_R + L_W$) in Fig. 4.3a and Fig. 4.3b. The edge of a ribbon is defined as the location where the maximum of the magnetic field is divided by e. The values of L_R and L_W depend on the laser energy deposition, larger intensities of laser pulse giving wider bubbles. Fig. 4.3c displays a lineout in the radial direction (along white line on Fig. 4.3a) for simulation

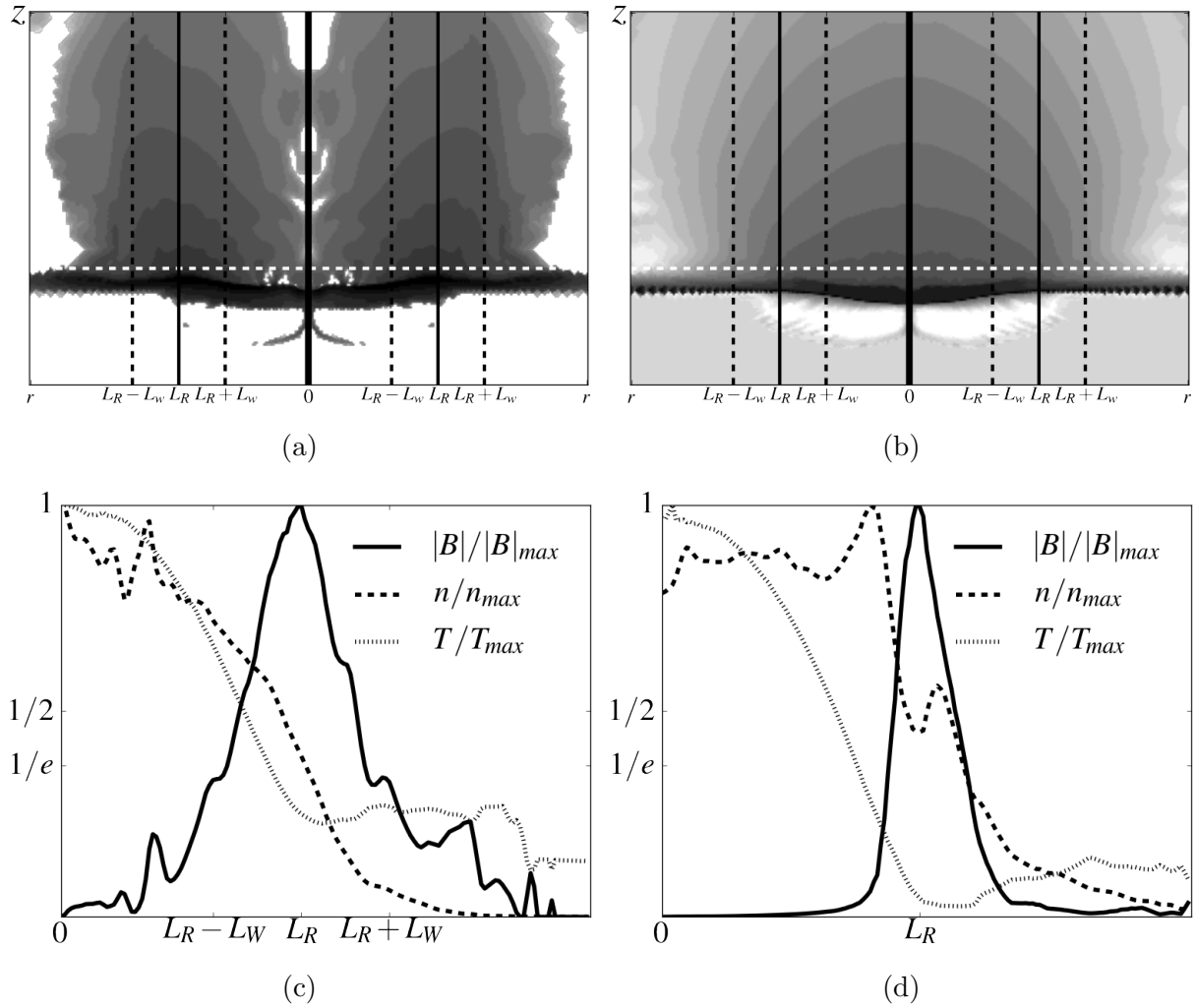

Figure 4.3: FCI2 simulations: (a) magnetic field, and (b) plasma density at $t = 2$ ns, both normalized to the initial maximum value. The grayscale range from 0 (white) to 1 (black). line out along the white dashed line (c) at $t = 2$ ns, (d) at $t = 3$ ns of the magnetic field (solid), plasma density (dashed) and electron temperature (dash-dot).

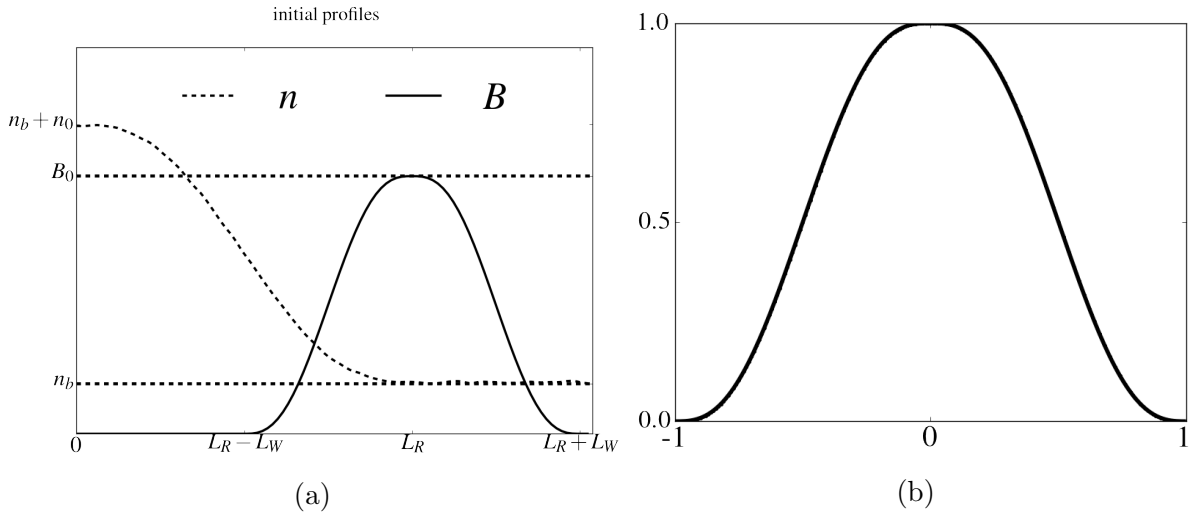

Figure 4.4: (a) Initial plasma density and magnetic field lineouts in the radial direction, the origin being at the center of the bubble. (b) Profile of the fifth order polynomial given by Eq. 4.3.

results of FCI2 at $t = 2$ ns, all quantities being normalized to their maximum value. The mean radius of the plasma bubble is comparable with the focal spot size. From the FCI2 simulation associated with the realistic case of the LMJ experiment, the asymptotic magnetic field, electron density and electron temperature are $B_{max} = 600$ T, $n_{max} = 2 \times 10^{28}$ m^{-3}, and $T_{max} = 400$ eV. The global picture is the following: electron temperature decreases in radial direction, as well as plasma density, while magnetic field increases forming magnetic shells. Fig. 4.3d displays the same along white dashed line at $t = 3$ ns; the magnetic field profile is compressed and has a sharp gradient at its front.

4.1.5 Initial analytical profiles

The initial state for the hybrid simulations is chosen according to the results of FCI2. The HECKLE code is three-dimensional, but such simulations are costly from the computational point of view. In the work, as already mentioned, we focus on two-dimensional reconnection where self-generated magnetic field can not be taken into account. The magnetic field is given as an initial condition, corresponding to the moment of the experiments, where the magnetic fields have been already generated, but before the bubbles have begun to interact. Hence, the two magnetic bubbles move one toward the other, meaning the current sheet associated with the field reversal is building up. The goal of such simulations is to focus on this dynamics and clarify the causes and the consequences for fast reconnection.

In such configuration the inflow velocity depends on the initial thermal pressure of the

bubbles, rather than on magnetic pressure of the surrounding media like in Harris sheet. In such topology great difference from the Harris sheet case is that the initial maximum of the electron density is at the middle of the sheet in the Harris-type configuration, while in colliding bubbles the maximum is out of the sheet (in the inner part of the magnetic ribbons). As the gradient pressure term significantly contributes to the electric field, the dynamics of the reconnection process should be quite different for these two topologies.

Fig.4.4a provides the initial plasma density n and magnetic field $\mathbf{B}$ profiles in the radial direction. We remind L_R the mean radius of each shell and L_W the half width of each magnetic shell. The initial density is $n_b + n_p$, where n_b a constant background density, and n_p the density profile in the shell. As for the Harris sheet the background population is important to get rid of the divergence of the Ohm's law terms proportional to the inverse of the electron density.

To analytically describe the density and magnetic field profile, we define the fifth order polynomial

$$P(x) = -6|x|^5 + 15|x|^4 - 10|x|^3 + 1 \tag{4.3}$$

To satisfy the following conditions: $P(0) = 1$, $P(\pm 1) = 0$, $P'(0) = P'(\pm 1) = 0$. Fig.4.4b displays this polynomial. The density profile in the shell is

$$n_s(r) = n_b + n_0 P\left(\frac{r}{L_R}\right) \tag{4.4}$$

and the magnetic field profile is

$$B(r) = \mathbf{B}_0 P\left(\frac{|L_R - r|}{L_W}\right) \tag{4.5}$$

The profile is smooth enough to satisfy divergence-free condition for the magnetic field with a better accuracy than using the trigonometric functions for initialization, as previously (see [FBG11]).

4.1.6 Initial setup for bubbles

This section describes the simulations, we performed, for the reconnection between HED plasma bubbles. The motivation is to understand what do we need to simulate realistic or close to realistic laser-plasma experiment. There are five main differences with reconnection in a Harris sheet :

- the current sheet in a Harris configuration is stationary, while for colliding bubbles it is building up through time
- reconnection is not driven in a Harris sheet, while in colliding bubbles the super-Alfvénic expanding velocity of the bubbles is a term forcing the reconnection

- the initial amount of magnetic flux in colliding bubbles is finite
- the plasma β (ratio between kinetic to magnetic pressure) is higher in colliding bubbles than in a Harris sheet[1]
- the density gradient is initially toward the center of the Harris sheet, while it is toward the center of plasma bubbles

The plasma β parameter is a dimensionless parameter characterizing magnetization of the plasma. It is defined as the ratio between kinetic and magnetic pressure:

$$\beta = 2\mu_0 P/B^2 \tag{4.6}$$

depending on the pressure of the particles. This pressure writes

$$P = nmv^2 \tag{4.7}$$

In Eq. (4.7) the velocity can be either thermal, usually called thermal pressure, or associated with the bulk flow, called ram pressure. For the sake of clarity we call kinetic pressure the sum of these two terms. In this chapter we use two particle populations: the main proton population which populates the inner of the plasma bubbles with index 1, and a background population with index 2, initially distributed uniformly all over the computational domain. We keep index 0 for the electron population. Such background population, while not physical, is widely encountered in numerical simulations of such topologies. In fact, it is mandatory because if not considered, the asymptotic null density value far from the bubbles make diverge the electric field given by the Ohm's law, Eq.(2.8). We also need to initialize the electrons which have to satisfy the quasineutrality condition. The β_i for $i = 0$, 1 and 2 are defined at the center of bubble, where the density is maximum for electrons, main and background population, respectively.

In the following four sections we present a parametric study of reconnection triggered by the collision of two bubbles. In the previous chapter we use a single point reconnection in Harris sheet configuration, and a normalized reconnection rate as a quantitative measure of the process for comparison. In a Harris sheet the magnetic pressure in the lobes is rather constant through time, as the amount of magnetic flux in the lobe is large compared to the reconnected one. As the plasma is frozen-in in the lobes, the plasma density in the lobes is also quite constant. To calculate reconnection rates comparable between different plasma parameters, the out-of-plane electric field is normalized to the upstream magnetic field multiplied by the upstream Alfvén speed. While being stationary in a Harris sheet, both the magnetic field and density fluctuate at a given point in the bubble colliding case.

The plasma bubbles dynamically expand because of the high initial thermal pressure resulting in a strong pressure-imbalance. As a result, the initial width of the plasma

[1] in Harris sheet, the pressure is totally kinetic in the middle of the sheet, and totally magnetic far from the sheet. As a result, the β parameter is infinite in the middle of the sheet and null far from it. In this peculiar case, we call β the ratio between the maximum kinetic pressure in the sheet and the maximum magnetic pressure far from the sheet.

shells rapidly decreases during the compression phase [FBG11] associated with a strong magnetic pile-up. The plasma flow, crossing the X-point during the reconnection, has its maximum at the beginning of simulation and decreases in time, as hot particles quickly leave the bubbles. As result it is difficult to choose a stationary point where we can pick a density and magnetic field appropriate for normalization, since both can significantly fluctuate at this point. Instead of a normalized reconnection rate, we are going to compare non normalized out-of-plane electric field at X point, as it is the only common characteristic given by the same Ohm's law (Eq. 2.8) for all the simulations, we performed. To collide bubbles we need to define the position of the bubbles, whether the outer boundaries of magnetic shells are close or far to each other. We also need to consider or not an initial expansion velocity. From FCI2 simulations we know that electron temperature is not uniform, and thermalization between protons and electrons is effective because of collisions. Hence, it is more preferable to put the same initial temperature for protons and electrons, even if we investigate parametric cases to identify the role of the different populations temperature. We also have to keep a uniform electron temperature profile even out of the spots in the isothermal case. If not, any initially imposed temperature gradient will be kept as is during the simulation.

Simulation domain

For the following discussion we chose the bubble size according to the scaled FCI2 simulations, $L_R = 15$ and $L_W = 5$. As in the FCI2 simulation the cold target is used providing a high level of ionization, and as consequence greater inertia lengths. The simulation domain is a rectangular with length $L_X = 80d_0$ and width $L_Y = 120d_0$ to fit both bubbles. The computational domain contains two full-bubbles, one centered at $(L_X/2, L_Y/3)$, and another at $(L_X/2, 2L_Y/3)$. We use a 400×600 grid, the mesh resolution equals 0.2 in both directions. We use fully-periodic boundary conditions. As hot particles can quickly reach the boundaries, we use an extended (up to $L_X = 120d_0$) simulation box with 600×600 grid mesh. The time-step is 10^{-3} to satisfy the CFL conditions for the fastest whistler modes. We have 1.5×10^7 macro particles for the main population of protons and 1.5×10^7 for the background protons, which corresponds on average to 125 particles per cell, being large enough to prevent numerical growth of the electric field because of terms proportional to $1/n$ at the grid scale.

Bubbles shape

In contrast to FCI2, we do not simulate the laser energy deposition into the plasma, as consequence the expansion of the bubbles is defined by an initial thermal pressure. Bubbles should be close enough to spend major part of its initial energy to compression of magnetic ribbons, rather than to expansion and transporting of magnetic field to the middle of simulation box. We put bubbles in close proximity to start reconnection, such configuration helps to skip the phase of expansion of magnetic shells through the decelerating background media. In this work, as already introduced, we use three particle populations: electron fluid tagged 0, *main* proton population tagged 1 filling the bubbles plasma, and *background* population tagged 2 distributed uniformly all over the computational domain. Fig. 4.5 displays the initial main proton population density n_1

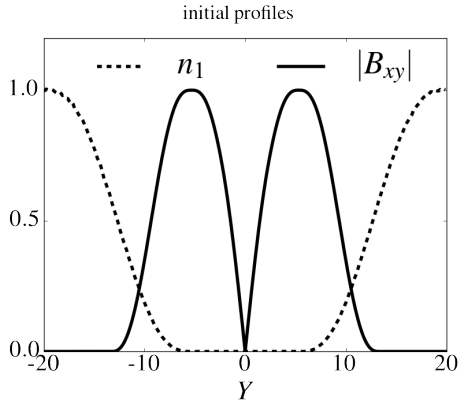

Figure 4.5: Initial proton density and modulus of magnetic field lineout over the spot centers for run with two bubbles initially close.

and modulus of magnetic field **B**. Background proton population density n_2 equals 0.2, we use charge equal 2 to artificially increase electron density, it helps to stabilize Ohm's law terms proportional to $1/n$. We modify mass for the background population to increase the inertial effects and make a contrast difference from the low background density simulations (section 4.3.6). To be closer to vacuum laser experiments it would be a better idea to get a smaller mass, while for interstellar media we could use increased mass and charge.

Initial pressure imbalance

Depending on the initial main population, an important thermal pressure gradient arises toward the center of the bubbles, making the bubbles expand. The same holds for the electron population, as their density gradient is the same (the background population plays nominal role in the pressure imbalance). In addition, there is also a magnetic pressure in the middle of the magnetic ribbon pushing out of it. These two pressure terms will have the same consequences on the plasma, i.e. make it expand out of the bubble. The case of the ram pressure is discussed later, while physically important, this term is quite hard to consider from the numerical point of view (since any initial bulk velocity rapidly vanishes). The initial electron temperature T_0 partly controls the initial in-plane electric field through divergence of pressure in Ohm's law (Eq. 2.8). Furthermore, the background temperature T_2 regulates the pressure equilibrium between bubbles and surrounding media. If the background pressure exceeds the main pressure in the bubble, namely $n_2 k_B T_2 > n_1 k_B T_1$, there is no expansion, as background particles press the bubbles, and reconnection is quenched. Proton temperature T_1 also tunes the Larmor radius; if the particle Larmor radius exceeds the width of the magnetic ribbon (initially 2 L_W), the particles can escape from the inner of the bubble. It has to be also noted when the magnetic ribbons are compressed, the increase of the magnetic field makes the Larmor radius decrease.

Closure for the electron fluid

Run tag	β_0	β_1	β_2
A	0.08	4	0.04
B	0.08	40	0.04
C	0.08	100	0.04

Table 4.1: Definition of the tags used for runs A, B, C.

In the following section we use the isothermal closure equation for the electron fluid (Eq. 2.9). This is because as a first study, we don't want to be bothered with eventual biases of electron pressure treatment. Full electron pressure tensor is considered in a second step, at the end of this chapter. In the isothermal case the pressure divergence term in Ohm's law depends only on electron density, since there are no temperature gradients. A restrictive approximation of the isothermal model is in the same temperature, which has to be applied to electrons all over the simulation box. At the same time there are no physical reasons for the same temperature of background electrons and electrons in the bubbles. From transport theory we know that the gradient of a physical quantity is associated with a flux decreasing this gradient. As a consequence of the isothermal closure the initial electron temperature is kept constant until the end of the simulation, whatever the electrons are close to the hot center of bubble.

4.2 Role of the ions temperature

We focus in this section on the role of the temperature of ions populations (treated as particles) for the reconnection process, as was introduced the *main* and the *background* populations. We start with a parametric study for three different values of the main population temperature in the first sections, the case of the background population being treated in the last one. To clear the picture, both the background and electron temperatures are cold and kept constant from run to run. By cold, we mean $T_0 = T_2 = 0.1$. The associated β values are given in Tab. 4.1.

The initial temperature of the main proton population T_1 is a free parameter. These initial proton temperatures have been chosen as they are associated with peculiar dynamics of the magnetic reconnection process: $T_1 = 2$, 20 and 50, labeled as run A, B and C, respectively. The associated β values are reported in Tab. 4.1. For these runs the β_i values have to be understood as being associated with the thermal pressure of the i^{th} population. It is clear in each case the main population temperature is the main contribution to the total β value.

4.2.1 Reconnection electric field

We first focus on the time evolution of the out-of-plane electric field associated with the reconnection process, as this quantity gives insights on the dynamics of the reconnection process, discussed in section 1.2.1. Fig.4.6 displays the out-of-plane electric field component at the X point for runs A (dash-dot), B (dashed) and C (solid). The X point is identified as the saddle point of the Z component of the vector potential. To remove the small-scale fluctuations and keep the smallest peak distortion, we use a Savitzky-Golay filtering [Orf95] with a third order polynomial and a frame equals to 21, which corresponds to 4.2 Ω_0^{-1}. Such a frame removes the small scale fluctuations and preserve the gradients having a physical meaning, and are connected to onset and quenching phases of the reconnection process.

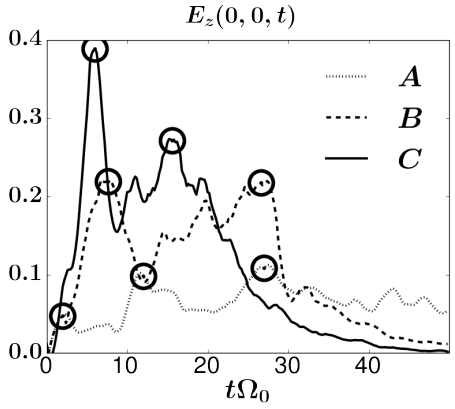

Figure 4.6: Out-of-plane electric field component at X point for cold background and electrons $T_0 = T_2 = 0.1$. Run A, B and C are displayed in dash-dot, dashed and solid line styles respectively.

In all cases the electric field grows from the beginning of the simulation. The initial setup is not associated with a kinetic equilibrium: because of the kinetic pressure inside the bubbles and the magnetic pressure in the magnetic ribbon each bubble has an expansion phase associated with the creation of a current sheet in between. As a result, the collision of these bubbles is associated with the growth of the out-of-plane electric field. For all cases we indicated the local maximum of E_z by open circles. For run A ($\beta_1 = 4$), the electric field oscillates around 0.05 until the end of simulation. This means that at the end ($t = 50$) a fraction of the magnetic flux initially embedded in the two bubbles is not yet reconnected. For run B ($\beta_1 = 40$) E_z oscillates between 0.1 and 0.2 for $5 < t < 30$, and reconnection is almost finished at $t = 30$. For run C ($\beta_1 = 100$) the reconnection process takes less time and has a maximum value of the electric field ~ 0.4. Increasing of the initial β also leads to increasing of the out-of-plane electric field and decreasing the time required for the two bubbles fully reconnect.

For run A the nature of the first peak is not yet clear, as the associated electric field vanishes, the reconnection process is not clearly established. For all cases one can observe

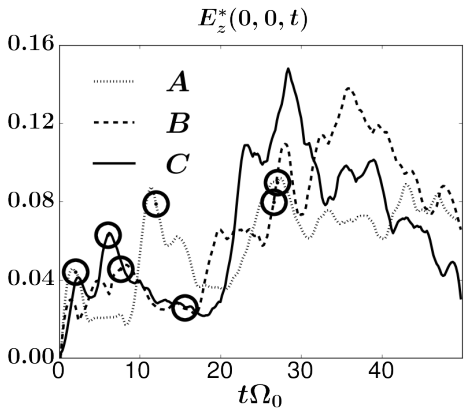

Figure 4.7: Out-of-plane electric field component at X point normalized on maximum magnetic field and minimum density in inflow direction. Run A, B and C are displayed in dash-dot, dashed and solid line styles respectively.

at least two peaks on the electric field. These two peaks have already been reported in hybrid simulations [SAB$^+$14], while their origin remain unclear. The energy needed to let the plasma flow through the reconnection region is provided by the magnetic tension of the magnetic field lines. But this flow is limited by the inertia of the plasma either because of the plasma density or because of the ion mass. Hence, the larger inertia means the smaller outflow, meaning the smaller inflow, as consequence smaller reconnection rate. At the onset of the reconnection process, there are no plasma of the main population outward of the reconnection region, meaning the plasma inertia is small. The same holds at the end of the reconnection process, but upstream of the reconnection region. While not demonstrated, we conjecture that these two peaks are associated with the weak inertia of the plasma prior and after the reconnection.

To make a connection to the steady state reconnection and try to get a "universal" value characterizing the reconnection process, free of the local values of the plasma parameters, we normalize the out-of-plane electric field to the product of the asymptotic magnetic field by the asymptotic Alfvén velocity. To do so, we use the maximum magnetic field and the minimum electron density in the inflow direction to calculate an Alfvén velocity [FBG11]. The electric field is divided by the product of this Alfvén velocity by the maximum magnetic field. As already pointed out, this normalized value of the out-of-plane electric field $E_z^\star$ is called the reconnection rate. We see in Fig. 4.7 the reconnection rate is of the order of 0.1, being pretty consistent with the steady state reconnection in Harris sheet Fig. 3.18. Circles mark times when the electric field E_z has a local maximum. We should emphasize that the first peak in E_z is smoothed-out by this normalization, while the second one can be amplified. While this definition is well-suited in a Harris sheet where the upstream magnetic field and Alfvén velocity are quite stationary, it is not appropriate for colliding bubbles, as at the end of the bubble collision, the upstream magnetic field and electron density are vanishing, the associated Alfvén velocity is asymptotically meaningless. As a consequence, it seems more relevant to keep the raw

value of the electric field to discuss the reconnection process in bubbles collision.

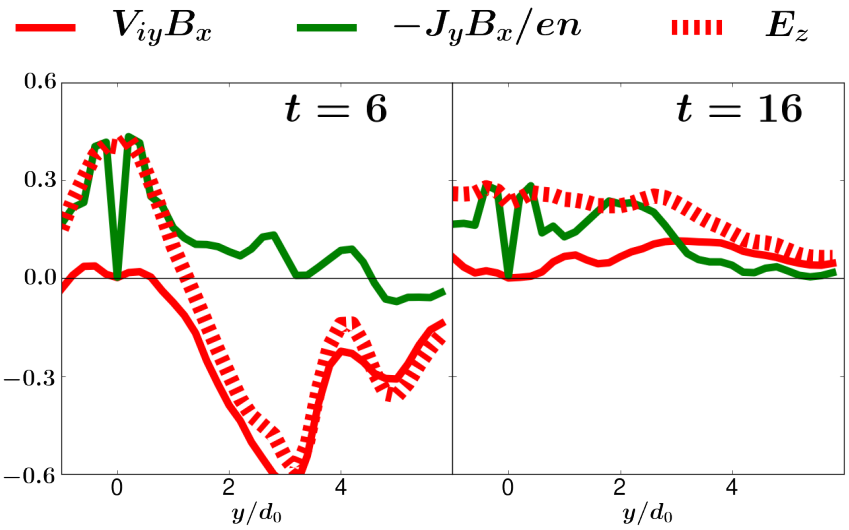

Figure 4.8: Lineout of the Ohm's law terms of the out-of-plane electric field E_z through the X point for run C ($\beta_1 = 100$).

To explain the origin of the two peaks of the out-of-plane electric field, we focus on the highest β case, namely run C. The local values at the X point of the Z component of the electric field are 0.4 and 0.3, at $t = 6$ and 16, respectively. Fig. 4.8 is a lineout of each terms in the Ohm's law. In the first peak, associated with the compression phase, the electric field is defined by the Hall term in the vicinity of the X point, mainly because of the $-J_yB_x/en$ term (B_y being negligible). This is a clear consequence of the development of the out-of-plane magnetic field as in the two-dimensional case, $\mu_0 J_y = -\partial_x B_z$. Farther from the X point, in the inflow direction $1 < y < 4$, the ideal term $V_{iy}B_x$ prevails. Magnetic field component B_x around X point is positive for $y > 0$ (upper bubble) and negative for $y < 0$ (lower bubble), the ideal term at $t = 6$ shows that total fluid ion velocity V_{iy} is directed outward the X-point. It means there is a particle flow outward from the X-point, which is the opposite of what we observe during reconnection. The origin of this plasma flow is the demagnetization of the particles escaping from the opposite bubble by finite Larmor radius effects and streaming in a ballistic way. The resulting profile of E_z is quite unusual, as it is not constant across the reconnection region, as expected in stationary reconnection. This questions the nature of the process we observe.

For the second peak of the electric field the Hall term in the vicinity of X point dominates, as generally observed in fast reconnection. It is so, because in the ion diffusion region ions are demagnetized, while electrons are not, resulting in a strong current. The second peak is coherent with the classical picture of fast reconnection: the electric field is pretty constant, mainly due to the ideal term in the MHD region, driven by the Hall term in the ion diffusion region, and supported by anomalous viscosity in the electron diffusion region. For run A and B the picture is similar. As a conclusion of this paragraph, while the second peak can be explained by the classical fast reconnection process, the first one

is not, and the role of demagnetized particles is important. As demagnetization decreases with temperature, this effect is lowered for run A and B.

4.2.2 Density structure

In this subsection we focus on the time evolution of the density structure of a bubble during its collision with the other one. To do so, we use the way presented in section 1.3.1 : a color code picture with the time on the abscissa-axis and the X or Y coordinate on the ordinate-axis. It is a two-dimensional generalization of a lineout at a given X or Y position including its time evolution. As a first example, Fig. 4.9 displays the electron density depending on the Y coordinate and time t, at $X = 0$.

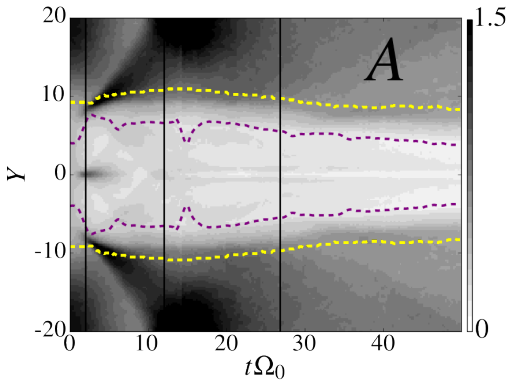

Figure 4.9: Lineout of electron density through spots centers in time for run A (Table. 4.1). Yellow line represents the inner border of magnetic shells. Magenta line represents position of the maximum magnetic field inside the ribbons.

One remember that by quasineutrality the electron density equals to total ion density, i.e. the main population (n_1) plus the background population(n_2). The lineout through the X point along Y shows what happens in the inflow direction. The yellow line represents the inner border of magnetic shells and the magenta line represents the position of the maximum of the magnetic field inside the ribbons. There are several features to note:

i a redistribution of the density inside the magnetic bubble from $t = 0$ to 10

ii an increase of the density at $t = 3$ at the inner edge of magnetic ribbons

iii the filling of the inner of bubbles at $t = 10$, followed by a gentle and gradual emptying

iv an increase of the density in mid-plane for $2 < t < 8$

The first feature is a decrease of the density inside the magnetic bubble from $t = 0$ to 10, connected to the decreasing of the initial density gradient because of particles

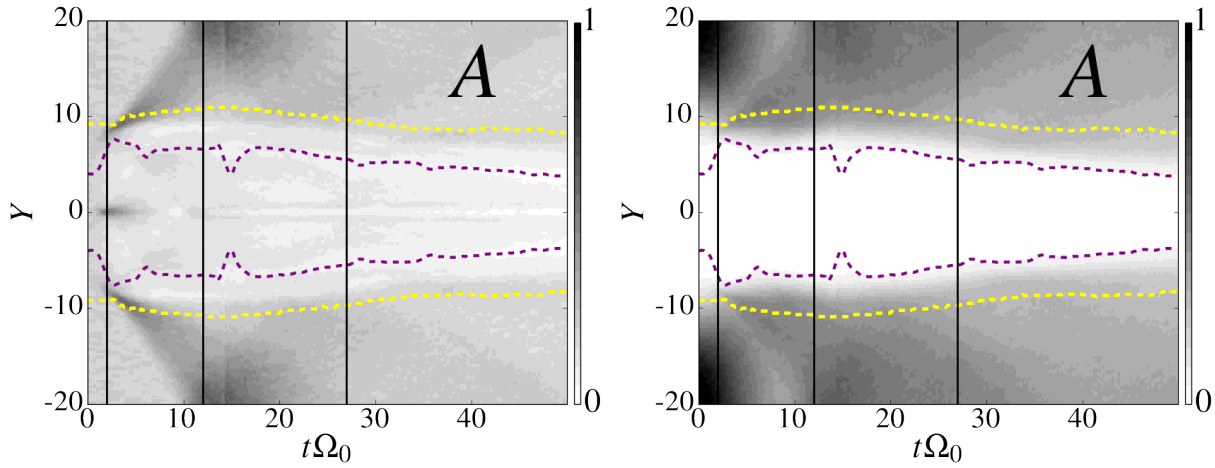

(a) (b)

Figure 4.10: Lineout of the (a) background n_2 and (b) main protons density n_1 through spot centers $X = 0$ in time for run A (Table. 4.1). Yellow line represents inner border of magnetic shells. Magenta line represents position of maximum magnetic field inside the ribbons. Vertical lines show time instants at which local maximum of electric field is reached.

escaping out of the dense center. The particles rush to the inner border of the shells, where magnetic shell reacts in the following manner: hotter particles having greater velocities penetrate deeper inside the shell and become magnetized, while warm particles having smaller velocities are deflected by magnetic wall and go back to the center staying demagnetized. Which contributes to the second feature, an increase of the density at $t = 3$ at the inner edge of the magnetic ribbon.

The third feature is a filling of the interior of the bubble at $t = 10$, followed by a gentle and gradual emptying. The distribution of the main population in the bubble gets homogeneous because the electric field (defined by the Ohm's law), and decreases the pressure gradient (temperature of the main population being quite constant). When reconnection is occurring, the particles of the main population are leaving the bubbles and going through the reconnection site in the outflow direction. That leads to decreasing of the density inside the bubbles and the motion of the inner border of the magnetic shells toward the mid-plan.

The source of the fourth feature is the background population. Fig. 4.10a displays the background density n_2. The cold background is expelled by magnetic pressure out of the shell and accumulates in front of the shell. The snowplowing of the background gas at the leading edge is a typical effect for expansion of laser-generated plumes into low-pressure ambient gas, and called *snowplow effect* [LCD$^+$96, WCL$^+$97]. Fig. 4.10b displays the main proton population density n_1. Hot particles of the main proton population from the center are accumulated close to the inner border of the magnetic shell. While the hottest part diffuses into the shell and become magnetized, we see an increase of the density

between inner border and the maximum of the magnetic field for $t > 3$. But the major warm part is reflected and we observe the back motion of the density to the center of the bubble.

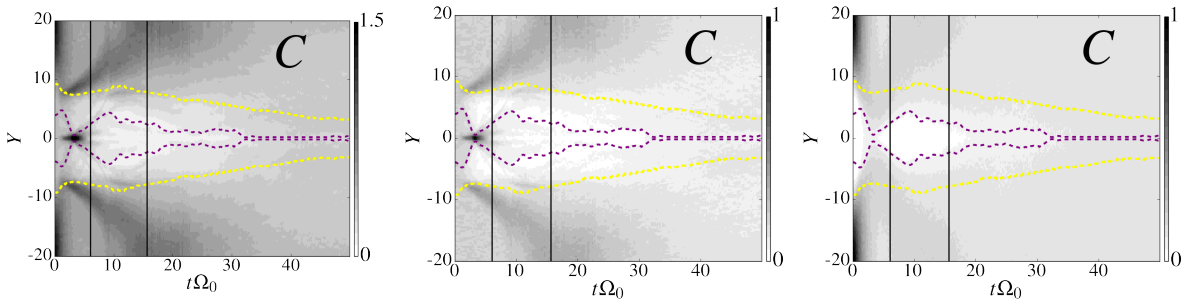

(a) (b) (c)

Figure 4.11: Same display (a) as Fig. 4.9, (b) as Fig. 4.10a, (c) as Fig. 4.10b for run C ($\beta = 100$).

To point out the differences and similarities for the highest β case, Fig. 4.11 displays densities in inflow direction for run C (Table. 4.1). Panels a, b and c display the density of the electrons, main and background populations, respectively. The increase of density in the mid-plane for t < 8 is still observable, but in contrast to run A, it is synchronized with the strong compression of the magnetic shells. In the case of run C stronger compression is associated with the higher thermal pressure of the main population and the dense structure at the mid-plane is also associated with the background population. Hence, whatever the β value, background population slows down the reconnection process because of its inertia and the snowplow effect.

To examine the ouflow, Fig. 4.12 depicts the background (n_2) and the main population (n_1) density in the X direction for run A. The first maximum of the electric field is associated with the expelling of the background population and its expansion in the X directions. Also at that time a dense plasmoid originates around $X = 0$, and moves in the cavity of low density in the $-X$ direction. At the time of the second peak of the reconnection electric field, we observe a second expelling of the background population out of the reconnection site. These two density structures for the background population clearly demonstrate the effect of this population; once the plasma is expelled out from the bubbles by compression for the first structure and by magnetic reconnection for the second structure, the background population has also to be removed as they are frozen in the convecting magnetic flux tubes.

Another important feature of the outflow direction is the generation of plasmoid, that looks like a dense filament with size of the order of ion inertia length d_0. This dense structure is located at the O point, which is the region of closed field lines in a plasmoid, surrounded on each of its sides by an X point. While the density is minimal at X points, it is maximal at O points. One bright plasmoid is born in the beginning, and connected to the existence of background population. This plasmoid moves accelerating in the -X

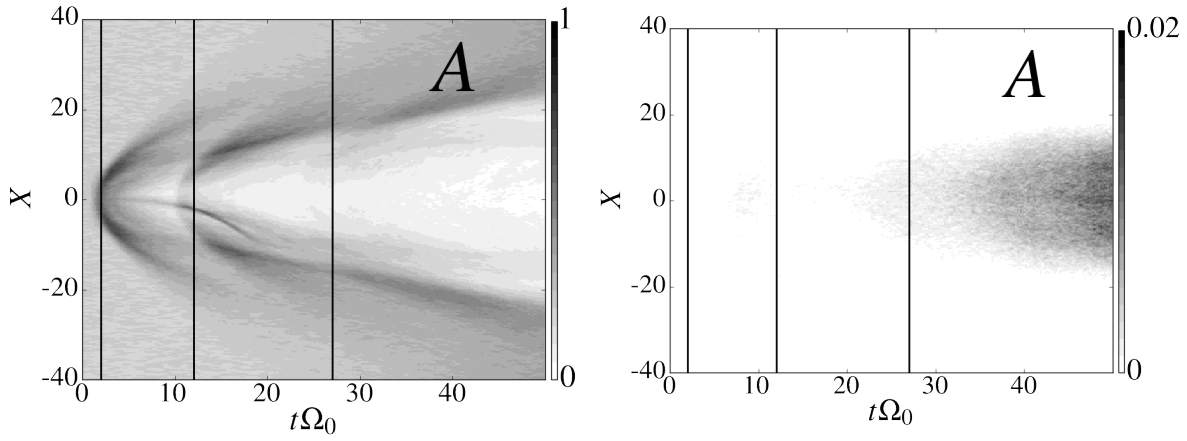

Figure 4.12: Lineout of the background density n_2 (a) and the main density n_1 (b) through the mid-plane $Y = 0$, depending on time for run A.

direction and reaches the bulge of plasma at t $\sim$ 20. To summarize the four important features in the outflow direction:

(i) initial increase of the background density between the two bubbles and its transportation along the X direction

(ii) dense plasmoid formation at $t = 2$ associated with the increase of background density in the mid-plan

(iii) low density cavity resulting from the background remove for $2 < t < 10$

(iv) outflow of the main population density for $t > 25$

Fig. 4.13 displays the same as Fig. 4.12 for run C. Similarly to run A we observe a dense front expansion for the background particles, but in contrast to run A the hottest part of the main population can easily cross the shells. At the time of the first peak on the electric field (see Fig. 4.6, $t = 6$), demagnetized protons from the main population reach the edge of the boundaries in X direction, meaning their velocity is larger than 6 V_A. The main protons population outflow increases after the first peak, the velocity is about 2 V_A, and after the second peak the flow is slowed down by the background population. While we can observe 2 clear archs on the density for run A, they can be hardly seen for run C. In facts, these two archs can also be observed for run B, but they are closer in time, because the reconnection is faster. For run C the two archs are so close that they are mingled. Similarly to run A one dense plasmoid originates initially in the mid-plane and moves in $X > 0$ direction. Fig. 4.13a shows that source of the plasmoid is the background population simulated because of numerical reasons. The plasmoid travels accelerating up to $2V_A$.

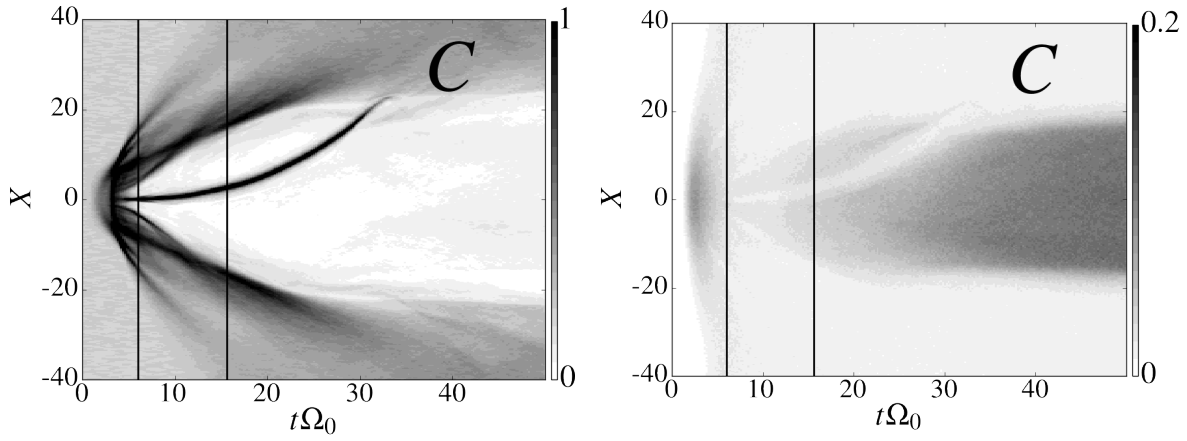

(a) (b)

Figure 4.13: (a) Lineout of the (a) background n_2 and (b) protons density n_1 through the mid-plane Y=0 in time for run C(Table. 4.1)

For run B the global picture is similar to run C, both represent the case of driven reconnection, i.e. reconnection driven by a forcing term resulting from the strong compression of the two magnetic bubbles by pressure imbalance. On the opposite, for run A the initial thermal pressure is not enough to strongly compress the bubbles. For all the cases during the pile-up phase, i.e. compression of the magnetic field, a plasmoid can grow as a consequence of the presence of background population. Generally we observe two main stages:

i onset of the reconnection: background accumulation and expelling out of the reconnection site, while only hot particles of the main population escape from the bubble centers

ii during the reconnection: increase of the main population exhaust out of the bubbles

4.2.3 Magnetic structure

We describe in this section the time evolution of the magnetic field during the collision of the two bubbles. Our first motivation is to understand how the magnetic field initially enclosed in each magnetic ribbon evolve, prior to the reconnection process, at the onset and during the reconnection process. A first insight was given in Fig. 4.9 where the inner boundaries of each ribbons are displayed. We can deduce the width of these ribbons: using the same threshold value of 10^{-2} as for Fig. 4.9. To connect the width of the shells with the magnitude of the reconnection field, Fig. 4.14 displays the time evolution of

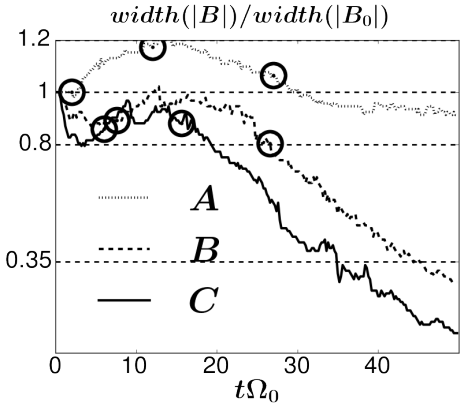

Figure 4.14: Width of magnetic shells along cross section through spot centers $X = 0$ for cold background and electrons. Run A, B and C are displayed in dash-dot, dashed and solid line styles respectively. Meaning of tags is in Table. 4.1.

the width of the magnetic ribbon in the Y direction at $X = 0$. The circles indicate the position of the peaks of E_z, as in Fig. 4.7.

For run A this width increases from $t = 0$ to $t = 12$, meaning prior the reconnection onset, the thermal pressure in each bubble is not enough to compress the two ribbons, and thin the current sheet. It suggests that the reconnecting instability does not have a threshold, or the threshold is not associated with the thickness of the current sheet. The width of the magnetic ribbons decreases as a consequence of the reconnection and the draining of the newly reconnected magnetic flux. For run B and C the magnetic shells are compressed up to 20 % of their initial width because of the higher thermal pressure associated with the larger β values. The magnetic width slightly increases before being decreased by the reconnection as for run A. At higher β values the instability also behaves apparently independently from a width threshold.

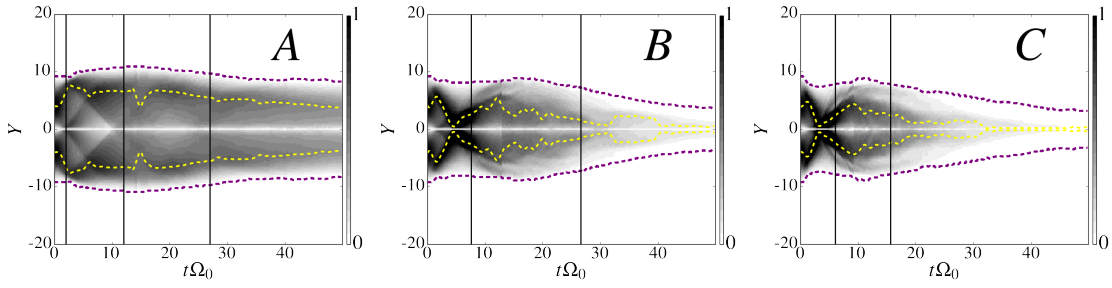

(a) (b) (c)

Figure 4.15: Lineout of modulus of magnetic field through spot centers $X = 0$ in time for cold background and electrons: run A - (a), B - (b), and C - (c). Vertical lines show positions of maximum electric field. Meaning of tags is in Table. 4.1

To look at the full picture of the distribution of magnetic field inside the shells, Fig. 4.15 portrays a lineout of the modulus of the magnetic field at the spot centers $X = 0$. For run A an interesting structure arises, which looks like beating of the magnetic field inside the magnetic ribbons. This could result from the initial pressure imbalance and the weak value of the thermal pressure unable to stem these beating. For larger β values these beatings are less pronounced and limited to the beginning of the reconnection process. Moreover, for run B and C the first peak seems to be connected to the maximum compression of the shells which is represented by the dark area close to the mid-plan. Latter on the pattern of the flow velocity in the Y direction will help to understand the beating of the magnetic field.

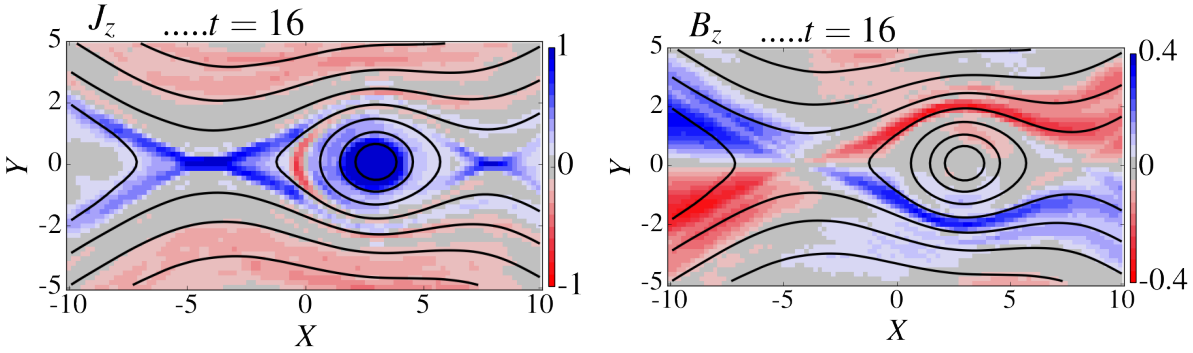

(a) (b)

Figure 4.16: (a) out-of-plane current, and (b) out-of-plane magnetic field for run C (Table. 4.1). Black lines represent the magnetic field lines.

Because of the Ampere's law the width of magnetic ribbons is connected to the out-of-plane current J_z. Fig. 4.16a shows a snapshot of the out of plane current J_z for run C at $t = 16$. The current structure has a width larger than the ion inertia length, which has a 2 Y point structure, around X = -5. While the elongation of the current sheet in the X direction is moderate, this is generally the kind of structure we observe in full-PIC simulations. But interestingly, this structure can also be observed if using the full electron pressure tensor, as in chapter 3.

Another important feature is the ejection of a plasmoid moving in $X > 0$ direction. The middle of the plasmoid, the O-point, is associated with a strong out-of-plane current. As discussed just above, the strong value of the current is colocated with the strong value of the density of the plasma confined in the plasmoid.

To demonstrate the quadrupolar structure of the out-of-plane magnetic field Fig. 4.16b portrays a snapshot of the B_z component in coordinates $X - Y$ for run C. For all cases the field appears at the collision of the bubbles, prior the onset of the stationary reconnection. This structure is observed until the end of the simulation, which is coherent with the fact that at the end t = 50 Ω_0^{-1} all the magnetic flux is not yet reconnected. At the right of the plasmoid ($X = 6$), the quadrupolar structure of the magnetic field is also observable, but with a smaller magnitude. At this point the reconnection electric field is insignificant,

essentially because the point is already moving at the Alfvén speed, as result almost no outflow can escape from it. This point has already been pointed out by [SAB+14] where the close connection between the amplitude of B_z and E_z was outlined.

As a partial conclusion, we observe driven magnetic reconnection only for run B and C. For run A the plasma is trapped in magnetic ribbon, and reconnection proceeds in non-forced manner. We mean by "forced" there exists an external force driving the reconnection. In our case, this force is clearly the strong thermal pressure inside the bubbles which is not counterbalanced neither by the magnetic pressure of the ribbon nor by the thermal pressure of the background. At larger β values the reconnection process is driven by the thermal pressure of the plasma, resulting in a speed-up of the reconnection. The current layer can also be destroyed by a plasmoid carrying an increased out-of-plane current.

4.2.4 Inflow and outflow velocity structure

We have already seen that the outflow velocity increases proportional to the initial temperature inside the bubble. In this section we inspect both the inflow and outflow velocities.

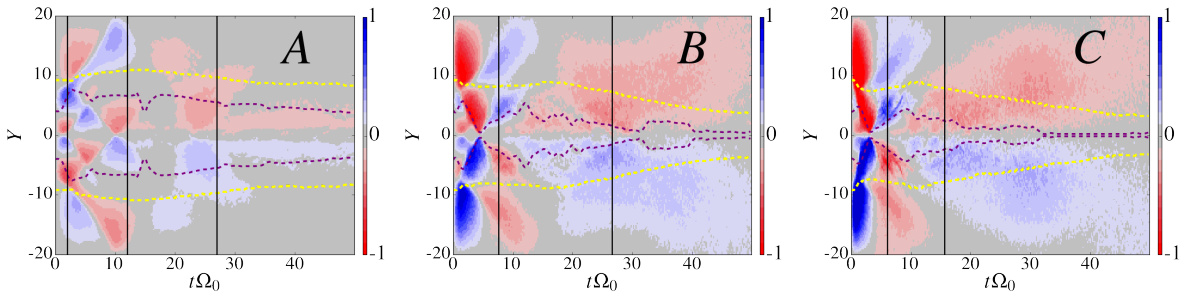

(a) (b) (c)

Figure 4.17: Lineout of the ion flow velocity in Y direction through the spot centers for run A - left panel, run B - central panel, and C - right panel. Vertical lines show positions of maximum electric field. Meaning of tags is in Table. 4.1.

Fig. 4.17a displays the ion inflow velocity in Y direction (at $X = 0$) for run A. Inside the bubbles ($10 < |Y| < 20$), the velocity is initially directed outward from the bubble. This is a clear consequence of the ballistic motion of the particles, because of their thermal motion inside the unmagnetized bubble. Inside the magnetic ribbon ($|Y| < 10$), half of flow moves inward of the bubble and the other half moves outward from it. This results from the magnetic pressure maximum at the middle of the magnetic ribbon pushing on the particles and expelling them out of the ribbon. Later in time these particles are

trapped between $Y = 0$ and the locus of the maximum of the magnetic field by magnetic confinement. Later in time, until $t = 12$, a clear flow velocity directed toward the center of each bubble rises up as a consequence of the particles escaping by finite Larmor radius effect, the ones ending up in a bubble coming from the other one. Finally, after $t = 15$, a large scale pattern of particles flowing from the inner of each bubble toward the reconnection point is clearly observable, which outlines the fact that the reconnection process is started and proceeds in a quite stationary way.

Fig. 4.17b and 4.17c displays the ion inflow velocity in the Y direction for run B and C. We see how hot fraction of demagnetized particles easily penetrate into the opposite bubble because of Larmor radius larger than the width of the shells, and create outflow directed outward the mid-plan. Such a flow is responsible for the out-of-plane electric field in the opposite direction as the reconnection one, already pointed out in Fig. 4.8. We can also see how this flow transports the maximum of magnetic field to the mid-plane for $t < 5$. Later in time ($t > 5$), this flow, in the opposite direction because of the demagnetized motion of particles coming from the other bubble, transports this magnetic field back in the other direction. For $t > 10$ we observe the formation of a stationary flow toward the mid-plane with sub Alfvén velocities. This flow having a smaller velocity stands even when magnetic reconnection is halted because of the plasma inertia (run A).

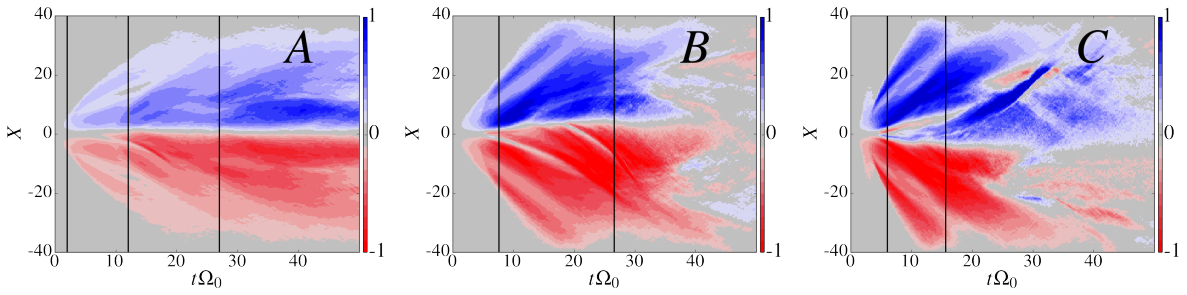

(a) (b) (c)

Figure 4.18: Lineout of the ion flow velocity in X direction for run A - (a), B - (b), and C - (c). Vertical lines show positions of maximum electric field. Meaning of tags is in Table. 4.1

Fig. 4.18 shows the outflow velocity in the X direction for run A, B and C for panels a, b and c, respectively. For run B and C we see cavities of motionless plasma travelling in both direction. For run C the local minimum of the velocity appearing around $t = 6$ at X point is associated with the density structure observed in Fig. 4.13a. The reason is quite clear : downstream of the plasmoid moving in the $+X$ direction the ejecta of plasma is at a speed comparable to the plasmoid's one, resulting in the motionless plasma. For run B the second structure appearing around $t = 20$ is associated with the second plasmoid, ejected from the X point.

From the very beginning of the simulations particles are flowing out from the bubbles, driving with them the magnetic field. A rebound can be observed at high enough value

Run tag	β_0	β_1	β_2
A′	0.2	1	4
B′	4	20	4

Table 4.2: Meaning of the four tags used for runs A′ and B′ for simulations using hot background.

of β, resulting from the counter motion of unmagnetized particles originating from the opposite bubble. Such effect off course delay the onset of reconnection. In all the cases for $t > 10$ we observe a formation of a stationary flow toward the mid-plan.

4.2.5 On the role of the background

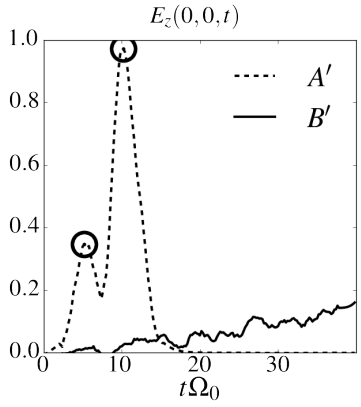

Figure 4.19: Out-of-plane electric field component at X point for simulations with hot background: (a)run A′, and (b) run B′. Meaning of tags is in Table. 4.2.

To demonstrate the importance of the background, we consider two extreme cases. We performed two simulations with hot background $T_2 = 10$ corresponding to $\beta_2 = 4$, and the same temperature for the protons and the electrons. More precisely, we have $T_0 = T_1 = 0.5$ and 10 for run A′ and B′, respectively. The associated β values are given in Tab. 4.2.

Fig. 4.19 displays the reconnection field. We observe two pronounced peaks for run B′ at $t = 5$ and 10. The reconnection process takes less than 20 gyro-periods and maximum magnitude peaks up to 1, while for run A′ the reconnection process significantly slows down. As we choose low temperature for run A′, we can compare the result with low temperature and cold background case run A, where we have observed reconnection rate oscillations around 0.1. As conclusion, just increasing the temperature of the background

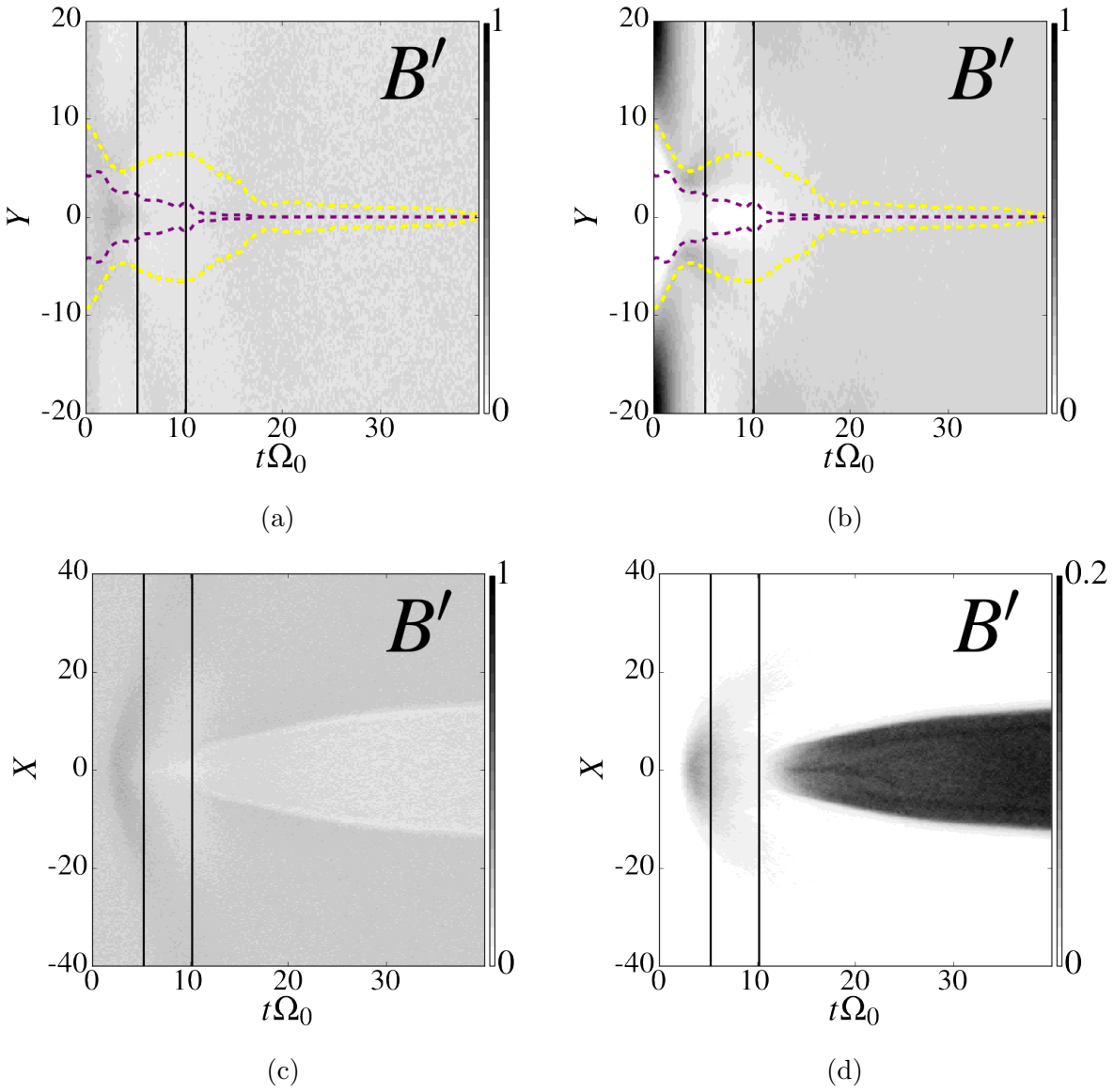

Figure 4.20: Lineout of the (a) background and (b) protons density through spot centers in time. Yellow line represents inner border of magnetic shells. Magenta line represents position of maximum magnetic field inside the ribbons. Lineout of the (c) background and (d) main protons density through mid-plane in time for run B′ (Table. 4.2).

does not affect the reconnection process, while increasing also bubbles temperature the reconnection process accordingly speeds up. We should keep in mind using the background population is unphysical and considered from the numerical point of view to prevent any divergence of the electric field in region where the density of the main population is close to zero.

Fig. 4.20 displays the background (left) and main (right) density population depending

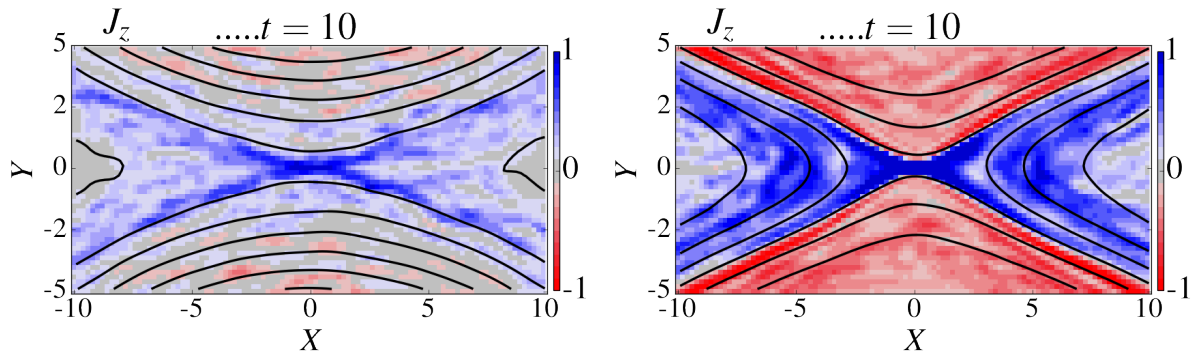

Figure 4.21: Out-of-plane current (a) run A′, and (b) run B′. Meaning of tags is in Table. 4.2.

on time and X (lower) and Y (upper) panels, for run B′. As the background population is hot, these particles are demagnetized, and their distribution neither depends on the magnetic structure nor on the stage of the reconnection process. As a result, the increase of background temperature diminishes the snowplow effect clearing up the way for outflowing jets.

To highlight the differences in the manner the reconnection process occurs, on Fig. 4.21 we show the out-of-plane current. At the comparable time the current is twice smaller in magnitude, and less compressed for run A′ than for B′. In both cases, reconnection proceeds in a single X-point, in contrast to the cold background case with elongated current sheets breaking up into plasmoids.

Hot or cold background does not significantly affect the reconnection process, as the reconnection rate still depends on the bubbles β parameter. As background is distributed uniformly all over the simulation domain, it has almost homogeneous pressure, while the bubbles pressure is the only driver of the magnetic shells compression. Hence, hot background can speed up the reconnection process only for the high β plasmas. The maximum reconnection field is 1 for run B′ ($\beta_1 = 20$), the reconnection proceeds in a single X point without plasmoids formation.

4.3 Physics of the electron fluid

While we investigated in the previous section the role of main population temperature, the temperature of the electron fluid also plays a role in the dynamics of the bubbles collision. Reminding that the electron temperature appears in the Ohm's law, it means the larger T_e, the larger electric field associated with the density gradients for the isothermal closure. The case of the full pressure tensor is treated at the end of this section.

Run tag	β_0	β_1	β_2
A″	0.08	2	0.04
B″	8	20	0.04
C″	16	40	0.04

Table 4.3: β values for each population for the runs tagged A″, B″ and C″.

As in the previous section we keep the background temperature constant, with $T_2 = 0.1$, and the same temperature for the main population and electrons. We have three runs with $T_0 = T_1 = 1$, 10 and 20 for runs tagged A″, B″ and C″, respectively. The associated β values are provided in Table. 4.3.

4.3.1 Time evolution of E_z

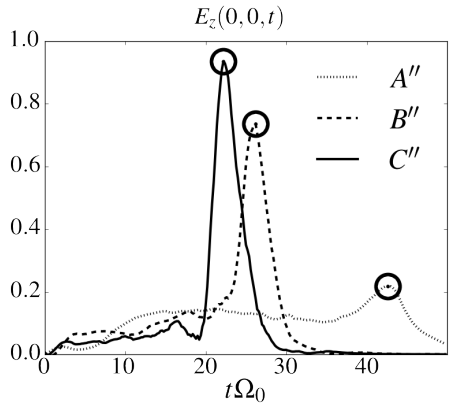

Figure 4.22: Out-of-plane electric field component at X point. Run A″, B″ and C″ are displayed in dash-dot, dashed and solid line styles respectively. Meaning of tags is in Table. 4.3.

Fig.4.22 displays the out-of-plane electric field at the X point. For all these runs we observe a single peak of the electric field; the larger the β, the larger maximum value of the electric field, and the sooner it appears. Run A″ is quite comparable to run A of section 4.2, except that for A'' electrons are hotter. While weak, the electron temperature seems to affect the magnetic reconnection by making it faster for hotter electrons. As a consequence, the reconnection electric field drastically increases with the electron temperature. To understand the reason for this, we investigate in the next section the different terms at play in the Ohm's law.

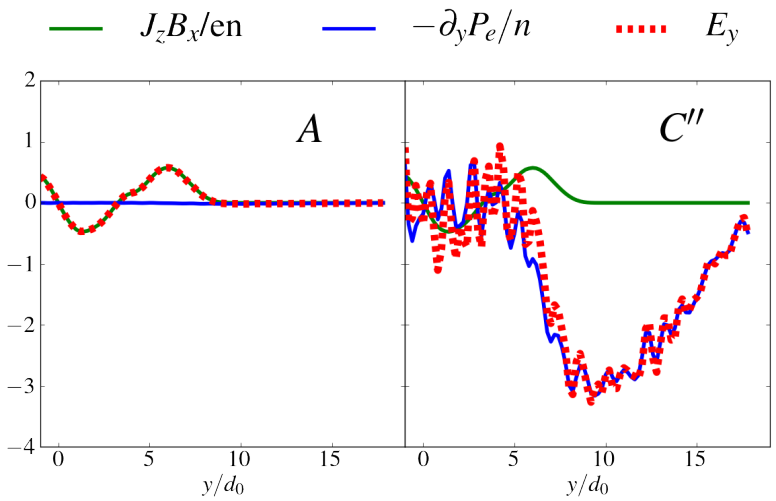

Figure 4.23: Ohm's law for E_y: left panel - run A, and right panel - run C″.

To understand how the initial electron temperature affects the initial topology of the electric field, Fig. 4.23 portrays all the terms of Ohm's law for E_y. For hot electrons (right panel of Fig. 4.23) the pressure gradient term is the main contributor to the electric field. The negative E_y value of the pressure term has a gradient in the Y direction, resulting in the growth of the out-of-plane magnetic field because of the Maxwell-Faraday equation. It is important to note this situation is the opposite to the one in a Harris, while the density gradient is directed toward the mid-plane of the current sheet in a Harris configuration, but outward from the mid-plane for magnetic bubbles. Later in time, a density gradient is building-up, because of the compression of the background plasma, resulting in a negative component of the associated electric field. But while this term is important at the middle of a Harris sheet and decreasing outer of it, in the bubbles configuration this term reaches its maximum value at $Y = 10$, and is vanishing at $Y = 0$. As a consequence, the in-plane electric field is higher in magnetic bubbles, increases with the electron temperature, but has its maximum value farther from the current sheet.

The Hall term J_zB_x does not depend on the electron temperature, and in the hot electron case stays too weak to counterbalance the pressure gradient term. Increasing the electron temperature increases the pressure term in the Ohm's law for E_y and the associated out-of-plane magnetic field. This term is crucial because, as already explained, it is associated with an in-plane current J_{xy} which, through the Hall term, is the main contributor of the out-of-plane electric field in the ion demagnetized region.

Fig. 4.24 displays two terms of the Ohm's law for E_z for run C″ at $t = 6$ (before the reconnection), and $t = 22$ (during the peaking of reconnection). During the compression phase, at $t = 6$, the contribution of the Hall term to the E_z electric field is weak. From what we said previously, it should not be so, because of the pressure term. But once the bubbles start to collide, the background plasma is compressed, building-up a density gradient directed toward the center of the current sheet. As a consequence, the in-plane

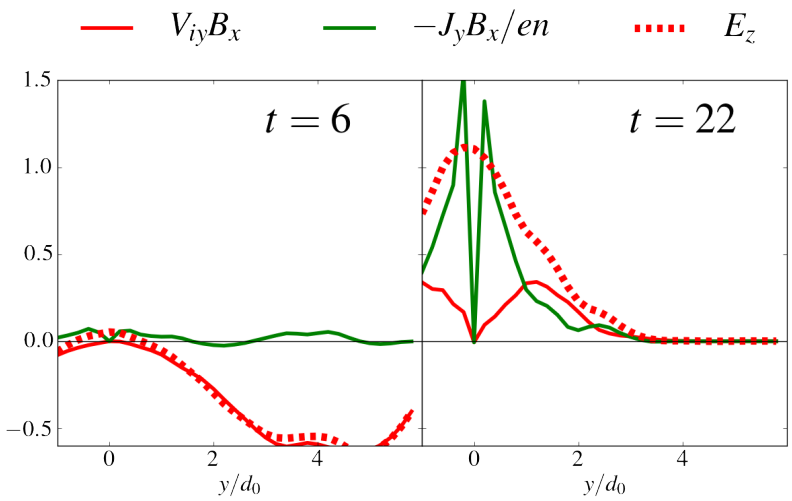

Figure 4.24: Ohm's law term through X point for run C″ (Table 4.3).

electric field decreases, as well as the associated Hall magnetic term B_z. The smaller B_z means the smaller J_{xy}, as consequence the smaller E_z. Out from the ion demagnetized region the electric field is mainly defined by the ideal term $V_{iy}B_x$ associated with the unmagnetized particles flowing from the opposite bubble. At $t = 22$ the picture is similar to the one for cold electrons: the electric field is supported by the Hall term in the vicinity of the X point, and by both the Hall term and the ideal one in the inflow direction.

We understand that hotter electrons contribute to a larger E_y electric field, which curl is important for the growth of the out-of-plane magnetic field. But once the bubbles start to collide, the associated compression of both the plasma and the magnetic field decreases E_y and as consequence B_z. The reconnection onset is delayed as it takes time to remove the particles in the ejecta because of its inertia. After the snowplowed plasma removal the magnetic field is enhanced by compression, as well as the in-plane current J_{xy} associated with B_z, making the Hall term of E_z growing. Once this term is large enough, the reconnection process can be triggered.

4.3.2 Density structure

In this section we observe the time evolution of the density when increasing the electrons and main temperature for runs A″, B″ and C″. As we have seen in the previous section, electron temperature generates a strong initial in-plane electric field inside the bubbles, accelerating particles.

Fig. 4.25 displays the background and main proton density depending on time for run A″. On panel (a) we observe a dense structure in the mid-plane for t $<$ 12 being a consequence of the snowplow effect, i.e. accumulation of matter by compression of

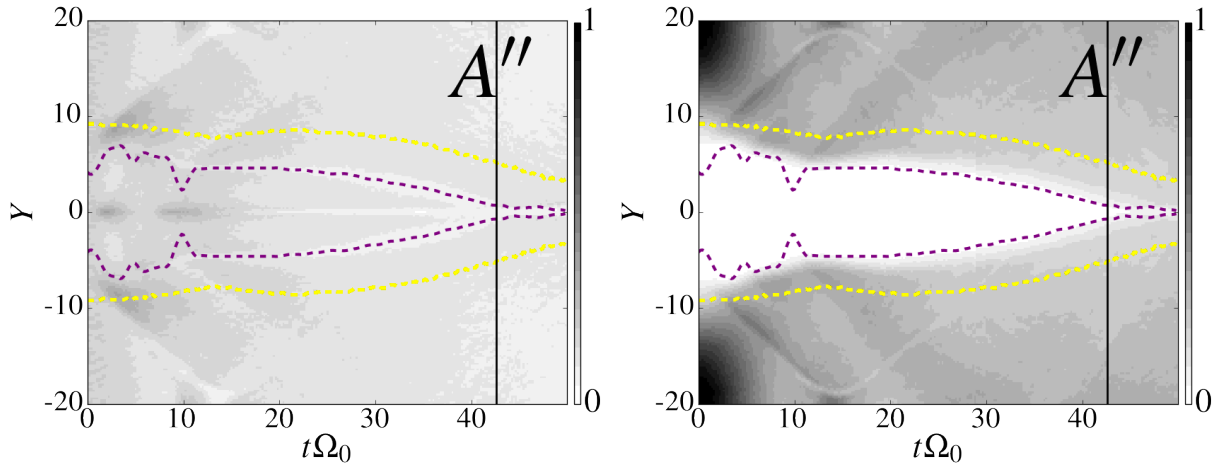

Figure 4.25: Lineout of the (a) background and (b) main proton population density through $X = 0$ for run A″. Yellow lines represent the inner border of magnetic shells, and magenta lines represent position of maximum magnetic field inside the ribbons.

the background protons. Comparing Fig. 4.25b with Fig. 4.10b, it appears that the compression is already stronger for run A″ than for run A, meaning the electron thermal pressure plays a significant role in driving magnetic reconnection for colliding bubbles. Fig. 4.26b displays the same as in Fig. 4.25b for run B″. One essentially notes, because of the increased thermal pressure the compression features are enhanced.

Fig. 4.26 displays the background and main protons population density in the outflow direction for run B″. On Fig. 4.26c we see a dense expanding front, a short period for $2 < t < 10$ showing a low density and the second expansion front consisting of background particles. The first front is the one associated with the initial compression of the background population by pressure imbalance, the bubbles pushing out the surrounding plasma. The second front is the ignition of the reconnection process, as can be seen in Fig. 4.22 where one have $E_z = 0.15$ until the peaked value. This peak, as already discussed, is the marker for the end of the reconnection process. The enhancement of the main population density around $X = 0$ is just a consequence of the demagnetization of this region: as all the magnetic flux is reconnected, there are no more magnetic frontier preventing the main population still embedded in each bubble to move in the mid-plane $Y = 0$, previously empty.

Examining the outflow direction for background in Fig. 4.26c for run B″, we can see the larger β, the larger the outflow velocity. In contrast to cold electrons, hot electrons diminish the snowplow effect. The main difference from cold electrons is the acoustic waves, rapidly crossing the boundaries of the computational domain and starting to interfere. In contrast to the cold electrons case no plasmoid appears after the onset of reconnection. We conclude that the acoustic waves can spread out the background density, and therefore reduce the snowplow effect.

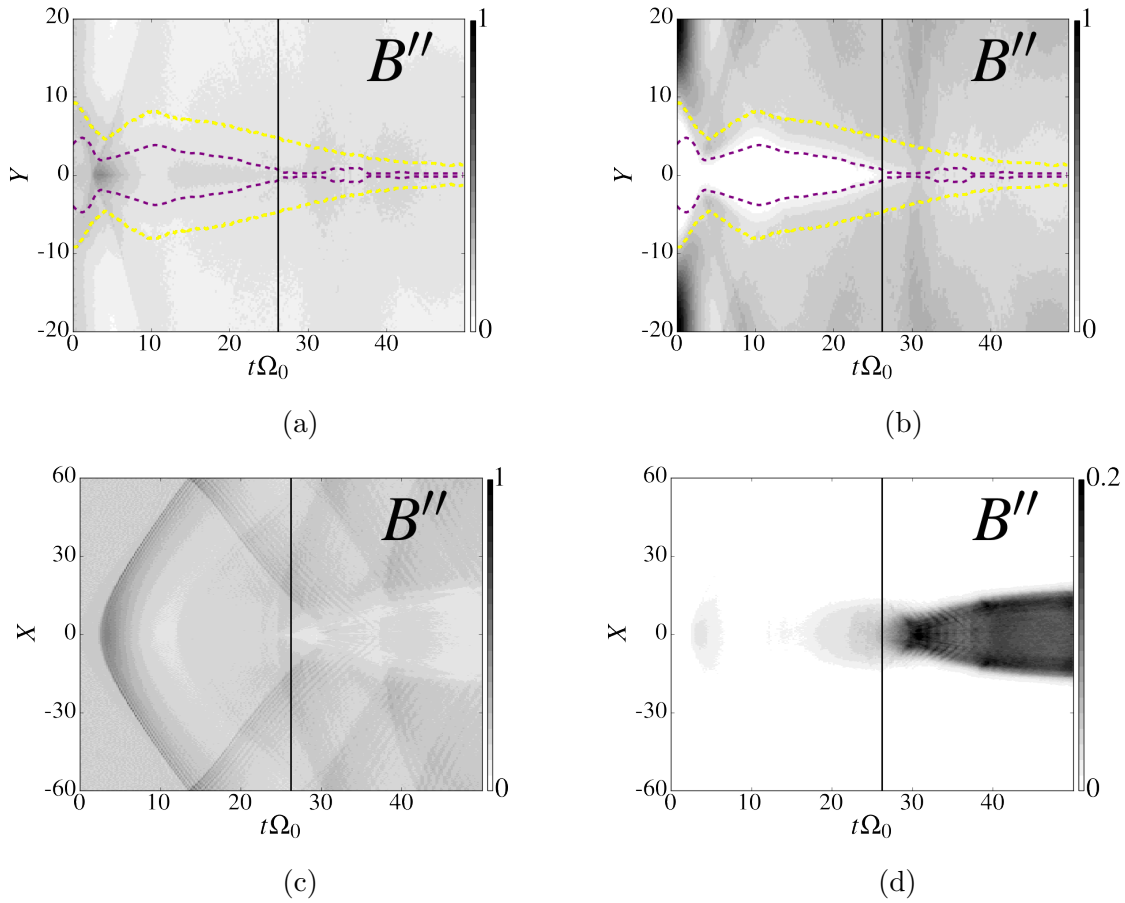

Figure 4.26: Lineout of the (left) background and (right) proton main population density through spot centers in time for run B″ depending on Y (upper) and X (lower). Yellow line represents the inner border of magnetic shells. Magenta line represents position of maximum magnetic field inside the ribbons.

4.3.3 Magnetic structure

On Fig. 4.27, we observe as a first stage, a compression phase of the magnetic ribbons, even for low β value for the main population. This results from the larger value of the thermal pressure of the electron population which contributes to compression of the magnetic structure. This larger thermal pressure is also responsible for the enhanced compression after this first stage, whatever the electron β value. As a consequence, inspecting the time evolution of the modulus of the total magnetic field on Fig. 4.28, this enhanced magnetic compression is clear, as well as the smaller time needed to reconnect all the flux, compared to the smaller T_e value cases.

Fig. 4.29a shows a snapshot of the out-of-plane current J_z for run C″ during the peak

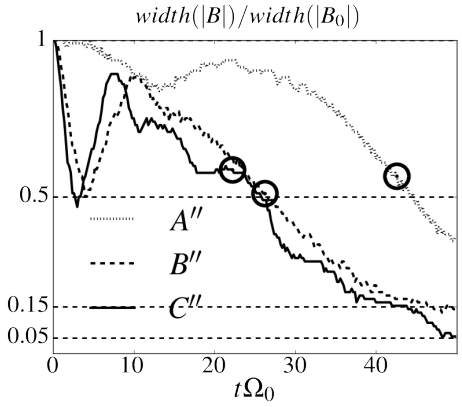

Figure 4.27: Magnetic shells width along lineout through spot centers $X = 0$. Run A″, B″ and C″ are displayed in dash-dot, dashed and solid line styles respectively. Meaning of tags is in Table. 4.3.

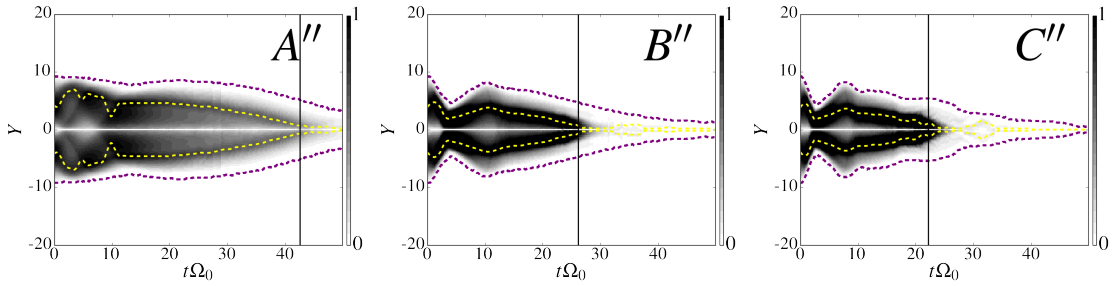

(a) (b) (c)

Figure 4.28: Lineout of modulus of magnetic field through spot centers $X = 0$ in time for hot electrons: (a) run A″, (b) B″, and (c) C″. Vertical lines show positions of maximum electric field. Meaning of tags is in Table. 4.3

in the reconnection field (Fig. 4.6). In contrast to the cold electrons (Fig. 4.16a) we observe a single point reconnection, and no plasmoids. Fig. 4.29b shows a snapshot of the out-of-plane magnetic field B_z for run C″ at the same time, where we can clearly see the quadropole structure, being stable until the enhancement of the reconnection field associated with the strong ion outflow.

4.3.4 Velocity structure

The inflow velocity structure for run A″ is similar to the one already discussed for run A. The patterns for run B″ and C″ are displayed in Fig. 4.30 and are clearly different from run B and C; one can observe the demagnetization of particles escaping from the

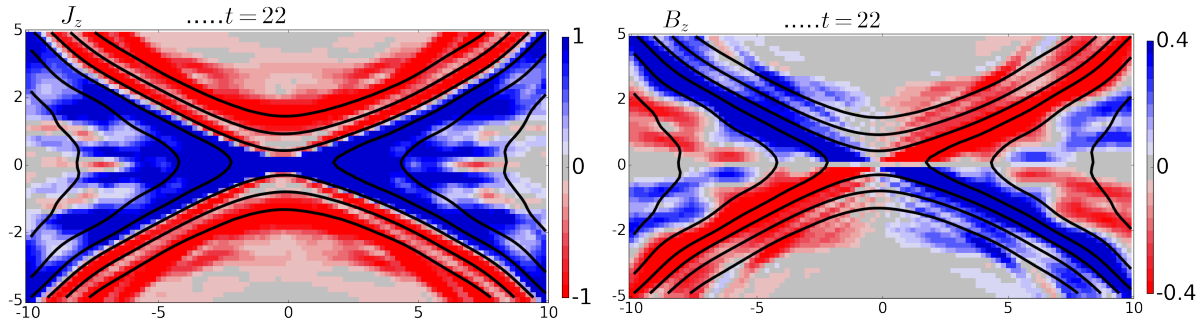

Figure 4.29: (a) out-of-plane current, and (b) out-of-plane magnetic field for run C′ (Table. 4.3). Black lines represent isocontours of vector potential.

inner part of their respective magnetic bubble, and crossing the other one before coming back... going so on in time. While the first crossing observed at $t = 5$ - 3 for run A″ - C″, is physical, all the other ones are artifacts arising from the periodic boundary conditions. Using specular reflexion and reflecting conditions will not be more physical. Of course, increasing the size of the simulation domain does not change the unmagnetized nature of the plasma. The only way to circumvent this drawback would be to loose these escaping particles while replenishing the inner of each bubble with the new one, as is the case in laser experiments. This was unfortunately beyond the scope of this thesis work.

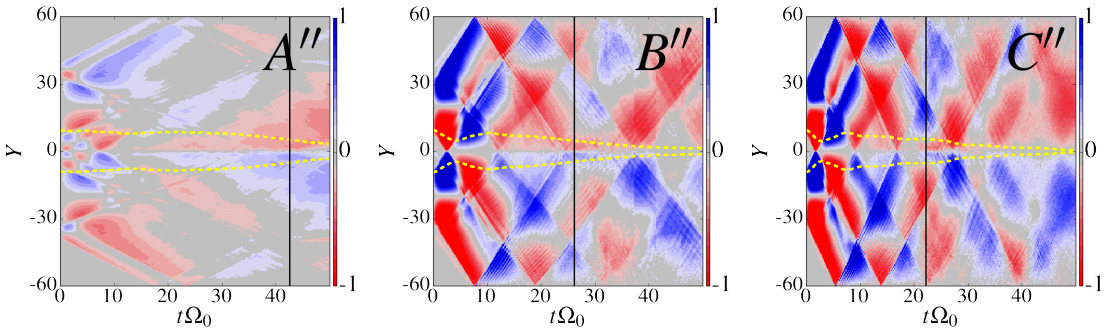

Figure 4.30: Lineout of the ion flow velocity in Y direction through the whole box for run B′ - left panel, run A′ - central panel, and C′ - right panel. Vertical lines show positions of maximum electric field. Meaning of tags is in Table. 4.3.

Fig. 4.30a displays ion flow velocity in the Y direction for run A (Table. 4.3). The initial global picture is similar to the cold electrons case. We see that inside the bubbles $10 < |Y| < 20$ the velocity is directed toward the mid-plane, while inside the shells $|Y| <$ 10 half of flow moves outward the mid-plane, and half moves towards the mid-plane. The difference is that initially expelled out of the shells ion flow vanishes, and we observe

the ion flow moving towards the mid-plane. Again we observe shaking of particles inside the bubble because of flow reflection by magnetic ribbons. A stationary flow toward the mid-plane is observed For $t > 15$.

Increasing the electron temperature increases the associated electric field as well as the efficiency of the reconnection process. The weak part of the approach is that, the electron temperature being kept constant, it has to be initially uniform all over the computational domain. To circumvent this constraint, one should consider the way to make this temperature evolve through time. As we already developed in chapter 3 the way to do so in a Harris sheet, we introduce the full electron pressure closure for the colliding bubbles problem.

4.3.5 Including the full electron pressure tensor

As a short conclusion of the simulations using isothermal closure equation we have observed:

- maximum reconnection field is close to 1 and observed for $\beta_1 = 20$, when background population has the same temperature as maximum of the main proton population
- main contribution to the out-of-plane electric field is the Hall term associated with the J_y current
- origin of the dense layer in mid-plane is the snowplow effect on the background population
- larger plasma β parameter, larger the fraction of demagnetized hot particles quickly leaving the reconnection site and modifying the initial inflow velocity
- major part of reconnection proceeds with warm particles trapped by magnetic field
- hot electrons in the bubbles significantly contribute to the reconnection electric field

Whatever cold or hot electrons, one observes a compression phase resulting from the thermal pressure inside the bubble, followed by a relaxation phase resulting from the inversion of plasma flow by the demagnetization of particles, and finally, followed by another compression. This mainly results from the fact that we treat the reconnection problem as an initial value problem. In the laser-plasma experiment because of continuous plasma outflow from the hotspot, one observes a continuous shells compression mainly driven by the fuelling of newly generated hot plasma during the solid target irradiation. To mock the continuous plasma flow in numerical simulations is not a trivial problem, as one has to continuously load particles into the computational domain leading to the memory overloading.

Run tag	β_0	β_1	β_2
A*	0.08	10	0.04
B*	0.08	40	0.04
C*	0.08	100	0.04

Table 4.4: Meaning of the four tags used for runs A*, B*, C* for full electron pressure tensor simulations.

As the isothermal closure imposes an homogeneous electron temperature profile, we inspect in this section the consequences for the reconnection process of using the full electron pressure tensor, allowing to initialize non uniform electron fluid temperature. For the following simulations the initial electron temperature equals to main proton population temperature, as already discussed in the previous section. Just as a reminder, the full electron pressure tensor is important for the reconnection because it is the ultraefficient term to support the reconnection electric field in the electron diffusion region. As we neglect the Z derivative in two-dimensional problem, E_z is supported by the $\partial_x P_{xz}$ and $\partial_y P_{yz}$ terms in the Ohm's law. In this section we have initially $\beta_0 = \beta_1$, since asymptotic electrons and background temperatures both equal to 0.1.

As now we need to define a profile for temperature of the electron fluid, we use our polynomial defined by Eq. 4.3 (displayed in Fig. 4.4b):

$$T_0(r) = T_{\max} P\left(\frac{r}{L_R}\right) + T_\infty \tag{4.8}$$

where T_∞ is an asymptotic temperature, and $T_{\max}$ is the maximum temperature in the bubble center. Such a profile repeats the density profile, meaning hot particles are located in the dense center, while cold one are located in the magnetized tail.

As was shown, increasing of initial electron temperature speeds up the reconnection process and increases the maximum reconnection field. For this set of runs we keep a cold background $T_2 = T_\infty = 0.1$, and have performed three runs A*, B* and C* for $T_{max0} = T_{max1} = 5$, 20 and 50, respectively. The associated β values are reported in Tab. 4.4. The "star" superscript refers to the full pressure tensor.

Evolution of the reconnection field

Fig.4.31 displays E_z at the X point for simulations using full electron pressure with sub-cycling and isotropization only on P_{xx} and P_{xy} for different initial temperatures. Such isotropization is enough to stabilize run, as was shown in chapter 3.

Comparing Fig. 4.31 with Fig. 4.6, the two-peak structure of the electric field is still observable, but there are mainly two (related) differences from the isothermal case : (i) the amplitudes of the electric fields are larger with the full electron pressure tensor and (ii) the time separation between the two peaks is smaller. The amount of magnetic flux to reconnect being the same whatever the way to treat the electrons, it reconnects faster with

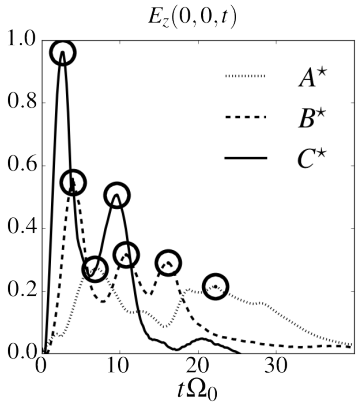

Figure 4.31: E_z at X point for simulations integrating the full electron pressure tensor with sub-cycling scheme and isotropization on P_{xx} and P_{xy}. Run A*, B* and C* are displayed in dash-dot, dashed and solid line styles respectively.

a larger electric field. This point is quite surprising, as in a Harris sheet the full pressure treatment leads to the opposite conclusion, i.e. to the decrease of the reconnection electric field because of the bifurcated nature of current sheet.

To get a clear picture of the physical process in the vicinity of the X point, Fig. 4.32 displays the Ohm's law components for run C*. We observe three stages: compression, mixing, and relaxation. At the first stage ($t = 2$), far from the reconnection region the strong initial thermal pressure inside the bubble creates the strong particle inflow. As a result, the main particles are strongly convecting toward the X point. An off-diagonal term of the electron pressure is at play at the X point to create the E_z electric field. It has to be noticed that in the ion diffusion region a Hall term exists, but with an inverse sign as the in-plane current is not the one associated with the quadrupolar structure of the out-of-plane magnetic field. At $t = 4$ the pressure tensor is still the one associated with the reconnection electric field, but the Hall term is not yet developed, and the ideal term is associated with a reverse flow because of the particles demagnetization. Finally, at $t = 8$ we obtain the classical picture of a quite constant E_z through the reconnection region defined by the electron pressure term in the electron diffusion region, by the Hall term in the ion diffusion region, and by the ideal term in the MHD region.

Density structures

Fig. 4.33 displays the background and the main protons population density in the inflow and outflow directions for run C*. The background population is less important in inflow direction than in the isothermal case of Fig. 4.11. This population is compressed in between the two bubbles, and expelled out of it in the X direction. This happens in the same way as in the isothermal case, but in a more efficient way as already pointed out. In the outflow direction the two archs that one can observe at smaller β values are mixed up creating the bulge of pressure as in the isothermal case. A plasmoid origins and moves in the $+X$ direction. The main difference from the isothermal case is a kind of striation

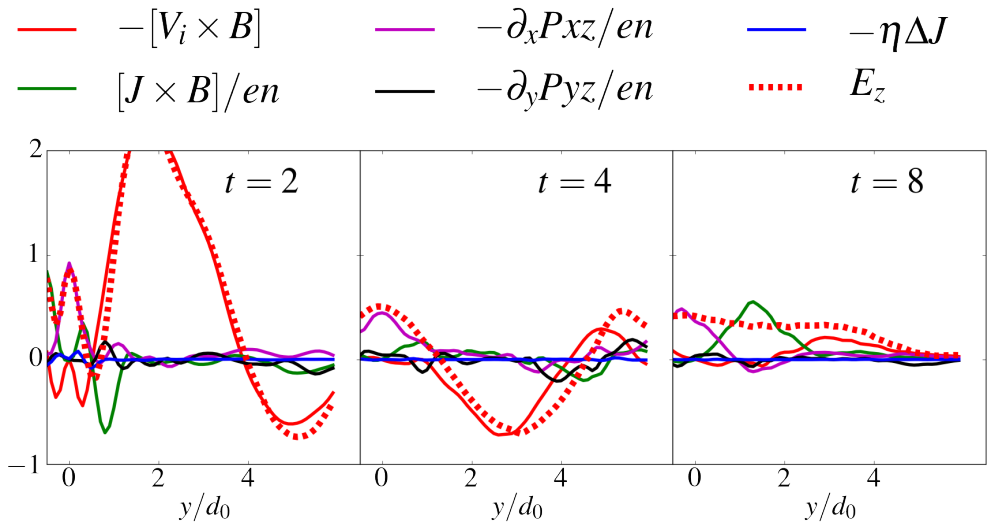

Figure 4.32: Ohm's law components for run C*.

of the density structure at small scale length, which origin is yet unclear.

In the outflow direction we still observe the snowplow effect (Fig. 4.33c) and an accelerating plasmoid as in the cold electrons case (Fig. 4.13). The main difference is that in the full electron pressure case the plasma from interior of the bubble also contribute to the plasmoid formation (4.33d for $3 < t < 10$).

4.3.6 Vacuum problem in colliding bubbles

In hybrid codes to handle the Ohm's law, we have to add a background ion population. Because of its inertia the reconnection rate might be larger in vacuum conditions. Although the snowplow effect during the expansion phase could play the dominant role in the current sheet formation, the associated current structure could also be modified by this population. In this section we check the role of the background population.

To be sure background population is not the only feature slowing down the current sheet formation, we have performed simulations with negligible background density. There are two places in the hybrid code where super low density is a strong restriction: (a) in the Ohm's law for the Hall term and pressure gradient, being inversely proportional to the electron density, and (b) calculating the electron velocity Eq. 2.15 needed for electron pressure tensor evolution. To control the regions with too low density, we multiply the terms where the inverse of the density appear by a limiting function of density $\alpha(n)$. While apparently unphysical, such function is not totally artificial; in critically low density regions, while there are very few particles to carry the current, the current and the pressure tensor should be of the order of epsilon. The divergence of these terms is arising essentially

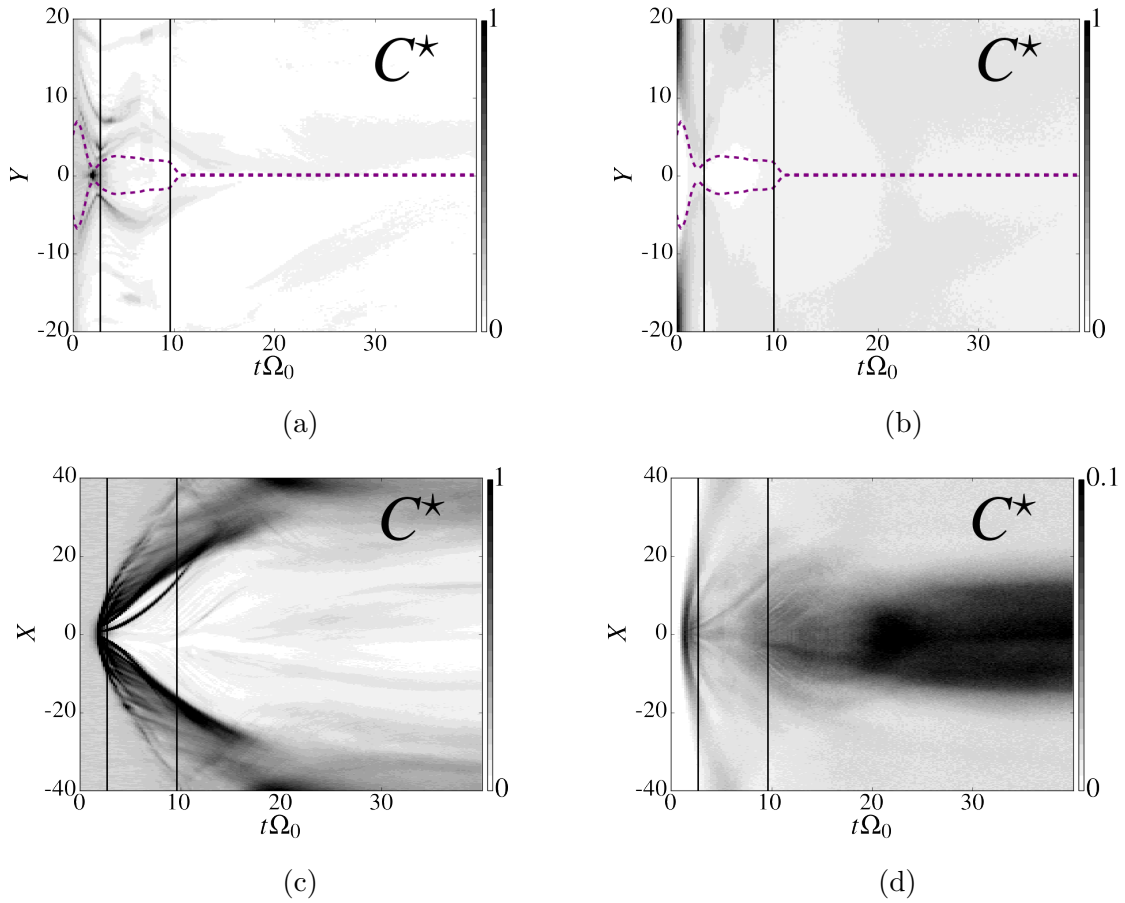

Figure 4.33: Lineout of the (a) background and (b) protons density in inflow direction. Lineout of the (b) background and (d) protons density in outflow direction through mid-plane in time for run C⋆.

for numerical reasons, because we divide two terms of order of epsilon. It is reasonable to lower these ratio by an appropriate factor. To do so, we use our polynomial already introduced:

- if density exceeds the high threshold $n > n_h$, polynom is one
- otherwise, we use the left part of the polynomial and an associated low threshold n_l

$$\alpha(n) = \begin{cases} 1, n > n_h \\ P\left(\frac{n-n_l}{n_h-n_l} - 1\right), n_l < n < n_h \\ 0, n < n_l \end{cases}$$

To have a smooth transition from maximum density to the problematic one, we choose $n_h = 1$ and $n_l = 10^{-2}$.

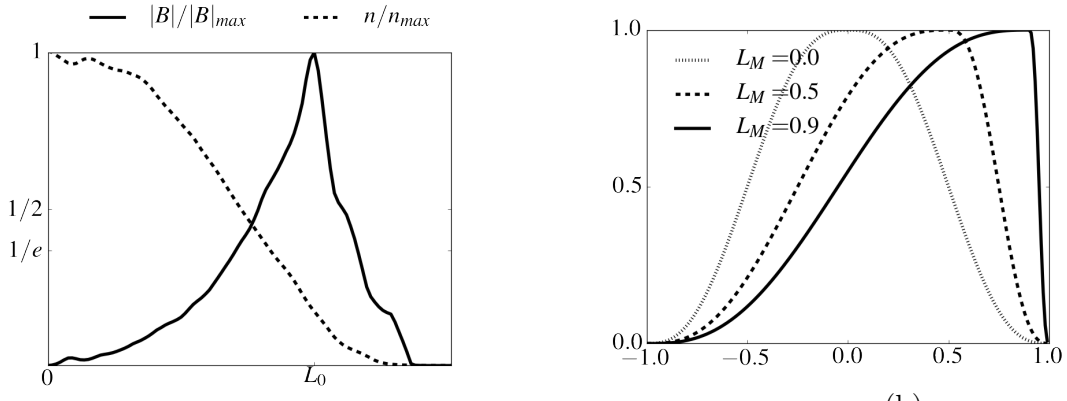

Figure 4.34: (a) FCI2 simulation snapshot at t = 1 ns. (b) The modified polynom P_M for given L_M values.

Going back to hydro-radiative simulations of plasma ablation process, Fig. 4.34a shows simulation results of FCI2 at $t = 1$ ns. Comparing with later times 2 ns Fig. 4.3c and 3n Fig. 4.3d, we see that initially magnetic field profile can be cutting on the outer edge of the shells. To mock such a profile we use a modified polynomial $P_M(x)$, which is an extension of the already known polynomial $P(x)$ Eq. 4.3:

$$P_M(x) = \begin{cases} P\left(\frac{x-L_M}{1-L_M}\right), x > L_M \\ P\left(\frac{x-L_M}{1+L_M}\right), x < L_M \end{cases}$$

Fig. 4.34b shows few specific polynomials for given L_M values. To initialized magnetic field we still use Eq. 4.5 but with the modified polynomial $P_M(x)$. We present comparison of the regular initialization $L_M = 0$ and an extreme case $L_M = 0.8$. By such a choice, we want to create initially the magnetic field gradient as sharp as possible for two reasons :

- reduce the pile-up phase
- use the benefit of the magnetic mirror, as hot particles from the bubble center hardly cross the full width of a shell with growing gradient, while for regular profile a particle has to cross only half of the width to start to be pressed out by the magnetic pressure of the shells

To show the difference between two cases (1) a regular initial magnetic field profile run $A^\diamond$, and (2) a sharp gradient on the outer edge run $B^\diamond$, we chose background density $n_2 = 10^{-3}$, and minimize the inertia of background population. In the previous simulations the bubble density profile ended at the middle of the shell. In this section we use extended one up to the outer boundary of the shell, as with such a low background level, we need to initialize the protons where magnetic field is non zero. Otherwise we stuck with the electric field divergence problem, the Hall term grows dramatically even using $\alpha(n)$, as

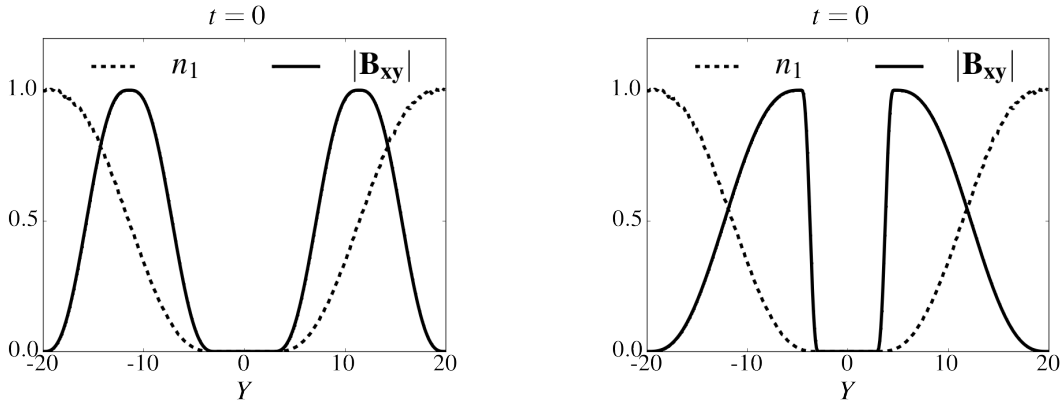

Figure 4.35: Initial density and magnetic field profiles for simulations A$^\diamond$ and B$^\diamond$.

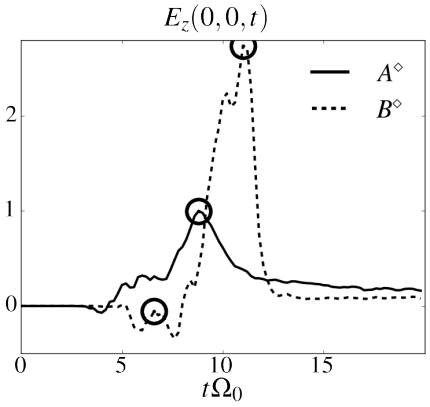

Figure 4.36: Reconnection electric field for simulations A$^\diamond$ (solid) and B$^\diamond$ (dashed).

magnetic field differs from zero, but the density vanishes. We choose a modest initial temperatures to compare with previous results $T_1 = T_0 = 10$ corresponding to $\beta_1 = 20$, and $T_2 = 0.1$ corresponding to $\beta_2 = 10^{-4}$. Fig. 4.35a shows the initial density and magnetic field profiles for run A$^\diamond$, and Fig. 4.35b displays the same for run B$^\diamond$.

Fig. 4.36 shows the reconnection electric field for the regular profile (solid) and the sharp one (dashed). For the regular profile, the maximum reconnection electric field is 1, while for the sharp profile, we observe for the first time a significant excess up to 2.6 at $t = 11\ \Omega_0^{-1}$. For run B$^\diamond$, just before the peak, $4 < t < 8$, we see a negative out-of-plane electric field, which origin is the pressure term, while for run A$^\diamond$ reconnection has already started. For both cases the reconnection time is comparable, while the regular profile case has a longer tail. The total time of active reconnection phase is considerably reduced for the run B$^\diamond$, namely $4\ \Omega_0^{-1}$ for run B$^\diamond$, while for run A$^\diamond$ it is twice longer.

Fig. 4.37 shows the density and magnetic field profiles at $t = 1\Omega_0^{-1}$ for run A$^\diamond$, and B$^\diamond$. We should note for both cases, traveling magnetic field gradient becomes stepper

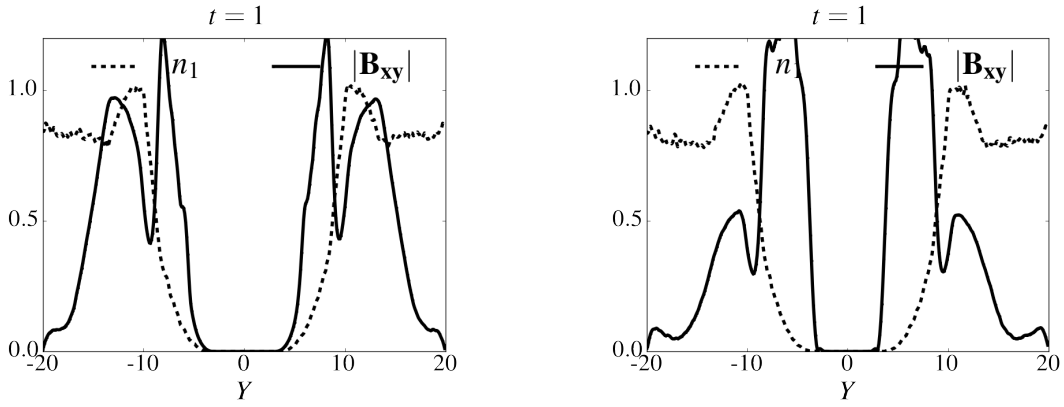

Figure 4.37: Density and magnetic field profiles at t = $1\Omega_0^{-1}$ for (a) run A$^\diamond$, (b) run B$^\diamond$.

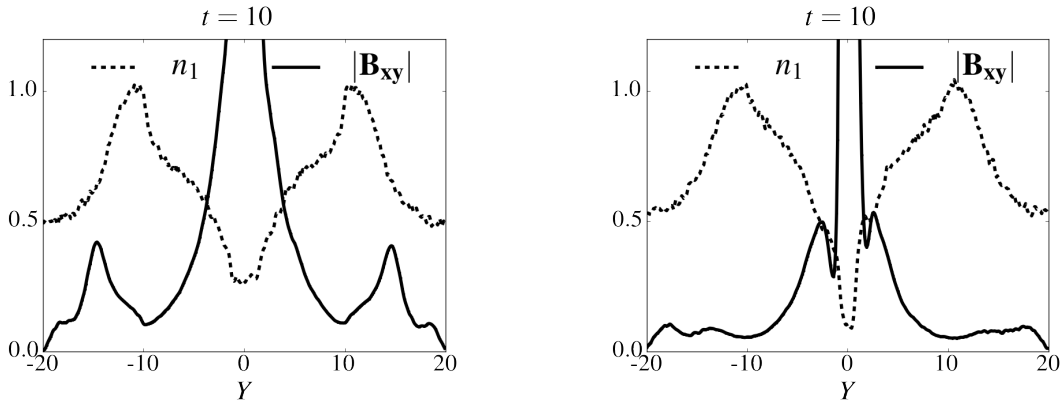

Figure 4.38: Density and magnetic field profiles at t = $10\Omega_0^{-1}$ for (a) run A$^\diamond$, (b) run B$^\diamond$.

on the outer edge. Also we observe the local maximum of magnetic field moving inward the bubbles. On later times at $t = 10\Omega_0^{-1}$ (Fig. 4.38) the maximum still exists inside the bubble for regular initial profile, while for sharp profile, the magnetic field is almost homogeneous. On the density profile we can see that the peak around $Y = 10$ does not move in time, the gradient is kept constant in time, that mimics the continuous particles production by the laser energy deposition. To do so, we add particles with a Maxwellian distribution and initial temperature each time step.

On the Fig. 4.38 we can clearly see the difference in how many particles in the mid-plane participate in the out-of-plane current creation for run A$^\diamond$ and B$^\diamond$. For run A$^\diamond$ the density grows up to 0.3, while for run B$^\diamond$ it stays less than 0.1. After reconnection the density reaches 0.4 for both cases. The amount of plasma pressed between two magnetic field maximums plays a crucial role in the plasmoid instability development. While we

have small amount for run B$^\diamond$ and no plasmoid during the reconnection, for run A$^\diamond$ current is forced to break up into several plasmoids to remove the snowplowed plasma from the reconnection site.

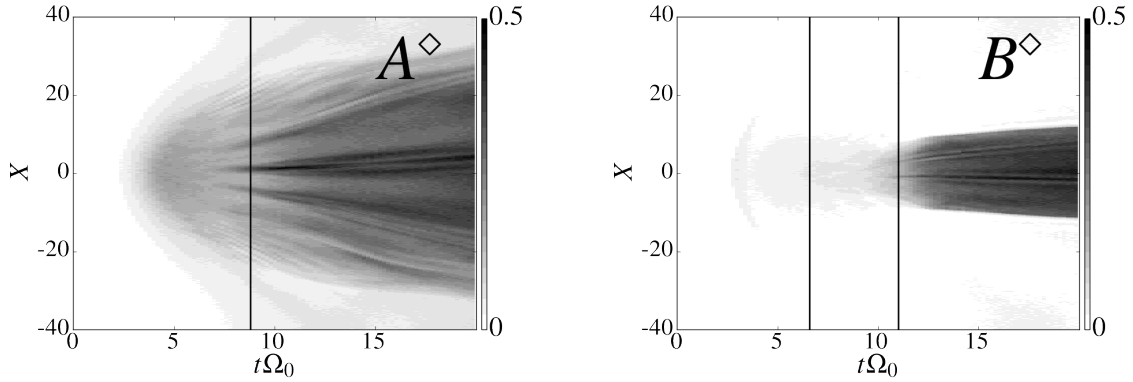

(a) (b)

Figure 4.39: Lineout of the main density n_1 in outflow direction (a) classic polynom run A$^\diamond$, and (b) sharp polynom run B$^\diamond$.

Fig.4.39 shows a lineout of the main density n_1 in the outflow direction for run A$^\diamond$ and B$^\diamond$. For run A$^\diamond$ protons expelled from the shells fill the reconnection site, while in run B$^\diamond$ the maximum density is observed after the peak on the reconnection field. During the pile-up phase, because of the considerable amount of particles in the reconnection site for run A$^\diamond$, we also see the strong out-of-plane current Fig. 4.40 breaking up into several plasmoids. Previously we have observed plasmoid formations in the mid-plane because of the snowplow effect and background plasma. But for run A$^\diamond$ the birth of the bright plasmoids is associated with a tiny filament accumulating plasma from its neighborhood and growing in time.

For run B$^\diamond$, Fig. 4.41, a compressed current structure during the maximum electric field also breaks up into plasmoids but after the maximum of the reconnection field. Hence, the greater electric field in the sharp profile case is associated with the fact that initially very few particles create the reconnection current, while during compression magnetic pressure

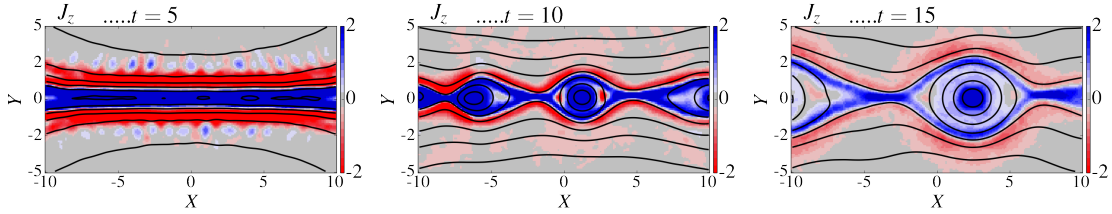

(a) (b) (c)

Figure 4.40: Snapshots of the out-of-plane current J_z for run A$^\diamond$.

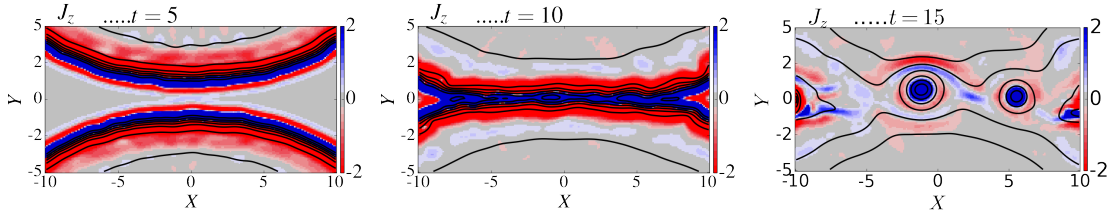

(a) (b) (c)

Figure 4.41: Snapshots of the out-of-plane current J_z for run B$^\diamond$.

cannot compensate thermal pressure, and pressure divergence term grows significantly "breaking through the dam".

To summarize this section about the low background:

- the maximum reconnection field is ~ 2.6 for sharp magnetic field gradient on the outer border of the shells
- the current breaks up into plasmoids when the snowplow effect on the main protons population reduces compression of the shells

4.4 Driven magnetic reconnection

In laser plasma experiments the main feature of the process is a continuous feeding of the bubbles with newly generated plasma. This has two important consequences for the plasma: (1) a density gradient directed toward the bubble center, and (2) an inflow of energetic particles out from the bubble, feeding the reconnection process at the outer edge of each bubbles just where they collide. It is clear that it should not be treated as an initial problem, as result just defining an initial density and temperature in simulations is not enough to mock the continuous pressing of magnetic shells like in a real experiment. In this section we describe the technique called *magnetic piston* and the associated results. To keep a high pressure in Eq. 4.7 there are two ways: (1) increase the thermal velocity, or (2) increase the bulk flow velocity. As we mentioned, when we set an initial bulk flow velocity for the main population out from the magnetic ribbon, this one quickly vanishes because of the associated ram pressure. To increase the velocity of the plasma outgoing from the bubble, which is the inflow velocity in the reconnection region, we need to add a source term creating such a flow. To do so, we use an out-of-plane "magnetic piston". The main idea to drive plasma, and mimic the forcing of the laser irradiation of the target, is to add an axial current J_z being associated with the azimutal magnetic field creating a radial electric field, which strongly accelerates the particles out from the center of each bubble.

4.4.1 The magnetic piston to drive reconnection

To simulate the driving of the plasmas because of laser irradiation, we use a current in the out-of-plane direction. We add this term in the Ampere's law, the total current is rewritten:

$$\mathbf{J} = \frac{1}{\mu_0}\boldsymbol{\nabla} \times \mathbf{B} + \mathbf{J}_L \tag{4.9}$$

where $\mathbf{J}_L$ is the current which mimicks the laser defined by $\mathbf{J}_L = \mathbf{J}_{\max} P_S(r) P_T(t)$, where $P_S(x)$ provides the spatial structure of the current and $P_T(t)$ is the temporal one. Initially $P_T(t = 0) = 0$, it smoothly grows to one on a time scale equal t_0, staying constant until the end of the simulation $P_T(t > t_0) = 1$. $P_S(r = 0) = 1$ at the center of the magnetic ribbon, and decreases to zero for $r > R_L$, where R_L is the "radius" of the laser spot. This technique has been suggested by Lembege et al.[LP82] to trigger shocking numerical simulations.

Run tag	β_0	β_1	β_2	J_{max}	R_L	$P(n)$
A^o	0.08	2	0.04	0	0	regular
B^o	0.08	2	0.04	0	0	extended
C^o	0.08	2	0.04	1	10	regular
D^o	0.08	2	0.04	1	20	extended

Table 4.5: Meaning of the four tags used for runs A^o, B^o, C^o, and D^o using piston current.

To focus on the importance of the additional current, we performed simulations using isothermal closure equation. First we start with a single bubble, and look at two cases: free expansion, and with an imposed current. We simulate cold background and electron fluid $T_2 = T_0 = 0.1$ associated with $\beta_2 = 0.04$ and $\beta_0 = 0.08$, and proton temperature $T_1 = 2$ corresponding to $\beta_1 = 2$, such parameters are comparable with run A (Tab. 4.1). The bubble has the following size: $L_R = 10$ and $L_W = 6$. Simulation domain is a rectangular, with length $L_X = 100$ and width $L_Y = 100$ using a 500×500 grid, the mesh resolution equals 0.2 in both directions. The time-step 10^{-3} is chosen to satisfy the CFL conditions for the fastest whistler modes. We use 30×10^6 macro particles for the main population of protons and 20×10^6 for the background protons, which correspond on average to 200 particles per cell. We performed four simulations:

- A^o is the standard density and magnetic field profile
- B^o is the extended density profile, which ends at the outer border of the magnetic shell
- C^o is the same profile as run A^o plus an imposed current with $J_{max} = 1$ and $R_L = 10$

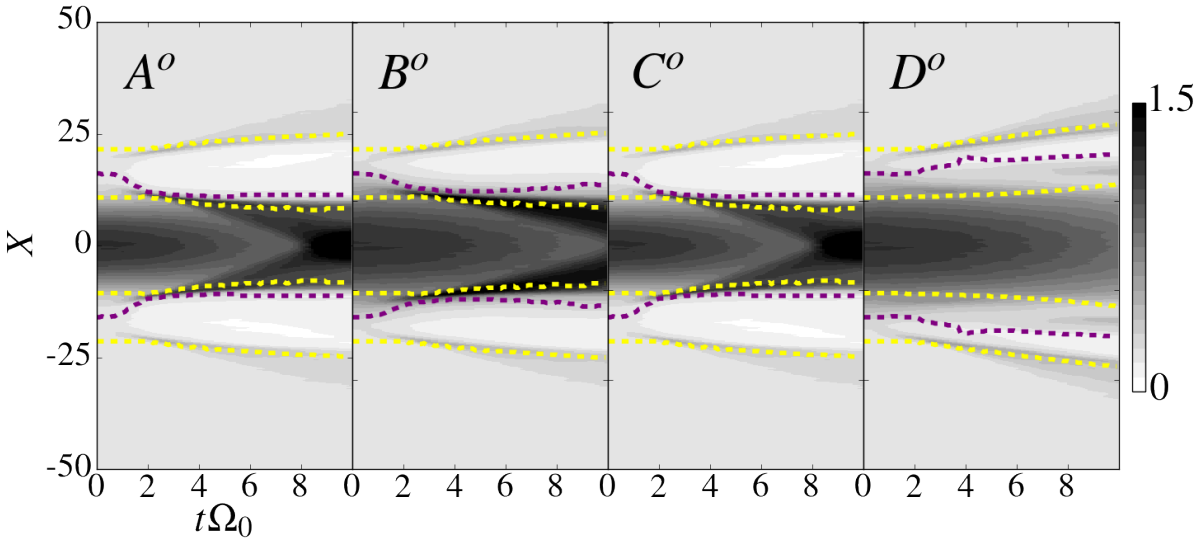

Figure 4.42: Line-out of the electron density at $Y = 0$. The yellow dashed lines indicate the minimum of the inner and outer border of the magnetic shells and the magenta line represents the position of the maximum magnetic field.

- D^o is the same profile as B^o plus an imposed current with $J_{max} = 1$ and $R_L = 20$

The meaning of the tags is given in Table 4.5. We use the same radius for the 'piston' and for the density profile. In run C^o, the density boundary is in the middle of the shell and in run D^o, it extends up to the outer border of the magnetic shell. We use a pulse duration equal 0, i.e. we apply the maximum current initially.

Fig. 4.42 is a line-out of the electron density, the yellow dashed lines represent the inner and outer border of the magnetic shells, the magenta line shows the position of the maximum magnetic field. For run A^o, B^o, C^o we observe reflected waves moving to the center for $t > 2$, those waves resulting from the plasma reflection on the magnetic shells and the background expelling. For run D^o the plasma moves strictly outward the spot center, making the piston a good candidate to remove plasma beating inside the bubbles. Also, it is the only case where we see the motion of the maximum magnetic field outward the center.

4.4.2 Radial expansion velocity profile

In two-dimensional simulations, as we can not consider the laser-plasma interaction, the magnetic field is imposed in the initial condition. Because of the Biermann-Battery effect, the magnetic fields should exist where there is a radial gradient of temperature (associated with the axial gradient of the density). For the isothermal closure equation

we cannot manage an initial temperature gradient, while the initial relation between density and magnetic field profiles is an open question. As we saw in the previous section, for the low background case it is important to feed the shells with particles of the main population to be able to transport magnetic field. In this section we inspect the effects of the imposed current on the expansion velocity.

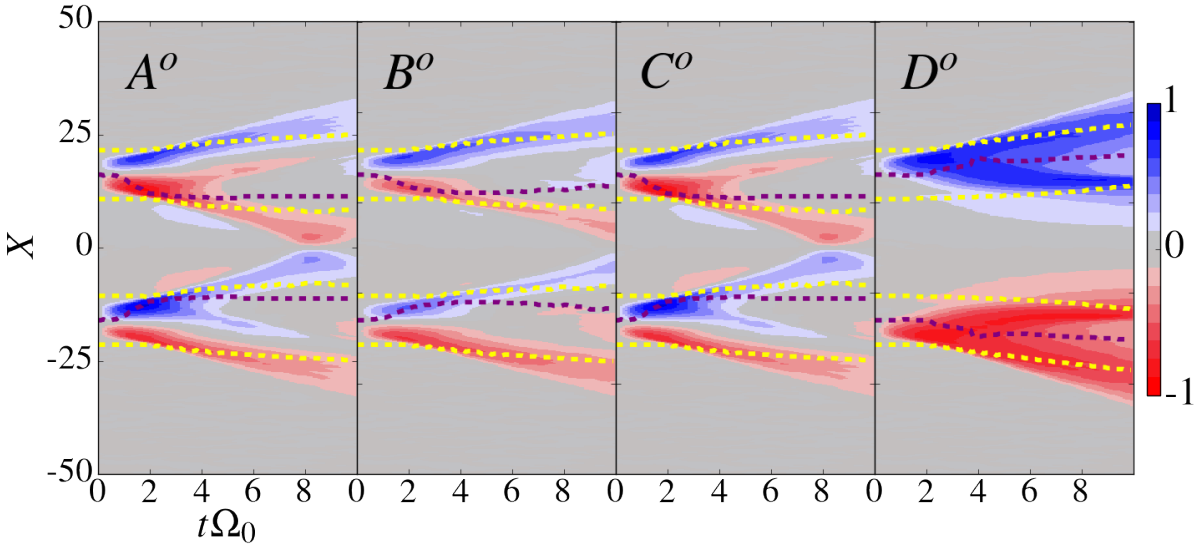

Figure 4.43: Lineout of the radial ion flow velocity. The yellow dashed lines indicate the minimum of the inner and outer border of the magnetic shells and the magenta line represents the position of the maximum magnetic field.

Fig. 4.43 shows a lineout of the ion flow velocity at $Y = 0$ in the outflow direction. Run A^o and B^o show similar picture, the radial velocity grows and expands out from the piston. But later in time this radial velocity vanishes. From what we conclude that the plasma expansion does not depend on the density extension. For run C^o the effect of the magnetic piston is not obvious, as we get a picture quite close to run B^o. Run D^o exhibits a clear change compared to the other runs, essentially because to let the Hall term be effective the current has to be large enough where the magnetic field is also large.

4.4.3 Spot-size and amplitude of the magnetic driver

In this section, we overview the importance of the laser spot size R_L and the amplitude $J_{\max}$ on the reconnection process. To compare the results with the high β simulations, we use the same bubbles proton density profile with radius $L_R = 10$ extending up to the middle of the shells with width $L_W = 5$.

We have performed three simulations:

- A^+ with a small current $J_z = 1$ and a small spot $R_L = 10$
- B^+ with a small current $J_z = 1$ and a big spot $R_L = 15$

Run tag	β_0	β_1	β_2	J_{max}	R_L
A^+	0.08	2	0.04	1	10
B^+	0.08	2	0.04	1	15
C^+	0.08	2	0.04	2	15

Table 4.6: Meaning of the four tags used for runs A^+, B^+, C^+ using piston current.

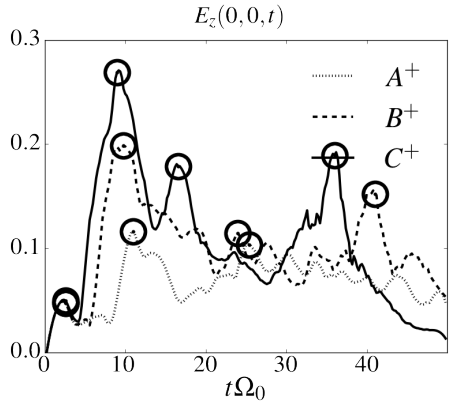

Figure 4.44: E_z at X point. Run A^+, B^+ and C^+ are displayed in dash-dot, dashed and solid line styles respectively. Meaning of the tags is in Table. 4.6.

- C^+ with a big current $J_z = 2$ and a big spot $R_L = 15$

We made this choice to outline the importance of both the size and the magnitude of the "laser". We use a cold background and electrons $T_2 = T_0 = 0.1$ associated with $\beta_2 = 0.08$ and $\beta_0 = 0.08$, and use a proton temperature $T_1 = 2$ giving $\beta_1 = 2$. To let the hot plasma leave the reconnection site and concentrate only on the importance of the laser, we use a laser pulse duration $t_0 = 8$. The simulation domain is as in run A (Table. 4.1), and we use the isothermal closure equation for electron pressure Eq. 2.9.

Fig. 4.44 portrays the out-of-plane electric field at X point. We observe the familiar two peaks structure. The first peak results from the collision during the onset phase of the reconnection, where we can see how increasing piston current increases the amplitude of the peak. The reconnecting process takes less time and has a greater magnitude for the big current and big spot case run C^+. Unsurprisingly, when the reconnection process is strongly driven, it happens in a more effective way.

Fig. 4.45 displays the width of the shells along $X = 0$. For the small spot (run A^+) the magnetic ribbons expand up to 1.1 of the initial width, while without piston for run A, the expansion was up to 1.2. In the case of the small current and big spot (run B^+), the compression up to 0.8 is similar to run C with $\beta_1 = 100$. The relaxation phase almost disappears in the case with the superposed laser current. The increase of the width for run C^+ for $10 < t < 15$ and the flatten part of the run B^+ for $12 < t < 20$ are associated with the plasmoid formation. As we measure width using lineout through the spot centers

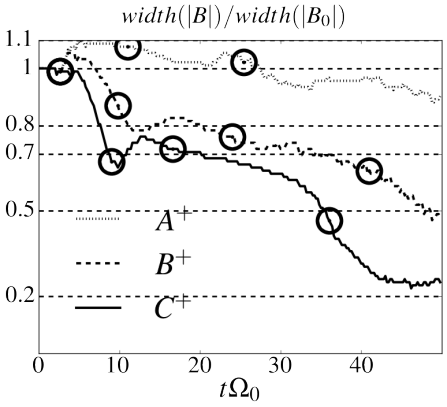

Figure 4.45: Width of magnetic shells measured in cross section through the spot centers. Run A^+, B^+ and C^+ are displayed in dash-dot, dashed and solid line styles respectively. Meaning of the tags is in Table. 4.6.

$X = 0$, and moving plasmoid makes width wider.

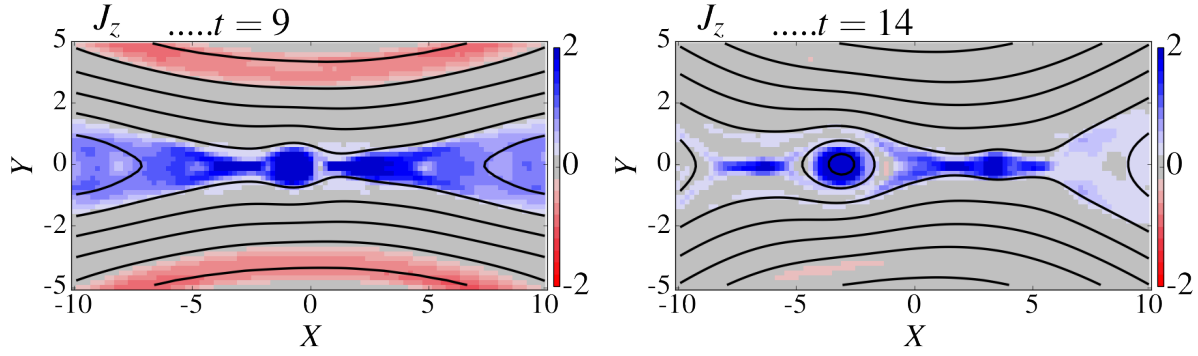

Figure 4.46: Out-of-plane current J_z at (a) t = 9, and (b) t = 14 for run C^+ (Table 4.6). Dashed line crosses the X point.

Fig. 4.46 shows a snapshots of the out-of-plane current J_z, dashed line crosses X point. We chose times to observe plasmoids formation, originating during all the reconnection process, and as consequence of the X point motion. The width of the current sheet is on sub ion scales, the imposed current does not affect the reconnection site. Therefore, it means whatever the parameters for the magnetic piston, we can impose an enhanced value of the plasma velocity outflowing from the inner of the magnetic ribbons without impinging the structure of the current sheet arising from the bubble collision.

As a conclusion, a magnetic piston alone is not as effective as expected. We outline the fact that the current associated with the laser has to be large enough where the magnetic field of the magnetic ribbon is also large, to get an effective $\mathbf{J} \times \mathbf{B}$ term to drive an efficient electric field. As a continuation of this work we could extend this study to larger values of

the current, considering that numerical instabilities could arise. Finally, such driving of the reconnection process results in the generation of many plasmoids, which origin should also be inspected. More precisely, it questions the nature of the reconnection process that could be more impulsive, and happen in a bursty way.

4.5 Ellipsis initialisation

The efforts presented in this thesis are dedicated in the way to treat from the numerical point of view the problem of magnetic reconnection in laser-induced high energy density plasmas. Few experiments have already been conducted by different teams, as well as by the team I belong. Hence, in 2015 and 2017, Julien Fuchs leaded two different four-week campaigns while investigating the effects of having non-coplanar solid targets at LULI2000. In 2015, the two targets were tilted by an angle around the axis along the outflow direction (X axis in our geometry) and in 2017, the two targets were also tilted by a small angle, but around the axis connecting the two hot spot (Y axis in our geometry). In the first case, the idea was to have, as initial conditions, an out-of-plane magnetic field, in the same direction as the quadrupolar one, or in the opposite direction. The measurement (essentially from proton radiography) outlined the slowing down of the reconnection process in the "anti-Hall" case, as predicted by [SAB+14]. In the second case, the idea was to initiate a guide-field, i.e. a component of the magnetic field along the current sheet (in the Z direction in our geometry). For totally different reasons than in 2015, such topology also slows down the reconnection process.

This thesis was also intended to prepare some measurements on a much larger facility, namely at the Laser Mega Joule (LMJ). In May and June 2019 Julien Fuchs also leaded a campaign of six shots on LMJ. The idea was to investigate how the reconnection developed with more than two bubbles colliding. We had two shots with three hot spots. Unfortunately, as these experiments were carried out just few weeks before the end of this work, we did not have yet significant results to discuss. But from FCI2 simulations we know that the size of the magnetic ribbons is much larger at LMJ than at LULI2000: we have $L_R = 30$ and $L_W = 20$ at LULI2000, while we have $L_R = 300$ and $L_W = 150$ at LMJ. It appears that the domain size to simulate for the LMJ case is much larger. Keeping a grid size of 0.2, and 100 particle per cells, such simulations would need 3.2 10^9 particles, which is quite prohibitive, and hardly manageable.

To circumvent this problem, we had the idea to modify the initial topology of the bubbles. A simple shrink of the bubbles is quite unrealistic, as it modifies the curvature radius of the magnetic field lines at the reconnection point. While the magnetic tension of the magnetic field lines is important in the energy balance of the process, this would be a too simple approach. We decided to modify the shape of the bubbles to get ellipses. Doing so, we keep a large axis to correctly treat the curvature radius of the magnetic ribbon, but decrease the size of the small axis to decrease the size of the simulation domain. Then

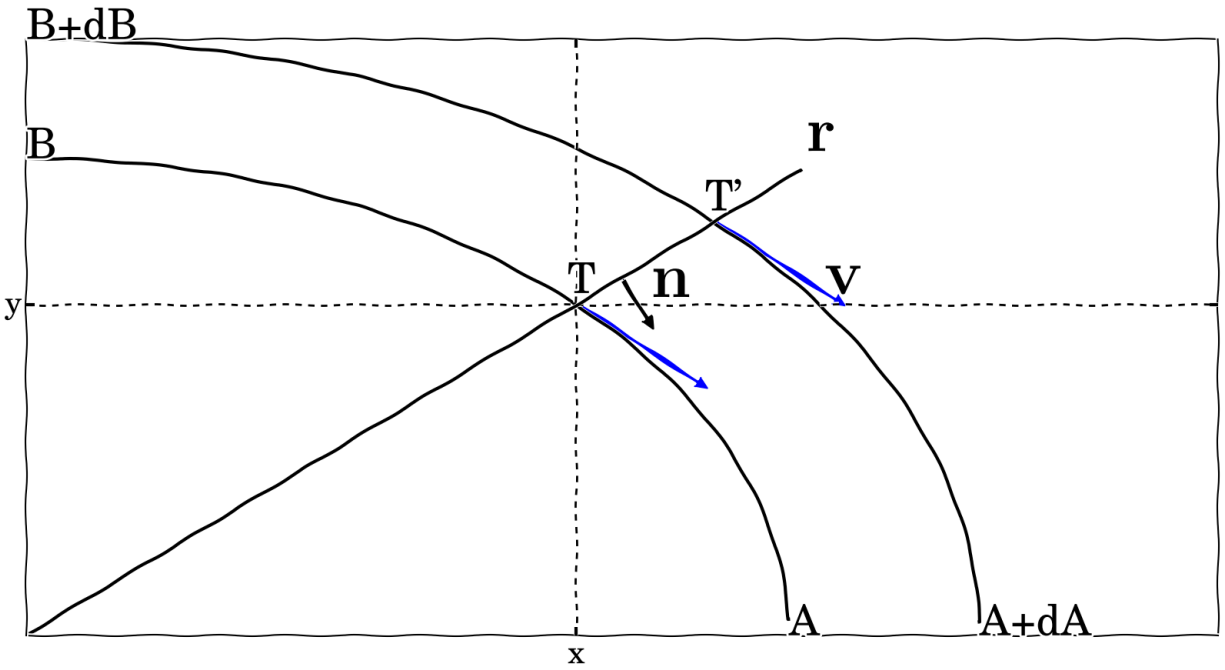

Figure 4.47: Schematically ellipse configuration for magnetic field, where **r** is the radius vector crossing the inner and out border of the magnetic shell, **n** is the normal to **r**, **v** is the vector along **B**, being parallel at points T and T'.

arise the question of getting an appropriate analytical profile for all the needed initial quantities. While there are no constraints for the density profile, the magnetic profile has to be defined correctly to be divergence free. We present how to do so in the next section.

4.5.1 How to define a divergence free magnetic field

In this section we describe the potential ways to initialize ellipses, keeping the free divergence condition for the magnetic field.

We consider the flux tube between the two ellipses, Fig. 4.47 displays the inner ellipse with major axis A and minor axis B, while the outer ellipse is arbitrary chosen such as:

$$\frac{A}{B} = \frac{A + dA}{B + dB}$$
$$\frac{dA}{A} = \frac{dB}{B} \tag{4.10}$$

meaning the associated magnetic ribbon is defined by inner and outer ellipses having the same ratio between major and minor axis. Such a choice simplifies the calculations.

At point B, the local value of the magnetic field is given by $S(y)$, where S is our fifth order polynomial and y is the abscissa along the vector $\mathbf{r}$. The magnetic flux at point B is $S(B)dB$. The Stocks theorem gives $\iiint \nabla \mathbf{B} d\mathbf{r} = \iint \mathbf{B} d\mathbf{S}$. This integral is null on the inner and outer surfaces as the local normals are perpendicular to $\mathbf{B}$. At point $\mathbf{r}(x, y)$ the thickness of the flux tube is $T' - T = (\alpha - 1)T$, as T has coordinates (x, y) we denote $T = (x^2 + y^2)^{1/2}$. Which gives:

$$\frac{x^2}{A^2} + \frac{y^2}{B^2} = 1 \tag{4.11}$$

$$\frac{\alpha^2 x^2}{A^2(1 + \frac{dA}{A})^2} + \frac{\alpha^2 y^2}{B^2(1 + \frac{dB}{B})^2)} = 1$$

giving $\alpha^2 = (1 + \frac{dA}{A})^2 = (1 + \frac{dB}{B})^2$. As a consequence:

$$dT = T' - T = (\alpha - 1)T = \frac{dB}{B}T \tag{4.12}$$

while we have the length of the flux tube at T, we also need to consider its orientation. We call θ the local angle between normal $\mathbf{n}$ and $\mathbf{v}$, where:

- $\mathbf{n}$ is the normal to $\mathbf{r}$: having coordinates $\mathbf{n}(y, -x)$
- $\mathbf{v}$ is the vector along $\mathbf{B}$: having coordinates $\mathbf{v}(y/B^2, -x/A^2)$

from $\mathbf{n}$ and $\mathbf{v}$ we can construct unitary vectors $\hat{\mathbf{n}}$ and $\hat{\mathbf{v}}$. It is important to note that for a given set of A and B, $\mathbf{v}$ only depends on the ratio y/x, as result the direction of $\mathbf{v}$ is the same at T and T'. Hence, $\cos(\theta)$ is also the same, this results from arbitrary choice of the two ellipses with the same ratio Eq. 4.10.

To be divergence free, $\mathbf{B}$ has to satisfy:

$$S(B)dB = S(T)\cos(\theta)dT \tag{4.13}$$

we define:

$$K^2 = \frac{x^2}{A^4} + \frac{y^2}{B^4}$$
$$T = |\mathbf{n}| = \sqrt{x^2 + y^2}$$

and get

$$\cos\theta = \frac{\mathbf{nV}}{TK} = \frac{u^2}{TK}$$

if defining

$$u^2 = \frac{x^2}{A^2} + \frac{y^2}{B^2}$$

The defining of u seems not in agreement with Eq. 4.11. But u has to be defined for whatever point $\mathbf{r}$ in the domain. It means for each point $\mathbf{r}$ a local ellipse has to be defined with a local value of the major and minor axis, that we call $\tilde{A}$ and $\tilde{B}$ different from A and B. These values are defined as:

$$\tilde{A} = \alpha A$$
$$\tilde{B} = \alpha B$$

that gives

$$\frac{\tilde{A}}{\tilde{B}} = \frac{A}{B} \tag{4.14}$$

for this local ellipse Eq. 4.11 also works, we have $\alpha = u$. We can rewrite Eq. 4.13

$$dT = dB\frac{T}{\tilde{B}}$$
$$\frac{dB}{dT} = \frac{uB}{T}$$

Inserting this Eq. in Eq. 4.13 one gets:

$$S(B)B = S(T)\frac{T}{u}\frac{u^2}{TK}$$
$$S(T) = \frac{S(B)BK}{u}$$

4.5.2 Numerical validation and gain

Fig. 4.48 displays the initial density profile in gray scale, where the magnetic field lines are superimposed in blue. This display is intended to show that in the contact region, the magnetic field lines are similar. Two remarks arise:

- the density profile is quite different, as for the ellipses the inner edge of magnetic ribbon is denser than for the circles
- the curvature radius of the magnetic field lines is larger for ellipses along the large axis

This have consequences on the reconnection process. For the first item at least initially we have a larger density gradient, as result larger in-plane electric field associated with the pressure gradient. This should have consequences on the development of the out-of-plane magnetic field, crucial for the dynamics of the reconnection process. For the second item this could increase at least initially the motion of one bubble against the other by magnetic tension. The time evolution of the electric field is needed to answer these questions.

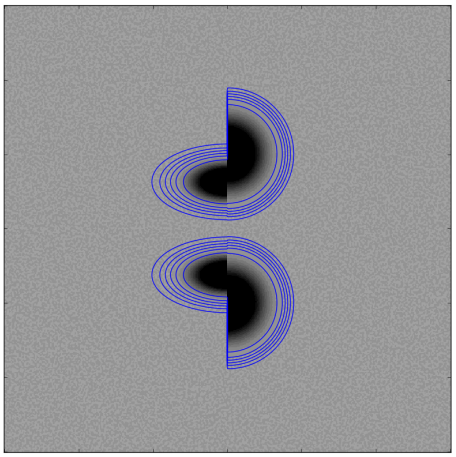

Figure 4.48: Density on the left half for ellipses initialization and on the right for circle initialization. Blue lines represent in-plane projection of the magnetic field lines.

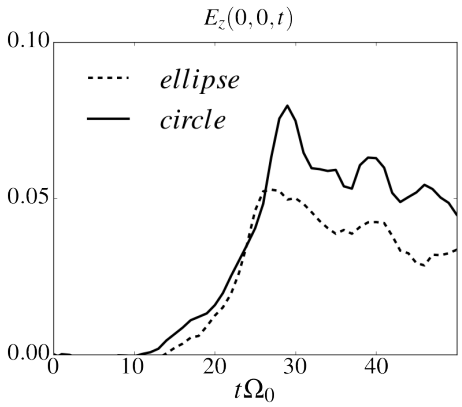

Figure 4.49: Time evolution of reconnecting electric field at X-point for circle and ellipses initialization.

Fig. 4.49 displays the time evolution of the E_z electric field at the X point, for the circles (solid lines) and the ellipses (dashed lines). It appears that the overall structure is quite similar, except that for the ellipses the electric field is decreased by about 30 %. One can conclude that even if the reconnection rate is smaller, the overall dynamics is comparable.

4.5.3 A test case for LMJ experiments

In this section we briefly look at the recent results from LMJ facility.

Fig. 4.50 shows the proton radiography, the upper panel depicts the two bubbles

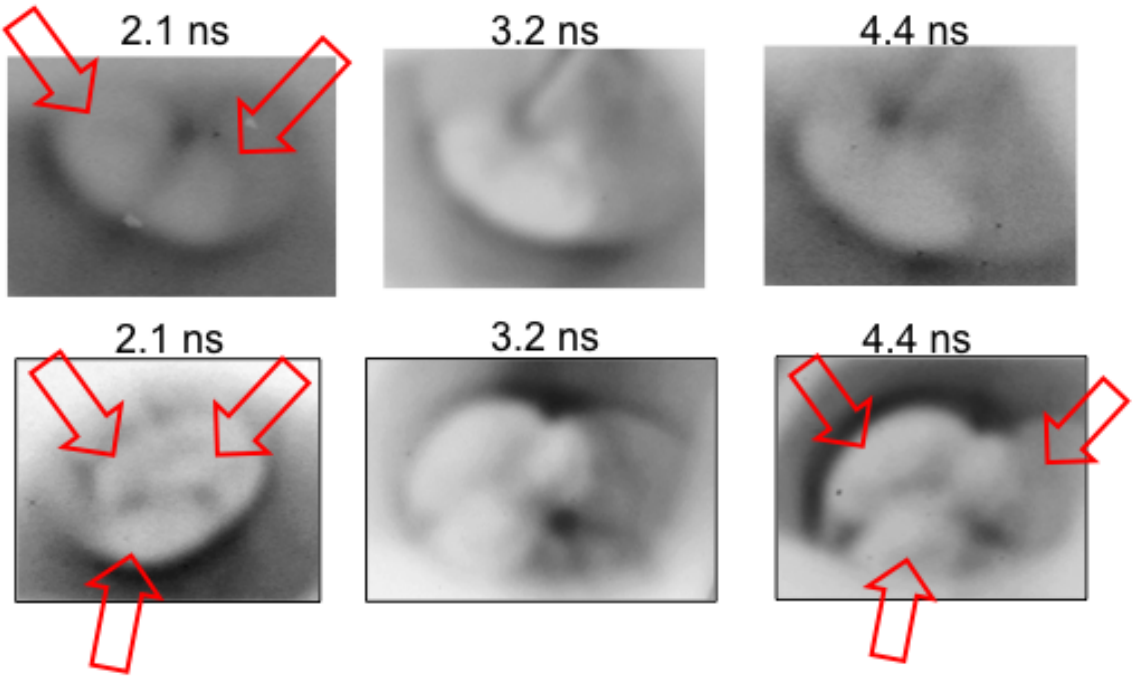

Figure 4.50: RCF films obtained at LMJ in 2019 (courtesy of S. Bolaños) for two bubbles (upper panel), and "shamrock" configuration (lower panel). Red arrows direct to the laser spot.

configuration, while the lower panel portraits the new three spots ("shamrock") configuration. In a such configuration, reconnection should be less efficient with respect to the two ribbons configuration, as we remove the second outflow jet. Recent simulations of asymmetric reconnection also observe only one jet, and states that the development of both Alfvénic outflows is not the necessary condition of fast reconnection [LH16]. But the obtained results should be properly processed before doing any conclusions.

Conclusions

In the thesis we have investigated the main aspects of collisionless magnetic reconnection in laser-induced high energy density plasmas. The work belongs to a numerical investigation as a support for the experimental approach. Because of numerical constraints we focus on the two-dimensional problem and do not take into account the Biermann-Battery effect on the origin of the magnetic field generation in laser experiments. Also we neglect the Nernst effect as well as the Righi-Leduc one, which describe the interplay between the magnetic field transport and the electron heat flux.

While these limitations are significant, the two-dimensional geometry of the two plasma bubbles topology is nonetheless rich in physical processes, and allow to understand many aspects. Among which:

- the dominant contribution of the full electron pressure tensor to the reconnection electric field in the close neighbor of the X point
- the development of a thin electron layer associated with a bifurcated current sheet, which gently slows down the process
- the effect of the high plasma temperature making the reconnection process more impulsive
- the role of continuous particles loading into the bubbles to drive the reconnection in a more realistic way

To point out the variety of possible current configuration, Fig. 4.51 shows three typical current sheets: (a) bifurcated current sheet, (b) single peak current sheet, and (c) "Mexican hat" shape current sheet. The bifurcation process is possible in low beta plasma and associated with the electron heating in the mid-plane, resulting in the electric field generation because of the pressure divergence term. For high beta case of colliding bubbles we observe typical single peak on ion scales. Increasing the compression we see the development of an amplified central peak with two opposite currents. We have never seen contrast single peak asymmetric currents but currents just after the bifurcation have two peaks close to each other. While fluctuating such peaks can exhibit asymmetry properties.

The nature of the forcing term through the magnetic piston described in chapter 4 is a promising point to properly describe the high expansion velocity of the magnetic ribbons even for expansion in the ambient plasma. The consequences of the background population, being mandatory in such configuration as hybrid codes can not manage pure

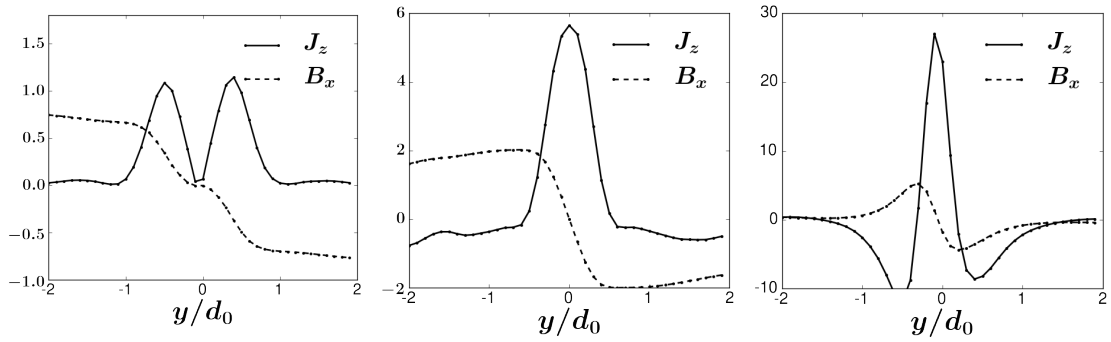

Figure 4.51: Lineout through the X point for out-of-plane current J_z and reversal magnetic field B_x. (a) Harris sheet initial $\beta = 1$ no isotropization on P_{yy} (Table. 3.1), (b) expanding bubbles in the ambient plasma $\beta = 100$ (Table. 4.4), and (c) bubbles with constant density gradient $\beta = 20$ (Section 4.3.6).

vacuum, can be reduced. Up to now only full PIC codes can describe the kinetic of a plasma surrounded by vacuum. While one has to treat usual limits of such code for the proton-electron mass ratio as well as the light to Alfvén speed ratio. The way to deal with vacuum in hybrid codes is yet unclear, it would be a very nice step to be able to manage vacuum to get rid of the parasite effect of the background population essentially because of its inertia.

These efforts have to be pursued to clear the picture of two-dimensional reconnection in HEDP. But the main step will be in a close future to work on the three-dimensional approach to keep the fundamental Biermann-Battery, Nernst and Righi-Leduc effects. For that issue, a promising tool is under development: a new generation hybrid code based on adaptive mesh refinement (by the team of LPP). Such a code will allow to describe in a refined way the region where reconnection develops, and with a coarser resolution in the other region (the inner of the magnetic ribbon as well as the outer one). Of course, the deposition of energy by the laser on the plasma would also be a great improvement, but this one seems —in a close future— inaccessible for such codes.

Bibliography

[AHB+13] Nicolas Aunai, Michael Hesse, Carrie Black, Rebekah Evans, and Maria Kuznetsova. Influence of the dissipation mechanism on collisionless magnetic reconnection in symmetric and asymmetric current layers. *Physics of Plasmas*, 20(4):042901, 2013.

[Alf42] Hannes Alfvén. Existence of electromagnetic-hydrodynamic waves. *Nature*, 150(3805):405, 1942.

[BB07] Naoki Bessho and Amitava Bhattacharjee. Fast collisionless reconnection in electron-positron plasmas. *Physics of Plasmas*, 14(5):056503, 2007.

[BBB+14] PR Bolton, M Borghesi, C Brenner, DC Carroll, C De Martinis, F Fiorini, A Flacco, V Floquet, J Fuchs, Pablo Gallegos, et al. Instrumentation for diagnostics and control of laser-accelerated proton (ion) beams. *Physica Medica*, 30(3):255–270, 2014.

[BDS+01] J Birn, JF Drake, MA Shay, BN Rogers, RE Denton, M Hesse, M Kuznetsova, ZW Ma, A Bhattacharjee, A Otto, et al. Geospace environmental modeling (gem) magnetic reconnection challenge. *Journal of Geophysical Research: Space Physics*, 106(A3):3715–3719, 2001.

[BGH+05] J Birn, Klaus Galsgaard, M Hesse, M Hoshino, J Huba, Giovanni Lapenta, PL Pritchett, K Schindler, L Yin, J Büchner, et al. Forced magnetic reconnection. *Geophysical research letters*, 32(6), 2005.

[Bis86] Dieter Biskamp. Magnetic reconnection via current sheets. *The Physics of fluids*, 29(5):1520–1531, 1986.

[BL91] CK Birdsall and AB Langdon. *Plasma Physics Via Computer Simulation (Bristol, UK.* IOP Publishing, 1991.

[BPL90] Wolfgang Baumjohann, Götz Paschmann, and Hermann Lühr. Characteristics of high-speed ion flows in the plasma sheet. *Journal of Geophysical Research: Space Physics*, 95(A4):3801–3809, 1990.

[Bra65] S. I. Braginskii. Transport processes in a plasma. *Reviews of Plasma Physics*, 1:205, 1965. None.

[BS51] Ludwig Biermann and Arnulf Schlüter. Cosmic radiation and cosmic magnetic fields. ii. origin of cosmic magnetic fields. *Physical Review*, 82(6):863, 1951.

[BS72] Jay P Boris and Ramy A Shanny. *Proceedings: Fourth Conference on Numerical Simulation of Plasmas, November 2, 3, 1970*. Naval Research Laboratory, 1972.

[BSD95] D Biskamp, E Schwarz, and JF Drake. Ion-controlled collisionless magnetic reconnection. *Physical review letters*, 75(21):3850, 1995.

[BTP+16] JL Burch, RB Torbert, TD Phan, L-J Chen, TE Moore, RE Ergun, JP Eastwood, DJ Gershman, PA Cassak, MR Argall, et al. Electron-scale measurements of magnetic reconnection in space. *Science*, 352(6290):aaf2939, 2016.

[BY70] A Bratenahl and CM Yeates. Experimental study of magnetic flux transfer at the hyperbolic neutral point. *The Physics of Fluids*, 13(11):2696–2709, 1970.

[BZ89] Jörg Büchner and Lev M Zelenyi. Regular and chaotic charged particle motion in magnetotaillike field reversals: 1. basic theory of trapped motion. *Journal of Geophysical Research: Space Physics*, 94(A9):11821–11842, 1989.

[CH98] Gerard Chanteur and Christopher C Harvey. Spatial interpolation for four spacecraft: Application to magnetic gradients. *Analysis Methods for Multi-Spacecraft Data*, pages 371–393, 1998.

[CLS17] PA Cassak, Y-H Liu, and MA Shay. A review of the 0.1 reconnection rate problem. *Journal of Plasma Physics*, 83(5), 2017.

[CS07] PA Cassak and MA Shay. Scaling of asymmetric magnetic reconnection: General theory and collisional simulations. *Physics of Plasmas*, 14(10):102114, 2007.

[DHT50] F De Hoffmann and E Teller. Magneto-hydrodynamic shocks. *Physical Review*, 80(4):692, 1950.

[DMZ04] D. C. Delcourt, H. V. Malova, and L. M. Zelenyi. Dynamics of charged particles in bifurcated current sheets: The kappa ap 1 regime. *Journal of Geophysical Research (Space Physics)*, 109:A01222, January 2004.

[DSM+01] E Dattolo, L Suter, MC Monteil, JP Jadaud, N Dague, S Glenzer, R Turner, D Juraszek, B Lasinski, C Decker, et al. Status of our understanding and modeling of x-ray coupling efficiency in laser heated hohlraums. *Physics of Plasmas*, 8(1):260–265, 2001.

[Dun61] James W Dungey. Interplanetary magnetic field and the auroral zones. *Physical Review Letters*, 6(2):47, 1961.

[EH86] EM Epperlein and MG Haines. Plasma transport coefficients in a magnetic field by direct numerical solution of the fokker–planck equation. *The Physics of fluids*, 29(4):1029–1041, 1986.

[FBG11] W Fox, A Bhattacharjee, and K Germaschewski. Fast magnetic reconnection in laser-produced plasma bubbles. *Physical review letters*, 106(21):215003, 2011.

[FBG12] W Fox, A Bhattacharjee, and K Germaschewski. Magnetic reconnection in high-energy-density laser-produced plasmas. *Physics of Plasmas*, 19(5):056309, 2012.

[FFB+14] G Fiksel, W Fox, Amitava Bhattacharjee, DH Barnak, P-Y Chang, K Germaschewski, SX Hu, and PM Nilson. Magnetic reconnection between colliding magnetized laser-produced plasma plumes. *Physical Review Letters*, 113(10):105003, 2014.

[fft] Fftw. `http://www.fftw.org/`.

[FKR63] Harold P Furth, John Killeen, and Marshall N Rosenbluth. Finite-resistivity instabilities of a sheet pinch. *The physics of Fluids*, 6(4):459–484, 1963.

[Fra74] A. G. Frank. Neutral current layers in a plasma. page 108–166, 1974.

[GLVC12] W Gekelman, E Lawrence, and B Van Compernolle. Three-dimensional reconnection involving magnetic flux ropes. *The Astrophysical Journal*, 753(2):131, 2012.

[GMF+05] Vincent Génot, F Mottez, G Fruit, P Louarn, J-A Sauvaud, and A Balogh. Bifurcated current sheet: Model and cluster observations. *Planetary and Space Science*, 53(1-3):229–235, 2005.

[GVD+17] Tingyu Gou, Astrid M Veronig, Ewan C Dickson, Aaron Hernandez-Perez, and Rui Liu. Direct observation of two-step magnetic reconnection in a solar flare. *The Astrophysical Journal Letters*, 845(1):L1, 2017.

[Hai86] MG Haines. Heat flux effects in ohm's law. *Plasma physics and controlled fusion*, 28(11):1705, 1986.

[Har62] Eo G Harris. On a plasma sheath separating regions of oppositely directed magnetic field. *Il Nuovo Cimento (1955-1965)*, 23(1):115–121, 1962.

[HP90] G. W. Hammett and F. W. Perkins. Fluid moment models for landau damping with application to the ion-temperature-gradient instability. *Physical Review Letters*, 64:3019–3022, jun 1990. None.

[HSBK99] Michael Hesse, Karl Schindler, Joachim Birn, and Masha Kuznetsova. The diffusion region in collisionless magnetic reconnection. *Physics of Plasmas*, 6(5):1781–1795, 1999.

[HSL+17] JD Hare, L Suttle, SV Lebedev, NF Loureiro, A Ciardi, GC Burdiak, JP Chittenden, T Clayson, C Garcia, N Niasse, et al. Anomalous heating and plasmoid formation in a driven magnetic reconnection experiment. *Physical review letters*, 118(8):085001, 2017.

[HW93] Michael Hesse and Dan Winske. Hybrid simulations of collisionless ion tearing. *Geophysical research letters*, 20(12):1207–1210, 1993.

[HW94] Michael Hesse and Dan Winske. Hybrid simulations of collisionless reconnection in current sheets. *Journal of Geophysical Research: Space Physics*, 99(A6):11177–11192, 1994.

[HWK95] M. Hesse, D. Winske, and M. M. Kuznetsova. Hybrid modeling of collisionless reconnection in two-dimensional current sheets: Simulations. *J. Geophys. Res.*, 100:21815–21826, nov 1995.

[JRKT16] AS Joglekar, Christopher Paul Ridgers, RJ Kingham, and AGR Thomas. Kinetic modeling of nernst effect in magnetized hohlraums. *Physical Review E*, 93(4):043206, 2016.

[JYHK98] Hantao Ji, Masaaki Yamada, Scott Hsu, and Russell Kulsrud. Experimental test of the sweet-parker model of magnetic reconnection. *Physical Review Letters*, 80(15):3256, 1998.

[KH85] TH Kho and MG Haines. Nonlinear kinetic transport of electrons and magnetic field in laser-produced plasmas. *Physical review letters*, 55(8):825, 1985.

[KHW98] M. M. Kuznetsova, M. Hesse, and D. Winske. Kinetic quasi-viscous and bulk flow inertia effects in collisionless magnetotail reconnection. *J. Geophys. Res.*, 103:199–214, January 1998.

[KJG+07] A Kuritsyn, Hantao Ji, SP Gerhardt, Y Ren, and M Yamada. Effects of global boundary and local collisionality on magnetic reconnection in a laboratory plasma. *Geophysical Research Letters*, 34(16), 2007.

[LAB+14] L Lancia, B Albertazzi, C Boniface, A Grisollet, R Riquier, F Chaland, K-C Le Thanh, Ph Mellor, P Antici, S Buffechoux, et al. Topology of megagauss magnetic fields and of heat-carrying electrons produced in a high-power laser-solid interaction. *Physical review letters*, 113(23):235001, 2014.

[LCD+96] JN Leboeuf, Kuan-Ren Chen, JM Donato, DB Geohegan, CL Liu, AA Puretzky, and RF Wood. Modeling of plume dynamics in laser ablation processes

for thin film deposition of materials. *Physics of Plasmas*, 3(5):2203–2209, 1996.

[LDK+13] Yi-Hsin Liu, W Daughton, H Karimabadi, H Li, and V Roytershteyn. Bifurcated structure of the electron diffusion region in three-dimensional magnetic reconnection. *Physical review letters*, 110(26):265004, 2013.

[LED+09] A Le, J Egedal, W Daughton, W Fox, and N Katz. Equations of state for collisionless guide-field reconnection. *Physical review letters*, 102(8):085001, 2009.

[LEV12] A Lazarian, Gregory L Eyink, and ET Vishniac. Relation of astrophysical turbulence and magnetic reconnection. *Physics of Plasmas*, 19(1):012105, 2012.

[LH16] Yi-Hsin Liu and Michael Hesse. Suppression of collisionless magnetic reconnection in asymmetric current sheets. *Physics of Plasmas*, 23(6):060704, 2016.

[LHG+17] Yi-Hsin Liu, M Hesse, F Guo, W Daughton, H Li, PA Cassak, and MA Shay. Why does steady-state magnetic reconnection have a maximum local rate of order 0.1? *Physical Review Letters*, 118(8):085101, 2017.

[LL92] PM Lyster and J-N Leboeuf. A fluid-ion and particle-electron model for low-frequency plasma instabilities. *Journal of Computational Physics*, 102(1):180–193, 1992.

[LMB85] J. F. Luciani, P. Mora, and A. Bendib. Magnetic field and nonlocal transport in laser-created plasmas. *Phys. Rev. Lett.*, 55:2421–2424, Nov 1985.

[LMV83] JF Luciani, P Mora, and J Virmont. Nonlocal heat transport due to steep temperature gradients. *Physical review letters*, 51(18):1664, 1983.

[LP82] B Lembege and R Pellat. Stability of a thick two-dimensional quasineutral sheet. *The Physics of Fluids*, 25(11):1995–2004, 1982.

[LR56] Peter D Lax and Robert D Richtmyer. Survey of the stability of linear finite difference equations. *Communications on pure and applied mathematics*, 9(2):267–293, 1956.

[LSF+07] C. K. Li, F. H. Séguin, J. A. Frenje, J. R. Rygg, R. D. Petrasso, R. P. J. Town, O. L. Landen, J. P. Knauer, and V. A. Smalyuk. Observation of megagauss-field topology changes due to magnetic reconnection in laser-produced plasmas. *Phys. Rev. Lett.*, 99:055001, Aug 2007.

[LU15] NF Loureiro and DA Uzdensky. Magnetic reconnection: from the sweet–parker model to stochastic plasmoid chains. *Plasma Physics and Controlled Fusion*, 58(1):014021, 2015.

[LV99] A Lazarian and Ethan T Vishniac. Reconnection in a weakly stochastic field. *The Astrophysical Journal*, 517(2):700, 1999.

[MPB+08] FS Mozer, PL Pritchett, J Bonnell, D Sundkvist, and MT Chang. Observations and simulations of asymmetric magnetic field reconnection. *Journal of Geophysical Research: Space Physics*, 113(A1), 2008.

[NBR+02] R Nakamura, W Baumjohann, A Runov, M Volwerk, TL Zhang, B Klecker, Y Bogdanova, A Roux, A Balogh, H Reme, et al. Fast flow during current sheet thinning. *Geophysical research letters*, 29(23):55–1, 2002.

[NFS06] Ph D Nicolaï, J-LA Feugeas, and GP Schurtz. A practical nonlocal model for heat transport in magnetized laser plasmas. *Physics of plasmas*, 13(3):032701, 2006.

[NN73] A Nishida and Nl Nagayama. Synoptic survey for the neutral line in the magnetotail during the substorm expansion phase. *Journal of Geophysical Research*, 78(19):3782–3798, 1973.

[NWK+06] P. M. Nilson, L. Willingale, M. C. Kaluza, C. Kamperidis, S. Minardi, M. S. Wei, P. Fernandes, M. Notley, S. Bandyopadhyay, M. Sherlock, R. J. Kingham, M. Tatarakis, Z. Najmudin, W. Rozmus, R. G. Evans, M. G. Haines, A. E. Dangor, and K. Krushelnick. Magnetic reconnection and plasma dynamics in two-beam laser-solid interactions. *Phys. Rev. Lett.*, 97:255001, Dec 2006.

[NYH+84] A. Nishiguchi, T. Yabe, M. G. Haines, M. Psimopoulos, and H. Takewaki. Convective amplification of magnetic fields in laser-produced plasmas by the nernst effect. *Phys. Rev. Lett.*, 53:262–265, Jul 1984.

[NZS+13] T Nagai, S Zenitani, I Shinohara, R Nakamura, M Fujimoto, Y Saito, and T Mukai. Ion and electron dynamics in the ion-electron decoupling region of magnetic reconnection with geotail observations. *Journal of Geophysical Research: Space Physics*, 118(12):7703–7713, 2013.

[OOK74] N Ohyabu, S Okamura, and N Kawashima. Simulation experiment of the current dissipation and plasma acceleration in the neutral sheet. *Journal of Geophysical Research*, 79(13):1977–1979, 1974.

[ØPF+01] M Øieroset, TD Phan, M Fujimoto, RP Lin, and RP Lepping. In situ detection of collisionless reconnection in the earth's magnetotail. *Nature*, 412(6845):414, 2001.

[Orf95] Sophocles J Orfanidis. *Introduction to signal processing*. Prentice-Hall, Inc., 1995.

[Par63] Eugene N Parker. The solar-flare phenomenon and the theory of reconnection and annihiliation of magnetic fields. *The Astrophysical Journal Supplement Series*, 8:177, 1963.

[PCP91] R Pellat, FV Coroniti, and PL Pritchett. Does ion tearing exist? *Geophysical Research Letters*, 18(2):143–146, 1991.

[Pet64] Harry E Petschek. Magnetic field annihilation. *NASA Special Publication*, 50:425, 1964.

[Pri05] PL Pritchett. The "newton challenge": Kinetic aspects of forced magnetic reconnection. *Journal of Geophysical Research: Space Physics*, 110(A10), 2005.

[RDDS01] BN Rogers, RE Denton, JF Drake, and MA Shay. Role of dispersive waves in collisionless magnetic reconnection. *Physical Review Letters*, 87(19):195004, 2001.

[RKT08] C. P. Ridgers, R. J. Kingham, and A. G. R. Thomas. Magnetic cavitation and the reemergence of nonlocal transport in laser plasmas. *Phys. Rev. Lett.*, 100:075003, Feb 2008.

[RLF+15] MJ Rosenberg, CK Li, W Fox, I Igumenshchev, FH Séguin, RPJ Town, JA Frenje, C Stoeckl, V Glebov, and RD Petrasso. A laboratory study of asymmetric magnetic reconnection in strongly driven plasmas. *Nature communications*, 6:6190, 2015.

[RNB+03] A Runov, R Nakamura, W Baumjohann, TL Zhang, M Volwerk, H-U Eichelberger, and A Balogh. Cluster observation of a bifurcated current sheet. *Geophysical Research Letters*, 30(2), 2003.

[RSN+06] A Runov, VA Sergeev, R Nakamura, W Baumjohann, S Apatenkov, Y Asano, T Takada, M Volwerk, Z Vörös, TL Zhang, et al. Local structure of the magnetotail current sheet: 2001 cluster observations. In *Annales Geophysicae*, volume 24, pages 247–262, 2006.

[SAB+14] Roch Smets, N Aunai, Gérard Belmont, C Boniface, and J Fuchs. On the relationship between quadrupolar magnetic field and collisionless reconnection. *Physics of Plasmas*, 21(6):062111, 2014.

[Sai15] Miho Saito. Themis two-point measurements of the cross-tail current density: A thick bifurcated current sheet in the near-earth plasma sheet. *Journal of Geophysical Research: Space Physics*, 120(8):6258–6275, 2015.

[SB03] I Silin and J Büchner. Nonlinear instability of thin current sheets in antiparallel and guided magnetic fields. *Physics of Plasmas*, 10(9):3561–3570, 2003.

[SD08] Jack Scudder and William Daughton. "illuminating" electron diffusion regions of collisionless magnetic reconnection using electron agyrotropy. *Journal of Geophysical Research: Space Physics*, 113(A6), 2008.

[SDDB98] Michael A Shay, James F Drake, Richard E Denton, and D Biskamp. Structure of the dissipation region during collisionless magnetic reconnection. *Journal of Geophysical Research: Space Physics*, 103(A5):9165–9176, 1998.

[SDRD99] MA Shay, JF Drake, BN Rogers, and RE Denton. The scaling of collisionless, magnetic reconnection for large systems. *Geophysical research letters*, 26(14):2163–2166, 1999.

[SDSM05] M Swisdak, JF Drake, MA Shay, and JG McIlhargey. Transition from antiparallel to component magnetic reconnection. *Journal of Geophysical Research: Space Physics*, 110(A5), 2005.

[SFK73] SI Syrovatskii, AG Frank, and AZ Khodzhaev. Current distribution near the null line of a magnetic field and turbulent plasma resistance. *Soviet Physics Technical Physics*, 18:580, 1973.

[SG06] H Schmitz and R Grauer. Kinetic vlasov simulations of collisionless magnetic reconnection. *Physics of plasmas*, 13(9):092309, 2006.

[SH53] L. Spitzer and R. Härm. Transport Phenomena in a Completely Ionized Gas. *Physical Review*, 89:977–981, March 1953.

[SHB88] K Schindler, M Hesse, and J Birn. General magnetic reconnection, parallel electric fields, and helicity. *Journal of Geophysical Research: Space Physics*, 93(A6):5547–5557, 1988.

[SK07] Tooru Sugiyama and Kanya Kusano. Multi-scale plasma simulation by the interlocking of magnetohydrodynamic model and particle-in-cell kinetic model. *Journal of Computational Physics*, 227(2):1340–1352, 2007.

[SKH+00] RA Snavely, MH Key, SP Hatchett, TE Cowan, M Roth, TW Phillips, MA Stoyer, EA Henry, TC Sangster, MS Singh, et al. Intense high-energy proton beams from petawatt-laser irradiation of solids. *Physical review letters*, 85(14):2945, 2000.

[Sme13] R. Smets. The heckle code. *Technical Report No. 1, Lab. Phys. Plasmas*, 2013.

[Spe65] TW Speiser. Particle trajectories in model current sheets: 1. analytical solutions. *Journal of Geophysical Research*, 70(17):4219–4226, 1965.

[Swe58] PA Sweet. The production of high energy particles in solar flares. *Il Nuovo Cimento (1955-1965)*, 8(2):188–196, 1958.

[TB13] Rudolf A Treumann and Wolfgang Baumjohann. Collisionless magnetic reconnection in space plasmas. *Frontiers in Physics*, 1:31, 2013.

[TBP+18] RB Torbert, JL Burch, TD Phan, M Hesse, MR Argall, J Shuster, RE Ergun, Love Alm, R Nakamura, KJ Genestreti, et al. Electron-scale dynamics of the diffusion region during symmetric magnetic reconnection in space. *Science*, 362(6421):1391–1395, 2018.

[TFS10] Kentaro G Tanaka, Masaki Fujimoto, and Iku Shinohara. Physics of magnetopause reconnection: A study of the combined effects of density asymmetry, velocity shear, and guide field. *International Journal of Geophysics*, 2010, 2010.

[UK00] DA Uzdensky and RM Kulsrud. Two-dimensional numerical simulation of the resistive reconnection layer. *Physics of Plasmas*, 7(10):4018–4030, 2000.

[VKA+04] A Vaivads, Y Khotyaintsev, M André, A Retino, SC Buchert, BN Rogers, P Décréau, G Paschmann, and TD Phan. Structure of the magnetic reconnection diffusion region from four-spacecraft observations. *Physical review letters*, 93(10):105001, 2004.

[WCL+97] RF Wood, Kuan-Ren Chen, JN Leboeuf, AA Puretzky, and DB Geohegan. Dynamics of plume propagation and splitting during pulsed-laser ablation. *Physical Review Letters*, 79(8):1571, 1997.

[WH94] D. Winske and M. Hesse. Hybrid modeling of magnetic reconnection in space plasmas. *Physica D Nonlinear Phenomena*, 77:268–275, October 1994.

[WHBG15] L. Wang, A. H. Hakim, A. Bhattacharjee, and K. Germaschewski. Comparison of multi-fluid moment models with particle-in-cell simulations of collisionless magnetic reconnection. *Physics of Plasmas*, 22(1):012108, January 2015.

[WLC+01] SC Wilks, AB Langdon, TE Cowan, M Roth, M Singh, S Hatchett, MH Key, D Pennington, A MacKinnon, and RA Snavely. Energetic proton generation in ultra-intense laser–solid interactions. *Physics of plasmas*, 8(2):542–549, 2001.

[WNK+10] L Willingale, PM Nilson, MC Kaluza, AE Dangor, RG Evans, P Fernandes, MG Haines, C Kamperidis, RJ Kingham, CP Ridgers, et al. Proton deflectometry of a magnetic reconnection geometry. *Physics of Plasmas*, 17(4):043104, 2010.

[WQ86] D Winske and KB Quest. Electromagnetic ion beam instabilities: Comparison of one-and two-dimensional simulations. *Journal of Geophysical Research: Space Physics*, 91(A8):8789–8797, 1986.

[WYO+03] Dan Winske, Lin Yin, Nick Omidi, Homa Karimabadi, and Kevin Quest. Hybrid simulation codes: Past, present and future—a tutorial. In *Space plasma simulation*, pages 136–165. Springer, 2003.

[YJH+97] Masaaki Yamada, Hantao Ji, Scott Hsu, Troy Carter, Russell Kulsrud, Yasushi Ono, and Francis Perkins. Identification of y-shaped and o-shaped diffusion regions during magnetic reconnection in a laboratory plasma. *Physical review letters*, 78(16):3117, 1997.

[YWDC04] L Yin, D Winske, W Daughton, and FV Coroniti. Electron quasi-viscous effects in collisionless slow-mode shocks. *Geophysical research letters*, 31(9), 2004.

[YWGB01] L. Yin, D. Winske, S. P. Gary, and J. Birn. Hybrid and Hall-MHD simulations of collisionless reconnection: Dynamics of the electron pressure tensor. *J. Geophys. Res.*, 106:10761–10776, jun 2001.

[ZHK+11] S. Zenitani, M. Hesse, A. Klimas, C. Black, and M. Kuznetsova. The inner structure of collisionless magnetic reconnection: The electron-frame dissipation measure and Hall fields. *Phys. Plasmas*, 18(12):122108–122108, December 2011.

[ZMP03] L. M. Zelenyĭ, H. V. Malova, and V. Y. Popov. Splitting of Thin Current Sheets in the Earth's Magnetosphere. *Soviet Journal of Experimental and Theoretical Physics Letters*, 78:296–299, September 2003.

[ZSNW13] Seiji Zenitani, Iku Shinohara, Tsugunobu Nagai, and Tomohide Wada. Kinetic aspects of the ion current layer in a reconnection outflow exhaust. *Physics of Plasmas*, 20(9):092120, 2013.

[ZY16] Ellen G Zweibel and Masaaki Yamada. Perspectives on magnetic reconnection. *Proceedings of the Royal Society A: Mathematical, Physical and Engineering Sciences*, 472(2196):20160479, 2016.

Appendix A

Algorithm

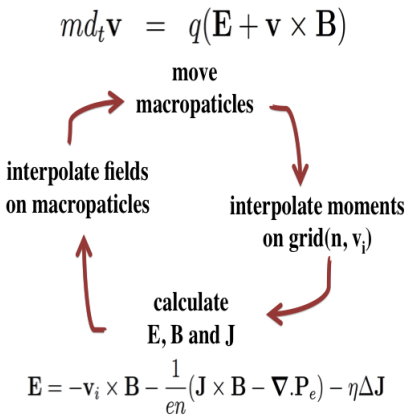

Figure 1: The full cycle of the simulation.

One cycle of the simulation is illustrated on the Fig. 1. First we move particles, then gather the fluid moments density and flow velocity. These are used in electro magnetic fields calculation. The updated fields are implied to the particles, and cycle repeats. For the particles motion, we use so called "Buneman" pusher [BS72]. We use predictor-corrector scheme [WQ86] centered both in space and time.

.1 Main part

Predictor :

Calculations start with the predictor step, first we find velocities

- $\mathbf{v}_{n+1/2} = \mathbf{v}_{n-1/2} + \frac{q\Delta t}{m_p}\left[\mathbf{E}_n + \frac{\mathbf{v}_{n+1/2} + \mathbf{v}_{n-1/2}}{2} \times \mathbf{B}_n\right]$

then we calculate particles displacement

- $\mathbf{x}_{n+1} = \mathbf{x}_n + \Delta t \mathbf{v}_{n+1/2}$

then gather moments on grid

- $\mathbf{N}_{n+1/2} = \Sigma_s q_s (S_n + S_{n+1})/2$
- $\mathbf{V}_{n+1/2} = \Sigma_s (S_n + S_{n+1}) \mathbf{v}_{n+1/2} / 2\mathbf{N}_{n+1/2}$

and calculate magnetic field and current

- $\mathbf{B}_{n+1/2} = \mathbf{B}_n - \dfrac{\Delta t}{2} \boldsymbol{\nabla} \times \mathbf{E}_n$
- $\mathbf{J}_{n+1/2} = \boldsymbol{\nabla} \times \mathbf{B}_{n+1/2}$

use appropriate closure equation for pressure

- $\mathbf{P}_{n+1/2}$

the main part is the electron Ohm's law

- $\mathbf{E}_{n+1/2} = -\mathbf{V}_{n+1/2} \times \mathbf{B}_{n+1/2} + \dfrac{1}{N_{n+1/2}} \left(\mathbf{J}_{n+1/2} \times \mathbf{B}_{n+1/2} - \boldsymbol{\nabla} P_{n+1/2} \right) + \eta \mathbf{J}_{n+1/2}$

the last step is to extrapolate em fields for the next time step

- $\mathbf{E}_{n+1} = -\mathbf{E}_n + 2\mathbf{E}_{n+1/2}$
- $\mathbf{B}_{n+1} = \mathbf{B}_{n+1/2} - \dfrac{\Delta t}{2} \boldsymbol{\nabla} \times \mathbf{E}_{n+1}$
- $\mathbf{J}_{n+1} = \boldsymbol{\nabla} \times \mathbf{B}_{n+1}$

the same must be repeat for corrector step :

Corrector :

- $\mathbf{v}_{n+3/2} = \mathbf{v}_{n+1/2} + \dfrac{q \Delta t}{m_p} \left[\mathbf{E}_{n+1} + \dfrac{\mathbf{v}_{n+3/2} + \mathbf{v}_{n+1/2}}{2} \times \mathbf{B}_{n+1} \right]$
- $\mathbf{x}_{n+2} = \mathbf{x}_{n+1} + \Delta t \mathbf{v}_{n+3/2}$
- $\mathbf{N}_{n+3/2} = \Sigma_s q_s (S_{n+1} + S_{n+2})/2$
- $\mathbf{V}_{n+3/2} = \Sigma_s (S_{n+1} + S_{n+2}) \mathbf{v}_{n+3/2} / 2\mathbf{N}_{n+3/2}$
- $\mathbf{B}_{n+3/2} = \mathbf{B}_{n+1} - \dfrac{\Delta t}{2} \boldsymbol{\nabla} \times \mathbf{E}_{n+1}$
- $\mathbf{J}_{n+1/2} = \boldsymbol{\nabla} \times \mathbf{B}_{n+1/2}$
- $\mathbf{P}_{n+3/2}$ with the appropriate law.
- $\mathbf{E}_{n+3/2} = -\mathbf{V}_{n+3/2} \times \mathbf{B}_{n+3/2} + \dfrac{1}{N_{n+3/2}} \left(\mathbf{J}_{n+3/2} \times \mathbf{B}_{n+3/2} - \boldsymbol{\nabla} P_{n+3/2} \right) + \eta \mathbf{J}_{n+3/2}$

the last step is to interpolate em fields for the next time step

- $\mathbf{E}_{n+1} = \dfrac{1}{2} (\mathbf{E}_{n+1/2} + \mathbf{E}_{n+3/2})$
- $\mathbf{B}_{n+1} = \mathbf{B}_{n+1/2} - \dfrac{\Delta t}{2} \boldsymbol{\nabla} \times \mathbf{E}_{n+1}$
- $\mathbf{J}_{n+1} = \boldsymbol{\nabla} \times \mathbf{B}_{n+1}$

.2 Implicit scheme for the pressure tensor

Here we present implicit scheme for the pressure tensor integration

$\partial_t \mathbf{P} = D(\mathbf{P}) + C(\mathbf{P}) + I(\mathbf{P})$ with the 3 operators :
Driver : $D(\mathbf{P}) = -\mathbf{U}.\boldsymbol{\nabla}\mathbf{P} - \mathbf{P}\boldsymbol{\nabla}.\mathbf{U} - \mathbf{P}.\boldsymbol{\nabla}\mathbf{U} - (\mathbf{P}.\boldsymbol{\nabla}\mathbf{U})^T$
Cyclotron : $C(\mathbf{P}) = -\dfrac{e}{m} [\mathbf{P} \times \mathbf{B} + (\mathbf{P} \times \mathbf{B})^T]$

Izotropization : $I(\mathbf{P}) = -\frac{\Omega_e}{\tau_i}(\mathbf{P} - P_0\mathbf{1})$ with $P_0 = 1/3\mathrm{Tr}(\mathbf{P})$

τ_i being an izotropization time and $\mathbf{U}$ the electron velocity.

- Up-wind scheme for time integration of D.

- Semi-implicit scheme for C with an α coefficient.
- Izotropization term I is of weak importance, and is for simplicity not centered in time.

We solve the following equation

$$[\mathbf{1} - \alpha\Delta t C](\mathbf{P}_{n+1/2}) = \mathbf{P}_{n-1/2} + \Delta t[(1-\alpha)C(\mathbf{P}_{n-1/2}) - I(\mathbf{P}_{n-1/2}) + D(\mathbf{P}_n)] \equiv \mathbf{F}$$

- The $\mathbf{P}$ term can be linearly deduced from the $\mathbf{F}$ term, provided to be in the field-aligned frame.
- In C operator, $\Omega_e = eB/m_e$ where B is the local field and m_e the electron mass.
- With $\tau = \alpha\Omega_e\Delta t$, the implicit equation $[\mathbf{1} - \alpha\Delta t C](\mathbf{P}) = \mathbf{F}$ has the solution (direction 0 is along the magnetic field, 1 & 2 perpendicular to the magnetic field)

$$P_{00} = F_{00}$$
$$P_{01} = \frac{F_{01} - \tau F_{02}}{1+\tau^2}$$
$$P_{02} = \frac{F_{02} + \tau F_{01}}{1+\tau^2}$$
$$P_{11} = \frac{F_{11}(1+2\tau^2) + 2\tau^2 F_{22} - 2\tau F_{12}}{1+4\tau^2}$$
$$P_{12} = \frac{\tau F_{11} + F_{12} - \tau F_{22}}{1+4\tau^2}$$
$$P_{22} = \frac{F_{11}(2\tau^2) + 2\tau F_{12} + (1+2\tau^2)F_{22}}{1+4\tau^2}$$

Predictor :

- $\mathbf{C}_{n-1/2} = -\Omega_{n-1/2}\left[\mathbf{P}_{n-1/2} \times b_{n-1/2} + \left(\mathbf{P}_{n-1/2} \times \mathbf{b}_{n-1/2}\right)^T\right]$
- $\mathbf{I}_{n-1/2} = -\dfrac{\Omega_{n-1/2}}{\tau_i}\mathbf{P}_{n-1/2} - \dfrac{\mathbf{1}}{3}\mathrm{Tr}(\mathbf{P}_{n-1/2})$
- $\mathbf{F} = \mathbf{P}_{n-1/2} + \Delta t[(1-\alpha)\mathbf{C}_{n-1/2} - \mathbf{I}_{n-1/2} + \mathbf{D}_n]$[1]
- Rotate $\mathbf{F}$ to $\mathbf{B}_{n+1/2}$ aligned coordinate system.
- Solve $\mathbf{P}_{n+1/2}$ from $\mathbf{F}$ (linear system).
- Rotate $\mathbf{P}_{n+1/2}$ to cartesian coordinate system.
- $\mathbf{U}_{n+1/2} = \mathbf{V}_{n+1/2} - \dfrac{\mathbf{J}_{n+1/2}}{N_{n+1/2}}$
- $\mathbf{D}_{n+1/2}$ calculated with $\mathbf{U}_{n+1/2}$ and $\mathbf{P}_{n+1/2}$ (up-wind).
- $\mathbf{D}_{n+1} = -\mathbf{D}_n + 2\mathbf{D}_{n+1/2}$ (extrapolation)

Corrector :

- $\mathbf{C}_{n+1/2} = -\Omega_{n+1/2}\left[\mathbf{P}_{n+1/2} \times b_{n+1/2} + \left(\mathbf{P}_{n+1/2} \times \mathbf{b}_{n+1/2}\right)^T\right]$
- $\mathbf{I}_{n+1/2} = -\dfrac{\Omega_{n+1/2}}{\tau_i}\mathbf{P}_{n+1/2} - \dfrac{\mathbf{1}}{3}\mathrm{Tr}(\mathbf{P}_{n+1/2})$
- $\mathbf{F} = \mathbf{P}_{n+1/2} + \Delta t[(1-\alpha)\mathbf{C}_{n+1/2} - \mathbf{I}_{n+1/2} + \mathbf{D}_{n+1}]$
- Rotate $\mathbf{F}$ to $\mathbf{B}_{n+3/2}$ aligned coordinate system.
- Solve $\mathbf{P}_{n+3/2}$ from $\mathbf{F}$ (linear system).
- Rotate $\mathbf{P}_{n+3/2}$ to cartesian coordinate system.
- $\mathbf{U}_{n+3/2} = \mathbf{V}_{n+3/2} - \dfrac{\mathbf{J}_{n+3/2}}{N_{n+3/2}}$
- $\mathbf{D}_{n+3/2}$ calculated with $\mathbf{U}_{n+3/2}$ and $\mathbf{P}_{n+3/2}$ (up-wind).
- $\mathbf{D}_{n+1} = \dfrac{1}{2}(\mathbf{D}_{n+1/2} + \mathbf{D}_{n+3/2})$ (interpolation).

.3 Explicit Subcycling scheme for the pressure tensor

Predictor :

- $\mathbf{P}_{n+1/2} = \mathbf{P}_{n-1/2} + \Delta t D_n + C_{sub}$

  1. $\mathbf{C}_{sub} = (-1)\sum_{i=0}^{N}\dfrac{\Delta t}{N}\Omega_i\left[[P_i \otimes b_i] + [P_i \otimes b_i]^T\right]$

     i. $\mathbf{P}_i = P_{n-1/2} + \dfrac{\Delta t}{N}\Omega_i\left[[P_i \otimes b_i] + [P_i \otimes b_i]^T\right] \times (i)$

     ii. $\mathbf{b}_i = b_{n-1/2} + \dfrac{b_{n+1/2} - b_{n-1/2}}{N} \times (i)$ and $\mathbf{\Omega}_i = \frac{\mathbf{B}_i}{\mathbf{m}_e}$

  2 $\mathbf{W}^e_{n+1/2} = V_{n+1/2} - \dfrac{J_{n+1/2}}{N_{n+1/2}}$

  3. $\mathbf{D}_{n+1/2} = -\left[W^e_{n+1/2}.\nabla P_{n+1/2} + P_{n+1/2}\nabla.W^e_{n+1/2} + P_{n+1/2}.\nabla W^e_{n+1/2} + \left(P_{n+1/2}.\nabla W^e_{n+1/2}\right)^T\right]$

  4. $\mathbf{D}_{n+1} = -\mathbf{D}_n + 2\mathbf{D}_{n+1/2}$

[1] this last term coming from previous time step

Corrector :

- $\mathbf{P}_{n+3/2} = \mathbf{P}_{n+1/2} + \Delta t D_{n+1} + C_{sub}$

  1. $\mathbf{C}_{sub} = (-1)\sum_{i=0}^{N} \frac{\Delta t}{N} \Omega_i \left[[P_i \otimes b_i] + [P_i \otimes b_i]^T \right]$

     i. $\mathbf{P}_i = P_{n+1/2} + \frac{\Delta t}{N} \Omega_i \left[[P_i \otimes b_i] + [P_i \otimes b_i]^T \right] \times (i)$

     ii. $\mathbf{b}_i = b_{n+1/2} + \frac{b_{n+3/2} - b_{n+1/2}}{N} \times (i)$ and $\mathbf{\Omega}_i = \frac{\mathbf{B}_i}{\mathbf{m}_e}$

  2. $\mathbf{W}^e_{n+3/2} = V_{n+3/2} - \frac{J_{n+3/2}}{N_{n+3/2}}$

  3. $\mathbf{D}_{n+3/2} = -\left[W^e_{n+3/2}.\nabla P_{n+3/2} + P_{n+3/2}\nabla.W^e_{n+3/2} + P_{n+3/2}.\nabla W^e_{n+3/2} + \left(P_{n+3/2}.\nabla W^e_{n+3/2}\right)^T \right]$

  4. $\mathbf{D}_{n+1} = \frac{1}{2}(\mathbf{D}_{n+1/2} + \mathbf{D}_{n+3/2})$

Index

asymmetric current sheet, 7
asymmetric reconnection, 19

Biermann-Battery effect, 33, 85, 89, 130
bifurcated current sheet, 7

central current sheet, 7
code FCI2, 89
code HECKLE, 43
Courant–Friedrichs–Lewy condition, 42
cyclotron term, 48, 66

de Hoffmann-Teller frame, 4, 60
diffusion region, 4
drag force, 77, 80
driven reconnection, 21, 128
driver term, 48

electron diffusion region, 4, 84
electron heat flux, 50
electron inertia length, 4
electron pressure tensor, 48

fast reconnection, 10
finite Larmor radius effect, 41
frozen-in condition, 3

GEM Challenge, 12
guide field, 16

Harris sheet, 7, 59

ion diffusion region, 4, 63
ion inertia length, 4
isothermal closure, 47
isotropization term, 48, 66

LAPD, 31
Lundquist number, 10, 62

macro-particle, 44, 54
magnetic field lines, 2
magnetic piston, 128
magnetopause, 6, 18, 21, 26
magnetosheath, 6, 18, 26
magnetotail, 7, 13, 16, 22, 25, 27
MAGPIE, 28
meandering motion, 41
MMS, 25
MRX, 29
multi-point, 7, 25

Nernst effect, 53, 87
Newton Challenge, 22
normalized out-of-plane electric field, 98

Ohm's law, 10, 11, 46
out-of-plane electric field, 3, 4, 16, 21, 97
out-of-plane magnetic field, 17, 19, 31, 43, 63, 82, 99, 106, 113

Petscheck model, 10
plasmoid, 29, 35, 62, 81, 102, 103, 106, 121, 127, 132
proton radiography, 33, 87

quasineutrality, 45

RCF, 87
reconnection, 2
reconnection rate, 10, 16
Righi-Leduc effect, 52, 88, 89

slow reconnection, 10
snowplow effect, 101, 111, 115
Speiser orbits, 41
subcycling, 66
Sweet-Parker model, 9

THEMIS, 25
TNSA, 87

X point, 2, 12, 30, 41, 77, 132, 138

Titre: Modelisation numérique de la reconnexion magnétique dans les plasmas à haute densité d'énergie induit par laser.

Mots clés: simulation numérique, plasmas, laser, reconnection magnétique, astrophysique de laboratoire, schéma aux différences finies.

Résumé: Cette thèse est une étude numérique de la reconnexion magnétique dans les plasmas sans collision à l'aide d'un code cinétique. On peut étudier le processus de reconnexion magnétique lors d'expérience pour lesquels le plasma est creéṕar interaction d'un laser de puissance sur une cible solide. Durant cette thèse, nous avons inclus dans le code HECKLE les éléments permettant de rendre ces simulations plus réalistes pour les conditions lasers: les effets du tenseur complet des électrons ainsi que l'expansion super-Alfvénique du plasma. Nous avons ainsi mis en évidence le rôle du tenseur de pression pour réduire l'efficacité de la reconnexion, ainsi que les effets de température du plasma la rendant plus impulsionnelle.

Title: Numerical modeling of magnetic reconnection in laser-induced High Energy Density Plasmas

Keywords: numerical simulations, plasmas, laser, magnetic reconnection, laboratory astrophysics, finite difference scheme.

Abstract: This thesis is a numerical study of the magnetic reconnection in collisionless plasmas using a kinetic code. We can study the magnetic reconnection process during experiments for which the plasma is created by interaction of a power laser and a solid target. During this thesis, we included in the HECKLE code the elements allowing to make these simulations more realistic for the laser conditions: the effects of the electron six-component pressure tensor as well as the super-Alfvénic expansion of the plasma. We have thus highlighted the role of the pressure tensor to reduce the efficiency of the reconnection, as well as the plasma temperature effects making it more impulsive.